

https://dspace.org/

The layered marker sequence, main zone, Eastern Bushveld Complex - a model for modal layering.

Quadling, Kevin Edward

1996
https://hdl.handle.net/10539/27807

Downloaded from a DSpace repository. https://dspace.org/

The Layered Marker Sequence, Main Zone, Eastern Bushveld Complex- A Model for Modal Layering

Kevin Edward Quadling

Degree awarded with distinction on 4 December 1996.

A dissertation submitted to the Faculty of Science, University of the Witwatersrand, Johannesburg, in fulfilment of the requirements for the degree of Master of Science in Geology.

Johannesburg, 1996

Abstract

This project involved the study of the Layered Marker Sequence of interbedded melanocratic and leucocratic rocks that occurs in the Main Zone of the Eastern Limb of the Bushveld Complex. The main aim was to develop a model for the formation of the observed layering. To achieve this a wide range of data has been gathered. In the field the layered package can be followed for a considered distance along strike. Individual layers however tend to terminate along strike. Layer contacts are sharp and there is a distinct lack of grading within layers. Modal variations between layers caused primarily by a change in the relative proportion of plagioclase, are pronounced, whilst the ratio of clinopyroxene to orthopyroxene remains reasonably constant. The rock types making up the sequence exhibit a planar fabric defined by the bedding parallel orientation of the tabular plagioclase crystals. These crystals also appear orientated within this plane. Mineral compositions vary between layers and can be ascribed to trapped liquid shift effects. Whole rock geochemistry varies strongly between rock types. The variation in the concentrations of the more compatible elements can be explained by modal variation. The trends shown by the incompatible elements indicate the importance of the trapped liquid shift effects within these rocks. From these lines of evidence, the Layered Marker Sequence under discussion cannot be explained by models such as in situ crystallization, rhythmic nucleation, magma injection, pressure fluctuations, or the mass transfer of material due to differences in grain surface energies. The evidence collected may best be explained by a physical separation of phases out of a density current flowing into the chamber after detachment of the boundary layer from the sidewalls of the chamber.

Declaration

I declare that this dissertation is my own, unaided work. It is being submitted for the Degree of Master of Science in Geology in the University of the Witwatersrand, Johannesburg. It has not been submitted before for any degree or examination in any other University.



Kevin Edward Quadling

30th day of March 1996

Acknowledgements

I would like to thank my supervisor, Prof. R.G. Cawthorn, for his patience and invaluable assistance in many aspects of this study. Thanks are due to AAPS for making available borehole core and to the AARL for the use of their facilities in probing certain of the samples. Funding for this project was provided by the University of the Witwatersrand and the FRD.

Table of contents

1. Introduction 1-1

2. The Layered Marker Sequence 2-1

2.1 Profile A 2-3
2.2 Locality B 2-4
2.3 Locality C 2-6
2.4 Locality D 2-6
2.5 Locality E 2-6
2.6 Vertical and lateral characteristic of individual layers 2-10

2.6.1 Layer contacts 2-10
2.6.2 Lateral continuity of layers 2-12
2.6.3 Variation in layer thickness 2-16
2.6.4 Poikilitic anorthosite bodies 2-17

3. Techniques and sample preparation 3-1

3.1 Magnetic separation 3-4

3.1.1 Plagioclase separation 3-4
3.1.2 Pyroxene separation 3-4

3.2 X-ray Fluorescence Spectrometry 3-5
3.3 Instrumental Neutron Activation Analysis (INAA) 3-5
3.4 Mass Spectrometry 3-5
3.5 Electron Microprobe 3-6

4. Petrography 4-1

4.1 Mineralogy 4-2

4.1.1 Modal abundance 4-9
4.1.2 Vertical and lateral variation in mode within a layer 4-19

5. Petrofabric of plagioclase grains 5-1

5.1 Orientation 5-1
5.2 Grain size 5-3

6. Plagioclase compositions 6-1

6.1 Introduction 6-1
6.2 Analysis of plagioclase compositional variation in three profiles within Sekhukhuneland 6-3

6.2.1 Determination of the anorthite content of plagioclase 6-3
6.2.2 Vertical variation in plagioclase composition 6-14
6.2.3 Vertical variation in plagioclase composition through the layered marker 6-16
6.2.4 Microprobe analysis of selected plagioclase grains 6-17
6.2.5 Comparison between microprobe and XRF analyses 6-18

7. Pyroxene 7-1

7.1 Introduction 7-1
7.2 Analysis of pyroxene from three profiles within the eastern limb 7-3

7.2.1 Pyroxene compositions 7-7
7.2.2 Vertical variation of pyroxene compositions 7-14
7.2.3 Lateral variation in pyroxene composition 7-15
7.2.4 Comparison with other studies 7-16
7.2.5 Low-calcium pyroxene 7-17
7.2.6 Clinopyroxene 7-18

8. Whole rock geochemistry 8-1

8.1 Variation in major element abundances 8-4
8.2 Incompatible trace element distribution 8-6
8.3 Variation in compatible trace element abundances 8-8

9. Trace element analysis of mineral separates 9-1

9.1 Analysis of mineral separates by Instrumental Neutron Activation Analysis 9-1

9.1.1 Clinopyroxene 9-4
9.1.2 Low-calcium pyroxene 9-4
9.1.3 Plagioclase separates 9-5

9.2 REE abundances within the whole rock 9-6
9.3 Partitioning of selected trace elements between phases 9-6
9.4 Rb-Sr isotopes 9-7
9.5 Ba, Sr, Rb and K_2O in plagioclase 9-9

10. Discussion 10-1

10.1 Review of salient aspects 10-1

10.1.1 Field relations 10-1
10.1.2 Petrography 10-1
10.1.3 Petrofabrics 10-3
10.1.4 Mineral chemistry 10-4
10.1.5 Whole rock chemistry as determined by XRF analysis 10-11

10.2 Models to explain the layering 10-15

10.2.1 Pattern formation 10-16
10.2.2 Chemical effects of a magma injection 10-17
10.2.3 Change in a physical parameter 10-18
10.2.4 Rhythmic nucleation 10-18
10.2.5 In-situ crystallization 10-19
10.2.6 The mechanical separation of minerals into different layers 10-19

10.3 A depositional model for the formation of the marker 10-21

10.3.1 Observations which support such a model 10-22

10.4 Conclusions 10-23

List of figures

Figure 1.1 Geological map showing the lateral distribution of the Bushveld Igneous Complex rocks. (1-1)

Figure 1.2 Stratigraphic position of the Layered Marker Sequence within the Main Zone of the Bushveld Complex. (1-2)

Figure 2.1 Locality map showing the approximate positions of the sample profiles. (2-1)

Figure 2.2 Distribution of the layered marker in a portion of the eastern limb of the Bushveld Complex.(2-2)

Figure 2.3 Stratigraphic column for profile A on the farm Quartz Hill. To the right of the column is listed the samples at their approximate stratigraphic positions. H=hangingwall; F=footwall; M=melanocratic; L=leucocratic; t=top of layer; m=middle of layer; b=bottom of layer. N refers to profile A. (2-3)

Figure 2.4 Stratigraphic column for profile B. The samples are listed to the right of the column at their appropriate stratigraphic positions. Sample nomenclature is as per Fig. 2.3. S refers to profile B. The numbers for sample 19MS refer to the distance along strike, measured from the southernmost limit of the outcrop, from where the samples have been taken. (2-5)

Figure 2.5 Stratigraphic column for profile C. The exposure of the hangingwall and footwall lithologies is poor. For this reason only the layered marker sequence was sampled. (2-7)

Figure 2.6 Stratigraphic column for a portion of borehole MG4. This borehole was drilled on the farm Mapochsgronde, near the town of Roossenekal. (2-8)

Figure 2.7 Stratigraphic column for the Layered Marker Sequence exposed at locality E. (2-9)

Figure 2.8 Map of a pavement exposure of the Layered Marker Sequence near locality B. (2-11)

Figure 2.9 Schematic diagram showing typical layer termination morphology. (2-12)

Figure 2.10 Map of the accessible portion of the vertical exposure of the Layered Marker Sequence as exposed at locality E. (2-15)

Figure 2.11 (a) Variation in underlying leucocratic layer thickness with the overlying melanocratic layer thickness. (2-16)
(b) Variation in underlying melanocratic layer with the overlying leucocratic layer thickness.

Figure 3.1 Sketch of a jolly balance used to measure the specific gravity of samples (after Klein et al., 1985). (3-3)

Figure 4.1 Modal distribution of minerals in a portion of the main Zone (after Molyneux, 1974). The two arrows define the approximate stratigraphic interval studied in this project. (4-1)

Figure 4.2 Sketch of a thin section from a leucocratic samples towards the top of the layered marker sequence. Note the irregular plagioclase outlines but distinctive lath shapes. Note also the infilling nature of the pyroxene phases. (4-3)

Figure 4.3 (insert) Sketch of a portion of a thin section taken from a melanocratic layer towards the top of the sequence. The width of the field of view is approximately 4mm. Note the large granular pyroxene grains and irregular interstitial plagioclase crystals. (4-3)

Figure 4.4 Variation in mode of samples as determined by point counting of one thin section per sample. The figures attached to each bar reflect the calculated pyroxene content as inferred from the specific gravity of the sample. (4-10)

Figure 4.5 Variation in modal abundance for samples from profile B, as determined by point counting and specific gravity measurements (figures in brackets). Key is as per Fig. 4.4. (4-11)

Figure 4.6 Variation in modal abundances for selected samples from profile C. Modal data is as determined by Pillay (1990). (4-12)

Figure 4.7 Variation in modal abundances for samples from profile A, B and C. Solid symbols refer to those samples classified as mafic in the field, whilst the empty symbols refer to the leucocratic samples. H and F refer to hangingwall and footwall samples. the arrows indicate the inferred modal abundances as determined by specific gravity measurements. (4-13)

Figure 4.8 Calibration curve for the analysis of plagioclase volume % from specific gravity measurements. (4-15)

Figure 4.9 Plagioclase abundance as calculated from specific gravity measurements of samples taken from profile B. (4-16)

Figure 4.10 Plagioclase abundance as calculated from specific gravity measurements of samples taken from profile A. (4-17)

Figure 4.11 Plagioclase abundance as calculated from specific gravity measurements of samples taken from profile E. (4-18)

Figure 5.1 A: Sketch of a portion of a vertically orientated thin section from a leucocratic layer. Note the well developed horizontal fabric. This is well illustrated by the rose diagram. (5-2)
B: Sketch of a portion of a thin section that was cut parallel to the plane of layering. This shows the linear habit of plagioclase within this plane. This lineation is clearly shown by the attached rose diagram. (5-2)

Figure 5.2 Rose diagram showing the orientation of plagioclase laths in numerous samples from profile A. The left column of rose diagrams refers to the elongate grains (aspect ratio> 2). The right column refer to the equant grains. "Top" and "base" refers to the position from where the sample was taken within a layer. The numbers to the top left of each rose diagram refer to the number of well-formed plagioclase laths measured from each thin section. Solid and open shading refer to melanocratic and leucocratic samples respectively. (5-4)

Figure 5.3 Plot of the average plagioclase grain size, calculated from the 30 largest grains measured from a single thin section per sample, plotted against the volume % plagioclase (determined from point counting using the same thin sections). (5-5)

Figure 6.1 Variation in the composition of plagioclase through subzone B and a portion of subzone C (after Molyneux, 1974). The two line styles refer to two different profiles in the eastern Bushveld. (6-1)

Figure 6.2 Variation in plagioclase composition across the Pyroxenite Marker along four profiles in the eastern limb of the Bushveld Complex (after Marais, 1977). (6-2)

Figure 6.3 Variation in plagioclase compositions across the Layered Marker up to and including the Pyroxenite Marker. (6-15)

Figure 6.4 Variation in %An. for samples from the Layered Marker. Filled symbols refer to the mafic samples, open symbols to the leucocratic samples. The dashed lines refer to the average composition of direct hangingwall and footwall samples. (6-16)

Figure 6.5 Comparison of plagioclase compositions as determined from XRF and microprobe analyses. (6-18)

Figure 7.1 Variation in the composition of orthopyroxene, measured microscopically, across the Pyroxenite Marker (from Molyneux, 1974). (7-1)

Figure 7.2 Variation in orthopyroxene composition across the Pyroxenite Marker (0m). The numbers next to each curve refer to compositions determined by XRF analysis of separates (diagram modified after Marais, 1977). (7-2)

Figure 7.3 Comparison of pyroxene compositions from selected samples as determined by microprobe (p) and XRF analysis (x). Field and tie lines join data points for one sample whilst the other data refer to the other sample. (7-11)

Figure 7.4 Variation in pyroxene compositions for profiles A and B. The filled symbols refer to the hangingwall and footwall samples whilst the hollow symbols refer to those samples from the Layered Marker Sequence. (7-14)

Figure 7.5 Vertical variation in pyroxene composition for samples from the Layered Marker Sequence. Symbol size is proportional to the calculated analytical error. (7-15)

Figure 7.6 Ternary plot showing the overall range in composition of the pyroxenes analysed in this study. Also included, for comparison, is data from other studies. (7-16)

Figure 7.7 Detailed plot of the compositional variation shown by low-calcium and clinopyroxene separates as analysed in this study. The comparison of those separates analysed by XRF are identified by the enclosed fields. Those data points that plot outside these fields have been analysed by microprobe. (7-17)

Figure 8.1 Stratigraphic column showing the approximate positions from where the whole rock samples, that have been analysed, were taken. (8-1)

Figure 8.2 Variation of MnO abundance with MgO. (8-4)

Figure 8.3 Variation of TiO_2 abundance with MgO. (8-5)

Figure 8.4 Variation of Al_2O_3 abundance with MgO (8-5)

Figure 8.5 (A) Variation in P_2O_5 concentration with changing mode. (8-7)
(B) Variation in P concentration between samples from profile B. Samples are arranged in stratigraphic order but not to scale. (8-7)

Figure 8.6 Variation in Ba concentration with changing mode. (8-7)

Figure 8.7 Plot of Ni versus Co. (8-8)

Figure 8.8 Plot of Ni versus Cr. Data points in the main graph are for samples from the layered interval. Additional samples points plotted in the inserted graph reflect the composition of hangingwall samples. (8-9)

Figure 8.9 plot of Sr versus Al_2O_3 (8-9)
Figure 9.1 Chondrite normalized rare earth element abundances (Evenson, 1978) in clinopyroxene separates from profile A. (9-1)
Figure 9.2 Chondrite normalized REE abundances in orthopyroxene separates from profile A samples. (9-3)
Figure 9.3 Chondrite normalized REE abundances in plagioclase separates from selected profile A samples. (9-3)
Figure 9.4 Concentration of REE in clinopyroxene separates from the Layered Marker Sequence. (9-4)
Figure 9.5 Concentration of REE's in low -calcium pyroxene separates from profile A. (9-5)
Figure 9.6 Concentration of REE's in plagioclase separates from profile A samples. (9-5)
Figure 9.7 Vertical variation in the initial Sr-isotopic ratio. The symbol width reflects the approximate magnitude of the analytical precision. Solid symbols refer to mafic samples; open to leucocratic samples; stippled to gabbronoritic samples. The remaining sample has been taken from the leuconoritic rock type that occurs within the Pyroxenite Marker. (9-10)
Figure 9.8 Variation in Ba, Rb, Sr and K_2O in selected plagioclase separates from profile A. Samples are in stratigraphic order but not to scale. (9-11)
Figure 10.1 Variation in clinopyroxene and low-calcium pyroxene abundance in selected whole-rock samples as measured using a CIPW normalization calculation. The pluses refer to the hangingwall samples, crosses to the footwall samples, large filled circles to leucocratic samples and the smaller filled circles to the melanocratic samples. The weight percent of total pyroxene is shown by the numbered diagonal lines. (10-2)
Figure 10.2 Variation in the mg-number of low-calcium pyroxene with varying proportions of pyroxene within the samples analysed. The trends shown by the clinopyroxene are similar. (10-5)
Figure 10.3 Abundance of selected REE in liquids in equilibrium with each sample. In calculating these values 10% trapped liquid has been assumed. The thick solid (green) line represents the top envelope of the compositonal range for marginal rocks of the upper critical zone, as determined by Harmer et al., (1985). The thick dashed (purple) line defines the top envelope of the compositional range for 'B1-type' marginal rocks and sills, including pyroxenites and norites (Harmer and Sharpe, 1985). Note that a greater proportion of trapped liquid would push the calculated curves, for samples from the Layered Marker Sequence, to lower abundances. (10-8)
Figure 10.4 Ba versus P diagram for selected samples from profile B. The empty symbols refer to the leucocratic and the filled symbols to the melanocratic samples. (10-14)

List of photographic images presented

Plate 2.1 Photograph showing the non-graded character of melanocratic and leucocratic layers. (2-10)

Plate 2.2 These two photographs show the type of layer terminations the morphology of which is illustrated in Fig. 2.9. this type of layer morphology is common and could indicate channel development. (2-13)

Plate 2.3 Photograph of two vertical rock faces that meet at ~90°. It illustrates the fact that the mafic layers terminate both along strike and down dip. Note also the wispy nature of the lowermost melanocratic layer. (2-14)

Plate 2.4 Photograph of the upper portion of the Layered Marker at a locality near profile B. Towards the bottom of the photograph mottled anorthosite domes upwards, cutting into the melanocratic layers. (2-18)

Plate 2.5 (Insert) Starkly layered east/west orientated vertical outcrop.
(Principle image) The layering (seen in the insert) fades into mottles 10m down dip. (2-18)

Plate 2.6 Chaotically disturbed layering seen just south of locality E. Note that towards the top of the sequence the mafic layers pass undisturbed over the disturbed and brocken layers. (2-19)

Plate 4.1 Large inverted pigeonite grain with coarse exsolution lamellae, seen under normal and crossed polars. Lower photograph rotated through 90°. Field of view= 4mm. (4-4)

Plate 4.2 Typical inverted pigeonite grain, with partial rim of biotite, seen under normal and crossed polars. Note the well developed orientations of exsolution textures. Field of view=4mm. (4-5)

Plate 4.3 Top: large orthopyroxene grain form a melanocratic layer near the top of the layered marker;
Bottom: same grain seen under crossed polars. Note the distinct lack of exsolution. (Field of view=4mm) (4-6)

Plate 4.4 Top: irregular grain of low-calcium pyroxene from a leucocratic sample. (4-7)
Bottom: sketch of a field of view showing the irregular and often interstitial character of the orthopyroxene and clinopyroxene grains within the highly leucocratic samples. (4-7)

Plate 4.5 (top) Irregular clinopyroxene grain seen under crossed polars. This is the typical character of clinopyroxene in the anorthositic layers. Field of view 4mm wide. (4-8)
(Bottom) Anhedral clinopyroxene grain from a replacement anorthositic body, showing replacement by biotite and rimming by green amphibole. (4-8)

List of tables presented

Table 3.1	List of samples studied from profiles A and B.	(3-2)
Table 4.1	Specific gravity measurements for selected samples. Thin section off-cuts and rock chips were used to determine the samples SG's.	(4-14)
Table 4.2	Specific gravity and plagioclase model variations within single layers. The errors in plagioclase modes is ~3%.	(4-19)
Table 5.1	Grain size data from the analysis of selected orientated thin sections.	(5-3)
Table 6.1	Duplicate major element analyses of selected plagioclase separates from profile B.	(6-4)
Table 6.2a	Average plagioclase analyses for samples from profile A.	(6-5)
Table 6.2b	Results of a CIPW normalization of plagioclase analyses for samples from profile A.	(6-6)
Table 6.3a	Average plagioclase analyses from samples from profile B.	(6-7)
Table 6.3b	Results of a CIPW normalization of plagioclase analyses for samples from profile B.	(6-8)
Table 6.4a	Average plagioclase analyses for samples from profile C.	(6-9)
Table 6.4b	Results of a CIPW normalization of plagioclase analyses for samples from profile C.	(6-9)
Table 6.5	Errors calculated from the duplicate analysis of plagioclase samples. The method used to calculate the errors listed in this table is outlined in Appendix 4.	(6-9)
Table 6.6	Modelled oxide abundances within plagioclase of a specific anorthite composition and the calculated composition based on these values.	(6-11)
Table 6.7	% An. In plagioclase calculated from oxide abundances (with free quartz and K_2O excluded) from profile C.	(6-12)
Table 6.8	% An. In plagioclase calculated from oxide abundances (with free quartz and K_2O excluded) for samples from profile A.	(6-13)
Table 6.9	% Anorthite in plagioclase calculated from oxide abundances (with free quartz and K_2O excluded) for samples from profile B.	(6-14)
Table 6.10	Microprobe analyses and composition (%An.) of selected plagioclase grains from samples of the layered marker sequence at locality B.	(6-17)
Table 6.11	Microprobe analyses and compositions (%An.) of selected plagioclase grains from locality B	(6-17)
Table 7.1a	Analysis of orthopyroxene separates from profile A.	(7-3)
Table 7.1b	Analysis of orthopyroxene separates from profile B.	(7-4)
Table 7.2a	Analysis of clinopyroxene separates from profile A.	(7-5)
Table 7.2b	Analysis of clinopyroxene separates from profile B.	(7-6)
Table 7.3	Analysis of analytical errors.	(7-7)
Table 7.4	Analytical error in the calculation of pyroxene compositions.	(7-7)
Table 7.5	Cationic proportions of Ca, Mg, Fe and mg-number for low-calcium pyroxene separates from profile A.	(7-8)
Table 7.6	Cationic proportions of Ca, Mg and Fe and mg-number for low-calcium and clinopyroxene separates from profile B.	(7-9)
Table 7.7	Cationic proportions of Ca, Mg, Fe and mg-number for low-calcium and clinopyroxene separates from profile C.	(7-10)
Table 7.8	Microprobe analyses of orthopyroxene grains within selected samples from profile A.	(7-11)
Table 7.9	Microprobe analyses of clinopyroxene grains within selected samples from profile A.	(7-12)
Table 7.10	Microprobe analyses of low-calcium pyroxene grains within selected samples from profile B.	(7-13)
Table 7.11	Microprobe analyses of clinopyroxene grains within selected samples from profile B.	(7-13)
Table 7.12	Comparison of mg-number of low-calcium pyroxene with height in the three profiles.	(7-16)
Table 8.1	Geochemistry of selected whole rock samples from profile B.	(8-2)
Table 8.2	Geochemistry of selected whole rock samples from profile C. These samples were analysed prior to this study. P was analysed for in the same run as for samples from profile B.	(8-3)
Table 9.1	Concentrations of selected trace elements, as determined by Neutron Activation Analysis, in separates from selected profile A samples (calibration data is presented in appendix 6).	(9-2)
Table 9.2	REE abundances in the whole rock samples as calculated from the individual analyses for the mineral separates.	(9-6)
Table 9.3	Ratios of selected trace elements analysed by INAA of separates from profile A.	(9-7)
Table 9.4	Rb-Sr isotopic analyses of selected samples from profile A.	(9-8)

Table 9.5 Variation in Ba, Sr, Rb and K_2O in selected plagioclase separates from profile A samples (Values determined by XRF are in a normal typeface, those determined using INAA are in bold and those measured by isotope dilution mass spectrometry are underlined. The errors for the method are listed at the bottom of the table. (9-11)

Table 10.1 CIPW normalized abundances for selected samples from profile B. The figures in brackets refer to point counting measurements. (10.3)

Table 10.2 Crystal melt partition coefficients for selected REE. Values for clinopyroxene for La, Nd, Sm and Yb have been taken from Hart et al. (1993) and those for Ce, Eu and Ho from Irving (1978). (10-7)

Table 10.3 Composition of liquid calculated as having been in equilibrium with the footwall sample (F2N). 10% trapped liquid was assumed. (10-8)

Table 10.4 Calculated mineral compositions (in ppm) for each sample assuming that the liquid, which produced each layer, was similar to that which produced the footwall samples. The actual values measured are listed in the shaded columns. (10-9)

Table 10.5 Variation in the calculated liquid and plagioclase compositions in response to a 10% decrease in plagioclase mode and a 5% increase in the abundance of each pyroxene phase. All values represent averages of calculated values for the Layered Marker Sequence samples. Subscript o refers to the initial condition and subscript m to the modified data. The modes are listed in % plagioclase and the other calculated data in ppm of the listed element. (10-10)

Table 10.6 Calculated Rb abundances in plagioclase (C_p^*) and the whole rock sample (C_s) with differing proportions of trapped liquid (calculated using equation 5) compared to the actual measured abundances. (10.11)

1 Introduction

The Bushveld Complex formed 2060ma ago (Walraven et al., 1990). The complex formed by the intrusion of a significant volume of magma into approximately 9km of lithic and volcanic deposits of the Transvaal Sequence on the Kaapvaal Craton (Button, 1976). The intruded magma may have filled an array of conical shaped magma chambers that then merged to form the northern,

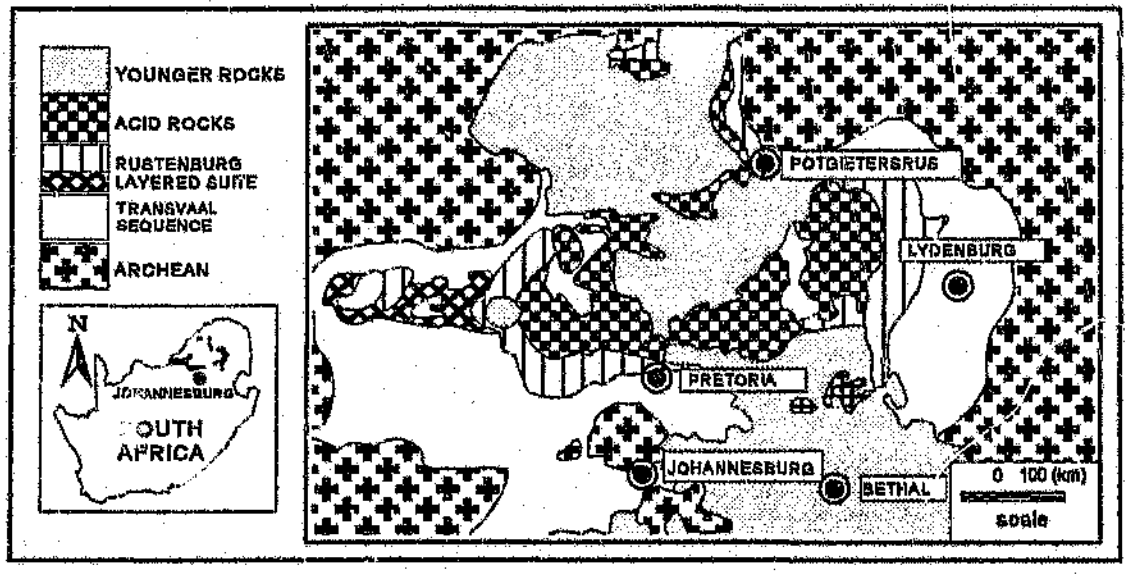


Figure 1.1 Geological map showing the lateral distribution of the Bushveld Igneous Complex rocks.

eastern and western compartments (Sharpe and Snyman, 1980). The rocks overlying the complex and the complex itself have since then been extensively eroded. Even so the complex still outcrops over an area of 12200 km^2 (SACS, 1980) with a maximum diameter of ~450km (Fig. 1.1).

The complex has ultramafic, mafic and felsic components. The marker under discussion comes from the Main Zone of the mafic portion of the complex. This zone has traditionally been subdivided into a number of subzones (von Gruenewaldt, 1973; Molyneux, 1974). Subzone A consists of gabbronoritic rocks, pyroxenite, spotted and mottled anorthosites. The top of this subzone is defined by the "upper mottled anorthosite" marker which consists of 200m of poikilitic anorthosite, leucogabbro and gabbro. Subzone B consists of gabbronoritic rock and represents some of the most differentiated rock within the zone. There are very few markers within this subzone. The top of this subzone is defined by the Pyroxenite Marker (von Gruenewaldt, 1970). It is within this subzone that the layered marker under discussion occurs (Fig. 1.2). Subzone C

consists of gabbronoritic rock, pyroxenite and poikilitic anorthosite. The top of this subzone is defined by either the first appearance of cumulus magnetite, defined by a conspicuous magnetite anorthosite some 30m below the lowest magnetite layer (Molyneux, 1974) or at the so-called Main Magnetite Layer (Willemse, 1969). The former is more logical.

The Main Zone has been studied in less detail than the other zones due to its mostly homogenous nature and relatively few marker horizons. One horizon that does occur is the Pyroxenite Marker. This occurs in both the eastern and western compartments. It is made up of one or a series of pyroxenites (von Gruenewaldt, 1973; Molyneux, 1974; Klemm et al., 1985 and

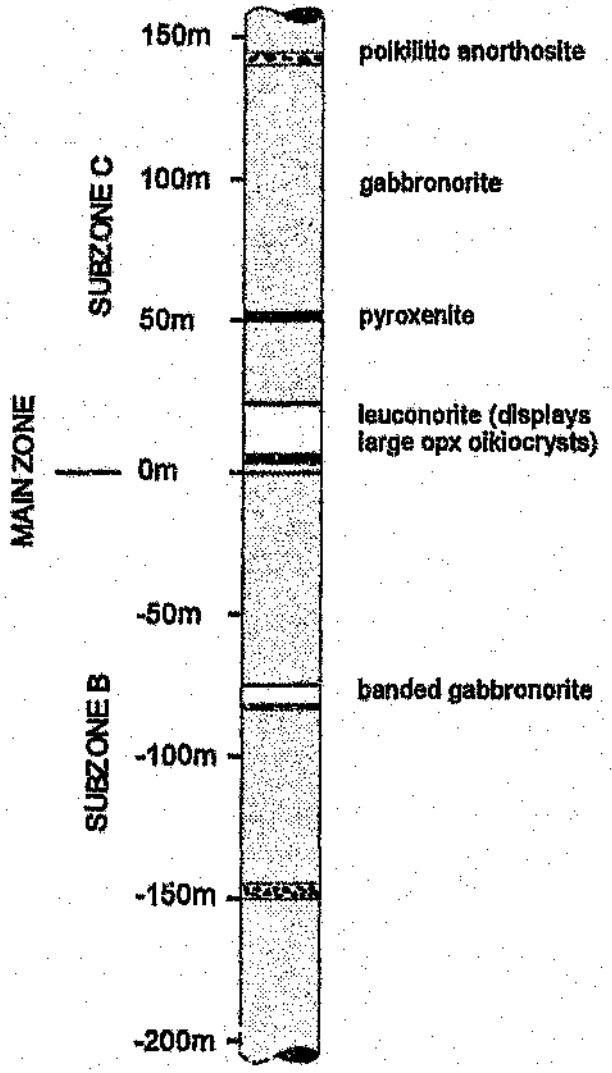


Figure 1.2 Stratigraphic position of the Layered Marker Sequence within the Main Zone of the Bushveld Complex.

Cawthorn et al., 1991) and has been attributed to the injection of less differentiated magma due to mineralogical and geochemical breaks across it. Sr-isotopic systematics conclusively prove that the magmas that produced the rocks above the Pyroxenite Marker and those below are not the same (Hamilton, 1977). However the interpretation of the chronology of events that lead to the stratigraphic package is debated. Sharpe (1981 & 1985) argued in favour of the residual magma, after crystallizing the Critical Zone cumulates, being jacked up by the magma that formed the subzones A and B of the Main Zone and which subsequently mixed with the residual magma above it to produce the Pyroxenite Marker sequence, the cumulates of subzone C and those higher up in the sequence. Others (Cawthorn et al., 1991) argue that the magmas that produced the Critical, Main and Upper Zones were separate magmas generated and emplaced successively.

Immediately below the Pyroxenite Marker occurs an interlayered sequence of melagabbronorite/gabbronorite and leucogabbronorite/anorthosite. It was first identified by Molyneux (1974), who photographed it and traced it laterally in his mapping of a portion of the Eastern Limb, but did not offer any explanation of how such layering may have occurred. The layering within the layered marker under discussion differs from the well-known mono-mineralic layers of chromite (Critical Zone), magnetite (Upper Zone), pyroxenite and anorthosite (Critical Zone) that occur elsewhere in the Bushveld succession, in that they contain variable proportions of plagioclase and two pyroxenes.

Modal layering is a commonly seen feature of many layering intrusions. The layering under discussion appears similar to the "intermittent layering" of the Skaergaard intrusion as documented by McBirney and Noyes (1979) and Conrad and Naslund (1989). The gabbroic zone of the Lilloise intrusion of East Greenland, which is approximately 2000m thick, is also strongly layered with modal layering dominating. Layers varying in size from centimetres to metres thick. However, as in the case of the layering under discussion, grading is never conspicuous (Brown, Chambers and Becker, 1987). The Fongen-Hyllingen layered mafic complex of Norway is also dominated by modally layered, mainly gabbroic and dioritic rocks (Wilson et al., 1987). Individual modal layers are isomodal or density graded and vary from inch scale to layers of over a metre thick. In addition marker horizons are not well developed as layers are often not traceable over distances of more than 10's of metres. The layering also occasionally displays features associated with sedimentary rocks. These include trough structures, angular discordances, load-casts and slumps. Mathison and Booth (1990) described macro rhythmic layering (involving interlayered zones of melagabbronorite, 1 to 10m thick, and leucogabbronorite, 5 to 10m thick) in the Windimurra gabbroid complex of Western Australia. These layers appear very similar to those under discussion

here except for their thicknesses.

Several, vastly different, models have been developed to explain the modal layering seen in many layered complexes. The layered marker, of the Bushveld complex, is a good example of modal layering and the extensive development of the marker within the Eastern Limb of the complex affords the opportunity to study variations in chemistry and mode both vertically and over great distances laterally. Therefore modal, petrofabric, compositional and geochemical data has been collected from four profiles across the layered sequence and will be used to evaluate mechanisms of layering and to develop a model for the formation of the layered marker sequence under discussion.

2. The Layered Marker Sequence

The layered marker has been followed continuously for 17km along strike (Fig.2.2). It can be traced further southward (Fig. 2.1), from Madibaneng to the Steelpoort road (profile C) (Molyneux, 1974; D. Harney, pers. comm., Pillay, 1990). Further south thorough mapping failed to pick up this marker (von Gruenewaldt, 1973). However, exposure in this area is not as good as in the north and outcrops are often inaccessible. In and around Roossenekal small layered outcrops have been found by the author in the footwall to the Pyroxenite Marker. In addition Anglo American Prospecting Services intersected a starkly banded succession in a borehole on the

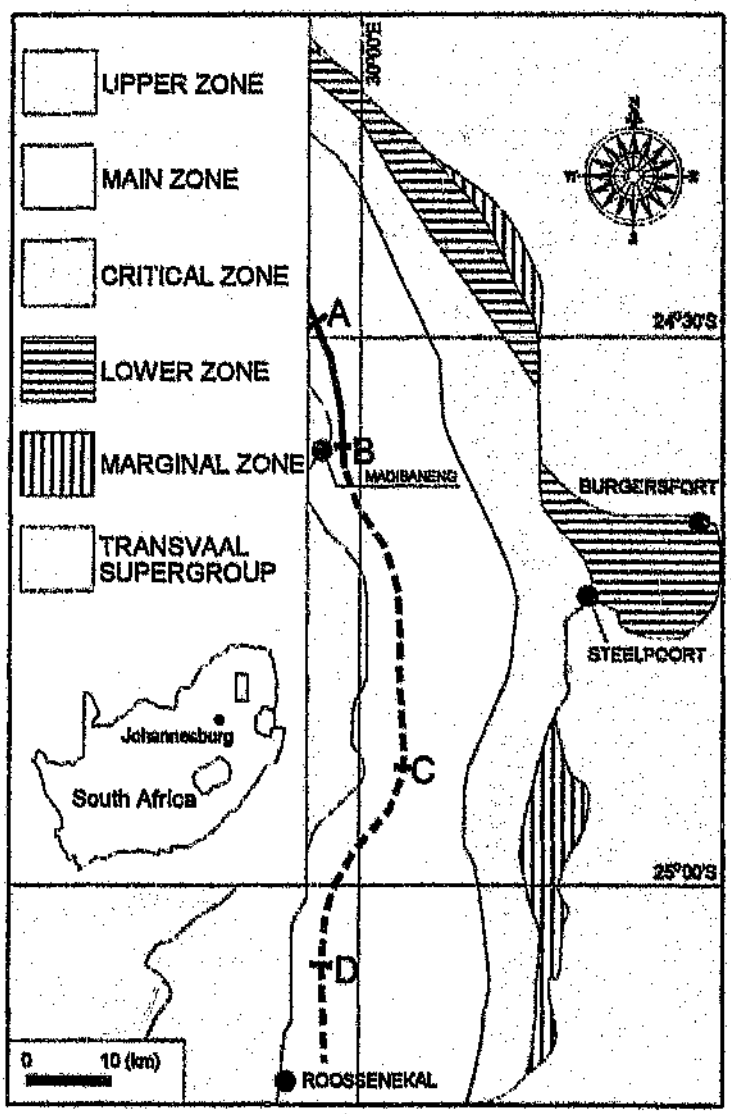


Figure 2.1 Locality map showing the approximate positions of the sample profiles

farm Mapochsgronde, just northeast of Roossenekal (locality D, Fig 2.1). Boreholes from the poorly exposed western Bushveld have not intersected this sequence (Mitchell, 1985; Cawthorn et al. 1990). Therefore the marker sequence would appear to be intermittently developed over a significant strike distance (>80km) in the Eastern Limb of the complex.

This marker was sampled at localities A-D (Fig. 2.1 & 2.2). A detailed description of the layered marker sequence at each of these localities as well as of the footwall and hangingwall lithologies is presented below.

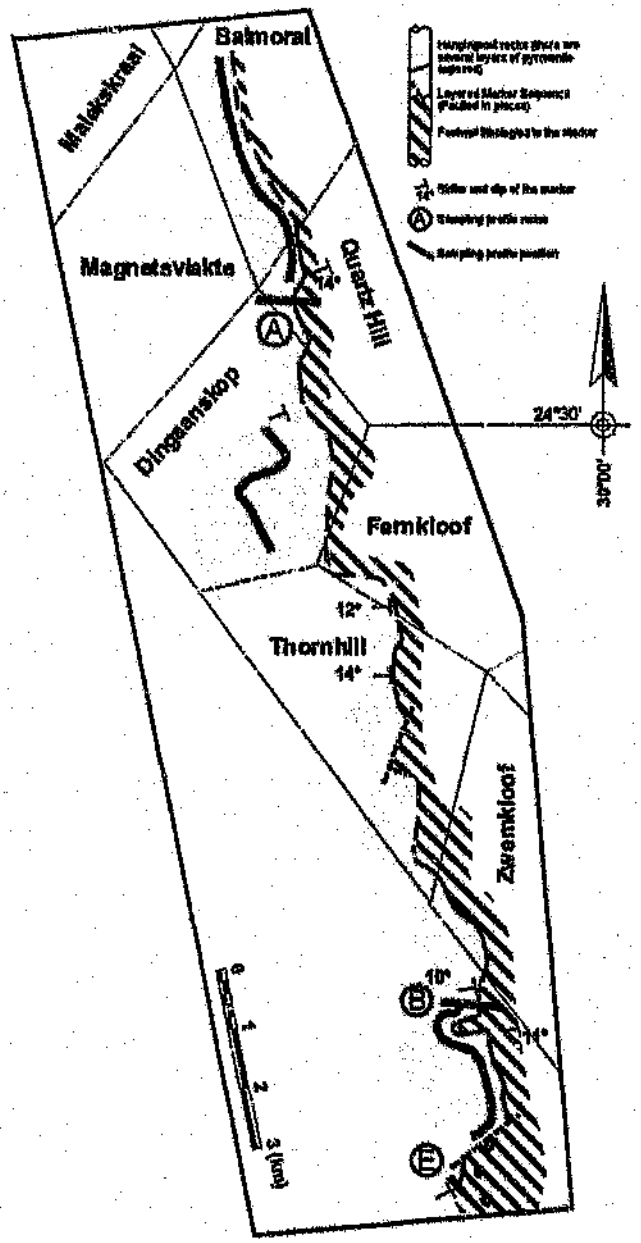


Fig. 2.2 Distribution of the layered marker in a portion of the eastern limb of the Bushveld Complex.

2.1 Profile A (Fig. 2.3)

Profile A is on the farm Quartz Hill, within Sekhukhuneland. Here the layered marker sequence outcrops at the foot of a range of low hills. As a result the exposure of the basal portion of the sequence in this area is not complete. The footwall is gabbronoritic. The layered sequence is approximately 12m thick (Fig.2.3) and dips to the west at a shallow angle. Forty-four layers are exposed. The leucocratic layers varying in thickness from 4 to 61 cm and the mafic layers from 1 to 26 cm. The average layer thicknesses are 24 and 7 cm for leucocratic and melanocratic layers respectively. Towards the base the mafic layers are gabbronoritic to mela-gabbronoritic, whilst towards the top they are considerably thinner and of feldspathic pyroxenite. The leucocratic layers towards the top are more leucocratic than towards the base. The direct hangingwall to the layered

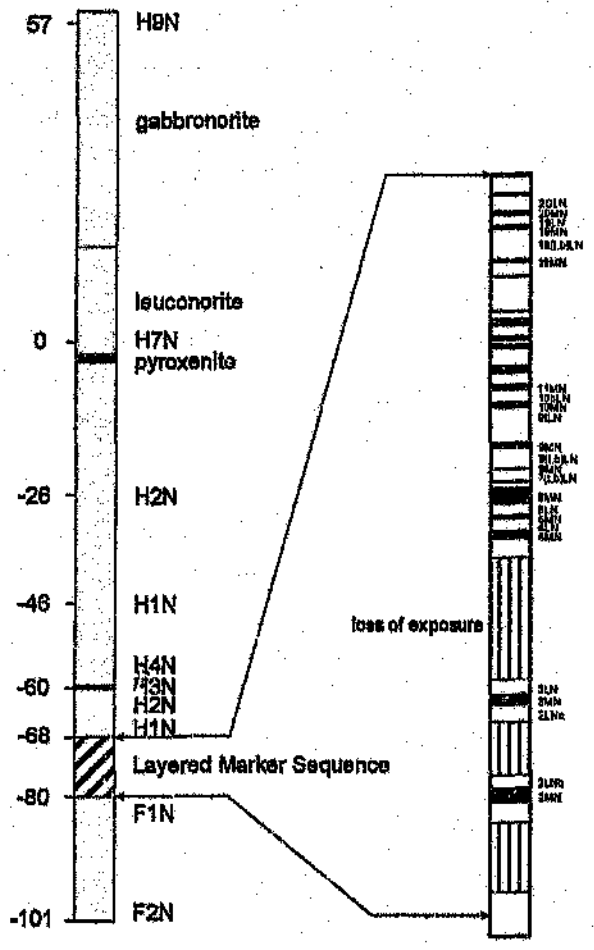


Figure 2.3 Stratigraphic column for profile A on the farm Quartz Hill. To the right of the column is listed the samples collected at their appropriate stratigraphic positions. H=hangingwall; F=footwall; M=melanocratic; L=leucocratic; t=top of layer; m=middled of layer; b=bottom of layer. N refers to profile A.

succession is laminated leucocratic gabbronorite. The rock appears laminated due to the layering parallel orientation of the plagioclase laths. The plagioclase laths, lying with their flat tabular sides parallel to the layering, often define an anorthositic, one crystal thick, layer overlain by a similarly thin layer containing the pyroxene and some plagioclase. This gives an almost pin-striped appearance to the rocks which is a characteristic of both footwall and hangingwall lithologies. Approximately 8 metres above the marker is a well defined pyroxenite layer. This is followed by 60m of uniform gabbronorite. The pyroxenites of the Pyroxenite Marker (as defined by Molyneux, 1974) were not precisely located. However pyroxenite rubble was found in the vicinity. A thick spotted leuconoritic package, with large (0.5cm) orthopyroxene crystals set in an anorthositic matrix, was noted. This is overlain by gabbronorite. The different lithological types were sampled, the samples being listed on the accompanying figure at their appropriate stratigraphic positions (Fig. 2.3).

2.2 Locality B

This locality is 12km to the south of A (Fig. 2.2) and occurs just south of the farm Zwemkloof. In this area the outcrops are typically near the top of the range of hills and therefore the complete succession is frequently well exposed (Fig. 2.4.). The footwall is of uniform gabbronorite. The layered marker sequence itself is approximately 10 metres thick and consists of about fifty-two layers. The average thickness of leucocratic and mafic layers is 24 and 9 cm respectively. The mafic layers range from 1 to 43 cm and the leucocratic layers vary from 7 to 116 cm thick. Ten metres above the layered sequence is a thick (1m) pyroxenite. This is overlain by 66m of uniform gabbronoritic material. This is in turn overlain by a thin pyroxenite layer. Above this layer is a thin spotted leuconoritic unit with large orthopyroxene crystals in an anorthositic matrix. This rock is very distinctive and can be correlated between the profiles. A thick (2m) pyroxenite is exposed above this leucocratic unit. The leuconorite then persists as a 20m thick succession above which another pyroxenite layer (1m thick) is exposed. This is overlain by uniform medium grained gabbronorite. Molyneux (1974) described the Pyroxenite Marker in this area as a 60 m thick package consisting of 2 pyroxenites subdivided by gabbroic rock. The 2m thick pyroxenite noted in the current study appears correlatable to the basal pyroxenite of the Pyroxenite Marker as defined by Molyneux (1974). The top pyroxenite noted by Molyneux (60m above the basal one) was not encountered.

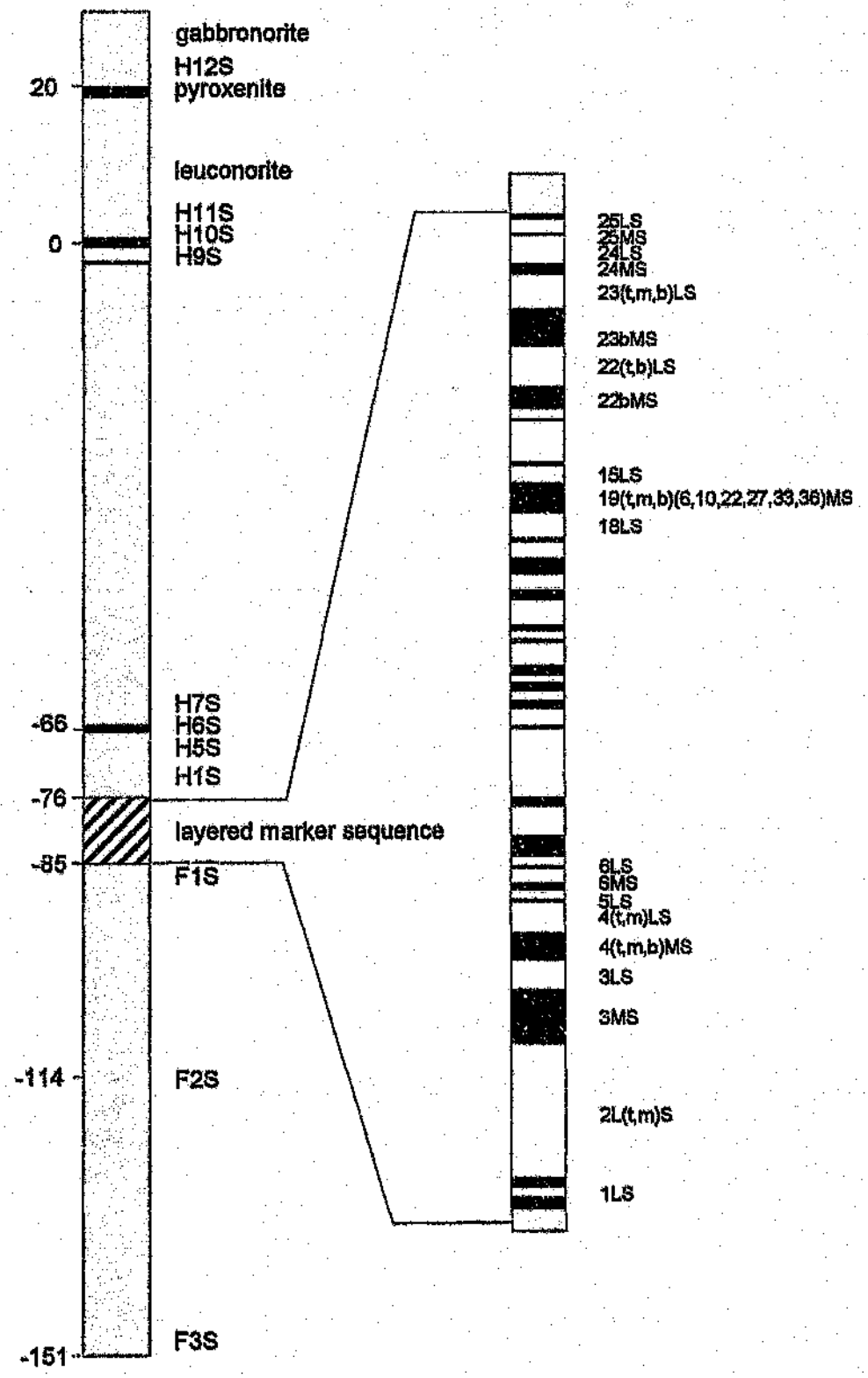


Figure 2.4 Stratigraphic column for profile B. The samples are listed to the right of the column at their appropriate stratigraphic positions. Sample nomenclature is as per Fig. 2.3. S refers to the profile B. The numbers for sample 19MS refer to the distances along strike, measured from the southernmost limit of the outcrop, from where the samples have been taken.

2.3 Locality C

The thickest section measured is exposed in a stream bed at locality C. This is ~45 km to the south of locality B. 190 layers are exposed with a cumulative thickness of 20 m. The average layer thicknesses are 13 cm for mafic layers and 9 cm for leucocratic layers. The mafic layers range in thickness from 2 to 56 cm and the leucocratic layers from 0.5 to 32 cm (Fig. 2.5). The basal contact to uniform gabbronorite is exposed, but the upper contact is hidden.

This locality has been documented by Pillay (1990), and her results are included in this study to allow for a discussion into the lateral variability of the sequence.

2.4 Locality D

Closer to Roossenekal the marker appears quite different. In this area surface exposure is generally poor, however small layered outcrops have been found. A borehole intersection of the Layered Marker, in this area, has been logged (Fig. 2.6). This intersection, though not complete due to the intrusion of a dyke, consists of a 3m succession consisting of ninety-two layers. The leucocratic layers are typically anorthositic and less than 0.5 cm thick and the mafic layers are predominantly of feldspathic pyroxenite. Due to the fact that core was available for logging, the hangingwall lithologies could also be studied in great detail. There is a wide variety of lithological types. The Pyroxenite Marker sequence is similar to that which occurs in the north but thinner. The marker appears to be made up of two thick orthopyroxenites subdivided by the same leuconoritic rock type identified in the north.

2.5 Locality E

This locality is a 40 m wide and 15 m high vertical exposure of the Layered Marker sequence ~3 km south of locality B. It was studied as an example of a down dip orientated outcrop. 39 mafic layers are exposed here (Fig. 2). The leucocratic layers range from 5 to 60 cm thick and mafic layers from 5 to 50 cm.

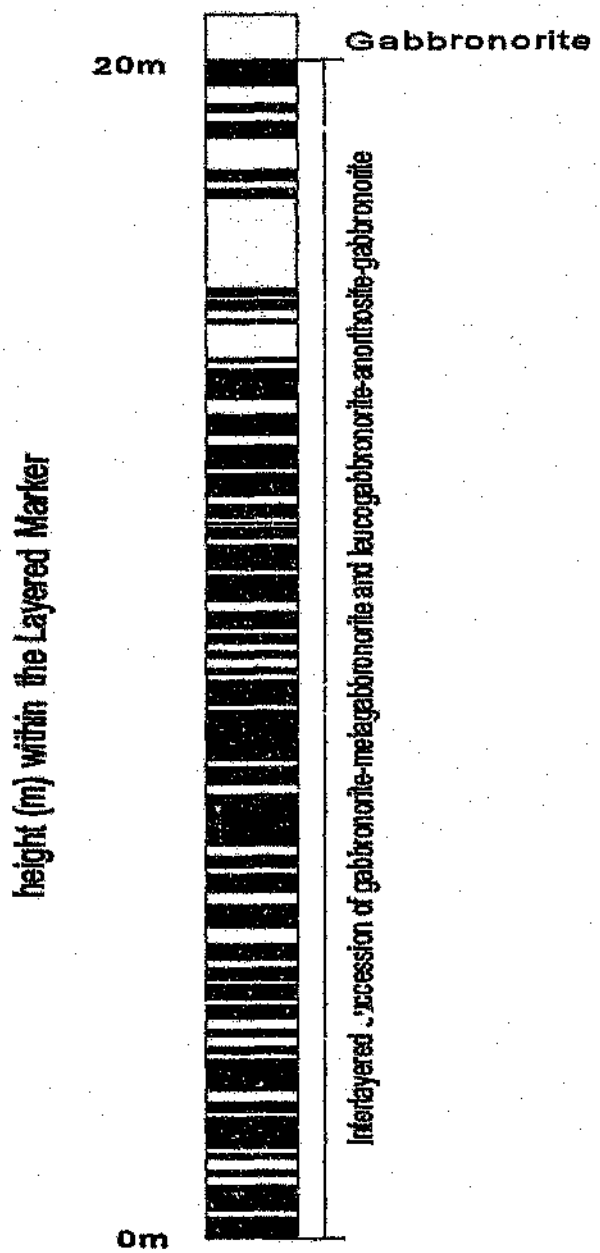


Figure 2.5 Stratigraphic column for profile C. The exposure of the hangingwall and footwall lithologies is poor. For this reason only the layered marker sequence was sampled.

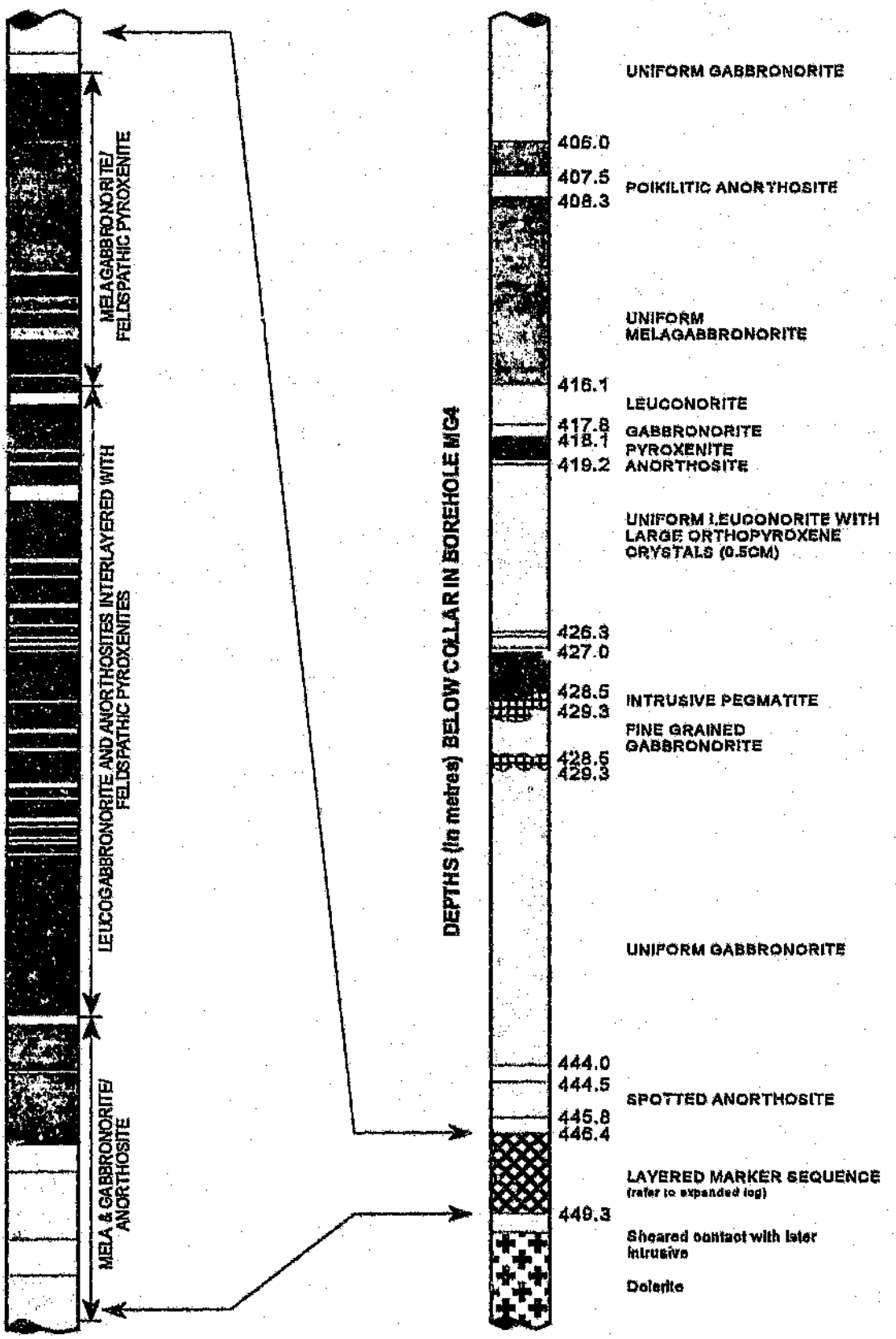


Figure 2.6 Stratigraphic column for a portion of borehole MG4. This borehole was drilled on the farm Mapochgronde, near the town of Roossenekal.

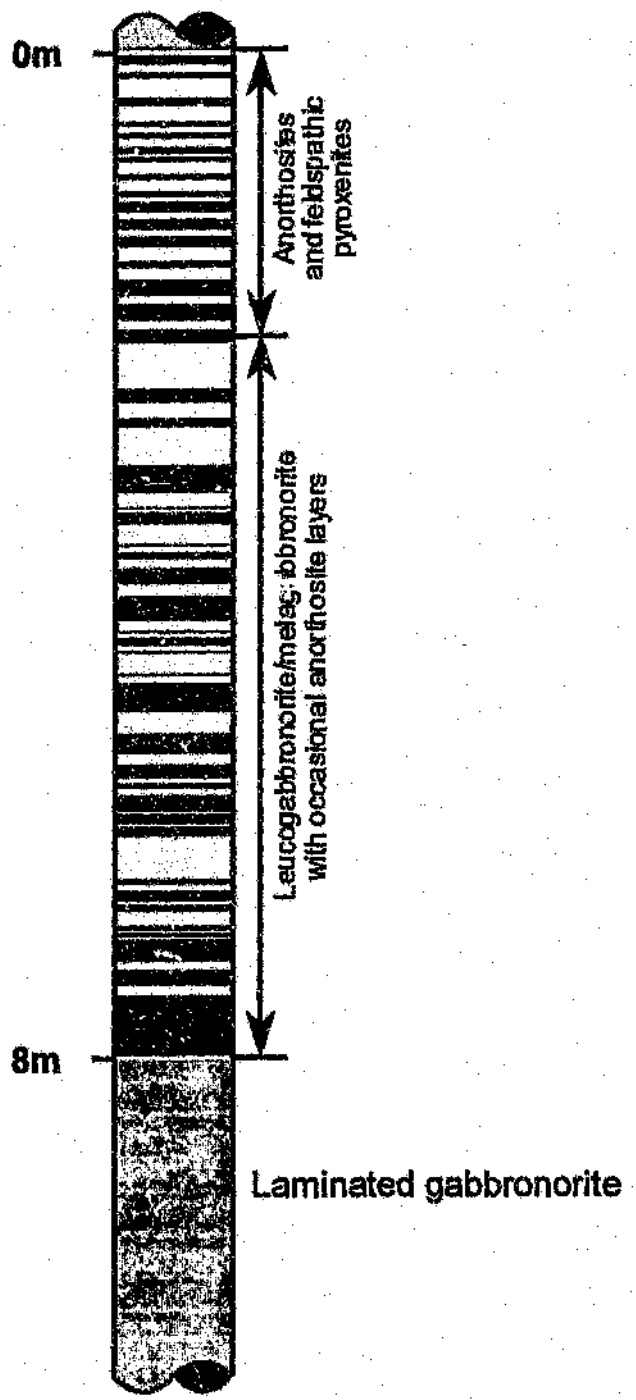


Figure 2.7 Stratigraphic column for the Layered Marker Sequence exposed at locality E.

2.6 Vertical and lateral characteristic of individual layers

In addition to following the layered marker sequence along strike individual outcrops have been studied in detail to determine

1. whether there was any grading within the layers.
2. the lateral continuity of individual layers both along strike and down dip.
3. the physical morphology of the layer types

2.6.1 Layer contacts

A dominant feature of these layers is the sharp contacts between and the lack of grading within most layers. Plate 2.1 is a photograph showing the well-defined nature of these layers. The lack of grading within both the melanocratic and leucocratic layers, is evident

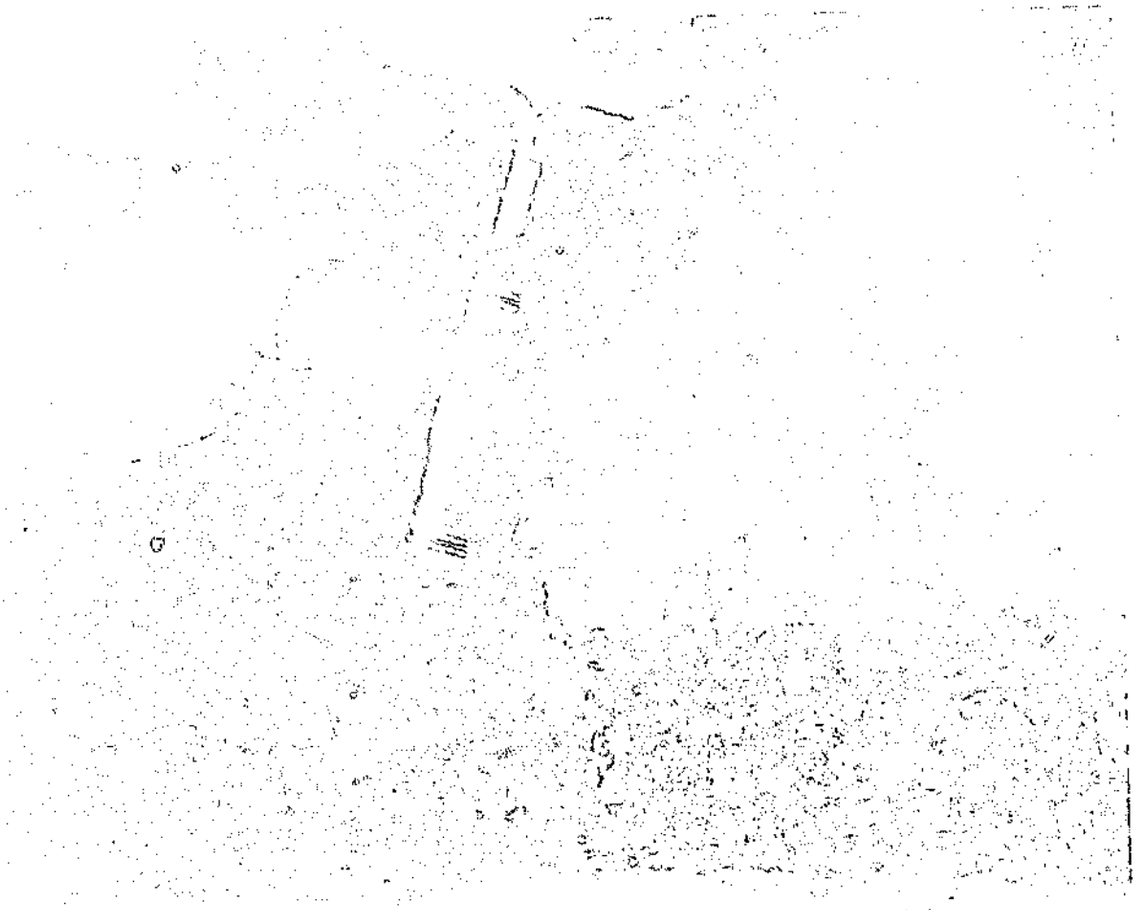


Plate 2.1 Photograph showing the well-defined nature of melanocratic and leucocratic layers

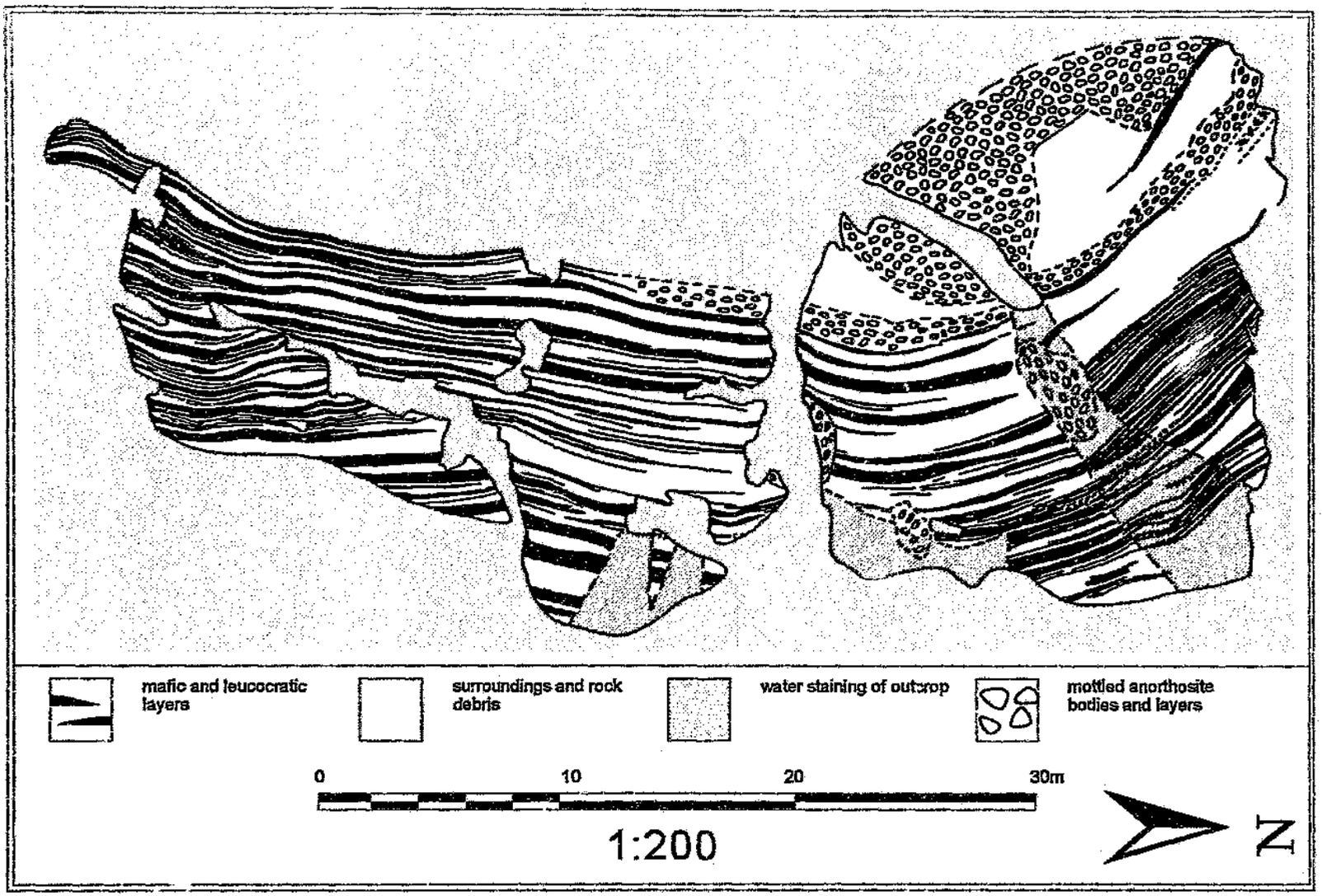


Figure 2.8 Map of a pavement exposure of the Layered Marker Sequence near locality B.

2.6.2 Lateral continuity of layers

Locality B is a large pavement exposure in which individual layers can be traced continuously for 50m along strike. This outcrop slopes to the east at an angle of between 18-30°. Very few other outcrops, that have 100% outcrop over 10's of metres, have been located. Although there are many outcrops and these afford the opportunity to trace the layered marker over considerable distances, individual layers can rarely be traced for more than 10 metres due to the size of individual outcrops. It is also difficult to correlate individual layers between exposures. This pavement was therefore mapped in detail to determine how continuous the individual layers are along strike. From this work (Fig. 2.8) it was discovered that individual mafic layers terminate frequently. In this outcrop alone, 88% of the mafic layers terminate at least once within the limits of the outcrop. Mafic layers also occasionally split. Individual layers range from one to ten's of metres long. This outcrop is domed and much of the irregular and wavy nature of individual layers on the map (Fig. 2.8) is the product of uneven topography. However although the layers appear to be planar for the most part, they terminate by wedging out either up or down (Fig. 2.9). This is well illustrated in the Plate 2.2. These photographs show a feature that appears to be quite common, whereby when a melanocratic layer terminates by wedging out towards its base, it is draped by a consistently thick leucocratic layer and in turn by a mafic layer that wedges out towards its top contact (as is diagrammatically illustrated in Fig. 2.9). Another intriguing feature of this outcrop is that the cumulative thickness of melanocratic layers varies along strike. Right at the base of the sequence in the northeastern corner of the outcrop the melanocratic layers are wispy and irregular. This feature is common towards the base of the sequence. A similar feature is shown in Plate 2.3.

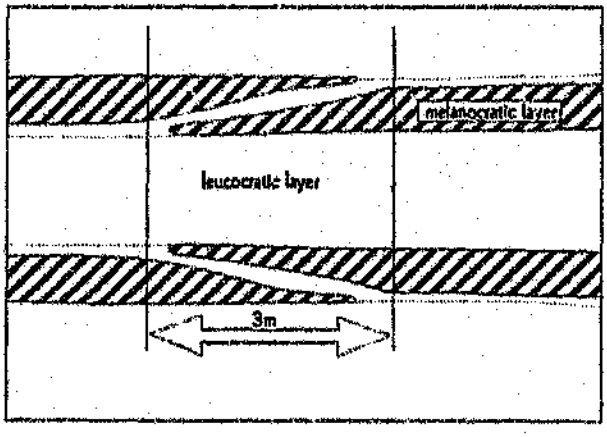


Figure 2.9 Schematic diagram showing typical layer termination morphology.



Plate 2.2 These two photographs show the types of layer terminations the morphology of which is illustrated in Fig. 2.9. This type of layer morphology is common and could indicate channel development.

At locality E the accessible portion of the outcrop was mapped (Fig.2.10). From this mapping it can be seen that the mafic layers also terminate in the dip direction. In addition the morphology of the layers is similar to that seen at B, with melanocratic layers wedging towards their lower contacts and being overlain by a melanocratic layer that pinches towards its top contact in the up dip direction. In addition there are numerous anorthositic layers defining both the lower and upper contacts of certain leucogabbronoritic layers. This feature has also been observed in samples collected from profiles A and B. However, in outcrop weathering usually obscures this feature. The mafic layers terminate equally frequently along strike and in the down dip orientation. Plate 2.3 shows a three dimensional view of the basal portion of the layered sequence close to locality B. The two vertical outcrops meet at an angle of close to 90°. Note that Every melanocratic layer varies significantly in its thickness across the field of view. Note also the irregularly terminations of the gabbronoritic lens towards the bottom of the field of view.



Plate 2.3 Photograph of two vertical rock faces that meet at ~90°. It illustrates the fact that the mafic layers terminate both along strike and down dip. Note also the wispy nature of the lowermost melanocratic layer.

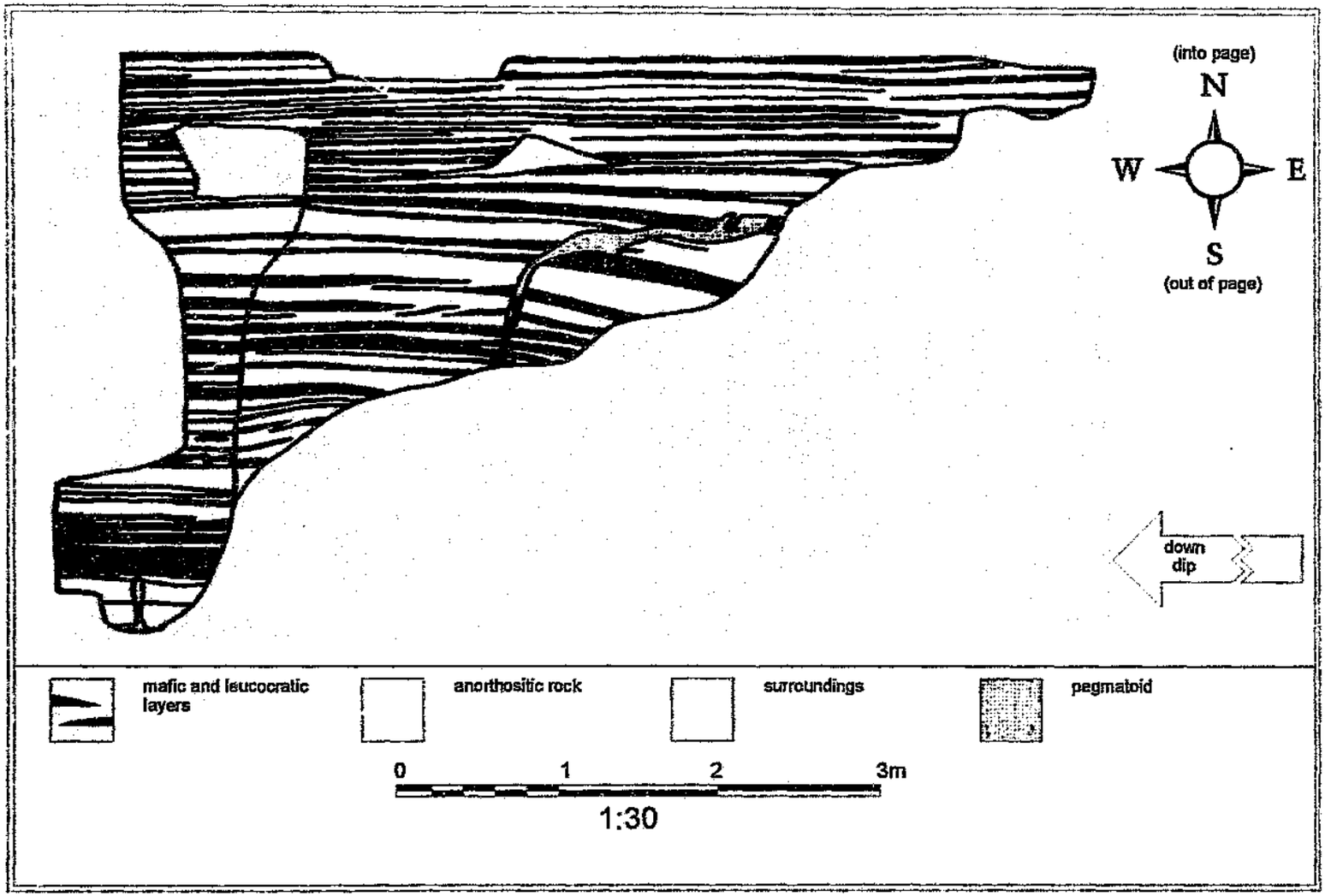


Figure 2.10 Map of the accessible portion of the vertical exposure of the Layered Marker Sequence as exposed at locality E.

2.6.3 Variation in layer thickness

On tracing a single layer along strike (Fig. 2.8 and 2.10) it is apparent that the layer thicknesses vary considerably. It is therefore not surprising that there is no apparent correlation between melanocratic and leucocratic layer thicknesses as diagrammatically illustrated in Fig. 2.11.

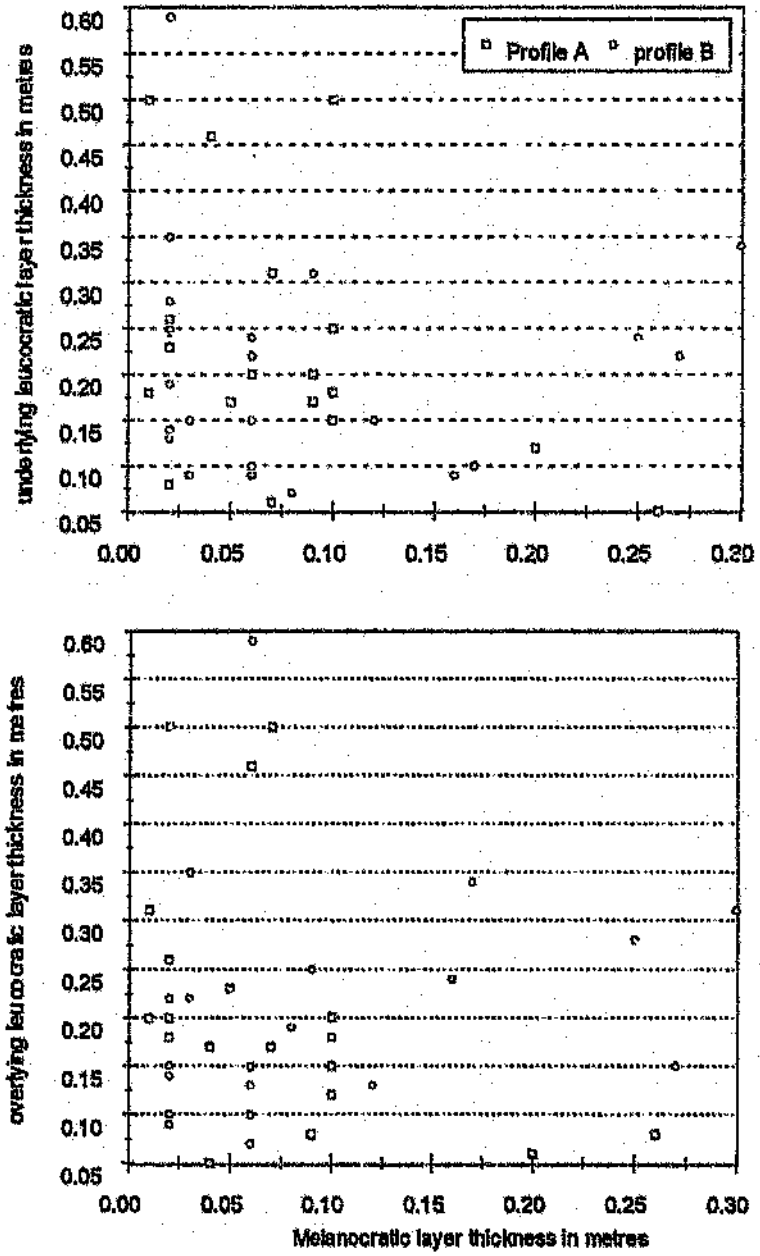


Figure 2.11 (a) Variation in underlying leucocratic layer with the overlying melanocratic layer thickness.
(b) Variation in underlying melanocratic layer with the overlying leucocratic layer thickness.

2.6.4 Poikilitic anorthosite bodies

Another rock type encountered frequently, when mapping the distribution of the Layered Marker Sequence, was "poikilitic anorthosite". This rock type is characterized by large dark patches surrounded by white cloudy plagioclase. The dark patches themselves are however not significantly enriched in pyroxene. The patches are often irregular. The pyroxene phase within these patches is dominantly clinopyroxene and many of these grains are in optical continuity within each patch. The grains are also frequently highly altered to hornblende, on their rims, and biotite within their cores.

The rock type often truncates the layering in a number of ways:

- The mottled outcrops usually occur within the layered interval as rounded to oblate bodies that could be indicative of a transgressive pipe type body (Fig. 2.8). This rock type also occurs within leucocratic layers towards the top of the layered sequence and periodically cuts upwards through the melanocratic layers (Plate 2.4).
- In other cases the layering is completely obliterated by this rock type. In some cases the layering fades out into mottles, as seen in plate 2.5, whereas elsewhere a well defined mottled front is evident across which the layering disappears only to reappear, just as abruptly, tens of metres along strike or down dip.

These field observations show the ways in which the poikilitic anorthositic rock type disturbs the layering and suggest that these are a replacement phenomenon. The leucocratic layers are most often mottled However there are leucocratic layers towards the base of the layered sequence that are not altered in this way and therefore it is believed that this alteration did not have any part to play in the primary development of these layers. As they are not relevant to this study they are not dicussed further, although their origin is enigmatic and warrants further attention.

Although the layering is normally undisturbed, other than by the mottled anorthosite replacement fronts, there are outcrops that display highly disturbed structures as is shown in plate 2.6. In this outcrop the layering, towards the base of the sequence, is highly disturbed, with rafts of mafic material haphazardly orientated. However towards the top of the sequence mafic layers drape undisturbed over the chaotic lower portion of the Layered Marker Sequence. This might reflect infrequent slumping within the chamber at the time the layering was forming.

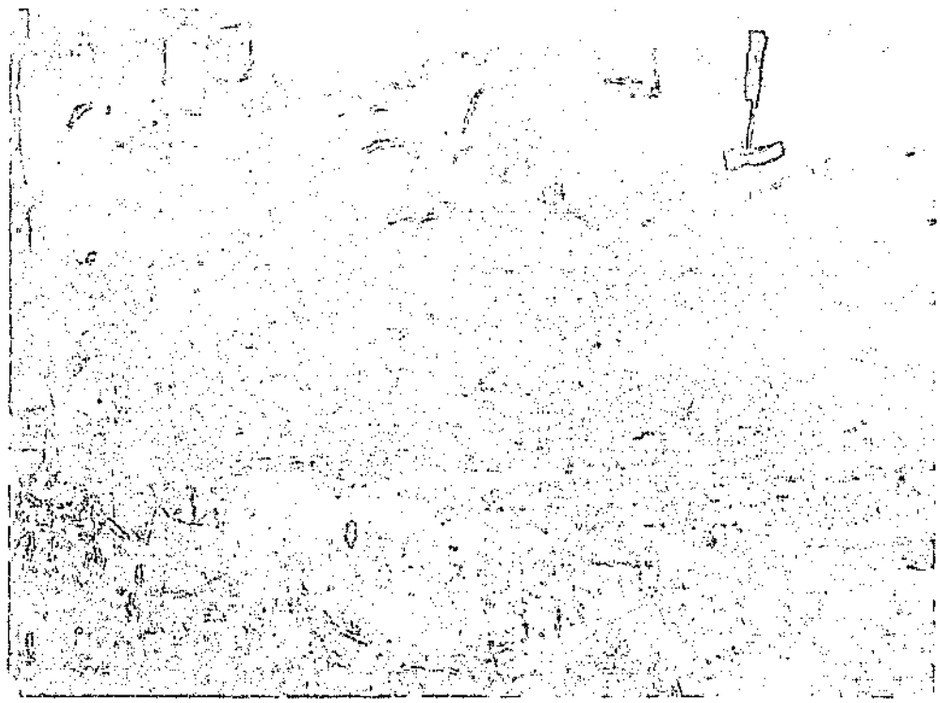


Plate 2.7 Photograph of the upper portion of the Layered Market at a locality near profile B. Towards the bottom the photograph mottled anorthosite domes upwards, cutting into the melanocratic layers



Plate 2.8 (Insert) Starkly layered east west orientated vertical outcrop.
(Principle image) The layering (seen in the insert) fades into mottles 10m down dip.

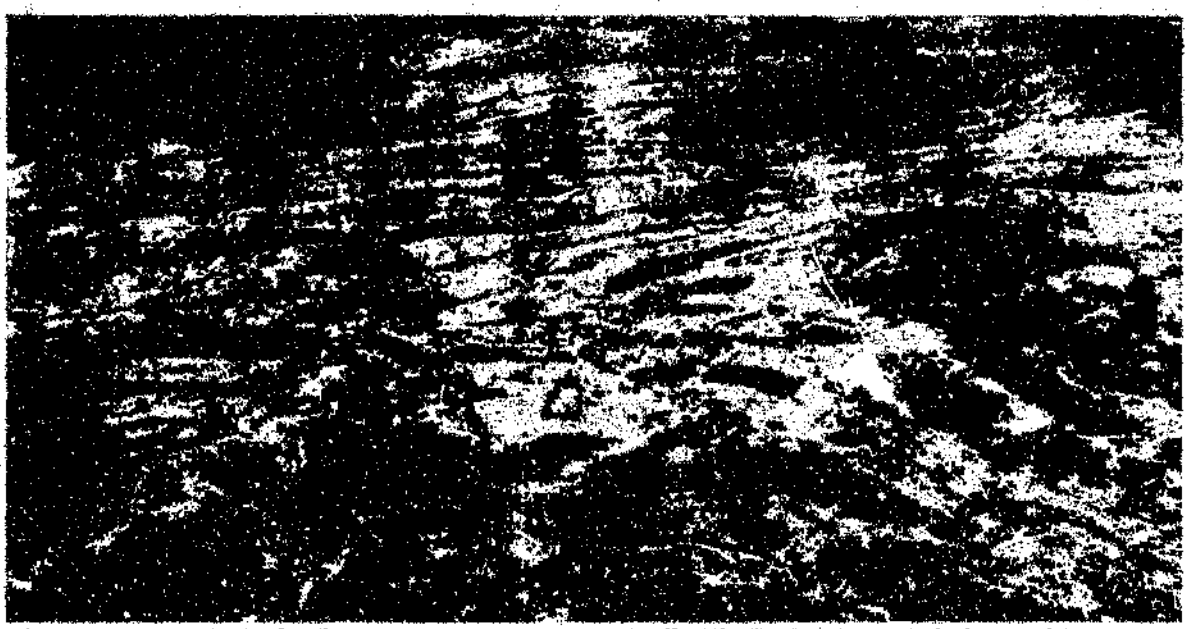


Plate 2.6 Chaotically disturbed layering seen just south of locality E. Note that towards the top of the sequence the mafic layers pass undisturbed over the disturbed and brecken layers.

3. Techniques and sample preparation

The Layered Marker Sequence was sampled at three localities in the eastern limb of the complex (localities A, B and D).The marker had previously been sampled at locality C (Pillay, 1990). Three of the localities (A-C) are well exposed and the layered marker can be traced between them (Molyneux, 1974). To the south of locality C the layered marker was not located in previous thorough mapping of the area (von Gruenewaldt, 1971). In addition the outcrop is not as good as in the north and outcrops are often inaccessible. As a result it was decided to focus the study on the three northern localities which cover approximately 45km of strike.

The layered marker at A and B was sampled in detail vertically and laterally. Several layers from the top, middle and bottom of the marker were sampled. In addition, the footwall lithologies down to 100m below the Pyroxenite Marker and the hangingwall up to and including the Pyroxenite Marker were also sampled. The footwall and hangingwall lithologies are very poorly exposed in the vicinity of locality C and were therefore not sampled.

Samples from profile A have been labelled with the suffix "N" and those from profile B "S". Footwall sample labels are prefixed with the letter "F" and hangingwall samples with "H". The layers from the layered marker have been numbered from the base of the sequence. Therefore the first melanocratic layer has been labelled "1M". The next layer is leucocratic and has been labelled "1L". This pairing of melanocratic and leucocratic layers has no genetic connotations. Some layers were sampled several times and these samples are distinguished with the letters T (for top of layer), M (for middle) and B (for base). Where samples have been collected along strike within a single layer, these have been labelled with a number attached, e.g. 17TM(16), with reference to the distance along strike, in metres, from where the sample was taken relative to a point of reference. Samples were, where possible, marked in the field so that their orientations could be recorded.

Thin sections were cut for selected samples. For the samples from the layered marker an attempt was made to cut these sections parallel and perpendicular to the strong bedding parallel fabric that exists within these rocks. However, in certain cases it proved difficult to get orientated material. From these thin sections, the modal abundance of individual minerals was measured by means of point counting. From the orientated sections, a 2.5cm diameter field of view was projected onto a wall using a slide projector fitted with a special thin section projection attachment. The long and short axes of all well-formed (rectangular) plagioclase laths were then measured as well as the orientations of the long axes with respect to the dip direction. From this

information grain size and orientation data were determined. In addition the specific gravity of each sample was determined using a Jolly Balance (Fig.3.1).

Table 3.1 List of samples studied for profiles A, B and C

Sample from profile A	Height (m) w.r.t. the Pyroxenite Marker	Sample from profile B	Height (m) w.r.t. the Pyroxenite Marker
	HANGINGWALL SAMPLES		
H8N	+57.00	H12S	+20.00
H7N	0.00	H11S	+1.00
H6N	-28.00	H10S	0.00
H4N	-59.50	H9S	-1.00
H3N	-60.04	H8S	-22.00
H2N	-65.00	H7S	-65.00
H1N	-68.00	H6S	-66.00
		H5S	-67.76
		H1S	-74.83
	SAMPLES FROM THE LAYERED MARKER SEQUENCE		
20LN	-68.85	25LS	-76.70
20MN	-68.92	25MS	-76.76
19LN	-69.10	24LS	-77.00
19MN	-69.14	24MS	-77.08
18LN	-69.20	23LS	-77.40
18MN	-69.66	23MS	-77.58
11MN	-71.56	22LS	-78.00
10LN	-71.65	22MS	-78.20
10MN	-71.78	19LS	-78.80
9LN	-71.90	19TMS	-78.92
9MN	-72.37	19MMS	-79.00
8LN	-72.46	19BMS	-79.10
8MN	-72.71	18LS	-79.30
7LN	-72.76	6LS	-82.21
6MN	-73.13	6MS	-82.27
5LN	-73.33	5LS	-82.34
5MN	-73.42	4LS	-82.42
4LN	-73.55	4MS	-82.82
4MN	-73.70	3LS	-83.06
3LN	-75.90	3MS	-83.48
3MN	-76.03	2LS	-83.65
2LNA	-76.20	2LS	-83.65
2LNB	-77.30	1LS	-84.87
2MN	-77.49		
	FOOTWALL SAMPLES		
F1N	-79.81	F1S	-86.01
F2N	-101.00	F2S	-114.00

Samples were then prepared for magnetic separation. All samples were crushed into chips using

a jaw crusher. Clean and non-weathered chips were selected and placed in a tungsten steel sieb. A portion of selected samples was pulverized to a fine powder for whole rock analysis. A further portion of all the samples was then crushed to extract a certain grain size. The pulverized samples were then sieved using two brass sieves (2.5 and 3.25ϕ) and a collector. The 2.5 to 3.25ϕ (0.177 to 0.105mm) fraction was retained whilst the coarse fraction was recrushed. If sufficient coarser material remained this was re-crushed and sieved.

Samples were cleaned repetitively with water to remove all the dust clinging to the individual grains. The dust content of each sample is considerable and may clog the separator if not removed.

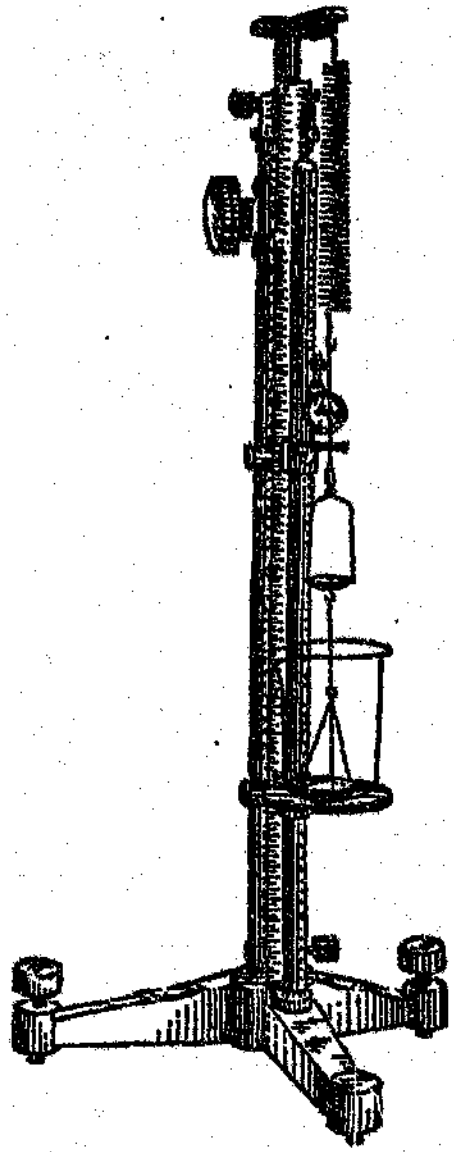


Figure 3.1 Sketch of a Jolly balance used to measure the specific gravity of samples (after Klein et al., 1985).

3.1 Magnetic separation

The highly magnetic fraction was removed from the samples with a magnet. A Frantz isodynamic separator was then used to separate the silicate minerals. This machine was set up with an inclination of 15° and a slope of 25°. The machine was partially dismantled and cleaned thoroughly with acetone before each sample was sent through.

3.1.1 Plagioclase separation

Plagioclase is non-magnetic and can be very efficiently separated. To do this, the current through the coil was set on 0.9A. The pyroxenes were then extracted as the magnetic fraction and placed in well labelled plastic bottles for further separation. The plagioclase separates were then fed through the separator a second time at a higher current setting. After this stage the plagioclase separates proved to be more than 99% pure.

3.1.2 Pyroxene separation

The two pyroxene phases present, orthopyroxene/pigeonite and clinopyroxene, can be efficiently separated using a magnetic separator.

3.1.2.1 Orthopyroxene

The pyroxene concentrate was sent through the separator at a current setting of 0.5A. The orthopyroxene rich separate was extracted as the magnetic fraction. After this first step the orthopyroxene/pigeonite fraction was generally better than 85% pure. These samples were sent through again at 0.375-0.4A. This effectively halved the separate. The magnetic fraction extracted after this stage was generally more than 99% pure low-calcium pyroxene. Very few separates contained some magnetic feldspar, magnetic by virtue of included magnetite, which proved very difficult to separate. These can be identified chemically, by anomalously high TiO_2 (>0.30%) and/or Al_2O_3 (>1.2%).

3.1.2.2 Clinopyroxene

After sending the samples through the magnetic separator at 0.5A, the clinopyroxene separates were generally more than 85% pure. These separates were sent through the separator at a current setting of between 0.525 and 0.55A. At this setting the separates were halved and the non-magnetic fractions were generally better than 97% pure clinopyroxene. These were then sent through the magnetic separator at an elevated current setting to get rid of any plagioclase bearing composite grains still included.

3.2 X-ray Fluorescence Spectrometry

Fusion discs were prepared for each separate and for selected whole rock samples. These were then analysed by X-ray fluorescence spectrometry. Plagioclase and selected pyroxene separates were run in duplicate to determine analytical precision. Samples from profile C had already been analysed (Pillay, 1990). A small set of samples from this study were re-analysed to check analytical precision before the two data sets were combined. A new set of calibration standards was prepared to cover the range of oxide abundances expected (refer to appendix 1 for calibration data). Selected plagioclase separates were taken and crushed to a fine powder with a pestle and mortar. This powder was used to make pressed briquettes, which were run on the Phillips 1400 X-ray Spectrometer to determine the abundance of Sr, Rb and Ba. However after the thorough separation there was not sufficient sample, for most pyroxene separates, to ensure infinite thickness in a pressed briquette. In addition the sieving method may cause contamination of the samples with certain compatible traces. As a result of these two considerations it was decided not to analyse the pyroxenes, for trace elements, by X.R.F.

3.3 Instrumental Neutron Activation Analysis (I.N.A.A.)

Selected separates were then taken and cleaned in a 10% solution of HCl, weighed into glass vials, that had previously been cleaned and labelled. A variety of standards were also weighed into vials. A tantalum monitor was weighed and wrapped around each vial. These vials were then placed in cadmium tins and sent for Instrumental Neutron Activation Analysis. This involved the irradiation of these samples for 3 days on the poolside in the reactor chamber. They were then allowed 4 days to cool, after which time the samples were placed in a chamber. The radiation emanating from them was measured, by a low energy planar detector and a high energy coaxial detector, for 1 hour per sample. After 11 days the second count was undertaken. On this occasion they were counted for 2 hours per sample. After 30 days each sample was recounted for 4 hours.

3.4 Mass Spectrometry

In order to determine the Rb and Sr isotope systematics of these rocks, selected plagioclase separates were crushed to a fine powder. Rb and Sr concentrations were determined by isotope dilution mass spectrometry, X.R.F. and I.N.A.A. Initially it was hoped that X.R.F. analysis of Rb and Sr would prove good enough. However even with significant work done to improve the X.R.F. accuracy and precision (refer to appendix 2), it was not possible to improve the confidence intervals to within 0.8ppm for Rb and 16ppm for Sr. These levels of uncertainty introduce

significant uncertainty in the calculated initial $^{87}Sr/^{86}Sr$ isotopic ratio. Therefore subsequent samples were analysed by isotope dilution. Those not analysed by I.D. were analysed for Rb by I.N.A.A., which proved more precise than by X.R.F. The $^{87}Sr/^{86}Sr$ ratio was determined on spiked and unspiked samples. Approximately 50mg of the sample powder was dissolved in open beakers with a mixture of HF and HNO_3. Most of these samples were dissolved with ^{87}Rb (20/30mg) and ^{84}Sr (10/20mg) spikes. The samples were then dried and redissolved in HCl, dried again and taken up in 1.5 ml of 2.59M HCl and centrifuged. Elution on a 20 cm cation exchange column was carried out using the 2.59 M HCl, and only the Sr fraction was collected, dried and converted to nitrate using 12 M HNO_3. Total method blanks were 48pg for Sr and 97pg for Rb. These were not significant with respect to the sample concentrations, and were ignored. Sr was loaded onto single outgassed Ta filaments with H_3PO_4 for determination of Sr isotopic composition and concentration. Unseparated Rb was loaded directly from the centrifuge tube as a chloride onto outgassed double Ta filaments. Both VG-354 and VG MM-30 mass spectrometers were used to determine the Sr isotopic composition and the MM-30 was used to analyse for Rb. The method described has been taken from Eales et al. (1990).

3.5 Electron Microprobe

The abundance of pyroxene phases within some of the samples was very low and the separation of these was complicated by magnetite clinging to individual grains and affecting their magnetic properties. Therefore selected mineral grains, from these samples, were analysed by means of a Cameca SX50 electron microprobe of the Anglo American Research Laboratories. Each grain selected was analysed three times on a traverse from the boundary to the centre of the grain. A number of grains of each pyroxene phase was analysed in each thin section. However it was found that the compositional variation was not large and therefore it was not necessary to analyse a large number of pyroxene grains in each sample. Pyroxenes from selected mafic samples were also probed to determine if there was any systematic difference between pyroxenes within the different rock types and also as an analytical comparison with the X.R.F. analyses of these samples. Plagioclase was also analysed by microprobe to determine the extent of zonation within this mineral and to compare the results with those obtained by X.R.F.

4. Petrography

The petrography of samples from the Main Zone within the eastern limb has been documented in detail by von Gruenewaldt (1970, 1971 and 1973), von Gruenewaldt and Weber-diefenbach (1977), Molyneux (1974), Marais (1977) and Klemm et al. (1985).

The mineralogy of these rocks is dominated by low-calcium pyroxene, clinopyroxene and plagioclase. Although these rocks are dominated by only three main phases, there are mineralogical variations that are worth noting.

Within the Main Zone the low-calcium pyroxene can be either primary orthopyroxene or inverted pigeonite. This later mineral is distinctive in that it has abundant exsolution lamellae of clinopyroxene (von Gruenewaldt, 1970). The height within the Main Zone at which the transition from primary orthopyroxene to pigeonite occurs changes from profile to profile (von Gruenewaldt, 1973; Molyneux, 1974). Von Gruenewaldt (1970) documented that these two minerals coexist for several hundred metres until the low-calcium pyroxene reaches a Mg:Fe ratio of 65:35. Pigeonite is then the dominant low-calcium pyroxene phase, along with clinopyroxene and plagioclase, up to the Pyroxenite Marker at which level the pigeonite abruptly disappears and is replaced by

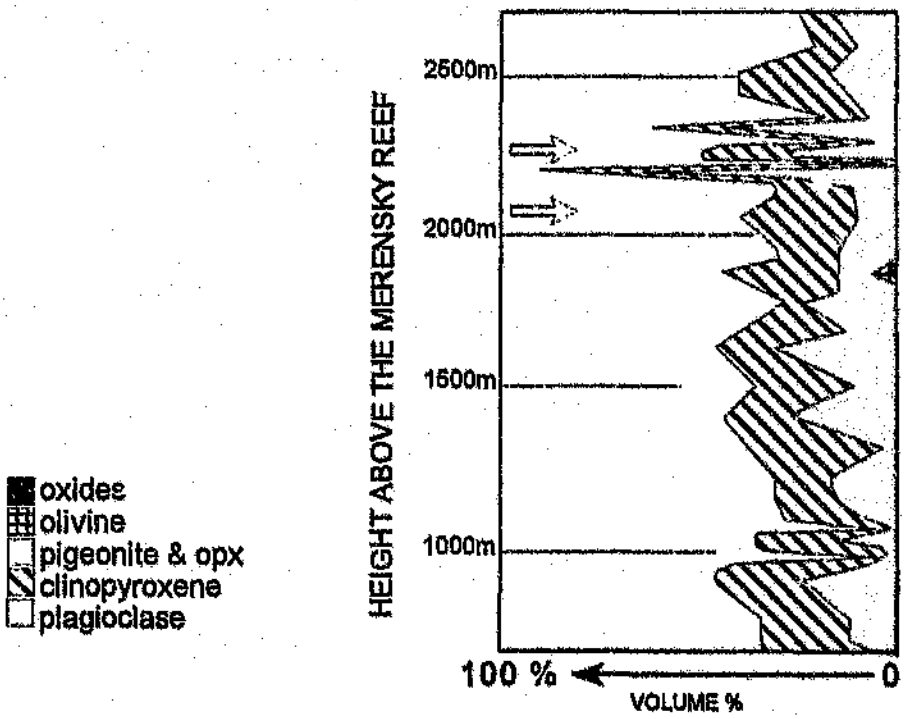


Figure 4.1 Modal distribution of minerals in a portion of the Main Zone (after Molyneux, 1974). The two arrows define the approximate stratigraphic interval studied in this project.

orthopyroxene.

4.1 Mineralogy

The plagioclase is euhedral to subhedral and is cumulus in all but the ultramafic samples. Interstitial plagioclase occurs in a few of the ultramafic layers towards the top of the sequence (Fig. 4.3). Even where it is the dominant phase, considerable overgrowth or recrystallization has produced fairly irregular grain boundaries (Fig. 4.2). The laths are typically 3mm long and 1.5mm wide.

The low-calcium pyroxene is easily identified due to its pink/green pleochroism, poor cleavage, sub-parallel extinction angle and often low birefringence. The low-calcium pyroxene may show extensive granular, blebby (plate 4.1) and fine scale exsolution lamellae of clinopyroxene (plate 4.2) indicating inversion from pigeonite (von Gruenewaldt, 1970). The blebby type of exsolution is normally randomly orientated when comparing one grain with another. The fine scale exsolutions however, generally exhibit the same orientation in several grains over a area of up to two centimetres. Over this area the low-calcium pyroxene grains display a common extinction position. This feature has been well documented (von Gruenewaldt, 1970). Other grains display limited exsolution (plate 4.3). While this may be a function of grain orientation, these are considered to be primary orthopyroxene. Both pyroxenes are collectively referred to as low-calcium pyroxene. In most samples they are granular. The grain size is however often difficult to determine due to the uniform extinction shown by numerous grains over an area. Within the anorthositic layers at the top of the sequence this mineral becomes highly irregular (plate 4.4).

The clinopyroxene displays strong cleavage, inclined extinction, non-pleochroism, is green in colour and often displays high interference colours. It displays abundant exsolution lamellae, is most frequently irregular and varies in size from <1mm to 3mm. Near the base of the studied sequence these grains are more robust. Overgrowth frequently produces an irregular outline. In the mafic layers these crystals often partially enclose the low-calcium pyroxene grains. Towards the top, in the anorthositic layers, they become very irregular (plate 4.5) to skeletal.

The accessory phases present include magnetite, which often occurs as minute euhedral crystals on grain boundaries, biotite and hornblende. These last two mineral occur most frequently within the replacement anorthositic bodies.

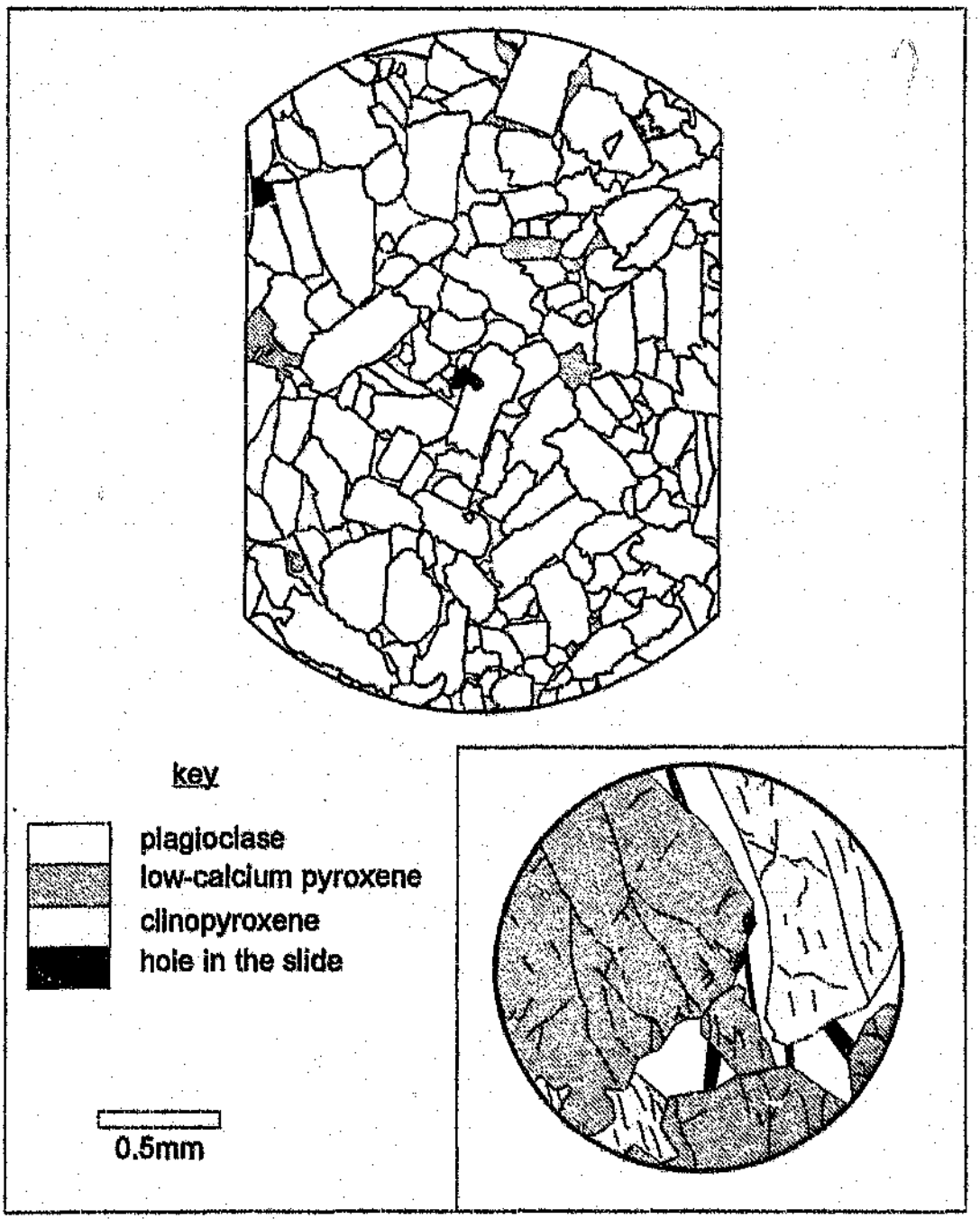


Figure 4.2 Sketch of a thin section from a leucocratic sample towards the top of the layered marker sequence. Note the irregular plagioclase outlines but distinctive lath shapes. Note also the infilling nature of the pyroxene phases.

Figure 4.3 (insert) Sketch of a portion of a thin section taken from a melanocratic layer towards the top of the sequence. The width of the field of view is approximately 4mm. Note the large granular pyroxene grains and irregular interstitial plagioclase crystals.

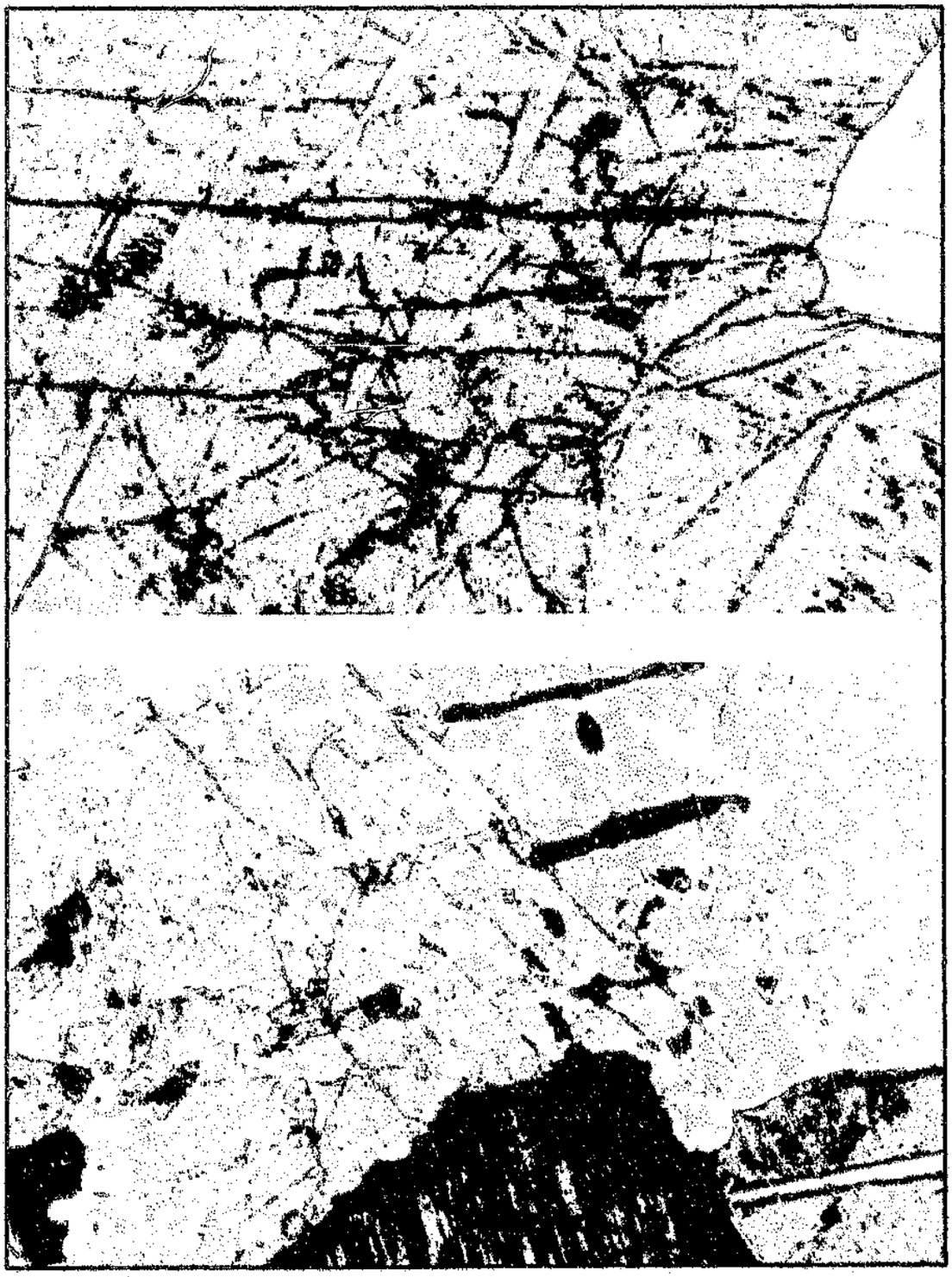


Plate 4.1 Large inverted pigeonite grain with coarse exsolution lamellae, seen under normal and crossed polars. Lower photograph rotated through 90°. Field of view= 4mm.

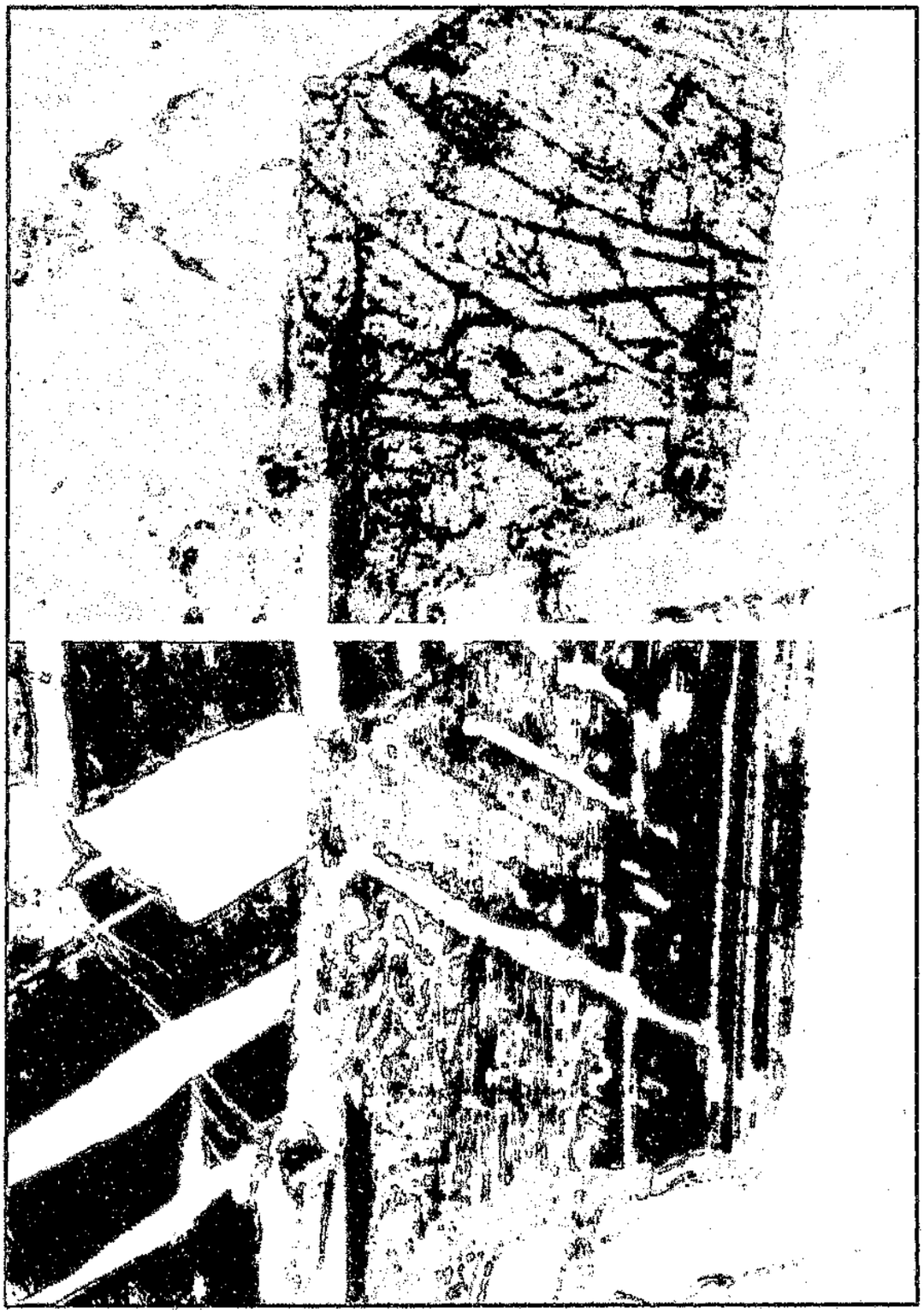


Plate 4.2 Typical inverted pigeonite grain, with partial rim of biotite, seen under normal and crossed polars. Note the two well developed orientations of exsolution texture. Field of view= 4mm.



Plate 4.3 **Top:** large orthopyroxene grain from a melanocratic layer near the top of the layered marker; **Bottom:** Same grain seen under cross polars. Note the distinct lack of exsolution. (field of view= 4mm)

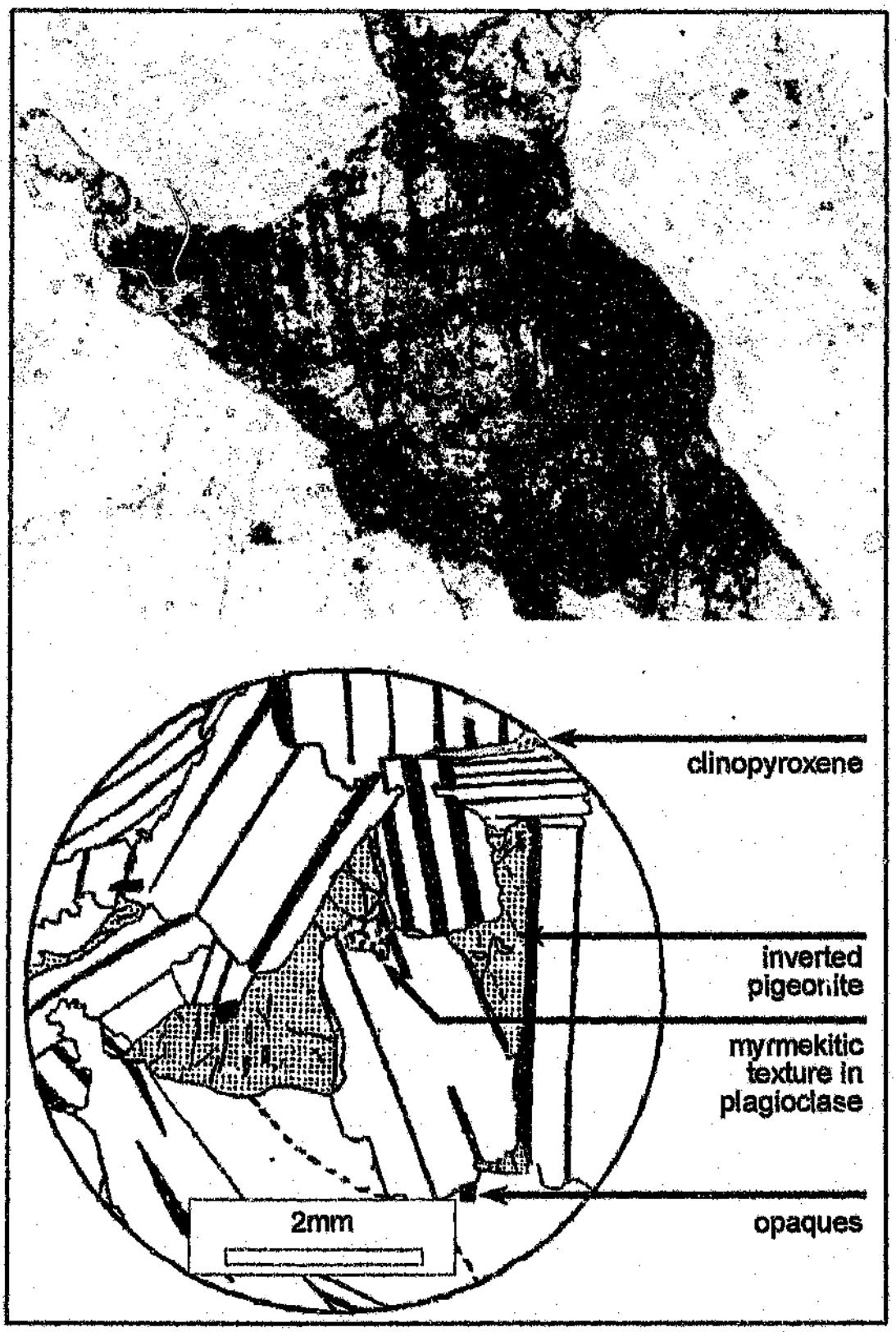


Plate 4.4 **Top:** irregular grain of low-calcium pyroxene from a leucocratic sample.
Bottom: sketch of a field of view showing the irregular and often interstitial character of the orthopyroxene and clinopyroxene grains within the highly leucocratic samples.

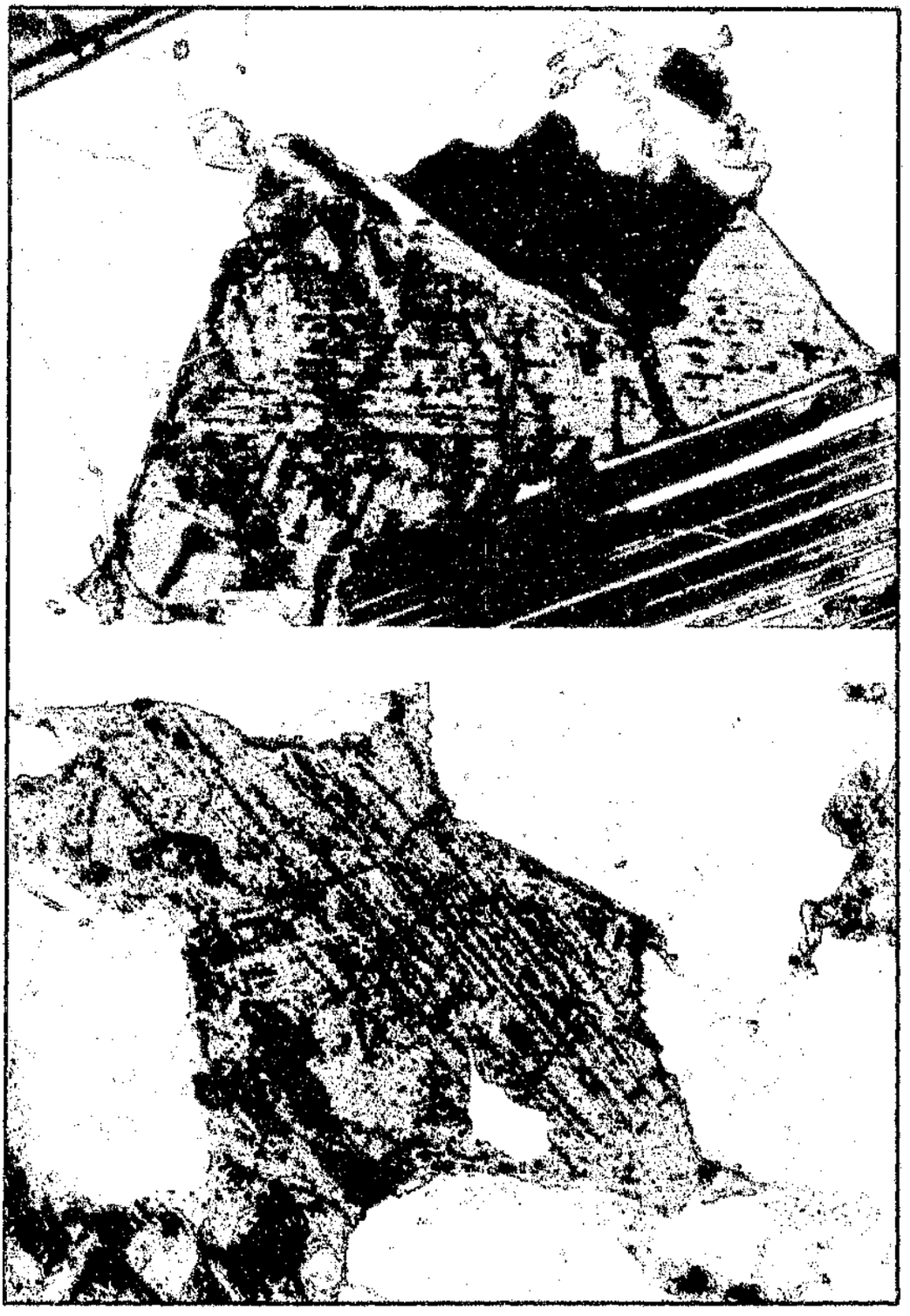


Plate 4.5 (top) Irregular clinopyroxene grain seen under crossed polars. This is the typical character of clinopyroxene in the anorthositic layers. Field of view 4mm wide.
(bottom) Anhedral clinopyroxene grain from a replacement anorthositic body, showing replacement by biotite and rimming by green amphibole.

4.1.1 Modal abundances

The modal abundances of the major minerals have been determined by means of point counting. A single thin section was taken and 500-1000 points identified within it. The modal data for profiles A, B and C are listed in appendix 3. The data from profile C has been taken from Pillay (1990). In some grains of low-calcium pyroxene it is not always possible to distinguish orthopyroxene from inverted pigeonite due to optical orientation and therefore the lack of significant exsolution. Hence there could be errors in the relative proportions of these two pyroxene phases.

Figure 4.4 to 4.6 illustrate the modal variations for selected samples from profiles A-C. It is apparent that the mafic layers vary from gabbronorite to melagabbronoritic and that the more melanocratic layers generally occur towards the top of the sequence. In a similar way the leucocratic layers tend towards anorthosites towards the top of the sequence. However certain of the mafic layers studied proved to be very leucocratic in thin section. This is an error as the specific gravity measurements suggest that these samples are more mafic. This error may be due to the fact that the plagioclase laths tend to orientate themselves so that their tabular faces lie within the plane of the layering. The thin sections were cut within this plane and represent a very limited view of the rock both in terms of area and in particular depth. The plagioclase grains are also of reasonably large size and therefore there are relatively few plagioclase grains within the thin section, whereas within a vertically orientated thin section there would be significantly more plagioclase crystals represented due to the fact that their crystal faces represented would have a smaller cross-sectional area. Therefore it is feasible that if the plane, that is represented in the thin section, happened to contain a concentration of plagioclase crystals due to the lamination of the rock, that rock would appear very leucocratic within that thin section. Therefore vertically orientated thin sections are probably more representative of the true mode of the rock type.

Figure 4.7 shows the variations in abundance of plagioclase, low-calcium pyroxene and clinopyroxene within selected samples from profiles A-C as determined by point counting. From this diagram it is clear that the ratio of pyroxene phases remains remarkably constant. The hangingwall samples deviate from this trend in that some of the samples contain significantly more low-calcium pyroxene. This trend of enrichment of low-calium pyroxene within the assemblage towards the Pyroxenite marker is also shown in work done by von Gruenwaldt (1973).

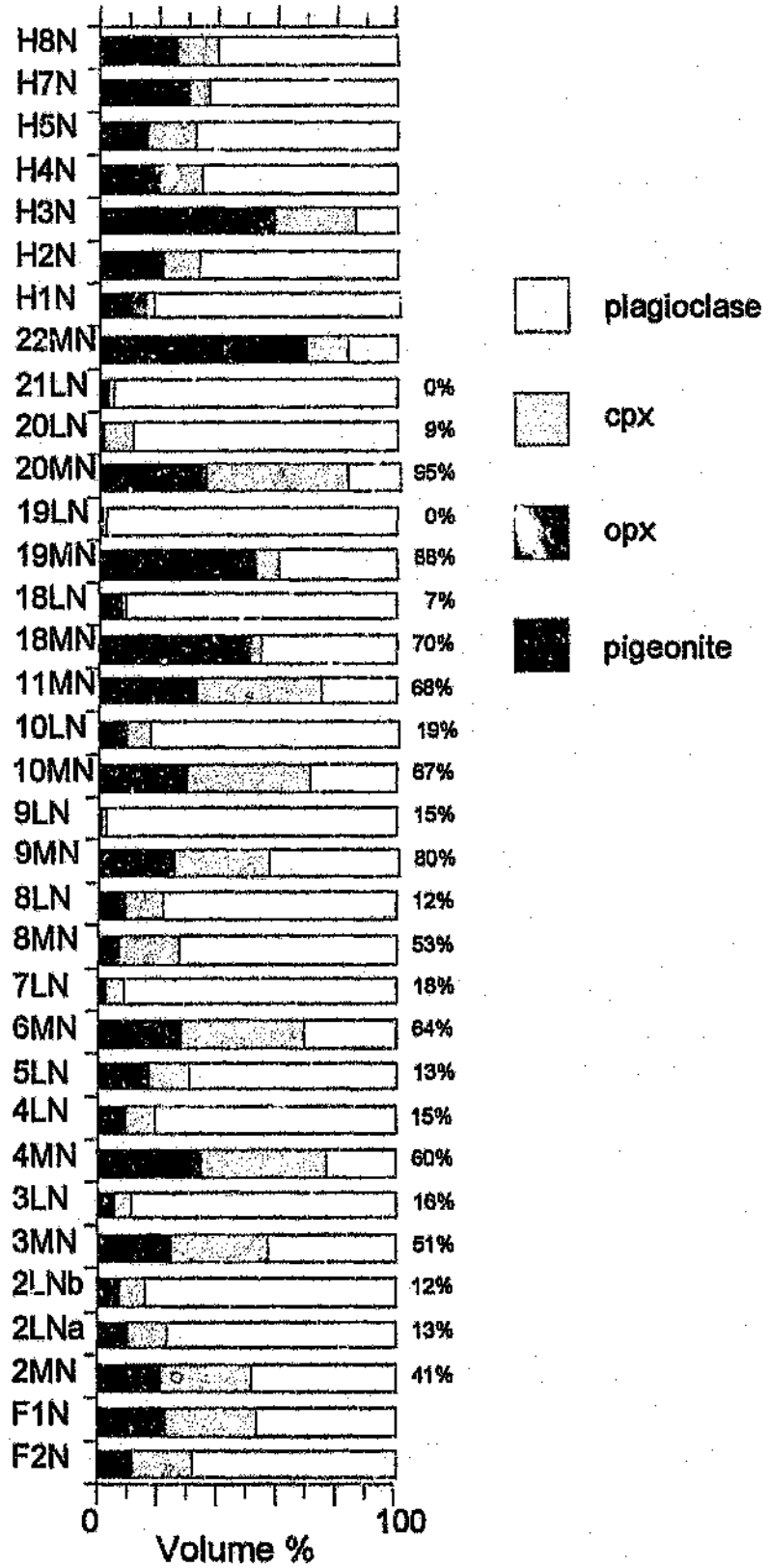


Figure 4.4 Variation in mode of samples as determined by point counting of one thin section per sample. The figures attached to each bar reflect the calculated pyroxene content as inferred from the specific gravity of the sample.

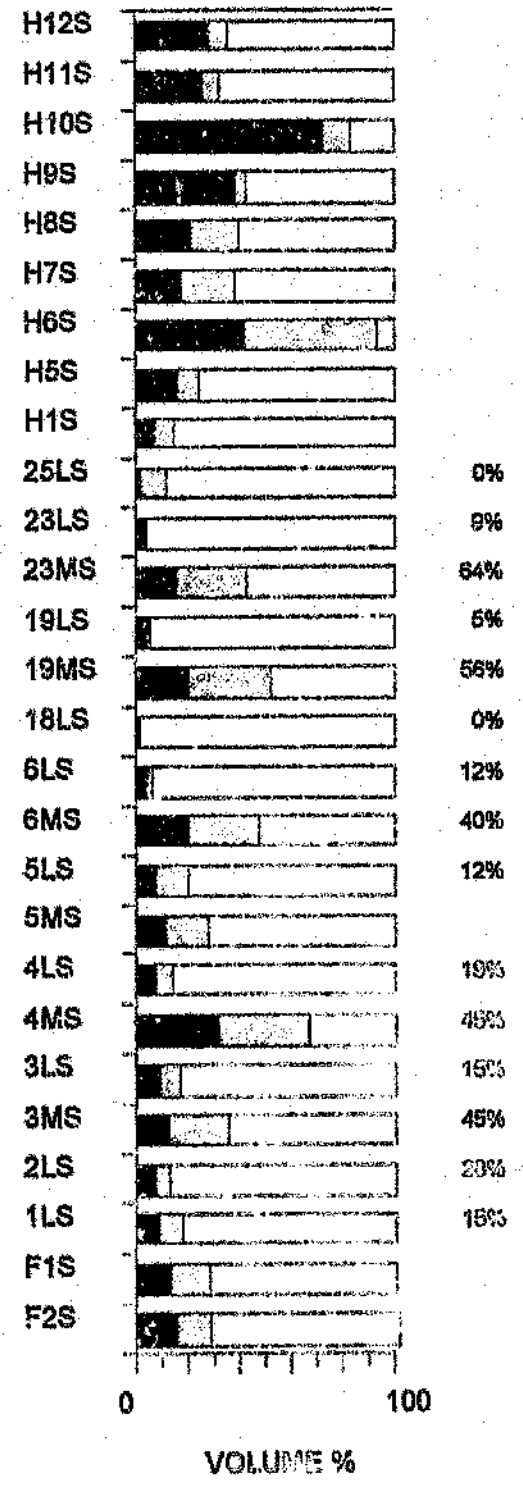


Figure 4.5 Variation in modal abundance for samples from profile B, as determined by point counting and specific gravity measurements (figures in brackets). Key is as per Fig. 3.4.

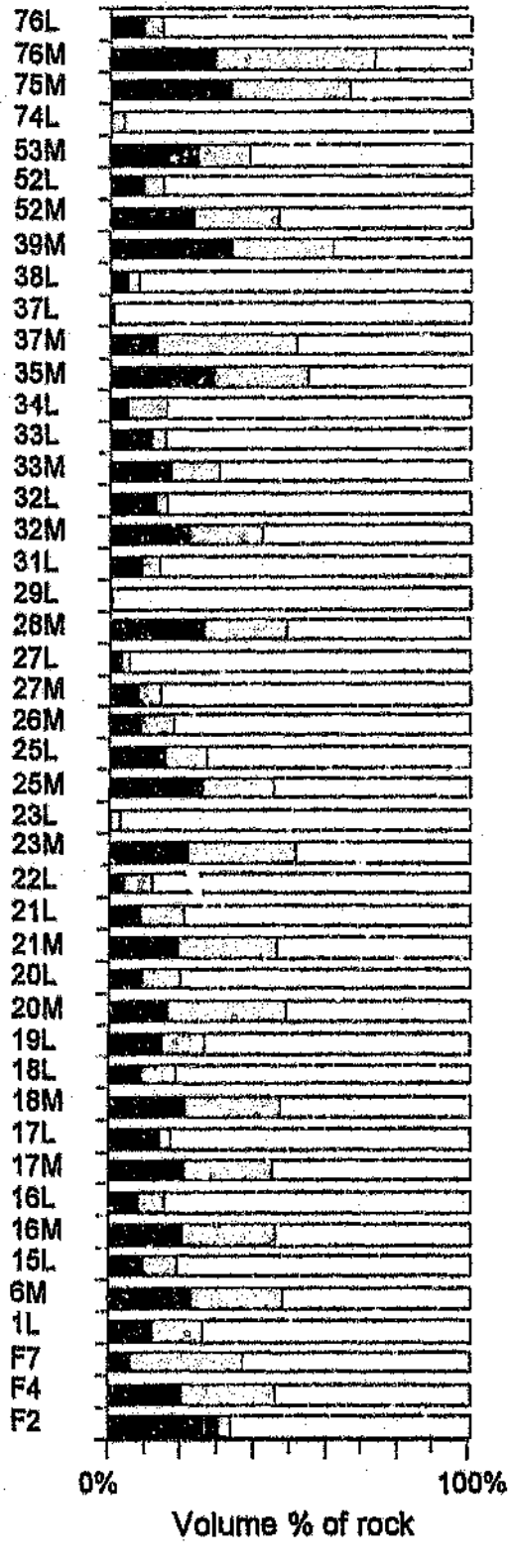


Figure 4.6 Variation in modal abaundances for selected samples from profile C. Modal data is as determined by Pillay (1990).

Three samples from the layered marker also display a remarkable enrichment in low-calcium pyroxene. These samples do however appear to be very mafic as shown by their high specific gravities.

Since the low-calcium pyroxene: clinopyroxene ratio remains relatively constant the specific gravity of the samples may provide a more accurate idea of the mode of each sample. 20 to 60 grams of sample weighed represents 1000-2000 grains whereas a single thin section typically contains fewer than a thousand grains. Certain of the samples were analysed numerous times in

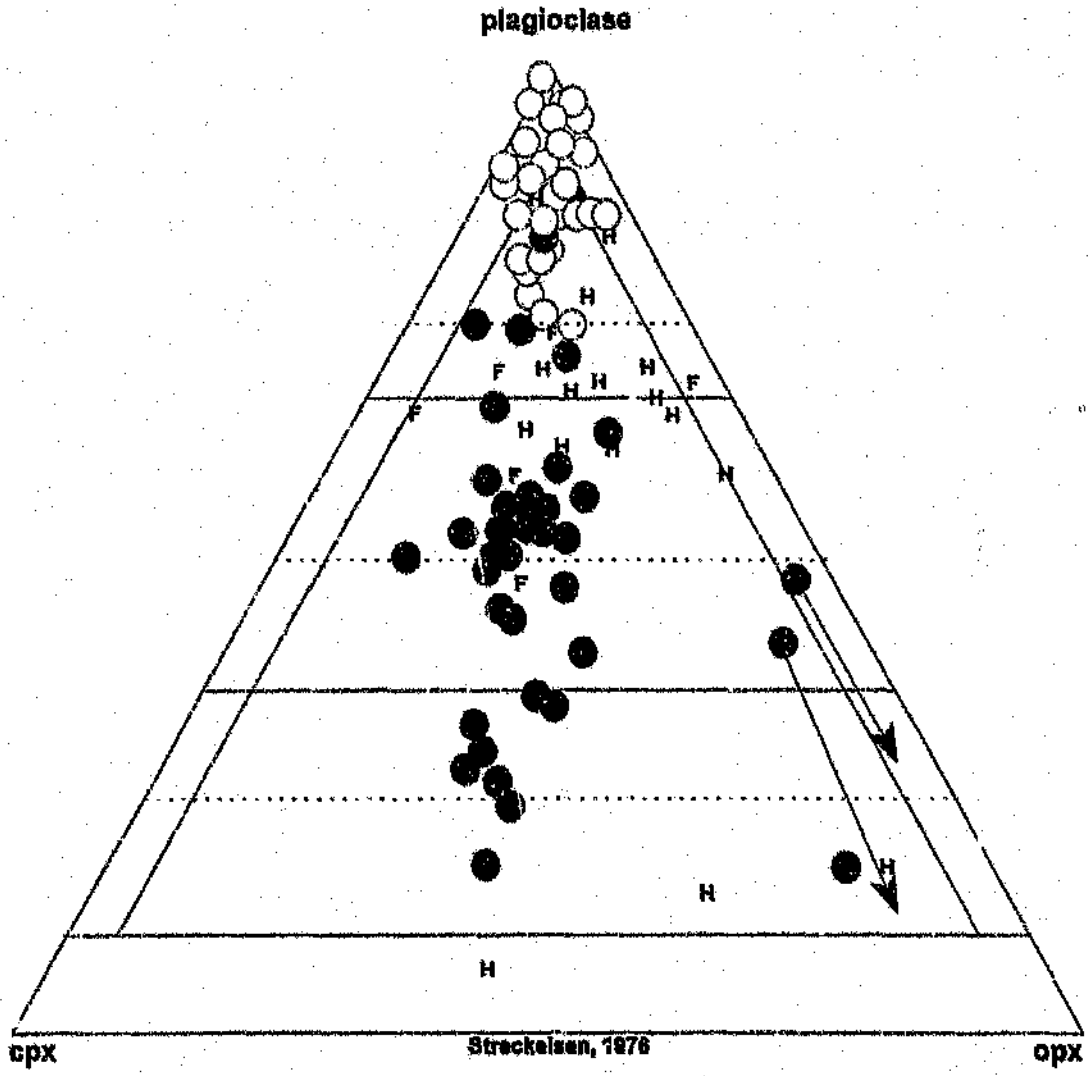


Figure 4.7 Variation in modal abundances for samples from profiles A,B and C. Solid symbols refer to those samples classified as mafic in the field, whilst the empty symbols refer to the leucocratic samples. H and F refer to hangingwall and footwall samples. The arrows indicate the inferred modal abundances as determined from specific gravity measurements.

order to determine how good the correlation between specific gravity and mode is, to calculate a calibration curve and to determine the analytical precision of the method. The specific gravity measurements are listed in Table 4.1.

Table 4.1

Specific gravity measurements for selected samples. Thin section off-cuts and rock chips were used to determine the samples SGs.

Sample	Thin section	Thin section	Rock chips
11MN	3.19	3.16	3.26
10LN	2.84	2.83	2.88
10MN	3.19	3.2	3.21
9LN	2.80	2.81	2.8[illegible]
9MN	3.30	3.25	3.25
8LN	2.84	2.84	2.84
8MN	3.15	3.16	3.11
7LN	2.87	2.86	2.87
6MN	3.21	3.21	3.19
5NL	2.89	2.88	2.84
4LN	2.82	2.83	2.85
4MN	3.18	3.18	3.16
3LN	2.79	2.79	2.86
3MN	3.04	3.06	3.10
2LNb	2.82	2.83	2.83
2LNa	2.83	2.84	2.84
2MN	3.11	3.11	3.03
18LN	2.80	2.80	2.79
18MN	3.27	3.29	3.23
H1N	2.93	2.92	2.91
H2N	2.99	2.99	2.98
H3N	3.39	3.39	3.42
H4N	3.01	3.01	3.01
23LS	2.94	2.93	2.81
23MS	3.13	3.12	3.19
4MS	3.18	3 18	3.06
F1S	2.96	2.94	2.79

With this data and modal data, as determined by point counting, a calibration curve has been derived (shown graphically in Fig. 4.8).

The equation for this calibration curve is $y=-0.00602x+3.370849$. The correlation coefficient (R^2) is 0.89. The confidence interval (2σ), as calculated from the pooled standard deviation of the duplicates, is 0.02 in terms of the S.G. This represents a 3% uncertainty in the calculated volume percent of plagioclase.

From this correlation the plagioclase content of all samples weighed has been determined. The variation in the plagioclase content determined in this way is shown in figures 4.9-4.11 for profiles A, B and E. These graphs show the sharp contrast in the modes between the two layer types and that there is a progressive increase in modal contrast towards the top of the sequence.

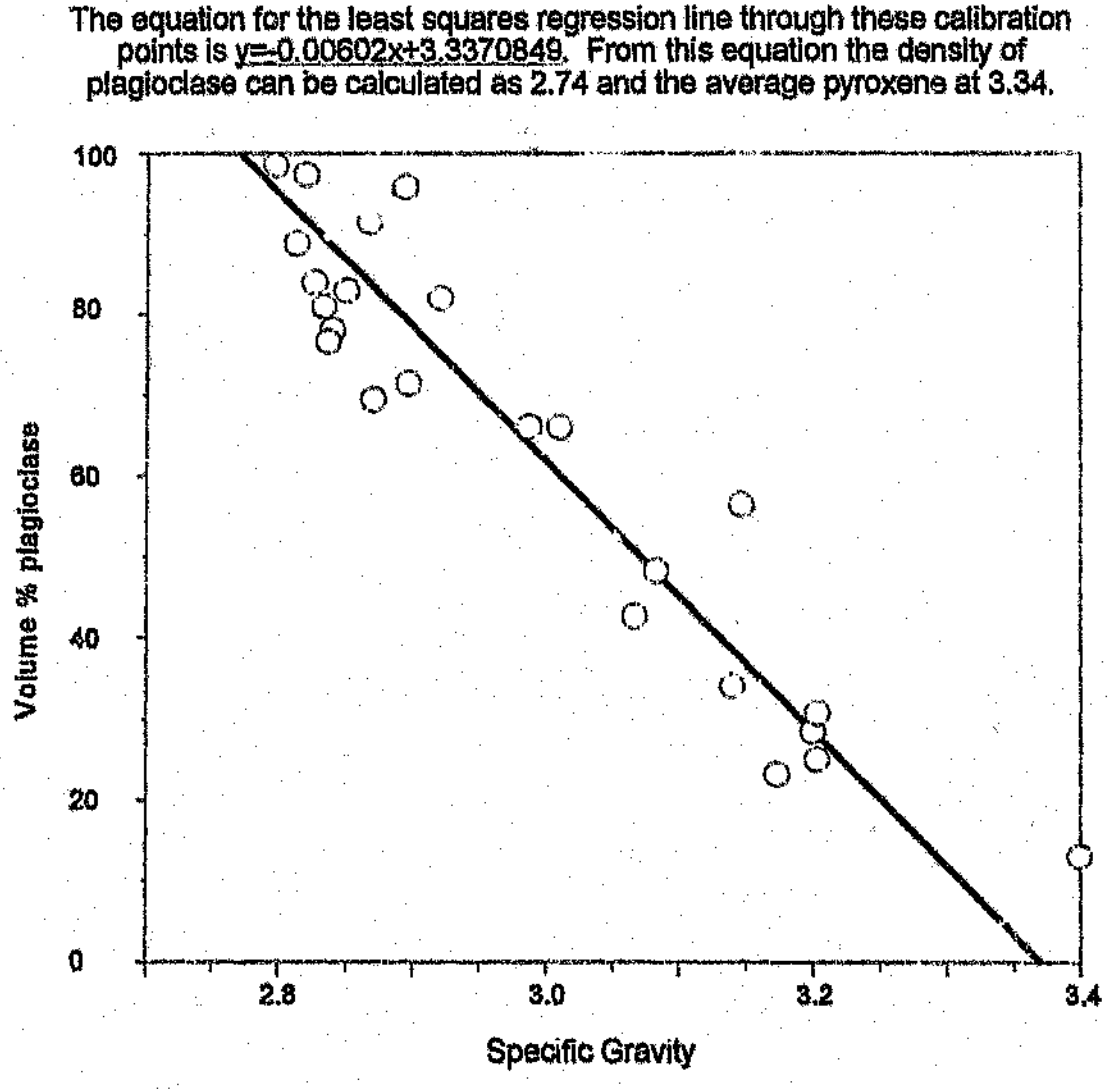


Figure 4.8 Calibration curve for the analysis of plagioclase volume % from speicific gravity measurements.

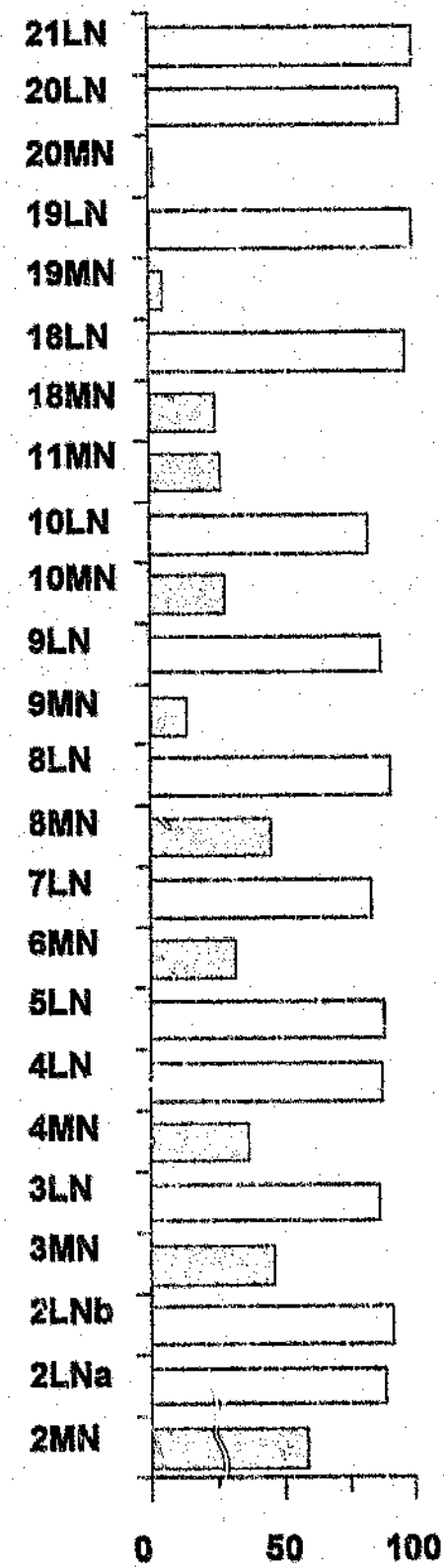


Figure 4.9 Plagioclase abundance as calculated from specific gravity measurements of samples taken from profile B.

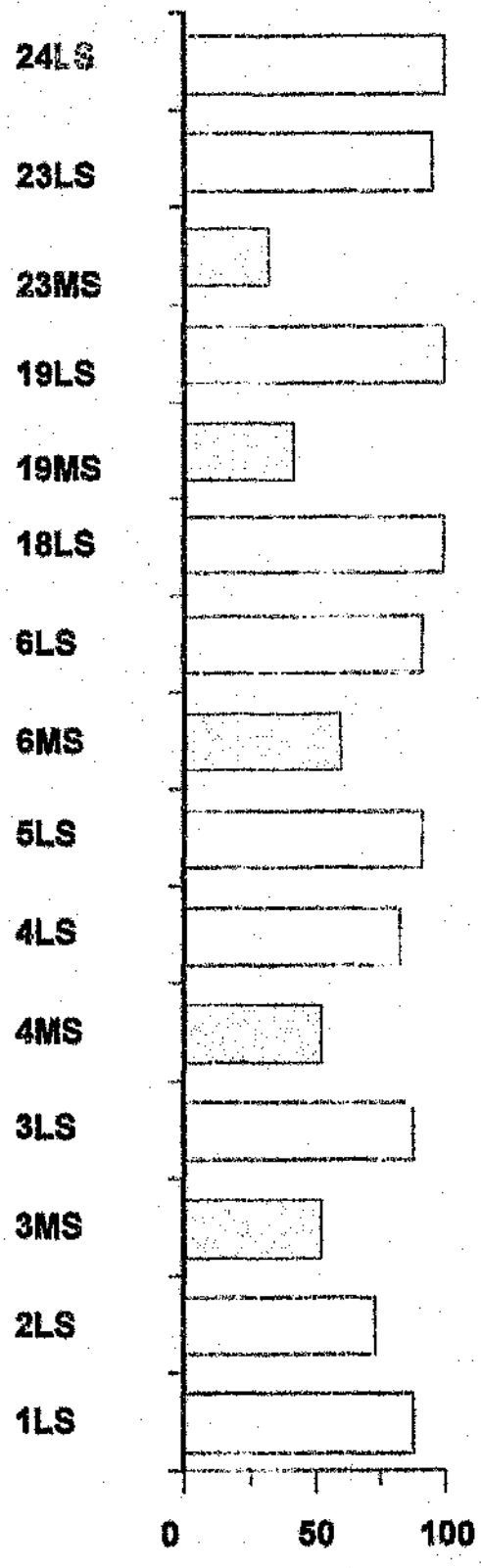


Figure 4.10 Plagioclase abundance as calculated from specific gravity measurements of samples taken from profile A.

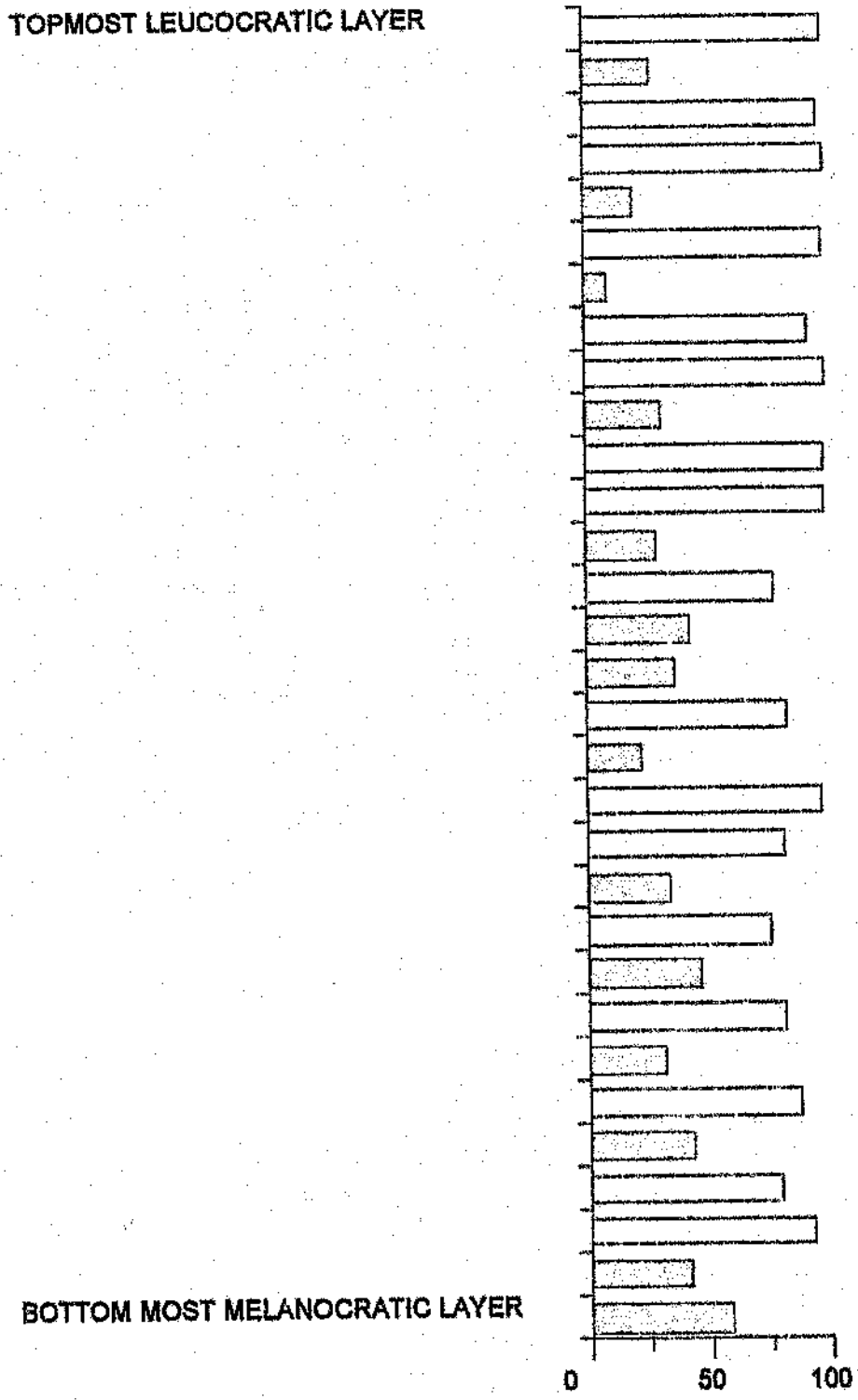


Figure 4.11 Plagioclase abundance as calculated from specific gravity measurements of samples taken from profile E.

4.1.2 Vertical and lateral variation in mode within a layer

Several layers were sampled more than once. The specific gravity of these samples was measured. From these few measurements (table 4.2) it would appear that there is no significant grading within these layers.

Table 4.2
Specific gravity and plagioclase modal variations within single layers. The error in the plagioclase modes is ~3%

Samples collected along strike (m)	
22LS(11)	2.75 (100% plag.)
22LS(22)	2.76 (100% plag.)
22LS(30)	2.76 (100% plag.)
22LS(37)	2.77 (100% plag.)
Samples collected vertically from within a single layer	
19mMS	3.12 (42% plag.)
19bMS	3.15 (37% plag.)
5tLS	2.88 (82% plag.)
5mLS	2.88 (82% plag.)
4tMS	3.06 (52% plag.)
4mMS	3.07 (50% plag.)
4bMS	3.05 (53% plag.)
18tLN	2.79 (96% plag.)
18bLN	2.78 (98% plag.)
10tMN	3.26 (18% plag.)
10bMN	3.17 (33% plag.)
28tLN	2.82 (91% plag.)
28NbL	2.84 (88% plag.)
30tLN	2.87 (83% plag.)
30bLN	2.86 (85% plag.)

5. Petrofabric of plagioclase grains

The rocks studied all display a fabric parallel to the layering which can be clearly seen in the field. It is defined by the plagioclase laths. Figure 5.1A is a sketch map of a portion of a vertically-orientated thin section. This figure shows the planar orientation of the majority of plagioclase laths. This is well illustrated by the rose diagram which reflects the orientation of the well-formed plagioclase laths. Whether the plagioclase laths are aligned within this plane is important to ascertain as it may indicate the significance of current activity within the chamber at the time the layers were forming. In order to study this aspect seventeen thin sections, orientated parallel to the plane of bedding, have been taken from selected samples and studied in terms of:

1- the orientation of the plagioclase laths;

2- the average grain size and length to breadth ratio of plagioclase grains.

Plagioclase grains were considered exclusively as the orthopyroxenes tend to form oikocrysts and it is often difficult to determine where the grain boundaries of the original grain were. The clinopyroxenes, on the other hand, rarely exhibit euhedral shapes, they are commonly highly irregular to skeletal; Hence elongation directions are impossible to determine. The plagioclase grains, by contrast, display good lath shape and it is therefore easy to assign a long and short axis to them. The lengths of the long and short axes have been measured, as well as the orientation of their long axes.

5.1 Orientation

Figure 5.1B is a sketch map of a portion of one of the thin section studied. This thin section was orientated parallel to the plane of layering. As can be seen from this diagram there is a distinct alignment of plagioclase laths within the section. This is further illustrated by the rose diagram which shows that a significant proportion of the laths are orientated parallel to the dip direction.

Based on the aspect ratio (length:breath), these grains have been divided into two categories. Those that have a length to breadth ratio of greater than 2, i.e. distinctly elongate grains (more elongate than grain X, Fig. 5.1B) and those that have a ratio of between 1 and 2, i.e. the equant crystals (grain Y, Fig. 5.1B has an aspect ratio of close to unity). It is possible that the equant shape is due to the cut effect and that these grains may be elongate in the third dimension but are lying at a significant angle to the plane of layering. However, in view of the strong fabric

parallel to layering this is probably not a common e ct. The reason for subdividing the grains in

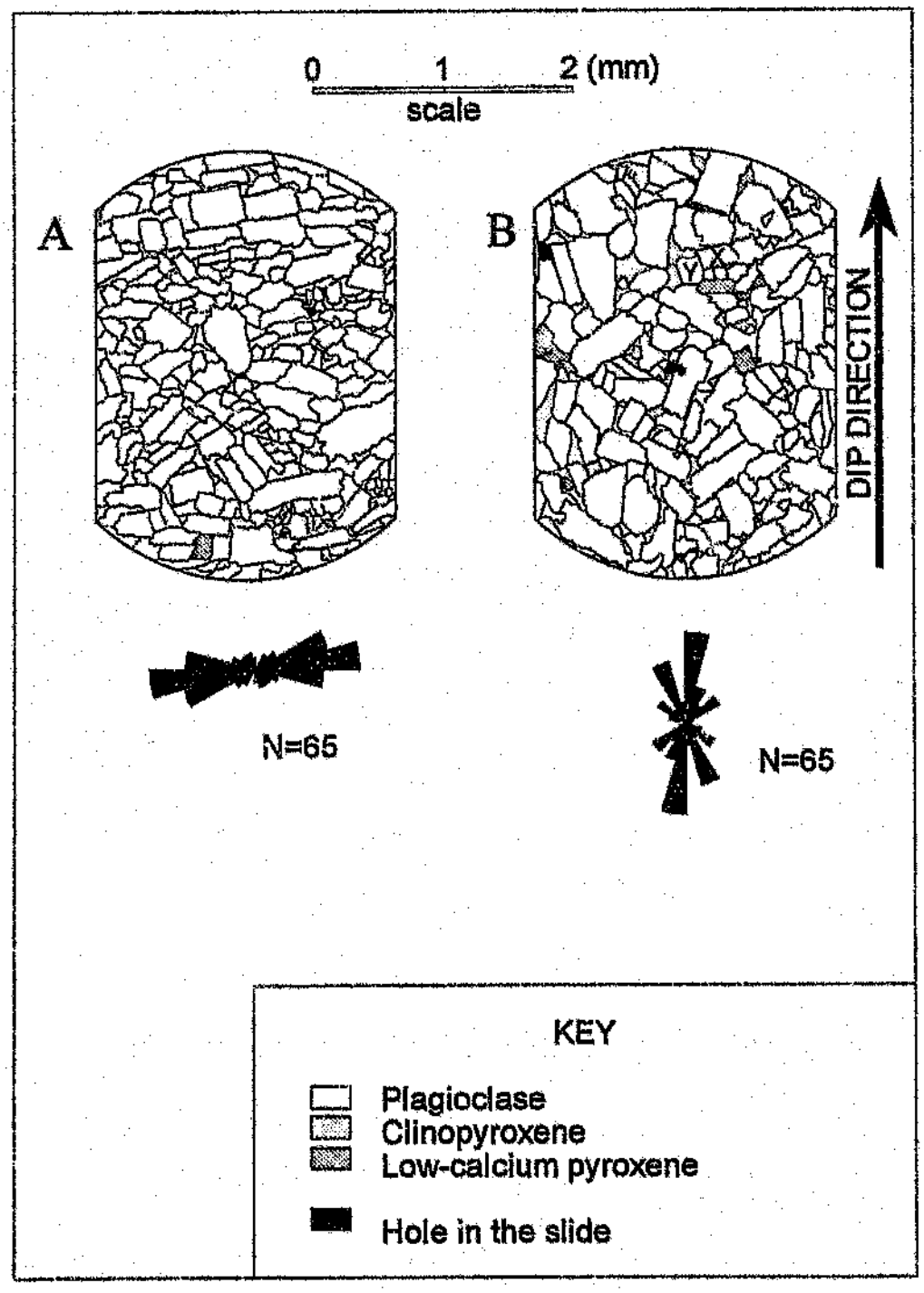


Figure 5.1 A: Sketch of a portion of a vertically orientated thin section from a leucocratic layer. Note the well developed horizontal fabric. This is well illustrated by the attached rose diagram.

B: Sketch of a portion of a thin section that was cut parallel to the plane of layering. This shows the linear habit of plagioclase within this plane. This lineation is clearly shown by the attached rose diagram.

this way is that the elongate grains are more likely to be physically aligned if their deposition is controlled by magmatic currents. Figure 5.2 displays rose diagrams for a number of samples from profile A.

Some display no fabric (e.g. 9LN). It would appear that where fabrics are developed within these samples, they tend to be either parallel to or perpendicular to the direction of dip. For the leucocratic samples the strong linear fabric tends to sub-parallel the dip direction (e.g. 5LN). In addition the samples taken from the top of these layers tend to show the better fabrics. Some of the melanocratic samples also display a linear fabric sub-parallel to the dip. However some melanocratic samples display a fabric that is sub-perpendicular to the dip direction. Usually the equant grains display a similar but poorer fabric than the elongate crystals do.

Table 5.1
Grain size data from the analysis of selected orientated thin sections.

Sample	% plag..	Position	grain size calculated from the 30 largest grains
21LN	95	TOP	3.80
20LN	89	TOP	4.00
20MN	17	TOP	2.15
19LN	98	BASE	3.20
18LN	91	BASE	3.07
18MN	45	TOP	3.00
9LN	97	BASE	3.40
9MN	42	TOP	3.30
8LN	78	BASE	3.60
7LN	92	TOP	3.08
6MN	31	BASE	2.40
5LN	70	TOP	3.50
4MN	23	BASE	2.37
3LN	89	TOP	3.20
3MN	43	TOP	2.80
2LNa	77	TOP	3.08
2MN	48	TOP	3.24

5.2 Grain size

In addition to considering the alignment of plagioclase grains the lengths of as many laths as possible were measured from each thin section. This data is listed in table 5.1 and is graphically illustrated in Figure 5.3. The grains were measured from a field of view projected onto a wall. This field of view represented a 2cm wide circular area of the thin section. It is probably not statistically valid to plot averages of all grains measured as in some cases very much fewer grains were measured than in others. For this reason the averages from the thirty largest grains in each sample have been considered and are plotted in Fig. 5.3.

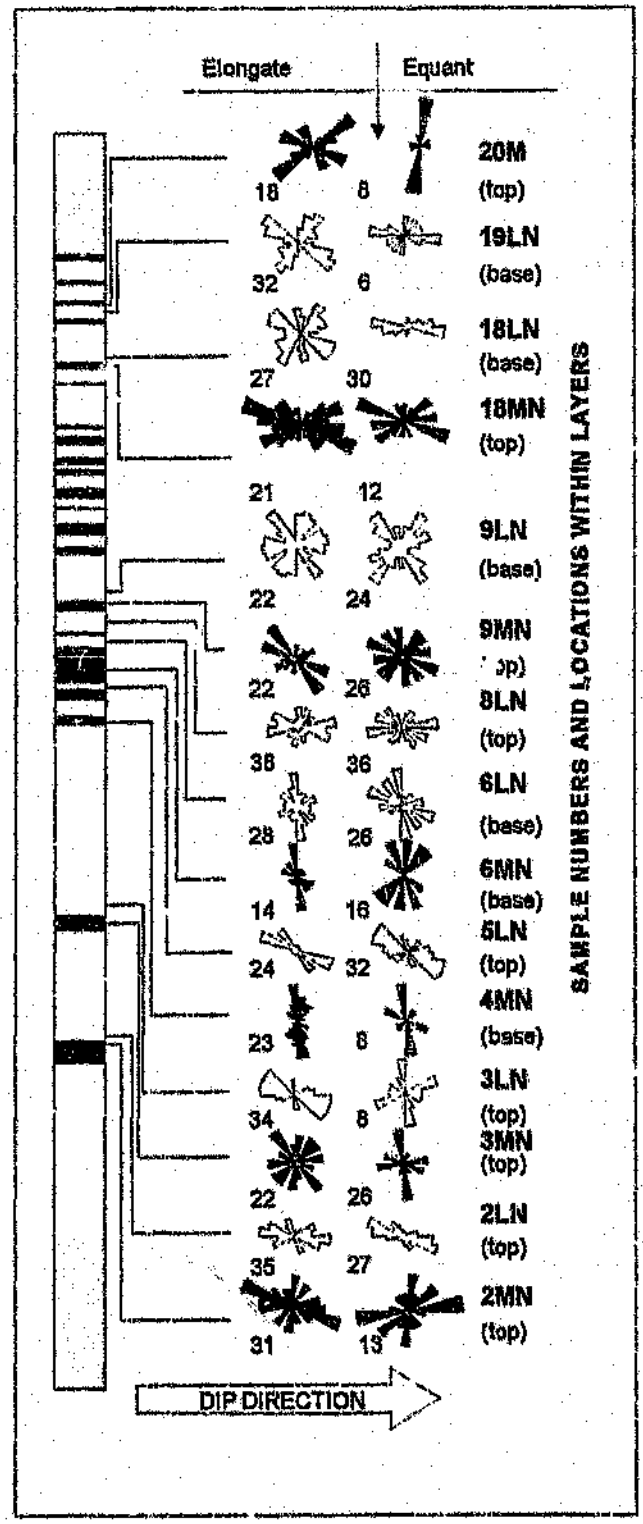


Figure 5.2 Rose diagrams showing the orientation of plagioclase laths in numerous samples from profile A. The left column of rose diagrams refers to the elongate grains (aspect ratio >2). The right column refers to the equant grains. "Top" and "base" refers to the position from where the sample was taken within a layer. The numbers to the top left of each rose diagram refer to the number of well-formed plagioclase laths measured from each thin section. Solid and open shading refer to melanocratic and leucocratic samples respectively.

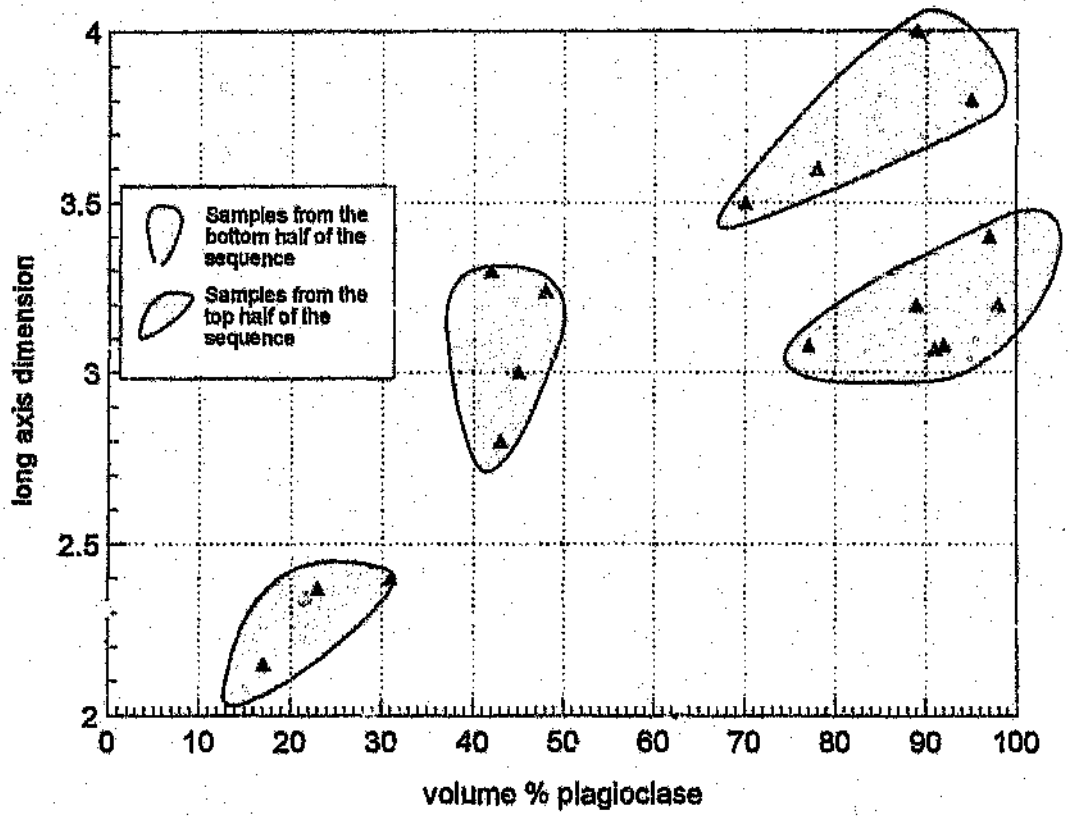


Figure 5.3 Plot of the average plagioclase grain size, calculated from the 30 largest grains measured from a single thin section per sample, plotted against the volume % plagioclase (determined from point counting using the same thin sections).

6. Plagioclase compositions

6.1 Introduction

Whole rock chemistry is variable due to the changing mineral assemblages and relative modal abundances (as will be shown later). Mineral compositions are, by contrast, more sensitive indicators of changes that may have occurred within the magma chamber.

Plagioclase compositions from the Main Zone of the eastern limb have been studied by von Gruenewaldt (1973), Molyneux (1974), Marais (1977) and Klemm et al. (1985). Molyneux (1974) measured the plagioclase compositions for numerous specimens of Bushveld rocks in the northern portion of the eastern limb. From his study it can be seen that the plagioclase compositions, in general, show a normal differentiation trend within the subzone B of the Main Zone (Fig.6.1). Close to the Pyroxenite Marker the trend reverses. At the level of the Pyroxenite Marker there is a strong reversal in plagioclase composition.

Marais (1977) studied the variation of plagioclase composition in four profiles over more than 80km of strike within the eastern limb (Fig.6.2). This work again showed the marked reversal in mineral compositions across the Pyroxenite Marker. However, in all these profiles the reversal begins very slowly ~200m below the marker.

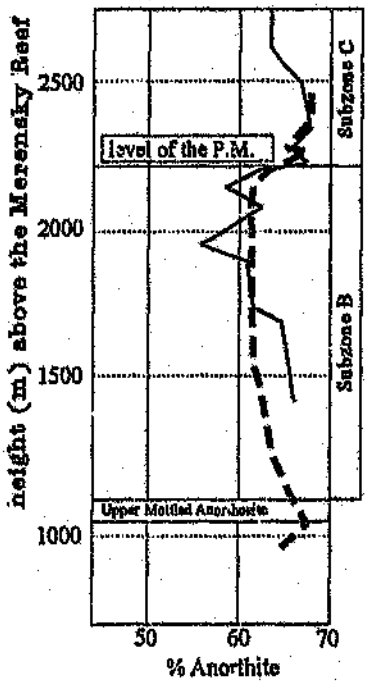


Figure 6.1 Variation in the composition of plagioclase through subzone B and a portion of subzone C (after Molyneux, 1974). The two line styles refer to two different profiles in the eastern Bushveld.

Klemm et al. (1985) undertook a detailed mapping program in the area between Laersdrift and

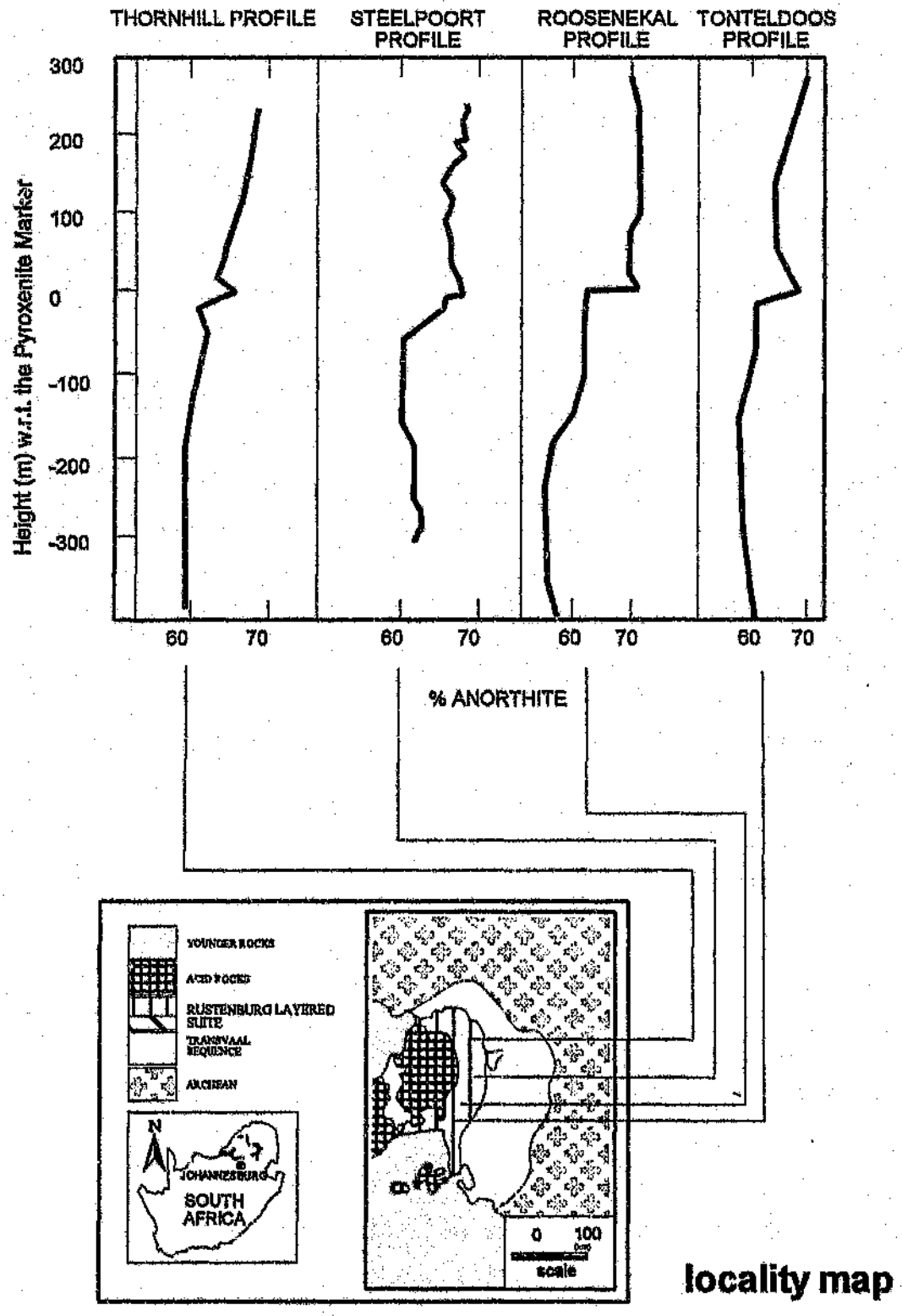


Figure 6.2 Variation in plagioclase composition across the Pyroxenite Marker along four profiles in the eastern limb of the Bushveld Complex (after Marais, 1977).

Roossenekal. With data collected from this study together with that compiled by von Gruenewaldt (1973) and Molyneux (1974), Klemm and his co-workers constructed a north-south-trending cross section showing vertical and lateral compositional changes. This work confirmed that there is a noticeable reversal of plagioclase composition some way below the Pyroxenite Marker in this area. From their profiles these authors also showed that the plagioclase became more evolved at the level of the Pyroxenite Marker to the south.

6.2 Analysis of plagioclase compositional variation in three profiles within Sekhukhuneland

Most previous work on samples from this area have made use of optical methods and norms in determining the mineral composition of plagioclase. Marais (1977) analysed a few separates as a means of checking the optical measurements. Although these are useful approachs, it is preferable to use a chemical analytical technique to accurately determine their compositions. Recent work on plagioclase from the Upper Zone of the Bushveld Complex has revealed that the core compositions within a single sample may vary as much as 9 mole % anorthite (Harney et al., 1990) and that individual cores may exhibit internal variations in composition of between 3 to 6 mole % anorthite. To get an accurate and reliable estimate of the plagioclase composition within each sample would require that an enormous number of plagioclase grains be probed. It was therefore decided to use mineral separates. In this way each analysis represents an average composition for thousands of crystals.

Tables 6.2a, 6.3a and 6.4a list the average of two geochemical analyses of the plagioclase separates from samples taken from profiles A, B and C. The results of a normative calculation undertaken on each sample are given in tables 6.2b, 6.3b and 6.4b.

6.2.1 Determination of the anorthite content of plagioclase

The An content of plagioclase is conventionally determined by the atomic ratio Ca/(Ca+Na) from an analysis. The Al and Si contents vary in a systematic way with changing An content, but rarely are the abundances of these elements compared with expected values to act as a check on the determined plagioclase composition. Furthermore, the error in the actual analysis, and this effect on the plagioclase composition, is not often reported. In this study several methods of calculating the An content are investigated and the precision and confidence in these values documented statistically.

Analytical precision

To determine the analytical precision achieved in the analysis of these separates, all samples were run in duplicate. A few of these duplicate analyses are presented, for comparative purposes, in the Table 6.1. From such results the pooled standard deviation was calculated for each variable. The errors have been calculated from the duplicate analyses. For analyses that are time consuming it is often impractical to run a single sample a considerable number of times to reliably measure the standard dev' 'ion for the population. However precision data from a series of samples accumulated over a specific period can be pooled to provide a reliable estimate of the standard deviation of the population (these values are listed in Table 6.5 and the method used to derive them is outlined in Appendix 4).

Table 6.1
Duplicate major element analyses of selected plagioclase separates from profile B.

	SiO_2	Al_2O_3	Fe_2O_3	MgO	CaO	Na_2O	K_2O	Total
H7S	52.43	29.39	0.38	0.22	12.32	4.17	0.32	99.26
H7S	53.37	29.27	0.34	0.13	12.23	4.08	0.33	99.82
23LS	53.48	29.04	0.31	0.13	12.07	4.18	0.38	99.61
23LS	53.70	28.85	0.42	0.15	12.14	4.20	0.38	99.93
23MS	55.77	26.77	0.62	0.21	11.21	3.95	0.31	98.98
23MS	56.68	26.96	0.51	0.16	11.24	4.05	0.30	100.1
3MS	52.76	29.34	0.48	0.14	12.27	4.18	0.31	99.53
3MS	52.63	29.34	0.44	0.10	12.24	4.17	0.32	99.29
2LS	52.33	28.84	0.40	0.64	12.12	4.12	0.33	98.82
2LS	52.37	28.86	0.40	0.92	12.03	4.04	0.33	99.01
2LS	52.31	29.00	0.38	0.63	12.09	4.17	0.34	98.97
2LS	53.06	29.09	0.39	0.16	12.12	4.30	0.33	99.49
F2S	53.30	28.89	0.47	0.13	12.13	4.07	0.35	99.40
F2S	53.42	28.85	0.52	0.18	12.15	4.19	0.36	99.72

The uncertainties for CaO and Na_2O are 0.10 and 0.13% respectively. An ideal plagioclase, with the composition An_{50}, contains 10.37% CaO and 5.73% Na_2O. Therefore the two worst combinations of errors in CaO and Na_2O determinations would lead to calculated An contents of 49.2 and 50.8%, an uncertainty of 1.6%. When dealing with a short vertical interval within a layered intrusion, it is possible that a real trend could be masked by such a relatively large uncertainty. The question is whether there are other ways of estimating the An content which yield smaller errors or where additional cross checks on analytical precision can be made.

Table 6.2a
Average plagioclase analyses for samples from profile A

	SiO_2	Al_2O_3	Fe_2O_3	MgO	CaO	Na_2O	K_2O	Totals
hangingwall samples								
H8N	50.18	30.45	0.44	0.26	14.04	3.20	0.27	98.88
H7N	51.49	30.19	0.50	0.20	13.42	3.25	0.31	99.42
H6N	52.92	29.01	0.42	0.17	12.37	3.72	0.34	99.00
H4N	52.53	29.24	0.28	0.12	12.35	4.05	0.30	98.90
H3N	54.61	28.08	0.37	0.34	11.37	4.59	0.36	99.75
H2N	52.71	29.29	0.41	0.18	12.38	3.95	0.32	99.27
H1N	53.28	29.31	0.38	0.24	12.28	4.18	0.29	99.97
samples from the layered sequence								
20LN	52.95	28.88	0.46	0.78	12.25	4.05	0.35	99.75
20MN	53.36	29.18	0.39	0.26	12.15	4.06	0.33	99.75
19LN	53.38	28.96	0.47	0.46	12.17	4.07	0.39	99.94
19MN	54.34	27.92	0.47	0.25	11.70	3.98	0.32	99.05
18LN	52.94	28.95	0.37	0.57	12.22	4.08	0.37	99.57
18MN	53.35	28.99	0.50	0.14	11.97	4.32	0.33	99.65
11MN	53.03	29.39	0.43	0.21	12.23	4.22	0.34	99.89
10LN	53.13	29.01	0.41	0.45	12.23	4.14	0.35	99.76
10MN	52.48	29.21	0.42	0.27	12.18	4.22	0.35	99.16
9LN	53.15	29.20	0.49	0.25	12.06	4.07	0.36	99.63
9MN	52.62	29.18	0.55	0.40	12.19	4.32	0.36	99.67
8LN	53.43	29.17	0.44	0.41	12.11	4.29	0.36	100.26
8MN	52.88	29.13	0.37	0.23	12.25	4.22	0.33	99.44
7LN	52.73	29.20	0.40	0.17	12.22	4.18	0.34	99.28
6MN	52.90	29.19	0.41	0.19	12.18	4.19	0.35	99.43
5LN	53.27	29.05	0.35	0.16	12.10	4.24	0.36	99.56
5MN	53.46	29.13	0.43	0.37	12.23	4.22	0.35	100.24
4LN	52.97	29.00	0.35	0.24	12.03	4.24	0.35	99.23
4MN	52.69	28.96	0.35	0.35	12.14	4.09	0.34	98.96
3LN	52.90	29.18	0.36	0.12	12.26	4.31	0.31	99.46
3MN	53.31	29.26	0.37	0.15	12.24	4.26	0.31	99.93
2LNA	53.30	29.04	0.32	0.09	12.17	4.29	0.33	99.60
2LNB	53.17	28.97	0.43	0.09	12.12	4.15	0.35	99.31
2MN	53.40	29.23	0.38	0.09	12.25	4.16	0.32	99.87
footwall samples								
F1N	52.98	28.90	0.43	0.23	12.18	4.08	0.33	99.16
F2N	52.76	29.01	0.33	0.12	12.25	4.12	0.33	98.94

Table 6.2b
Results of a CIPW normalization of plagioclase analyses for samples from profile A

Sample	Q/L	C	O	AB	AN	NE	DI	WO	HY
hangingwall samples									
H8N	0.43	0	1.6	27.07	67.93	0	1.34	0	0.03
H7N	2.34	0.11	1.83	27.5	66.58	0	0	0	0.5
H6N	3.22	0.03	2.01	31.47	61.37	0	0	0	0.42
H4N	1.3	0	1.77	34.27	60.73	0	0.42	0	0.1
H3N	1.97	0	2.13	38.84	54.96	0	1.13	0	0.32
H2N	1.75	0	1.89	33.42	61.25	0	0.13	0	0.39
H1N	1.3	0	1.71	35.37	60.37	0	0.44	0	0.4
samples from the layered marker sequence									
20LN	0.89	0	2.07	34.27	59.6	0	0.92	0	1.52
20MN	2.06	0.06	1.95	34.35	60.28	0	0	0	0.65
19LN	1.61	0	2.31	34.44	59.61	0	0.6	0	0.87
19MN	4.66	0	1.89	33.67	57.38	0	0.52	0	0.38
18LN	0.98	0	2.19	34.52	59.6	0	0.8	0	1.05
18MN	1.24	0	1.95	36.55	58.75	0	0.5	0	0.12
11MN	0.75	0	2.01	35.7	60.26	0	0.33	0	0.37
10LN	1.07	0	2.07	35.03	59.55	0	0.88	0	0.71
10MN	0.24	0	2.07	35.7	59.74	0	0.54	0	0.42
9LN	1.88	0.19	2.13	34.44	59.83	0	0	0	0.62
9MN	-0.37	0	2.13	36.19	59.18	0.2	1.01	0	0
8LN	0.71	0	2.13	36.3	59.28	0	0.62	0	0.73
8MN	0.73	0	1.95	35.7	59.58	0	0.93	0	0.14
7LN	0.83	0	2.01	35.37	59.92	0	0.55	0	0.17
6MN	0.94	0	2.07	35.45	59.82	0	0.48	0	0.25
5LN	1.24	0	2.13	35.87	59.18	0	0.66	0	0.09
5MN	1.06	0	2.07	35.7	59.52	0	0.9	0	0.5
4LN	0.96	0	2.07	35.87	59.07	0	0.48	0	0.38
4MN	1.18	0	2.01	34.61	59.67	0	0.44	0	0.67
3LN	0.51	0	1.83	36.47	59.37	0	0.64	0.26	0
3MN	1.09	0	1.83	36.04	59.81	0	0.71	0	0.04
2LNA	1.16	0	1.95	36.3	59.02	0	0.48	0.31	0
2LNB	1.74	0	2.07	35.11	59.39	0	0.48	0.05	0
2MN	1.73	0	1.89	35.2	60.15	0	0.48	0	0
footwall samples									
F1N	1.72	0	1.95	34.52	59.58	0	0.66	0	0.27
F2N	1.33	0	1.95	34.86	59.7	0	0.64	0.1	0

Q/L QUARTZ CONTENT (+VE); OLIVINE CONTENT (-VE)
C CORUNDUM
O ORTHOCLASE
AB ALBITE
AN ANORTHITE
NE NEPHELINE
DI DIOPSIDE
WO WOLLASTONITE
HY HYPERSTHENE

Table 6.3a
Average plagioclase analyses for samples from profile B

	SiO_2	Al_2O_3	Fe_2O_3	MgO	CaO	Na_2O	K_2O	Totals
hangingall samples								
H12S	50.69	30.96	0.55	0.28	14.14	3.02	0.25	99.96
H11S	52.43	30.00	0.39	0.00	12.62	3.85	0.32	99.68
H10S	53.74	28.27	0.43	0.25	11.69	4.32	0.29	99.07
H9S	52.44	30.01	0.44	0.13	12.64	3.70	0.36	99.79
H8S	51.71	30.82	0.30	0.07	13.36	3.10	0.21	99.61
H7S	52.90	29.33	0.36	0.18	12.28	4.13	0.33	99.54
H6S	55.20	27.37	0.56	0.34	11.11	4.36	0.46	99.54
H5S	53.22	29.23	0.36	0.10	12.30	4.25	0.32	99.81
H1S	53.46	29.11	0.42	0.11	12.18	4.26	0.32	99.90
samples from the layered sequence								
25LS	53.05	28.81	0.40	0.17	11.95	3.97	0.39	98.78
25MS	53.37	29.16	0.42	0.15	12.03	4.40	0.34	99.93
24LS	53.41	28.96	0.43	0.16	12.01	4.12	0.42	99.54
24MS	52.94	29.01	0.42	0.16	12.10	4.26	0.35	99.27
23LS	53.59	28.95	0.37	0.14	12.11	4.19	0.38	99.77
23MS	56.23	26.87	0.57	0.19	11.23	4.00	0.31	99.52
22LS	53.25	28.84	0.42	0.53	12.09	4.18	0.35	99.71
22MS	53.47	29.21	0.44	0.12	12.18	4.41	0.33	100.19
19LS	52.93	28.86	0.40	0.54	12.15	4.10	0.34	99.39
ML	53.15	28.40	0.41	0.37	11.69	4.15	0.54	98.75
19T	52.56	29.28	0.40	0.08	12.32	4.05	0.31	99.06
19M	53.83	29.49	0.44	0.14	12.43	4.08	0.33	100.79
19B	52.89	29.13	0.36	0.16	12.26	4.12	0.31	99.26
18LS	53.45	28.74	0.41	0.85	11.91	4.11	0.50	100.00
6LS	53.01	29.18	0.39	0.11	12.14	4.08	0.35	99.31
6MS	53.48	29.18	0.44	0.17	12.27	4.30	0.33	100.24
5LS	53.71	29.04	0.38	0.13	12.12	4.29	0.36	100.08
4LS	53.23	29.20	0.50	0.09	12.17	4.21	0.36	99.82
4MS	52.83	29.28	0.32	0.10	12.31	4.14	0.31	99.33
3LS	52.98	29.04	0.41	0.13	12.17	4.30	0.34	99.42
3MS	52.70	29.34	0.46	0.12	12.26	4.18	0.32	99.41
2LS	52.35	28.85	0.40	0.78	12.08	4.08	0.33	98.92
2LS	52.69	29.05	0.39	0.40	12.11	4.24	0.34	99.23
1LS	53.02	29.12	0.41	0.08	12.16	4.23	0.35	99.41
footwall samples								
F1S	53.04	29.28	0.42	0.13	12.29	4.25	0.33	99.78
F2S	53.36	28.87	0.50	0.16	12.14	4.13	0.36	99.56

Table 6.3b
Results of a CIPW normalization of plagioclase analyses for samples from profile B

Sample	Q/L	C	O	A	AN	NE	DI	WO	HY
hangingwall samples									
H12S	1.45	0.01	1.48	25.55	70.15	0	0	0	0.7
H11S	1.77	0.38	1.89	32.57	62.61	0	0	0	0
H10S	2.31	0	1.71	36.55	56.9	0	0.86	0	0.23
H9S	2.26	0.55	2.13	31.31	62.71	0	0	0	0.32
H8S	4.14	1.2	1.24	26.23	66.28	0	0	0	0.17
H7S	1.12	0	1.95	34.94	60.53	0	0.31	0	0.3
H6S	4.06	0	2.72	36.89	53.76	0	1.06	0	0.36
H5S	1.04	0	1.89	35.96	59.74	0	0.54	0.25	0
H1S	1.42	0	1.89	36.04	59.37	0	0.59	0.12	0
samples from the layered marker sequence									
25LS	2.6	0.13	2.31	33.59	59.29	0	0	0	0.42
25MS	0.66	0	2.01	37.23	58.82	0	0.67	0	0.06
24LS	1.92	0	2.48	34.86	59.3	0	0.23	0	0.29
24MS	0.87	0	2.07	36.04	59.01	0	0.8	0	0.03
23LS	1.82	0	2.25	35.45	59.07	0	0.75	0.02	0
23MS	7.7	0	1.83	33.84	54.46	0	0.98	0	0.02
22LS	1.13	0	2.07	35.37	58.91	0	0.84	0	0.93
22MS	0.6	0	1.95	37.31	58.94	0	0.64	0.28	0
19LS	1.14	0	2.01	34.69	59.35	0	0.73	0	1.01
ML	1.5	0	3.19	35.11	57.28	0	0.56	0	0.66
19T	1.36	0	1.83	34.27	60.81	0	0.25	0	0.09
19M	2.09	0	1.95	34.52	61.19	0	0.38	0	0.17
19B	1.39	0	1.83	34.86	60.08	0	0.58	0	0.13
18LS	0.97	0	2.96	34.77	58.5	0	0.46	0	1.91
6LS	1.76	0.02	2.07	34.52	60.23	0	0	0	0.27
6MS	0.99	0	1.95	36.38	59.35	0	0.91	0.15	0
5LS	1.47	0	2.13	36.3	58.93	0	0.7	0.13	0
4LS	1.29	0	2.13	35.62	59.72	0	0.48	0.01	0
4MS	1.18	0	1.83	35.03	60.4	0	0.52	0	0.01
3LS	0.7	0	2.01	36.38	58.94	0	0.7	0.23	0
3MS	0.81	0	1.89	35.37	60.36	0	0.36	0	0.13
2LS	0.41	0	1.95	34.52	59.44	0	0.38	0	1.76
2LS	0.36	0	2.01	35.87	59.24	0	0.66	0	0.69
1LS	1.09	0	2.07	35.79	59.44	0	0.43	0.14	0
footwall samples									
F1S	0.71		1.92						
F2S	1.79		2.07						

Table 6.4 a
Average plagioclase analyses for samples from profile C

	SiO_2	Al_2O_3	Fe_2O_3	MgO	CaO	Na_2O	K_2O	Totals
76L	53.25	29.45	0.73	0.51	12.17	4.63	0.36	101.17
76M	52.79	29.35	0.71	0.48	12.15	4.57	0.38	100.50
38L	52.86	29.04	0.60	0.36	12.01	4.51	0.45	99.90
38M	53.24	29.20	0.65	0.41	12.32	4.27	0.34	100.48
23M	53.22	29.49	0.77	0.48	12.33	4.13	0.37	100.86
16L	52.91	28.84	0.80	0.46	12.28	4.24	0.37	99.97
16M	53.07	29.07	0.77	0.56	12.36	4.71	0.39	100.99
7P	53.47	29.12	0.82	0.57	12.15	4.24	0.36	100.79
2P	52.96	29.44	0.60	0.41	12.11	4.51	0.33	100.45

Table 6.4b
Results of a CIPW normalization of plagioclase analyses for samples from profile C

Sample	Q/L	C	O	A	AN	NE	DI	WO	HY
76L	-0.42	0	2.13	36.3	58.52	1.56	1.45	0	0
76M	-0.38	0	2.25	35.51	58.46	1.71	1.42	0	0
38L	-0.15	0	2.66	36.2	57.67	1.06	1.49	0	0
38M	0.44	0	2.01	36.13	59.51	0	1.25	0	0.44
23M	0.71	0	2.19	34.94	60.84	0	0.26	0	1.08
16L	0.34	0	2.19	35.87	58.58	0	1.83	0	0.3
16M	0	0	2.31	35.02	57.04	2.62	3.01	0.18	0
7P	0.74	0	2.13	35.87	59.37	0	0.71	0	1.09
2P	-0.47	0	1.95	36.65	59.12	0.82	0.75	0	0
1	-0.2	0	0	0	0	0.28	0.09	0	0
2	-0.43	0	0	0	0	0.58	0.08	0	0

Table 6.5
errors calculated from the duplicate analysis of plagioclase samples

chemical analysis

	SiO_2	Al_2O_3	Fe_2O_3	MgO	CaO	Na_2O	K_2O	Total
2σ	0.58	0.23	0.11	0.26	0.10	0.13	0.02	0.70

on normative calculation

	Q/L	C	O	A	AN	NE	DI	WO	HY
2σ			0.97	1.08	0.77				0.74

Calculation of %An

There are a number of ways in which the anorthite content of the plagioclase could be calculated. The conventional way is based on the Ca/Ca+Na ratio. An alternative would be the calculation of a C.I.P.W. norm. This gives an estimate of what proportion of an, ab and or may be present in the sample analysed. However as can be seen from table 6.5 there is an element of uncertainty associated with each oxide analysed for and this adds up to a reasonably large uncertainty (~1%An) for the An value calculated in this way. A number of other minerals also appear in the norm., and their significance should be considered. The most abundant additional phase is that of quartz. This mineral was not identified in the microscopic work. However other authors have identified quartz in similar samples (von Gruenewaldt, 1971). It is also not unreasonable that some quartz may have crystallized as a trapped component. In magnetically separating the plagioclase, any quartz that is present in the specimen would separate into the non-magnetic "plagioclase" fraction. The highest normative quartz contents are in samples from the mafic layers, where the proportion of plagioclase is low. Most of the samples contain very low abundances of quartz and this indicates that the modal quartz content is actually extremely small. Furthermore if a ratio of elements is used to determine anorthite content the presence of normative quartz will have no effect. The other phases listed in a C.I.P.W. norm are hypersthene and clinopyroxene. Hypersthene content may be due to opx being present in the separate. The presence of cpx in the norm. shows that either there is some cpx in the separate or that there is insufficient Al_2O_3 in the analysis.

Use of oxide abundances in calculating the anorthite content of the plagioclase

Each major oxide present in plagioclase can also be used to calculate the anorthite content of the mineral. As the plagioclase evolves from anorthite to albite, so the major element concentrations within the mineral changes. If we assume ideal stoichiometry, then the following formulae describe how the major elements vary as a function of anorthite content:

$$An\ (CaO)=0.00005\ x^3+0.010.01315\ x^2+4.67699\ x+0.00002 \quad \ldots\ldots\ldots\ldots\ldots\ 1$$

where An(CaO) is the anorthite content calculated from the wt% of CaO in the analysis and x is the wt% of CaO in the analysis.

$$An\ (Na_2O)=-0.00025\ x^3+0.04644\ x^2-8.97869\ x+100.00017 \quad \ldots\ldots\ldots\ldots\ 2$$

An(Na_2O) is the anorthite content calculated from the wt% of Na_2O in the analysis.

$$An\ (Al_2O_3)=0.000069\ x^3+0.01\ x^2+4.8\ x-100.130052 \quad \ldots\ldots\ldots\ldots\ 3$$

$An(Al_2O_3)$ is the anorthite content calculated the Al_2O_3 abundances.

$$An\ (SiO_2) = -0.000021\ x^3 + 0.012569\ x^2 - 5.121516\ x + 299.461252 \quad \ldots\ldots\ldots\ldots\ 4$$

where $An(SiO_2)$ is the anorthite content calculated from the SiO_2 abundance.

These formulae have been determined by least squares approximation using model data. To demonstrate the accuracy of these mathematical expressions, the modelled abundances have been used to calculate the anorthite content from which they were originally calculated. These results are presented in table 6.6.

Table 6.6
Modelled oxide abundances within plagioclase of a specific anorthite composition and the calculated composition based on these values.

% An	SiO_2	$An(SiO_2)$	Al_2O_3	$An(Al_2O_3)$	CaO	An(CaO)	Na_2O	$An(Na_2O)$
100	43.2	99.98	36.65	100.02	20.16	100.04	0.00	100.00
90	45.62	89.98	35.02	90.03	18.25	90.04	1.12	90.00
80	48.07	79.98	33.37	80.03	16.31	80.00	2.25	80.04
70	50.55	69.97	31.70	70.02	14.36	70.02	3.40	70.02
60	53.05	60.00	30.01	60.02	12.38	60.01	4.56	60.05
50	55.59	49.99	28.30	50.01	10.38	50.02	5.73	50 13

The composition of plagioclase separates as calculated from major element abundances are listed in the tables 6.7, 6.8 and 6.9. These values have been calculated from:

1 the Ca:Ca+Na ratio i.e. the conventional method;

2 the actual abundance of CaO in the analysis (as per equation 1);

3 the abundance of CaO in the analysis normalized to 100%;

(this is an attempt to compensate for the fact that the analyses rarely add up to 100%)

4 the abundance of Na_2O (as per equation 2);

5 the abundance of Na_2O but with the analysis normalized to 100%;

6 the Al_2O_3 abundance (as per equation 3);

7 the Al_2O_3 abundance but with the analysis normalized to 100%;

8 the SiO_2 abundance (as per equation 4);

9 the SiO_2 abundance but with the analysis normalized to 100%;

10 using a CIPW normative calculation.

In addition K_2O has been excluded as $KAlSi_3O_8$ from the analysis prior to making these calculations. Similarly the free quartz, as calculated in the C.I.P.W. normalization program, has also been excluded. The analysis was recalculated back to the original total after removal of these components.

Table 6.7
% An in plagioclase calculated from oxide abundances (with free quartz and K_2O excluded) for samples from profile C.

	An(1)	An(2)	An(3)	An(4)	An(5)	An(6)	An(7)	An(8)	An(9)	An(10)	
76L	59.3	60.4	60.3	58.6	58.7	58.2	58.3	60.3	60.4	59.5	An(1)=Ca/Ca+Na
76M	59.5	60.7	60.2	59.0	59.5	57.6	58.1	62.1	62.6	59.9	An(2)=f(CaO)
38L	59.6	60.5	59.8	59.4	60.1	56.1	56.7	62.1	62.8	59.1	An(3)=f(CaO/T)
38M	61.5	61.6	61.2	61.6	62.0	57.4	57.7	61.0	61.4	60.9	An(4)=f(Na_2O)
23M	62.3	61.9	61.6	62.7	63.0	59.6	59.9	61.7	62.0	62.1	An(5)=f(Na_2O/T)
16L	61.6	62.0	61.1	61.8	62.7	55.1	55.9	62.2	63.1	60.6	An(6)=f(Al_2O_3)
16M	59.2	61.6	61.4	57.8	58.1	56.0	56.2	61.0	61.3	59.4	An(7)=f(Al_2O_3/T)
7P	61.3	61.0	60.6	61.7	62.2	57.4	57.8	60.7	61.1	60.9	An(8)=f(SiO_2)
2P	59.8	60.3	59.9	59.7	60.1	58.0	58.4	61.3	61.7	59.9	An(9)=f(SiO_2/T)
											An(10)=norm. calc.
average deviation from An(1) (the conventional method) based on all values (tables 6.7-6.9)											
		0.8	0.7	0.6	0.7	4.6	0.6	4.2	0.7	2.3	
precision based on the duplicate analyses for samples from profile A and B											
2σ	0.7	0.6	0.5	0.9	1.2	2.3	2.0	1.8	2.2	1.0	

In the conventional calculation of the An content (i.e. using the relationship Ca/Ca+Na) there are potential analytical errors in the analysis of Ca and Na. This could influence the accuracy of the determined An content, whereas when CaO or any other element is used exclusively in these calculations there is only the potential error in one elements abundance and so this method is potentially more precise.

Between An_{70} and An_{50} (the range investigated here) the CaO content ranges from 14.36 to 10.38 or 0.2% CaO per 1 mole An. As the precision for CaO is ~0.10 wt%, the precision in the An content calculated using equation 1 is ~0.6% An. A similar calculation for the other three elements gives 0.115% Na_2O, 0.17% Al_2O_3 and 0.25% SiO_2 per 1 mole An. Therefore the potential precision using SiO_2 should be greater than when CaO is used. However the prescence of quartz in the mineral separate renders this element unreliable. Thus the method using CaO is considered to be potentially the most precise. These theoretical considerations are borne out in a statistical analysis of the precision of each method (Table 6.7). From these results it appears that

the method employing CaO abundance does provide the most precise result. Using the Al_2O_3 abundance on the other hand gives a significantly and systematically lower anorthite content than expected based on CaO and Na_2O abundances. SiO_2 produces the reverse. On the basis of these anomalies ratios involving these elements have not been used to determine the anorthite content of the separates. The normal method of calculating the anorthite content is using the ratio Ca/Ca+Na (An(1)). Comparison between this and other methods shows that, those methods using CaO and Na_2O abundances provide similar results. Those employing SiO_2 and Al_2O_3 abundance are inaccurate.

Table 6.8
% An in plagioclase calculated from oxide abundances (with free quartz and K_2O excluded) for samples from profile A.

	An(1)	An(2)	An(3)	An(4)	An(5)	An(6)	An(7)	An(8)	An(9)	An(10)
hangingwall samples										
H8N	70.8	69.9	71.2	71.2	72.5	64.6	65.8	73.2	74.6	70.3
H7N	69.6	68.1	69.1	70.1	71.1	66.5	67.5	71.6	72.6	69.5
H6N	64.8	63.3	64.4	65.6	66.7	61.0	62.0	67.4	68.5	64.8
H4N	62.8	61.9	62.8	63.4	64.4	59.0	59.9	65.4	66.4	62.5
H3N	57.8	57.3	57.8	58.2	58.8	53.1	53.7	58.1	58.7	57.2
H2N	63.4	62.4	63.2	64.0	64.9	60.2	61.0	65.6	66.5	63.2
H1N	61.9	61.4	61.8	62.2	62.7	59.3	59.6	62.3	62.7	61.7
samples from the layered marker sequence										
20LN	62.6	61.2	62.2	63.4	64.4	56.3	57.1	63.0	64.1	62.2
20MN	62.4	61.3	62.0	63.0	63.6	60.0	60.5	63.5	64.1	62.3
19LN	62.4	61.4	62.1	62.9	63.6	58.0	58.6	62.7	63.4	62.0
19MN	61.9	60.5	61.6	62.7	63.9	56.6	57.6	63.9	65.1	61.6
18LN	62.4	61.2	62.1	63.0	64.0	56.9	57.7	63.2	64.2	61.9
18MN	60.5	59.9	60.5	60.9	61.6	57.3	58.0	61.9	62.6	60.2
11MN	61.6	61.0	61.5	62.0	62.5	59.1	59.5	62.4	63.0	61.4
10LN	62.1	61.2	61.9	62.5	63.3	57.3	58.0	62.6	63.3	61.6
10MN	61.5	60.5	61.5	62.1	63.1	57.3	58.3	64.0	65.0	61.2
9LN	62.1	60.8	61.6	62.8	63.6	59.9	60.6	64.0	64 8	62.1
9MN	61.0	60.4	61.3	61.3	62.1	56.7	57.5	62.8	63.7	60.5
8LN	61.0	60.6	61.0	61.2	61.6	58.2	58.5	61.2	61.7	60.5
8MN	61.7	61.0	61.8	62.0	62.8	57.4	58.2	63.0	63.7	61.2
7LN	61.8	61.0	61.8	62.3	63.1	58.0	58.8	63.7	64.6	61.5
6MN	61.7	60.9	61.6	62.1	62.9	58.1	58.9	63.3	64.0	61.4
5LN	61.2	60.7	61.3	61.5	62.2	57.9	58.4	62.3	62.9	60.9
5MN	61.6	61.2	61.6	61.8	62.2	58.0	58.3	61.2	61 6	61.1
4LN	61.1	60.1	61.0	61.7	62.5	57.1	57.9	63.0	63.9	60.8
4MN	62.2	60.8	61.9	63.0	64.1	57.2	58.3	64.6	65.8	61.9
3LN	61.1	60.9	61.5	61.3	61.9	57.2	57.8	62.4	63.1	60.5
3MN	61.4	61.1	61.5	61.5	61.9	58.6	59.0	61.7	62.1	61.0
2LNA	61.1	60.9	61.4	61.2	61.8	57.5	58.0	62.0	62.6	60.5
2LNB	61.8	61.0	61.8	62.2	63.0	58.2	59.0	63.6	64.5	61.5
2MN	62.0	61.6	62.0	62.2	62.6	59.6	60.0	62.6	63.0	61.7
footwall samples										
F1N	62.3	61.3	62.3	62.9	63.8	57.6	58.6	64.3	65.3	61.9
F2N	62.2	61.4	62.4	62.6	63.6	57.7	58.6	64.5	65.5	61.7

Table 6.9
% Anorthite in plagioclase calculated from oxide abundances (with free quartz and K_2O excluded) for samples from profile B

	An(1)	An(2)	An(3)	An(4)	An(5)	An(6)	An(7)	An(8)	An(9)	An(10)
					hangingwall samples					
H12S	72.1	71.0	71.7	72.5	73.2	69.3	70.0	73.0	73.7	72.1
H11S	64.4	63.5	64.0	64.9	65.4	64.3	64.8	66.6	67.1	64.4
H10S	60.0	58.9	60.0	60.6	61.7	54.7	55.6	62.1	63.2	59.5
H9S	65.4	64.1	64.7	66.0	66.6	65.4	66.0	67.6	68.2	65.4
H8S	70.4	68.6	69.1	71.2	71.8	73.2	73.8	73.7	74.3	70.4
H7S	62.2	61.4	62.1	62.6	63.3	59.3	59.9	63.6	64.3	62.1
H6S	58.5	57.5	58.4	59.1	60.1	52.6	53.4	59.6	60.6	57.9
H5S	61.5	61.4	61.8	61.6	62.1	58.5	58.9	62.1	62.5	61.0
H1S	61.3	61.1	61.5	61.4	61.9	58.3	58.7	61.8	62.2	60.9
					samples from the layered marker sequence					
25LS	62.5	60.9	62.0	63.4	64.6	58.9	60.1	65.8	67.1	62.4
25MS	60.2	59.9	60.3	60.4	60.9	57.4	57.9	60.9	61.3	59.9
24LS	61.7	60.8	61.5	62.2	63.0	58.7	59.4	63.2	63.9	61.6
24MS	61.1	60.4	61.3	61.5	62.4	57.0	57.8	63.0	63.9	60.7
23LS	61.5	61.1	61.6	61.7	62.3	58.2	58.7	62.1	62.6	61.1
23MS	60.8	59.8	60.7	61.4	62.4	55.0	55.8	61.5	62.5	60.3
22LS	61.6	60.5	61.4	62.2	63.0	56.4	57.2	62.2	63.0	61.1
22MS	60.4	60.6	60.8	60.4	60.6	57.6	57.8	60.3	60.6	59.8
19LS	62.2	60.8	61.9	62.9	64.0	56.5	57.5	63.5	64.6	61.8
MLPL	60.9	59.4	60.7	61.9	63.2	55.2	56.4	63.8	65.2	60.6
19TMS	62.7	61.7	62.6	63.3	64.2	59.3	60.2	65.2	66.2	62.6
19MMS	62.7	62.7	62.7	62.7	62.7	62.7	62.7	62.7	62.7	62.6
19BMS	62.5	62.0	62.5	62.7	63.2	59.4	59.9	63.1	63.6	61.9
18LS	61.6	60.0	60.9	62.5	63.4	56.1	56.9	61.6	62.4	61.5
6LS	62.2	61.2	62.0	62.8	63.6	59.6	60.3	64.4	65.2	62.2
6MS	61.2	61.3	61.6	61.2	61.5	58.1	58.4	61.0	61.3	60.6
5LS	61.0	60.9	61.2	61.0	61.4	58.2	58.5	61.0	61.3	60.5
4LS	61.5	61.0	61.6	61.8	62.3	58.8	59.3	62.6	63.1	61.2
4MS	62.2	61.5	62.2	62.6	63.3	59.0	59.6	63.9	64.6	61.9
3LS	61.1	60.7	61.4	61.3	62.0	56.9	57.6	62.5	63.3	60.5
3MS	61.9	61.1	61.8	62.4	63.1	58.8	59.5	63.8	64.6	61.7
2LS	62.1	59.9	61.4	63.3	64.8	55.2	56.5	64.5	66.1	61.9
2LS	61.3	60.1	61.1	61.9	62.9	56.4	57.3	63.2	64.2	60.9
1LS	61.4	60.9	61.6	61.7	62.4	58.0	58.7	63.0	63.7	61.0
					footwall samples					
F1S	61.6	61.3	61.7	61.7	62.2	58.4	58.8	62.4	62.9	61.1
F2S	61.9	61.3	62.0	62.3	63.0	57.9	58.6	63.2	63.9	61.5

6.2.2 Vertical variation in plagioclase composition

From the duplicate analyses it can be seen that those methods employing CaO, in the calculation of the anorthite content (An(2) and An(3)), are most precise (refer Table 6.7). In addition the method employing the actual CaO content is probably more accurate than that employing the CaO content normalized against the total as the accuracy of the values calculated is dependant only on

the accuracy in the analysis for CaO. Therefore in all future discussion the anorthite content quoted has been calculated using equation 1 and the actual CaO content analysed (An(2)). Figure 6.3 shows the overall variation in plagioclase composition for profiles A and B over the interval of stratigraphy considered. The sample that occurs 20m below the Pyroxenite Marker in profile B is regarded as an outlier sample. This sample may represent a sill of more mafic material that was intruded at the time the new magma, which formed the cumulates above the Pyroxenite Marker, was being injected. There is a subtle reversal in plagioclase composition from the base of the layered marker to the Pyroxenite Marker (this trend is shown by the arrows in Fig. 6.3). The

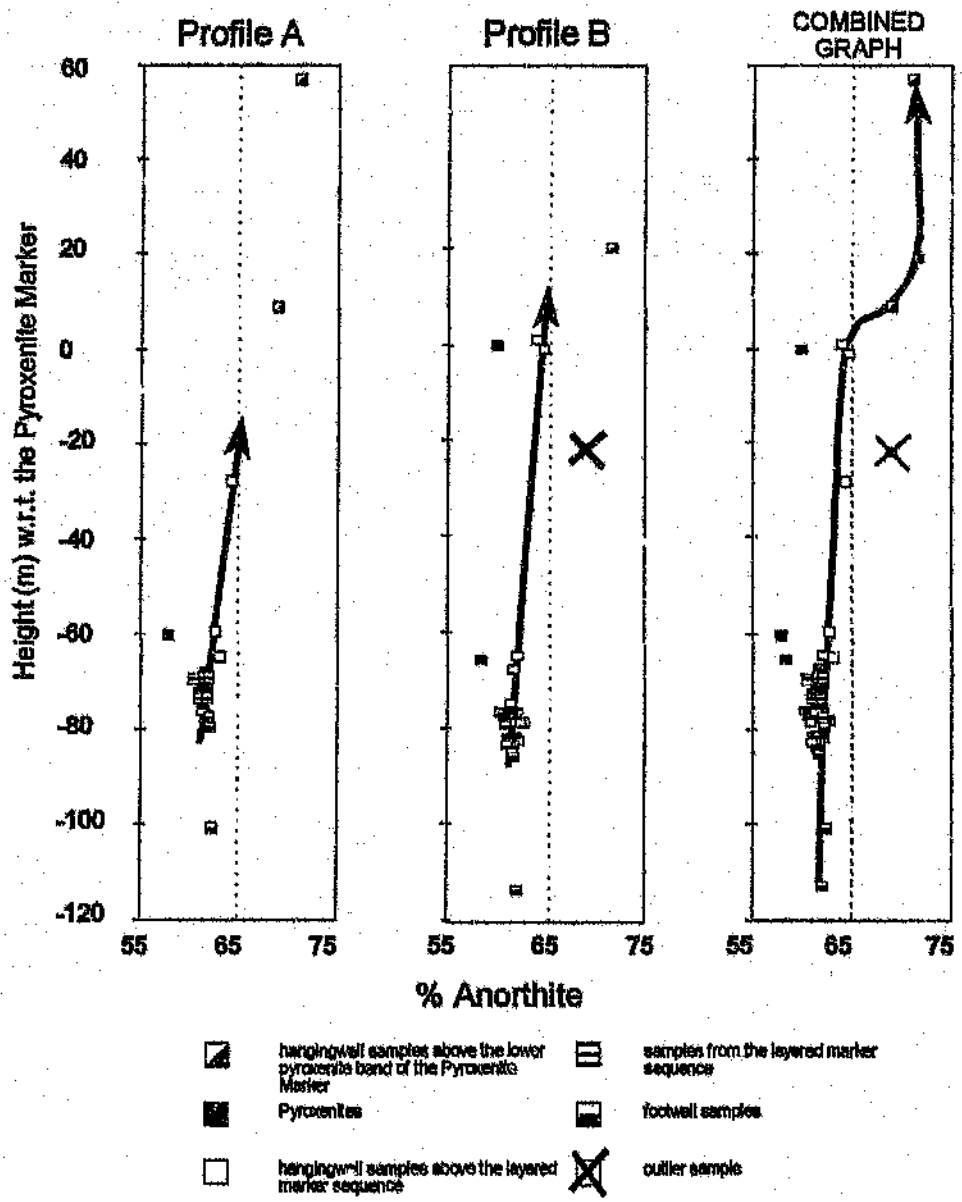


Figure 6.3 Variation in plagioclase compositions (An(2)) across the Layered Marker up to and including the Pyroxenite Marker.

samples above the Pyroxenite marker contain more primitive plagioclase. In profile B the thick (2m) basal pyroxenite marker was also sampled. This is the pyroxene layer that was first identified as the base of the Pyroxenite Marker. This sample together with other pyroxenites analysed contains more evolved plagioclase than expected when compared to neighbouring samples. This reflects the proportion of intercumulus plagioclase present within these samples. However, the samples from directly below and above contain plagioclase that are more primitive than that from some distance below the Pyroxenite Marker. Twenty metres above this layer the plagioclase composition is significantly more primitive.

6.2.3 Vertical variation of plagioclase composition through the layered marker

The variation in plagioclase composition through the layered marker is extremely limited and lies almost entirely within the limits of analytical precision (Fig.6.4). However repetitive sampling of a single layer shows that these results may be more precise than these errors suggest. Three samples, run in duplicate, from the top, middle and bottom of a single layer (19M; profile B)

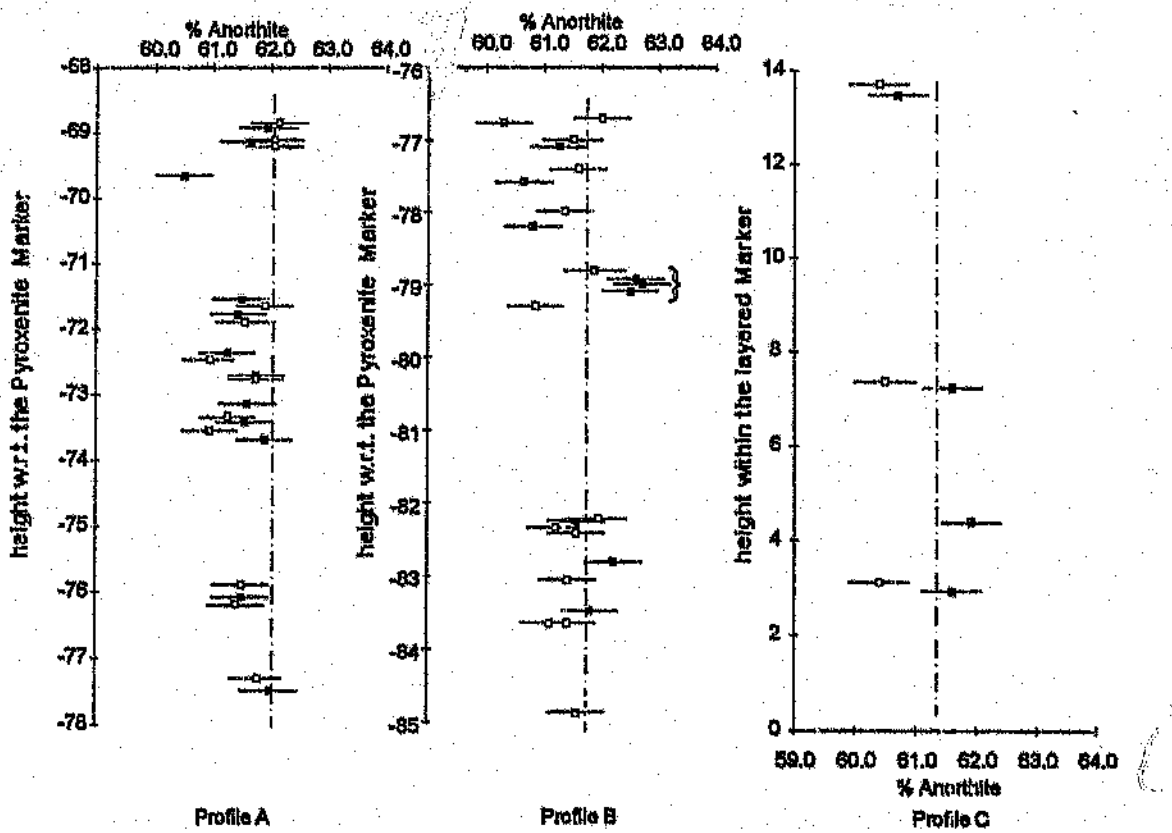


Figure 6.4 Variation in %An (An(2)) for samples from the Layered Marker. Filled symbols refer to the mafic samples, open to the leucocratic samples. The horizontal line through each data point represents the 2σ error calculated for these analyses. The dashed lines refer to the average composition of the direct hangingwall and footwall samples.

showed a variation in anorthite of 0.2%. This layer was also sampled at 5 sites, equally spaced over 40m, and the maximum variation in plagioclase composition for these samples was 1.3 % anorthite.

From Figure 6.4 and data presented in the preceding Tables, it would appear that towards the base of the sequence, the plagioclase from the mafic layers is more anorthite rich compared to that from the leucocratic layers. Towards the top this trend is reversed. The dashed lines drawn on figure 6.4 delineate the average composition of the direct footwall and hangingwall samples.

On a larger scale there is no significant change in the range of cumulus plagioclase composition between the three profiles considered (Fig. 6.4).

6.2.4 Microprobe analysis of selected pl[illegible]

Selected plagioclase grains have been analysed using the microprobe to study the extent of zonation and to compare with the XRF analyses of the mineral separates. Representative analyses are listed in the Table 6.10 and 6.11. In each case analyses are from core to rim.

Table 6.10

Microprobe analyses and compositions (%An) of selected plagioclase grains from samples of the layered marker sequence marker at locality B

Sample	SiO_2	Al_2O_3	Fe_2O_3	MgO	CaO	Na_2O	K_2O	Totals	An(1)	An(2)	An(4)	An(6)	An(8)
25LS-core	52.5	29.5	0.4	0.0	12.5	4.2	0.3	99.4	62.4	61.7	62.4	62.8	62.1
25LS	52.3	29.6	0.4	0.0	12.6	4.1	0.3	99.2	63.1	62.1	62.9	63.7	63.1
25LS-rim	49.2	31.4	0.4	0.0	14.7	3.0	0.1	98.8	73.1	72.4	73.7	73.3	73.0
23LS-core	52.5	29.2	0.4	0.0	12.4	4.2	0.3	99.1	62.2	61.4	62.3	62.6	63.5
23LS	53.0	28.9	0.4	0.0	12.3	4.3	0.3	99.3	61.1	60.7	61.4	61.4	62.1
23LS-rim	51.0	30.4	0.5	0.0	13.5	3.5	0.2	99.2	68.2	66.7	67.6	68.9	69.8
22LS-core	52.8	29.1	0.4	0.0	12.2	4.3	0.4	99.0	61.1	60.2	61.0	61.6	62.4
22LS	52.7	29.3	0.4	0.0	12.3	4.3	0.4	99.4	61.3	61.0	61.6	61.4	62.0
22LS-rim	53.0	29.1	0.6	0.0	12.2	4.3	0.3	99.5	61.0	60.3	61.0	61.5	62.2
19LS-core	53.4	28.7	0.4	0.0	12.1	4.5	0.3	99.4	59.7	59.7	60.3	59.8	60.4
19LS	53.2	28.9	0.4	0.0	12.0	4.4	0.3	99.3	60.0	59.3	60.0	60.5	61.2
19LS-rim	50.3	30.5	0.4	0.0	14.3	3.3	0.2	99.0	70.4	70.4	71.4	70.4	71.4
18LS-core	52.5	29.2	0.4	0.0	12.5	4.2	0.3	99.0	62.0	61.5	62.4	62.3	63.2
18LS	53.2	28.7	0.3	0.0	11.9	4.6	0.2	98.9	58.8	58.2	59.1	59.1	59.9
18LS-rim	50.2	30.6	0.4	0.0	14.3	3.3	0.2	99.0	70.8	70.3	71.3	71.0	72.1

Table 6.11

microprobe analyses and compositions of selected plagioclase grains from locality A.

Sample	SiO_2	Al_2O_3	Fe_2O_3	MgO	CaO	Na_2O	K_2O	Totals	An(1)	An(2)	An(4)	An(6)	An(8)
20LN-core	52.6	29.2	0.4	0.0	12.3	4.4	0.3	99.2	60.5	60.7	61.5	60.5	59.7
20LN	52.5	28.8	0.4	0.0	12.1	4.5	0.3	99.0	59.8	59.7	60.6	59.9	59.2
20LN-rim	51.1	30.2	0.3	0.0	13.6	3.8	0.2	99.3	66.5	67.0	67.8	66.3	65.8
20MN-core	52.1	29.4	0.3	0.0	12.7	4.2	0.3	98.9	62.7	62.6	63.5	62.7	63.6
20MN	52.6	29.4	0.4	0.0	12.4	4.2	0.4	99.4	62.3	61.7	62.3	62.6	63.2
20MN-rim (with plagioclase)	53.4	29.1	0.2	0.0	12.0	4.4	0.3	99.6	60.1	59.4	59.8	60.4	60.9
20MN-rim (with pyroxene)	52.3	29.4	0.4	0.0	12.7	4.1	0.3	99.3	63.3	62.5	63.2	63.7	64.3
20MN-core	53.0	29.3	0.3	0.0	12.2	4.2	0.3	99.4	61.5	60.3	60.9	62.2	62.8
20MN-rim	53.1	29.0	0.3	0.0	12.2	4.3	0.3	99.2	61.2	60.4	61.1	61.7	62.4

Table 6.11
microprobe analyses and compositions of selected plagioclase grains from locality A.

19LN-core	52.2	29.0	0.5	0.0	12.5	4.1	0.3	98.6	62.5	61.7	63.0	63.0	62.4
19LN	52.0	29.1	0.4	0.0	12.6	4.2	0.3	98.5	62.5	62.1	63.4	62.7	62.1
19LN-rim	50.1	30.5	0.4	0.0	14.0	3.4	0.2	98.6	69.7	69.2	70.5	69.9	69.5
19MN-core	53.9	28.5	0.4	0.0	11.5	4.8	0.3	99.3	56.2	55.7	56.4	56.6	57.2
19MN-rim	53.8	28.6	0.3	0.0	11.3	4.9	0.3	99.2	57.1	56.7	57.4	57.3	57.9
18LN core	52.7	29.2	0.4	0.0	12.4	4.4	0.3	99.3	60.7	61.1	61.8	60.4	59.7
18LN	51.7	29.5	0.3	0.0	12.9	4.0	0.3	98.8	64.1	63.9	65.0	64.3	63.7
18LN-rim	51.1	30.3	0.3	0.0	13.7	3.8	0.2	99.5	66.9	67.6	68.3	66.5	66.0

6.2.5 Comparison between microprobe and X.R.F. analyses

There is in general a very good agreement between the results obtained, on cores, by electron microprobe and X.R.F. analyses (Fig.6.5). In addition the composition of crystals, both within a single thin section and between samples, is similar. The range in composition is however significantly larger than the analytical precision calculated for the analysis of plagioclase separates (reflected in the symbol size [Fig.6.5]). The plagioclase analysed from leucocratic samples all exhibit anorthite-enriched rims. Plagioclase crystals analysed from two mafic samples however, did not appear to show reversed zonation.

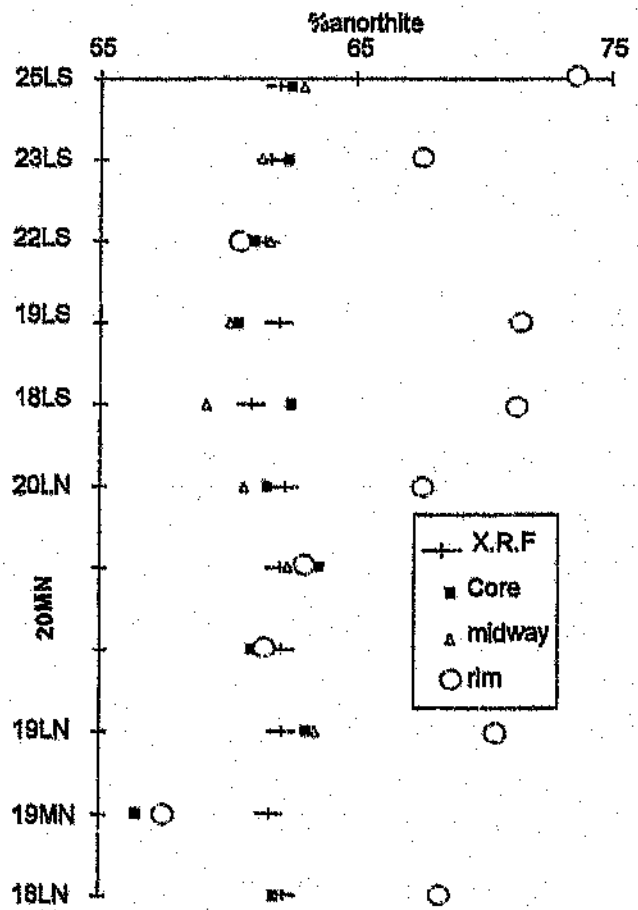


Figure 6.5 Comparison of plagioclase compositions as determined from XRF and microprobe analyses (An(2)).

7. Pyroxene

7.1 Introduction

Pyroxenes from the Main Zone, in the eastern limb of the complex, have been studied by von Gruenewaldt (1970, 1971 and 1973), Molyneux (1974), Marais (1977) and Klemm et al. (1985). Molyneux mapped and sampled in the northern portion of the eastern limb and provided the

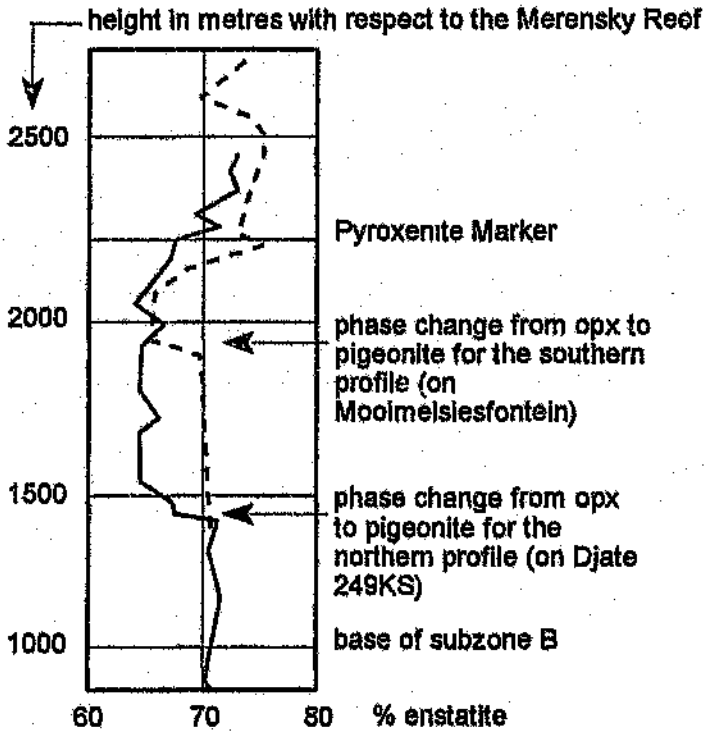


Figure 7.1 Variation in the composition of orthopyroxene, measured microscopically, across the Pyroxenite Marker (from Molyneux, 1974).

regional setting for this study. Figure 7.1 shows the variation in low-calcium pyroxene composition for two profiles, through subzone B and a portion of subzone C, in this area.

Several hundred metres below the Pyroxenite Marker there is a distinct change in the compositional trend. This can be related to the phase change from orthopyroxene to pigeonite. This phase change and the related change in mg-number, on the farm Mooimeisiesfontein (Molyneux, 1974) (which is just north of the farm Steelpoortpark), occurs several hundred metres higher in the sequence than further to the north on the farm Djate 249 KS. Above this phase change, the composition of the orthopyroxene remains more or less constant. Closer to the Pyroxenite Marker there is a reversal in the normal fractionation trend. The gradient of this

reversal becomes steeper across the Pyroxenite Marker.

Marais (1977) studied the changing pyroxene compositions, across the Pyroxenite Marker, along four profiles, over more than 80km, in the eastern limb. Figure 7.2 shows the variation in orthopyroxene composition from her study. The line graphs refer to those results obtained by optical methods. Chemical analysis of separates were also undertaken (Marais, 1977). The mg-

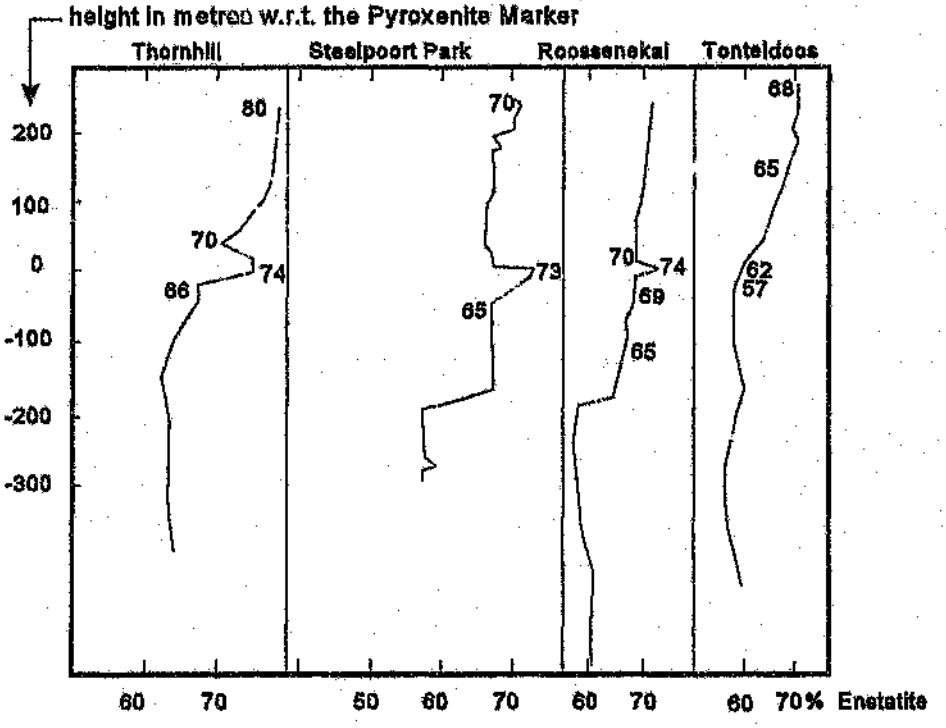


Figure 7.2 Variation in orthopyroxene composition across the Pyroxenite Marker (0m). The numbers next to each curve refer to compositions determined by X.R.F. analysis of separates (Diagram modified after Marais, 1977).

numbers for these samples (100xMg/Mg+Fe) have been plotted on the graph as labels at the appropriate stratigraphic positions.

The Thornhill profile (close to profile B) shows similar trends to the profiles presented by Molyneux (1974). With normal fractionation up to ~150m below the P.M., at which point there is a reversal in the normal compositional trend. At the level of the Pyroxenite Marker there is a distinct reversal in mineral composition. In the Steelpoortpark area (close to profile C) there is a sharp reversal significantly below the Pyroxenite Marker and the Marker is defined by still more mafic compositions. Above this level the pyroxene compositions appear to revert back to what they were below the marker. This profile is at variance with that presented by Molyneux (1974). For the Roossenekal profile there is a strong reversal significantly below the Pyroxenite Marker.

From this point there is a progressive reversal in pyroxene composition. The trend shown by pyroxenes along a profile near Tonteldoos appears similar to that from the Thornhill profile, except that the compositions are different and the reversal begins very close to the Pyroxenite Marker. From the studies of Marais (1977) and Klemm et al. (1985) it would appear that the composition of the pyroxene phases is more or less constant along strike and only starts to change significantly and progressively south of Roossenekal, where there appears to be a Fe-enrichment. Marais (1977) ascribed this change to a lateral temperature gradient during crystallization, whilst Klemm et al. (1985) suggested that this change may be due to differing degrees of mixing as the new magma plumed into the chamber and migrated away from its point of entry.

7.2 Analysis of pyroxene from three profiles in the eastern limb

Both clinopyroxene and orthopyroxene compositions have been determined for samples from 3 profiles covering 45km of strike. In certain layers there is a very small proportion of pyroxene present. In such cases it proved difficult to separate the phases effectively and yield a sufficient weight of separate to analyse by X.R.F. techniques. In these cases microprobe analyses have been undertaken. Other samples were also selected for microprobe work so that pyroxene composition as determined from X.R.F. analysis could be compared. The pyroxene analyses are listed in tables 7.1a, 7.1b, 7.2a and 7.2b. Analytical errors have been calculated from precision in the analysis of the calibration standards (Appendix 4). A few duplicate samples were also run as a check (Table 7.3). Data for profile C is taken from Pillay (1990). Two samples, from that study were re-analysed as between run analytical checks.

Table 7.1a
Analysis of orthopyroxene separates from profiles A.

Sample	SiO_2	TiO_2	Al_2O_3	FeO	MnO	MgO	CaO	Total
hangingwall samples								
H8N	53.23	0.29	0.87	17.93	0.35	25.09	1.6	99.39
H7N	52.64	0.24	0.81	21.06	0.38	22.78	1.62	99.57
H6N	52.11	0.32	0.86	21.36	0.43	21.84	2.18	99.16
H3N	52.25	0.28	0.60	21.65	0.45	22.56	1.46	99.28
H2N	51.67	0.79	1.12	21.37	0.42	20.00	2.04	98.63
H1N	52.98	0.29	1.18	21.53	0.44	21.01	2.83	100.3
samples from the layered marker sequence								
20MN	52.69	0.24	0.72	22.79	0.47	21.19	1.80	100.1
19MN	52.71	0.26	0.75	22.10	0.45	21.43	1.82	99.56
18MN	52.12	0.23	0.73	22.83	0.46	21.02	1.70	99.16
11MN	52.07	0.26	0.79	22.86	0.46	21.00	1.63	99.12
10LN	51.91	0.26	1.19	22.62	0.45	19.63	2.99	99.13

Table 7.1a
Analysis of orthopyroxene separates from profiles A.

10MN	52.04	0.24	0.78	22.46	0.44	21.24	1.77	99.03
9MN	51.80	0.24	0.79	22.33	0.45	21.29	1.79	98.75
8LN	51.66	0.28	1.30	22.73	0.44	19.42	3.20	99.07
8MN	52.10	0.26	0.86	22.72	0.46	20.39	2.36	99.19
7LN	51.61	0.26	1.10	22.86	0.45	19.45	2.87	98.66
6MN	52.38	0.25	0.73	22.76	0.44	21.39	1.62	99.62
5LN	52.09	0.27	1.03	23.07	0.44	19.61	2.77	99.34
5MN	51.97	0.27	0.94	22.68	0.45	20.51	2.52	99.42
4LN	52.03	0.27	1.04	22.71	0.44	20.12	2.27	98.93
4MN	52.01	0.27	0.72	22.47	0.45	21.40	1.48	98.86
3LN	51.72	0.26	0.98	22.82	0.44	20.37	2.36	99.02
3MN	52.50	0.27	0.73	21.93	0.43	21.46	1.81	99.17
2LNB	52.48	0.27	0.91	21.98	0.43	20.96	2.22	99.30
2LNA	52.54	0.25	0.82	22.71	0.43	20.34	2.54	99.68
2MN	52.13	0.23	0.67	22.59	0.46	21.57	1.42	99.12
samples from the footwall								
F1N	53.30	0.28	1.05	21.96	0.44	21.23	2.19	100.5
F2N	52.82	0.30	0.92	22.38	0.47	21.59	1.82	100.4

Table 7.1b
Analysis of orthopyroxene separates from profiles B.

Sample	SiO_2	TiO_2	Al_2O_3	FeO	MnO	MgO	CaO	Total
hangingwall samples								
H12S	52.54	0.27	1.01	17.80	0.37	24.93	1.66	98.63
H11S	53.25	0.23	0.96	20.20	0.44	22.43	2.20	99.78
H10S	52.95	0.23	0.63	20.45	0.00	22.62	1.70	99.03
H8S	53.33	0.15	0.85	20.00	0.43	22.71	2.33	100.90
H7S	52.74	0.24	0.72	21.97	0.47	21.87	1.61	99.66
H6S	52.79	0.25	0.68	21.16	0.46	22.31	1.58	99.26
H5S	52.14	0.29	1.02	22.52	0.45	20 25	2.84	99.68
H1S	50.90	0.28	1.54	24.26	0.46	17.78	3.74	99.02
samples from the layered marker sequence								
25MS	52.04	0.22	0.94	22.43	0.46	20.50	2.25	98.91
24MS	52.06	0.23	0.70	22.48	0.45	21.35	1.71	99.03
23MS	52.86	0.24	0.81	22.77	0.48	20.99	2.02	100.20
22MS	51.51	0.26	0.92	22.94	0.49	20.63	1.97	98.76
19tMS	52.43	0.26	0.91	22.17	0.47	20.81	2.26	99.36
19mMS	52.54	0.23	0.75	22.71	0.49	21.04	1.89	99.69
19bMS	52.01	0.26	0.87	22.47	0.46	20.64	2.40	99.17
6LS	51.48	0.27	1.26	23.07	0.44	19.94	2.56	99.60
6MS	52.15	0.27	1.76	22.84	0.46	20.32	2.03	99.88
5LS	51.61	0.28	1.36	23.05	0.44	19.71	2.75	99.26
4LS	51.99	0.27	1.17	22.82	0.45	19.97	2.42	99.16

Table 7.1b
Analysis of orthopyroxene separates from profiles B.

4MS	52.37	0.26	0.75	22.35	0.48	21.05	2.01	99.29
3LS	51.77	0.26	1.04	22.97	0.47	20.30	2.48	99.36
3MS	52.00	0.27	0.88	22.76	0.46	21.04	2.15	99.61
2LS	51.99	0.28	1.21	22.61	0.45	20.39	2.27	99.32
1LS	51.65	0.28	1.11	22.59	0.43	20.15	2.62	98.88
samples from the footwall								
F1S	52.03	0.26	0.94	22.05	0.00	20.91	2.39	99.07
F3S	51.81	0.25	0.86	22.23	0.46	21.09	2.02	98.78

Table 7.2a
Analysis of clinopyroxene separates from profiles A.

Sample	SiO_2	TiO_2	Al_2O_3	FeO	MnO	MgO	CaO	Total
hangingwall samples								
H8N	51.47	0.48	1.80	8.21	0.21	15.42	20.37	99.94
H7N	52.23	0.36	2.51	8.59	0.21	14.20	20.66	99.04
H6N	52.16	0.41	1.45	9.92	0.25	14.59	20.29	99.26
H4N	51.91	0.39	1.37	9.73	0.24	14.42	20.49	98.72
H3N	52.70	0.38	1.15	9.48	0.23	14.98	20.66	99.91
H2N	52.04	0.40	1.61	10.55	0.24	14.63	19.75	99.51
H1N	52.28	0.36	2.66	9.12	0.21	13.82	21.06	100.01
samples from the layered marker sequence								
20MN	51.90	0.38	1.30	10.55	0.25	14.33	20.10	98.97
19MN	52.67	0.38	1.22	10.24	0.25	14.73	20.10	99.73
18MN	52.49	0.35	1.31	9.96	0.24	14.36	20.68	99.61
11MN	51.94	0.35	1.39	9.73	0.24	14.25	21.18	99.28
10LN	51.97	0.35	2.46	10.19	0.23	13.34	20.57	99.49
10MN	52.88	0.34	1.35	10.01	0.24	14.60	20.63	100.60
9MN	52.01	0.36	1.30	10.18	0.26	14.56	20.35	99.26
8LN	50.90	0.39	2.58	10.43	0.26	13.25	20.26	98.60
8MN	51.70	0.37	1.51	10.11	0.25	14.09	20.88	99.19
7LN	51.88	0.34	2.94	10.07	0.22	13.13	20.51	99.53
6MN	51.66	0.38	1.37	10.21	0.25	14.51	20.37	99.01
5LN	51.27	0.35	2.25	10.78	0.26	13.43	20.03	98.80
5MN	51.59	0.37	1.65	10.44	0.25	14.07	20.18	98.89
4LN	51.45	0.35	2.02	10.18	0.25	13.37	20.58	98.56
4MN	51.79	0.37	1.27	10.01	0.25	14.38	20.57	98.87
3LN	51.42	0.38	1.75	10.33	0.24	13.73	20.67	98.77
3MN	52.42	0.38	1.26	9.75	0.24	14.31	21.05	99.59
2LNB	51.50	0.36	1.65	10.46	0.24	13.62	20.70	98.81
2LNA	51.84	0.39	1.79	10.16	0.26	13.74	20.38	98.94
2MN	52.43	0.40	1.32	10.46	0.25	14.43	20.49	100.10
samples from the footwall								
F1N	52.25	0.38	1.44	10.01	0.26	14.39	20.65	99.70

Table 7.2a
Analysis of clinopyroxene separates from profiles A.

F2N	51.89	0.41	1.63	10.46	0.26	14.71	19.56	99.24

Table 7.2b
Analysis of clinopyroxene separates from profiles B.

Sample	SiO_2	TiO_2	Al_2O_3	FeO	MnO	MgO	CaO	Total
Hangingwall samples								
H12S	52.32	0.44	2.19	7.80	0.21	15.60	20.58	99.46
H11S	52.00	0.36	1.58	8.89	0.22	14.54	20.92	98.92
H10S	52.73	0.33	1.23	9.03	0.00	14.90	20.74	99.58
H8S	52.74	0.24	2.11	7.77	0.20	14.59	21.32	99.36
H7S	51.47	0.37	1.26	10.39	0.27	14.93	19.91	98.76
H6S	51.95	0.38	1.22	10.31	0.28	15.25	19.54	99.06
H5S	51.55	0.40	1.80	10.73	0.25	13.93	20.55	99.45
H1S	51.74	0.36	3.03	11.44	0.25	12.54	20.02	99.81
samples from the layered marker sequence								
25MS	52.59	0.34	1.68	9.78	0.24	14.18	21.07	100.20
24MS	52.67	0.38	1.40	10.88	0.25	14.74	19.56	100.10
23MS	52.35	0.38	1.28	10.31	0.26	14.38	20.52	99.76
22MS	52.44	0.37	1.36	10.26	0.26	14.26	20.84	100.00
19tMS(22m)	52.13	0.37	1.79	9.97	0.24	14.14	20.98	99.90
19mMS(22m)	51.69	0.36	1.30	10.29	0.26	14.40	20.58	99.05
19bMS(22m)	51.68	0.35	1.29	10.49	0.25	14.25	20.64	99.17
6LS	51.15	0.41	2.60	11.64	0.26	13.87	19.05	99.27
6MS	51.36	0.39	1.54	10.12	0.25	14.04	20.89	98.82
5LS	51.29	0.36	2.64	10.33	0.23	13.12	20.35	98.79
4LS	51.38	0.39	1.92	10.56	0.23	13.60	20.47	98.89
4MS	51.62	0.38	1.39	10.05	0.24	14.14	20.85	98.97
3LS	52.30	0.36	2.15	10.19	0.25	13.57	20.95	100.10
3MS	52.31	0.40	1.57	10.74	0.26	14.40	20.20	100.10
2LS	52.40	0.38	2.07	10.21	0.25	13.66	20.95	100.30
1LS	51.85	0.38	1.85	10.61	0.26	13.92	20.54	99.70
samples from the footwall								
F1S	52.53	0.40	1.91	9.82	0.00	14.24	20.90	100.30
F2S	52.43	0.39	1.43	10.28	0.26	14.48	20.08	99.54

Table 7.3
Analysis of analytical errors. The 2σ errors quoted have been calculated from the precision in the analysis of the calibration standards (as very few duplicates were analysed). The replicates analysed vary within the limits of the calculated errors.

orthopyroxene analyses						clinopyroxene analyses					
	SiO_2	Al_2O_3	FeO	MgO	CaO		SiO_2	Al_2O_3	FeO	MgO	CaO
2σ	0.5	0.3	0.3	0.2	0.1	2σ	0.5	0.3	0.2	0.2	0.1
Replicate analyses											
1	52.11	0.93	22.64	20.37	2.83	1	52.53	1.91	9.82	14.24	20.90
2	52.14	1.02	22.52	20.25	2.84	2	52.34	1.91	9.82	14.02	20.85
						3	51.92	1.91	9.85	14.16	20.96
σ_{n-1}	0.02	0.06	0.08	0.08	0.01	σ_{n-1}	0.31	0.00	0.02	0.11	0.06

7.2.1 Pyroxene compositions

The cationic proportions of Ca^{2+}, Mg^{2+} and Fe^{2+} have been calculated from the oxide abundances, from which the mg-number (100xMg/Mg+Fe) has been calculated for each sample. All Fe has been taken as FeO for these calculations. These results are listed in tables 7.5, 7.6 and 7.7. Analytical errors (Table 7.4) have been calculated taking into account the errors determined for the major element analysis (Table 7.3).

Table 7.4
Analytical error in the calculation of pyroxene compositions.

orthopyroxene analyses					clinopyroxene analyses				
	Ca^{2+}	Mg^{2+}	Fe^{2+}	Mg-number		Ca^{2+}	Mg^{2+}	Fe^{2+}	Mg-number
2σ	0.2	0.3	0.1	0.2	2σ	0.3	0.04	0.3	0.3
Compositions determined by P.Pillay (1990)									
16M	3.6	59.3	37.1	61.5	38M	42.2	41.2	16.6	71.3
Compositions determined after re-analysis of separates									
16M	3.5	59.7	36.8	61.8	38M	43.1	40.1	16.8	70.5
S	0.1	0.4	0.3	0.3		0.9	1.1	0.2	0.8

Table 7.5
Cationic proportions of Ca, Mg, Fe and mg-number for low-calcium and clinopyroxene separates from profile A.

	low-calcium pyroxene				clinopyroxene			
Sample	Ca^{2+}	Mg^{2+}	Fe^{2+}	Mg-number	Ca^{2+}	Mg^{2+}	Fe^{2+}	Mg-number
hangingwall samples								
H8N	3.1	68.6	28.3	70.8	42.3	44.3	13.4	76.8
H7N	3.2	63.1	33.7	65.2	43.6	41.7	14.7	74.0
H6N	4.4	61.1	34.6	3.9	41.7	41.8	16.5	71.7
H4N	4.2	60.5	35.3	63.1	42.2	41.4	16.3	71.7
H3N	2.9	62.4	34.7	64.3	42.0	42.4	15.6	73.2
H2N	4.3	59.2	36.5	61.8	40.6	41.9	17.5	70.5
H1N	5.7	59.2	35.1	62.8	44.2	40.4	15.5	72.3
samples from the layered marker sequence								
20MN	3.6	59.4	37.0	61.6	41.4	41.1	17.6	70.1
19MN	3.7	60.3	36.0	62.6	41.2	41.9	16.9	71.2
18MN	3.4	59.3	37.3	61.4	42.5	41.0	16.5	71.3
11MN	3.3	59.3	37.4	61.4	43.4	40.6	16.1	71.6
10LN	6.2	56.3	37.5	60.0	43.4	39.2	17.4	69.3
10MN	3.6	59.8	36.6	62.1	42.1	41.4	16.5	71.5
9MN	3.6	60.0	36.4	62.2	41.7	41.5	16.9	71.1
8LN	6.6	55.7	37.7	59.7	43.0	39.1	17.9	68.6
8MN	4.8	57.9	37.3	60.8	42.9	40.3	16.8	70.6
7LN	6.0	56.0	38.1	59.5	43.8	39.0	17.3	69.3
6MN	3.3	59.9	36.8	61.9	41.7	41.4	16.9	71.0
5LN	5.7	56.1	38.2	59.5	42.2	39.4	18.4	68.2
5MN	5.1	57.9	37.0	61.0	41.9	40.6	17.5	69.9
4LN	4.7	57.7	37.6	60.5	43.4	39.2	17.4	69.3
4MN	3.0	60.3	36.7	62.2	42.3	41.1	16.6	71.2
3LN	4.8	57.8	37.4	60.7	43.0	39.7	17.3	69.6
3MN	3.7	60.6	35.8	62.9	43.1	40.8	16.1	71.7
2LNB	4.5	59.4	36.0	62.3	43.1	39.4	17.6	69.2
2LNA	5.2	57.7	37.2	60.8	42.7	40.1	17.2	69.9
2MN	2.9	60.5	36.7	62.3	41.8	41.0	17.3	70.4
footwall samples								
F1N	4.4	59.8	35.8	62.6	42.3	41.0	16.6	71.2
F2N	3.6	60.2	36.1	62.5	40.3	42.2	17.5	70.7

Table 7.6
Cationic proportions of Ca, Mg, Fe and mg-number for low-calcium and clinopyroxene separates from profile B.

	low-calcium pyroxene				clinopyroxene			
Sample	**Ca^{2+}**	**Mg^{2+}**	**Fe^{2+}**	**Mg-number**	**Ca^{2+}**	**Mg^{2+}**	**Fe^{2+}**	**Mg-number**
hangingwall samples								
H12S	3.3	68.4	28.3	70.8	42.4	44.7	13.0	77.5
H11S	3.4	63.4	33.2	65.7	43.3	41.9	14.9	73.8
H10S	4.4	62.8	32.8	65.7	42.5	42.5	15.0	74.0
H8S	4.7	63.1	32.2	66.2	44.5	42.4	13.1	76.3
H7S	3.2	61.2	35.6	63.2	40.6	42.3	17.1	71.2
H6S	3.2	62.5	34.3	64.5	39.8	43.2	17.0	71.8
H5S	5.7	57.4	36.9	60.9	42.2	39.9	17.8	69.1
H1S	7.8	51.6	40.6	55.9	42.9	37.4	19.7	65.4
samples from the layered marker sequence								
25MS	4.6	58.4	37.0	61.2	43.3	40.5	16.2	71.4
24MS	3.5	60.0	36.5	62.2	40.1	42.0	18.0	70.0
23MS	4.1	58.9	37.0	61.4	42.0	40.9	17.1	70.6
22MS	4.0	58.4	37.6	60.8	42.6	40.5	16.9	70.5
19tMS	4.6	59.0	36.4	61.8	43.1	40.4	16.5	71.0
19mMS	3.8	59.2	37.0	61.5	42.1	40.9	17.0	70.7
19bMS	4.9	58.4	36.8	61.4	42.2	40.5	17.3	70.0
6LS	5.3	56.8	38.0	59.9	39.9	40.4	19.7	67.3
6MS	4.2	58.1	37.8	60.6	43.0	40.2	16.8	70.5
5LS	5.6	56.3	38.1	59.7	43.3	39.0	17.7	68.8
4LS	5.0	57.2	37.8	60.2	42.7	39.5	17.8	69.0
4MS	4.1	59.4	36.5	61.9	42.9	40.4	16.7	70.8
3LS	5.1	57.4	37.6	60.4	43.6	39.3	17.1	69.6
3MS	4.3	58.9	36.8	61.5	41.3	41.0	17.8	69.8
2LS	4.6	58.1	37.3	60.9	43.5	39.4	17.1	69.7
1LS	5.4	57.4	37.2	60.7	42.4	39.9	17.7	69.3
footwall samples								
F1S	4.9	59.1	36.1	62.1	43.1	40.5	16.4	71.2
F2S	4.1	59.6	36.3	62.1	41.4	41.5	17.1	70.8

Table 7.7
Cationic proportions of Ca, Mg, Fe and mg-number for low-calcium and clinopyroxene separates from profile C.

	low-calcium pyroxene				clinopyroxene			
Sample	Ca^{2+}	Mg^{2+}	Fe^{2+}	Mg-number	Ca^{2+}	Mg^{2+}	Fe^{2+}	Mg-number
76L	4.3	58.8	36.8	61.5	36.7	43.6	19.7	68.8
76M	3.7	60.1	36.2	62.4	41.2	41.9	16.9	71.2
75M	4.0	61.0	34.9	63.6	37.8	43.1	19.1	69.3
38L	9.5	54.3	36.2	60.0	40.3	40.7	19.0	68.1
38M	6.3	57.7	35.9	61.6	42.2	41.2	16.6	71.3
37M	6.8	57.1	36.1	61.2	40.7	41.6	17.6	70.3
35M	6.1	56.8	37.1	60.5	41.8	40.7	17.4	70.0
24M	7.5	54.0	38.5	58.4	41.5	39.5	19.0	67.5
23M	10.3	54.2	35.4	60.5	41.0	40.5	18.6	68.6
17M	5.7	57.1	37.2	60.5	40.9	40.7	18.4	68.8
16L	7.0	55.8	37.2	60.0	36.7	43.6	19.7	68.8
16M	3.6	59.3	37.1	61.5	40.4	41.8	17.8	70.1
samples from the footwall to the marker								
7	5.0	58.1	36.9	61.1	41.5	41.4	17.1	70.7
2	9.9	52.0	38.1	57.7	41.0	39.1	19.9	66.3

Electron Microprobe analysis of pyroxenes

Within certain of the samples the pyroxene is a minor phase and the grains are frequently bounded by small euhedral magnetite crystals. These effect the magnetic properties of the different minerals phases and makes it difficult to separate these phases efficiently. In such cases the pyroxene phases have been analysed by electron microprobe. For these samples several grains were analysed. This data, together with the calculated cationic proportions of Ca, Mg, Fe and the mg-number, is presented in the tables 7.8 to 7.11.

From this data it can be seen that there is very little geochemical variation within a single pyroxene grain and between grains within a single sample. The pyroxene phases, from two samples, have been analysed by both X.R.F. and microprobe techniques. Figure 7.3 shows the compositions of these pyroxene phases as determined by these two different techniques From this figure it can be seen that the variations are small but systematic and reflects the effects of exsolution on the mineral compositions.

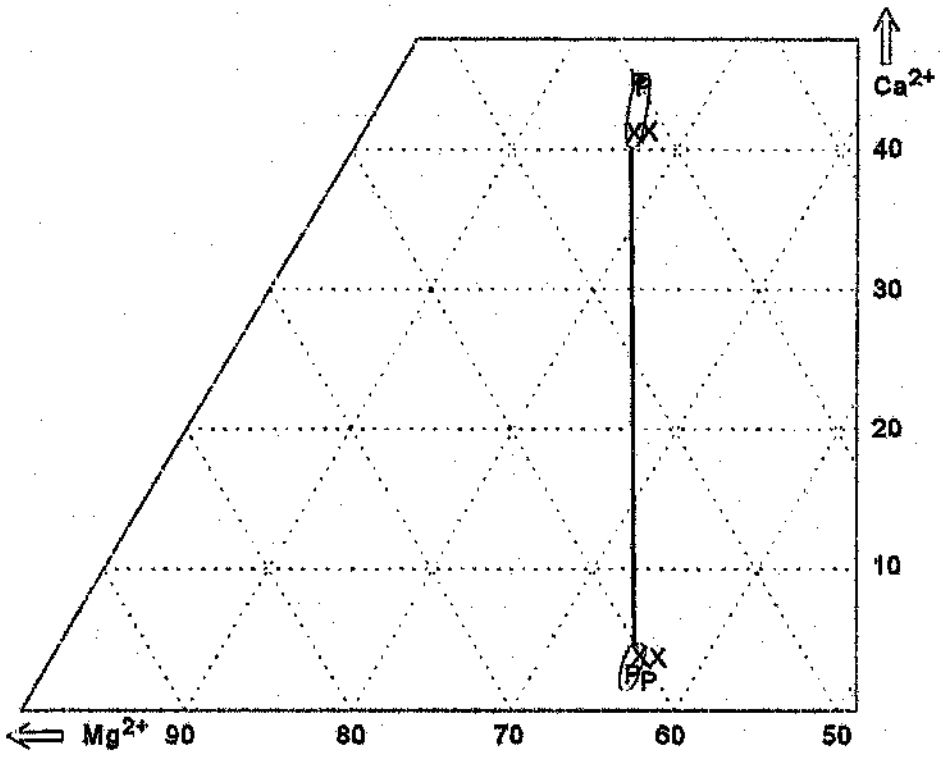


Figure 7.3 Comparison of pyroxene compositions from selected samples as determined by microprobe (p) and XRF analysis (x). Field and tie line join data points for one sample whilst the other data points refer to the other sample.

Table 7.8
Microprobe analyses of orthopyroxene grains within selected samples from profile A.

Sample	SiO_2	TiO_2	Al_2O_3	FeO	MnO	MgO	CaO	Cr2O3	NiO	Total	Ca^{2+}	Mg^{2+}	Fe^{2+}	Mg-number
20LN(4/1)R	51.31	0.10	0.62	27.09	0.65	18.56	0.81	0.03	0.00	99.20	1.7	53.5	44.8	54.4
20LN(4/2)H	51.11	0.15	0.60	27.00	0.59	18.83	0.70	0.01	0.01	98.99	1.4	54.1	44.5	54.9
20LN(4/4)C	51.22	0.18	0.63	26.91	0.69	18.78	0.83	0.06	0.00	99.32	1.7	53.9	44.4	54.8
20LN(1/4)R	51.31	0.20	0.63	26.44	0.53	18.43	0.98	0.03	0.00	98.57	2.1	53.8	44.2	54.9
20LN(1/5)C	51.27	0.23	0.65	25.99	0.57	18.72	1.08	0.03	0.01	98.62	2.3	54.4	43.3	55.7
20MN(1/1)R	52.67	0.22	0.63	23.47	0.38	21.54	0.90	0.01	0.03	100.10	1.8	60.4	37.8	61.5
20MN(1/2)H	52.65	0.18	0.63	23.36	0.55	21.75	0.70	0.02	0.09	99.95	1.4	61.0	37.6	61.8
20MN(1/3)C	52.46	0.20	0.65	23.54	0.49	21.71	0.86	0.01	0.05	99.96	1.7	60.6	37.7	61.7
20MN(4/1)R	52.46	0.21	0.59	23.87	0.56	21.19	0.86	0.00	0.03	99.81	1.7	59.7	38.6	60.7
20MN(4/2)H	52.23	0.23	0.60	23.12	0.51	21.55	0.95	0.04	0.04	99.31	1.9	60.7	37.4	61.9
20MN(4/3)C	53.15	0.18	0.67	22.55	0.54	21.77	1.84	0.00	0.05	100.80	3.7	60.4	36.0	62.7
19MN(4/1)R	52.46	0.23	0.61	22.94	0.55	21.82	0.89	0.00	0.02	99.54	1.8	61.2	37.0	62.3
19MN(4/2)H	52.51	0.24	0.63	22.72	0.53	21.94	0.99	0.03	0.04	99.63	2.0	61.5	36.6	62.7
19MN(4/3)C	52.36	0.22	0.72	22.45	0.51	22.02	0.98	0.00	0.03	99.30	2.0	61.8	36.2	63.1

Table 7.8
Microprobe analyses of orthopyroxene grains within selected samples from profile A.

19MN(2/1)R	52.75	0.25	0.61	22.67	0.50	22.07	0.99	0.01	0.05	99.91	2.0	61.7	36.4	62.9
19MN(2/2)H	52.59	0.24	0.83	22.04	0.51	21.56	2.01	0.01	0.01	99.85	4.1	60.5	35.5	63.0
19MN(2/3)C	53.18	0.20	0.55	22.37	0.55	22.05	1.45	0.01	0.01	100.40	2.9	61.3	35.8	63.2
18LN(1/1)R	51.60	0.13	0.63	26.08	0.60	19.84	0.71	0.00	0.00	99.58	1.4	56.2	42.4	57.0
18LN(1/2)H	51.45	0.16	0.57	25.24	0.58	20.19	0.65	0.03	0.00	98.88	1.3	57.4	41.2	58.2
18LN(1/3)C	52.27	0.16	0.60	24.94	0.58	20.45	0.64	0.02	0.02	99.68	1.3	58.0	40.7	58.8
18LN(2/1)R	51.15	0.19	0.65	25.84	0.62	19.55	0.82	0.01	0.01	98.87	1.7	55.9	42.4	56.8
18LN(2/2)C	51.71	0.24	0.64	26.31	0.58	19.40	0.90	0.01	0.03	99.82	2.1	49.4	48.5	50.5

R=RIM; H=HALFWAY FROM RIM TO CORE; C=CORE

Table 7.9
Microprobe analyses of clinopyroxene grains within selected samples from profile A.

Sample	SiO_2	TiO_2	Al_2O_3	FeO	MnO	MgO	CaO	Cr_2O_3	NiO	Total	Ca^{2+}	Mg^{2+}	Fe^{2+}	Mg-number
20LN(5/3)R	51.16	0.38	1.37	11.65	0.35	12.63	20.78	0.06	0.02	98.65	43.6	36.8	19.6	65.2
20LN(5/2)M	51.10	0.30	1.15	11.98	0.33	12.50	20.69	0.05	0.00	98.65	43.4	36.5	20.2	64.4
20LN(5/1)C	51.94	0.33	1.16	12.18	0.33	12.80	20.64	0.03	0.04	99.68	42.8	36.9	20.3	64.6
20LN(3/1)R	51.85	0.25	1.23	10.82	0.33	12.89	21.74	0.01	0.01	99.41	44.9	37.1	18.0	67.3
20LN(3/2)M	51.50	0.35	1.41	11.20	0.35	12.85	20.87	0.01	0.01	98.83	43.7	37.4	18.9	66.5
20LN(3/3)C	51.53	0.34	1.36	11.69	0.31	12.81	20.84	0.01	0.03	99.19	43.4	37.1	19.5	65.5
20MN(2/1)R	52.50	0.37	1.15	9.46	0.26	14.08	21.78	0.02	0.05	99.93	44.5	40.0	15.5	72.1
20MN(2/2)C	52.13	0.41	1.38	9.22	0.28	13.83	21.95	0.00	0.00	99.47	45.2	39.6	15.3	72.2
20MN(3/1)R	52.64	0.38	1.14	9.41	0.2[illegible]	14.17	21.74	0.00	0.05	100.00	44.4	40.2	15.4	72.3
20MN(3/2)H	52.08	0.44	1.45	9.26	0.23	14.02	21.89	0.01	0.06	99.72	44.9	40.0	15.2	72.5
20MN(3/3)C	52.46	0.37	1.41	9.39	0.28	13.93	21.87	0.00	0.02	100.00	44.8	39.7	15.5	71.9
19LN(1/1)R	51.50	0.26	1.26	11.41	0.25	13.00	20.89	0.02	0.01	98.86	43.5	37.6	18.9	66.5
19LN(1/2)C	51.33	0.30	1.38	11.38	0.40	12.80	20.85	0.04	0.00	98.76	43.6	37.2	19.2	65.9
19LN(2/1)R	51.65	0.33	1.33	10.86	0.40	12.61	21.47	0.00	0.00	98.93	44.9	36.7	18.4	66.6
19LN(2/2)H	51.73	0.38	1.47	11.38	0.39	12.70	20.95	0.02	0.00	99.34	43.8	36.9	19.2	65.8
19LN(2/3)C	51.74	0.29	1.32	10.74	0.32	12.86	21.59	0.01	0.00	99.17	44.9	37.2	18.0	67.4
19LN(3/2)R	51.70	0.31	1.43	11.00	0.26	12.75	21.52	0.00	0.00	99.29	44.8	36.9	18.3	66.9
19LN(3/1)C	51.15	0.29	1.51	11.26	0.31	12.53	21.16	0.02	0.02	98.49	44.4	36.6	19.0	65.9
19MN(3/1)R	52.26	0.39	1.22	9.30	0.29	14.07	21.76	0.02	0.03	99.61	44.6	40.1	15.3	72.3
19MN(3/2)C	51.96	0.42	1.36	9.53	0.24	14.01	21.48	0.01	0.05	99.35	44.2	40.1	15.7	71.9
19MN(1/1)R	52.23	0.39	1.35	9.13	0.23	13.93	21.91	0.00	0.02	99.45	45.1	39.9	15.0	72.6
19MN(1/2)H	52.39	0.41	1.43	10.03	0.29	14.09	21.13	0.02	0.03	100.10	43.3	40.2	16.5	70.9
19MN(1/3)C	52.39	0.39	1.43	9.07	0.26	13.81	22.03	0.00	0.06	99.69	45.4	39.6	15.0	72.5
18LN(3/3)C	52.18	0.29	1.28	10.53	0.17	13.18	21.47	0.02	0.01	99.39	44.6	38.1	17.4	68.7
18LN(4/2)R	51.71	0.26	1.20	10.68	0.34	12.91	21.50	0.02	0.01	98.85	44.7	37.4	17.9	67.6
18LN(4/3)C	51.36	0.40	1.43	11.69	0.31	12.63	21.00	0.04	0.01	99.14	43.8	36.6	19.5	65.2

R=RIM; H=H[illegible]LFWAY FROM RIM TO CORE; C=CORE

Table 7.10

Microprobe analyses of low-calcium pyroxene grains within selected samples from profile B.

Sample	SiO_2	TiO_2	Al_2O_3	FeO	MnO	MgO	CaO	Cr_2O_3	NiO	Total	Ca^{2+}	Mg^{2+}	Fe^{2+}	Mg-number
25LS(3/1)R	50.95	0.15	0.60	28.07	0.69	18.16	0.76	0.00	0.01	99.39	1.6	52.1	46.3	52.9
25LS(3/2)C	50.99	0.09	0.55	28.26	0.67	18.25	0.61	0.02	0.05	99.51	1.2	52.3	46.5	52.9
25LS(4/1)R	51.14	0.12	0.58	27.61	0.66	18.43	0.72	0.01	0.03	99.33	1.5	52.9	45.6	53.7
25LS(4/2)C	50.89	0.11	0.55	27.68	0.67	18.40	0.74	0.00	0.02	99.08	1.5	52.8	45.7	53.6
24LS(3/1)R	51.48	0.11	0.72	22.90	0.55	16.84	6.42	0.01	0.02	99.11	13.3	48.7	38.0	56.1
24LS(3/2)C	51.27	0.16	0.66	26.17	0.62	18.21	2.22	0.01	0.03	99.35	4.6	52.3	43.2	54.8
22LS(2/1)R	51.13	0.13	0.53	27.07	0.65	18.84	0.75	0.00	0.02	99.12	1.6	53.9	44.5	54.8
22LS(2/2)H	51.21	0.18	0.72	26.23	0.57	19.19	0.78	0.00	0.03	98.93	1.6	55.2	43.2	56 1
22LS(2/3) cpx exsolution	51.81	0.31	1.24	11.59	0.27	13.74	19.52	0.00	0.03	98.74	40.8	39.9	19.3	67.4
22LS(3/1)R	51.05	0.19	0.61	25.79	0.59	19.80	0.76	0.00	0.02	98.82	1.5	56.3	42.1	57.2
22LS(3/2)H	51.89	0.20	0.68	25.78	0.56	19.73	0.70	0.00	0.04	99.61	1.5	56.3	42.2	57.2
22LS(3/3)C	51.53	0.22	0.59	25.74	0.58	19.70	0.85	0.00	0.02	99.24	1.7	56.2	42.1	57.1
19LS(2/3)R	52.00	0.18	0.59	25.59	0.57	19.68	0.91	0.00	0.02	99.57	1.9	56.2	41.9	57.3
19LS(2/2)H	51.48	0.24	0.64	25.37	0.54	19.94	0.89	0.00	0.04	99.13	1.8	56.8	41.4	57.8
19LS(2/1)C	51.71	0.21	0.71	25.54	0.55	19.75	0.81	0.01	0.05	99.33	1.7	56.5	41.9	57.4
19LS(4/3)R	52.29	0.21	0.62	25.44	0.53	20.52	0.72	0.00	0.03	100.40	1.5	57.6	40.9	58.5
19LS(4/2)H	52.10	0.17	0.66	25.33	0.53	20.34	0.73	0.00	0.05	99.91	1.5	57.5	41.0	58.4
19LS(4/1)C	52.31	0.17	0.65	25.29	0.59	20.56	0.71	0.02	0.04	100.40	1.4	57.8	40.8	58.6

R=RIM; H= HALFWAY BETWEEN RIM AND CORE; C= CORE

Table 7.11

Microprobe analyses of clinopyroxene grains within selected samples from profile B.

Sample	SiO_2	TiO_2	Al_2O_3	FeO	MnO	MgO	CaO	Cr_2O_3	NiO	Total	Ca^{2+}	Mg^{2+}	Fe^{2+}	Mg-number
25LS(1/2)R	51.43	0.27	1.29	11.82	0.38	12.70	20.52	0.01	0.04	98.73	43.0	37.0	20.0	65.0
25LS(1/3)H	51.33	0.26	1.60	12.27	0.30	12.97	20.11	0.00	0.05	99.15	41.9	37.6	20.5	64.7
25LS(1/4)C	51.75	0.30	1.45	11.78	0.32	12.57	20.99	0.00	0.03	99.46	43.8	36.5	19.7	64.9
25LS(1/9)R	51.44	0.30	1.40	11.64	0.35	12.79	21.17	0.00	0.03	99.40	43.8	36.8	19.4	65.5
25LS(5/1)R	51.80	0.30	1.31	11.41	0.31	12.76	21.36	0.00	0.00	99.54	44.3	36.8	20.0	66.0
25LS(5/2)C	51.09	0.26	1.35	12.70	0.37	13.04	19.59	0.00	0.04	98.71	40.9	37.8	21.3	64.0
24LS(1/1)R	51.81	0.24	1.32	10.67	0.32	13.87	21.84	0.01	0.00	99.35	43.9	38.8	19.3	69.2
24LS(1/2)C	51.81	0.29	1.31	11.20	0.31	12.81	21.49	0.00	0.02	99.51	44.3	36.9	18.6	66.5
24LS(2/1)R	52.17	0.25	1.30	11.17	0.30	12.78	21.65	0.00	0.02	99.93	44.7	36.7	18.5	66.5
24LS(2/2)H	51.43	0.29	1.48	11.38	0.30	12.60	21.49	0.01	0.02	99.30	44.7	36.4	18.9	65.8
24LS(2/3)C	51.45	0.30	1.41	11.95	0.32	12.63	20.95	0.00	0.02	99.32	43.6	36.5	19.9	64.7
23LS(1/1)R	52.23	0.33	1.28	10.19	0.29	13.22	21.75	0.00	0.01	99.56	45.1	38.1	16.9	69.2
23LS(1/2)H	52.01	0.39	1.35	10.41	0.25	13.14	21.84	0.01	0.01	99.70	45.1	37.7	17.2	68.7
23LS(1/3)C	51.72	0.36	1.43	10.25	0.29	13.17	21.76	0.02	0.01	99.28	45.0	37.9	17.0	69.0
23LS(2/1)R	51.84	0.28	1.34	10.75	0.27	13.10	21.65	0.01	0.01	99.55	44.7	37.6	17.7	68.0
23LS(2/3)C	52.03	0.34	1.50	10.78	0.27	13.02	21.69	0.00	0.04	99.91	44.8	37.3	17.8	67.7
22LS(1/3) opx exsolution	50.69	0.07	1.01	26.43	0.65	18 83	1.06	0.00	0.01	98.77	2.2	54.1	43.7	55.3
22LS(1/2)H	51.54	0.42	1.41	11.22	0.28	13.05	21.29	0.00	0.00	99.49	44.0	37.5	18.5	66.9
22LS(1/2) opx exsolution	51.37	0.09	0.70	24.91	0.61	18.25	3.30	0.00	0.03	99.32	6.8	52.2	41.0	56.0

Table 7.11
Microprobe analyses of clinopyroxene grains within selected samples from profile B.

22LS(1/1)C	52.08	0.26	1.36	10.05	0.24	13.11	22.10	0.01	0.03	99.54	45.7	37.7	16.6	69.4
19LS(1/3)R	51.66	0.34	1.28	10.33	0.25	13.16	21.55	0.03	0.03	98.90	44.8	38.0	17.2	68.9
19LS(1/2)H	51.50	0.39	1.41	11.50	0.28	12.95	20.84	0.02	0.06	99.22	43.4	37.5	19.1	66.2
19LS(1/1)C	51.60	0.37	1.46	10.31	0.28	12.88	21.66	0.02	0.02	98.91	45.3	37.4	17.3	68.4
19LS(3/3)R	52.54	0.19	1.13	9.79	0.22	13.69	22.05	0.01	0.03	99.87	45.1	38.9	16.0	70.9
19LS(3/2)C	51.94	0.38	1.35	11.08	0.26	13.54	20.41	0.01	0.04	99.26	42.4	39.2	18.4	68.0
19LS(3/1)C	52.35	0.37	1.40	10.30	0.30	13.43	21.50	0.00	0.03	99.96	44.4	38.5	17.1	69.3
18LS(3/3)R	51.96	0.23	1.26	10.88	0.32	12.80	21.50	0.01	0.04	99.25	44.7	37.0	18.2	67.0
18LS(3/2)H	51.79	0.28	1.32	10.72	0.32	12.79	21.68	0.02	0.02	99.23	45.1	37.0	17.9	67.4
18LS(3/1)C	51.67	0.39	1.36	11.13	0.34	12.77	21.51	0.00	0.02	99.47	44.6	36.8	18.6	66.5
18LS(4/2)C	51.73	0.35	1.31	10.77	0.35	12.75	21.89	0.02	0.02	99.52	45.3	36.7	18.0	67.1
18LS(4/3)C	51.34	0.53	1.38	11.61	0.33	12.61	21.11	0.01	0.00	99.19	44.0	36.5	19.4	65.3

R=RIM; H= HALFWAY BETWEEN RIM AND CORE; C= CORE

7.2.2 Vertical variation of pyroxene compositions

Figure 7.4 shows the variation of the pyroxene compositions, for profiles A and B, from the footwall, to the Layered Marker Sequence through to the hangingwall samples.

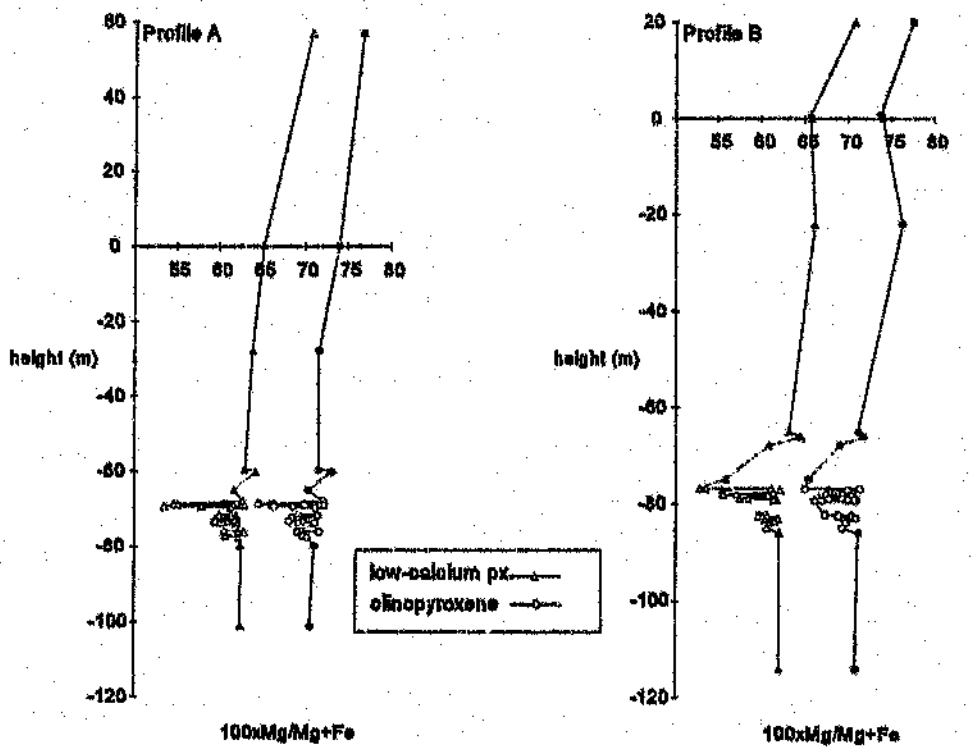


Figure 7.4 Variation in pyroxene compositions for profiles A and B. The filled symbols refer to the hangingwall and footwall samples whilst the hollow symbols refer to those samples from the Layers Marker Sequence.

From these graphs it can be seen that there is a subtle reversal in pyroxene compositions towards the Pyroxenite Marker (which occurs at 0m). The intensely sampled interval is the layered marker zone. The compositional variation within this interval is presented in greater detail in Figure 7.5. One of the mafic layers was sampled from its top, middle and bottom portions. For cpx, the range in mg-number determined for these samples was 1%. For opx, the difference was 0.4 %. Both these variations are larger than can be explained by analytical precision. In both cases

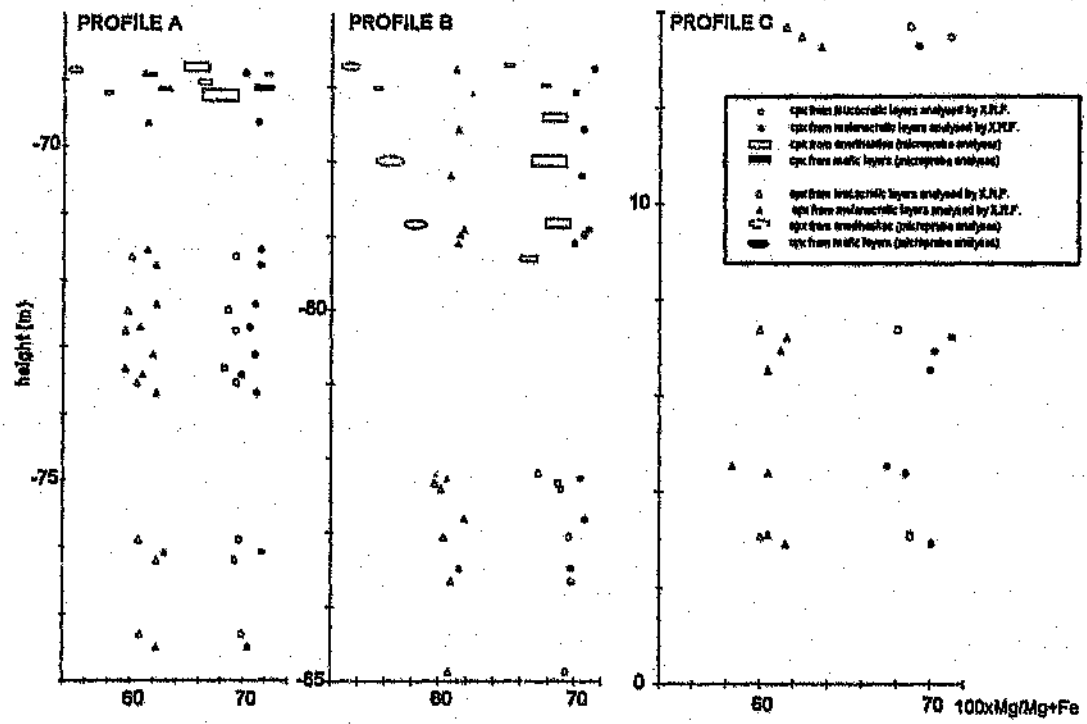


Figure 7.5 Vertical variation in pyroxene composition for samples from the Layered Marker Sequence. Symbol size is proportional to the calculated analytical error.

the pyroxene gets more magnesian towards the top of the layer. The same layer was sampled several times along strike. The mg-number of cpx from these samples varied by 1.3% and opx by 1.7%.

The variation in composition of the pyroxene phases between layers is significantly larger than that of the plagioclase. Pyroxenes from the mafic samples have a mg-number that is typically about 2% higher than that of the contiguous leucocratic samples. Towards the top of the sequence, the leucocratic samples are anorthosites and the pyroxene compositional difference between these and the mafic samples can reach 5%.

7.2.3 Lateral variation in pyroxene composition

On a larger scale there is no significant difference in range of pyroxene composition for samples

from the three profiles. Table 7.12 lists the range of low-calcium pyroxene compositions determined for intervals of stratigraphy from the three profiles.

Table 7.12
Comparison of mg-number of low-calcium pyroxene with height in the three profiles

	Profile A	Profile B	Profile C
Pyroxenite Marker interval	65.2-70.8	65.7-70.8	No outcrop
Layered Marker interval (mafic layers)	60.8-62.6	60.6-62.2	60.5-62.4
Footwall gabbronorite	62.5-62.6	62.1	61.1

7.2.4 Comparison with other studies

Figure 7.6 is a ternary plot showing the range of pyroxene compositions encountered. Pyroxene compositions from studies by Molyneux (1974), Atkins (1976), Marais (1977) have been included for comparison.

From this diagram it would appear that the pyroxene compositions, determined in this study, are similar to those determined by others. The microprobe analyses of clinopyroxenes are however

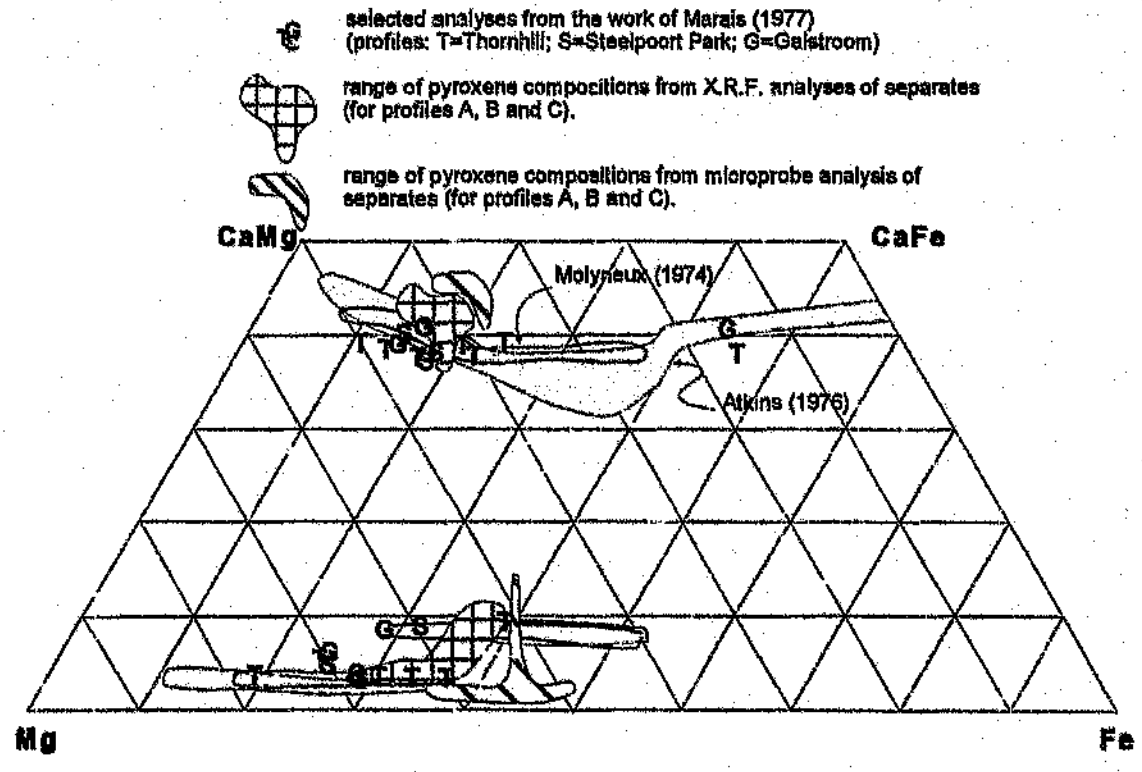


Figure 7.6 Ternary plot showing the overall range in composition of the pyroxenes analysed in the study. Also included, for comparison, is data from other studies.

considerably more Ca-rich due to the fact that the matrix of the grains have been analysed without taking into account the exsolution lamellae. The orthopyroxene grains analysed by microprobe show the reverse trend. The low-calcium pyroxene samples analysed by X.R.F. exhibit a range in composition spanning the gap between the orthopyroxene and pigeonite fields. These fields are delineated neatly by previous work on low-calcium pyroxenes from the Bushveld Complex.

Figure 7.7 shows the detailed compositional variation exhibited by the clinopyroxenes and low-calcium pyroxenes analysed in this study.

7.2.5 Low-calcium pyroxene

As has been pointed out previously, pyroxenes from the leucocratic samples (open circles in

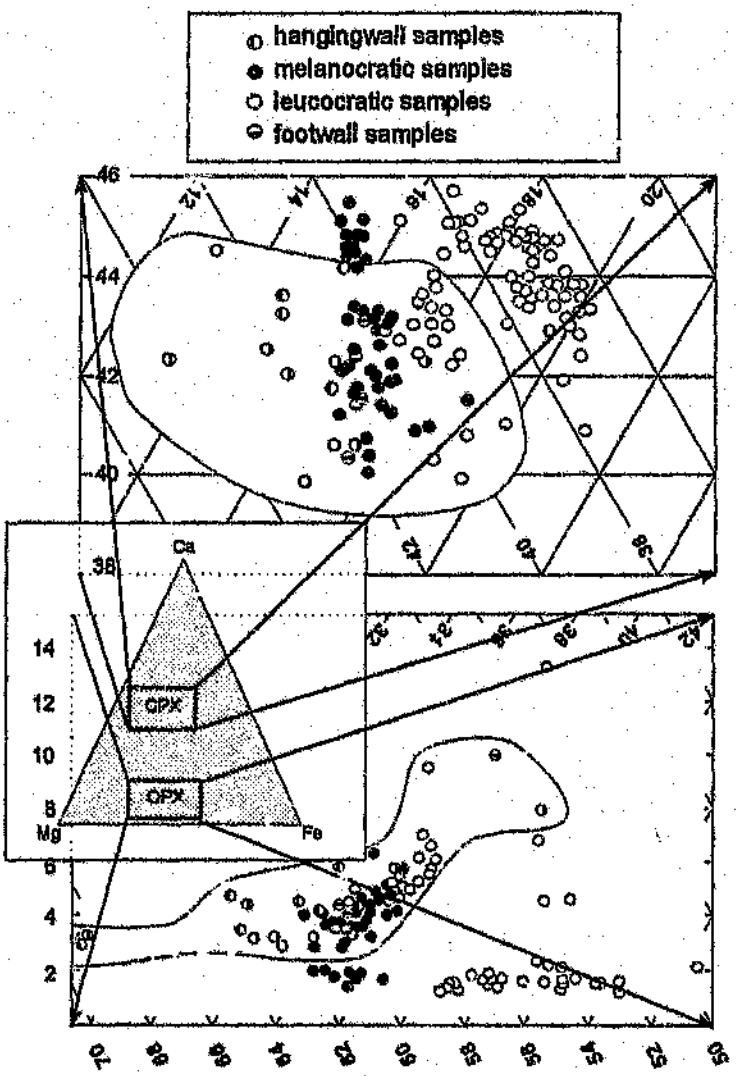


Figure 7.7 Detailed plot of the compositional variation shown by low-calcium and clinopyroxene separates as analysed in this study. The composition of those separates analysed by XRF are identified by the enclosed fields. Those data points that plot outside these fields have been analysed by microprobe.

Fig. 7.7) are Mg-deficient in comparison to those from the mafic samples. In addition the pyroxenes from the leucocratic samples are frequently more Ca-rich than those from the mafic samples. This trend is not seen in the microprobe analyses as the homogenous and equilibrated matrix has been probed without taking into account the exsolution lamellae. This trend cannot be explained by contamination of the separates by plagioclase as Al_2O_3 abundances, within these analyses do not appear systematically enriched in line with increased CaO concentrations.

7.2.6 Clinopyroxene

Leucocratic and melanocratic samples plot in distinct groups in Figure 7.7. There is a range in Ca content of 4%, which is quite significant, but, as it is shown by both leucocratic and melanocratic samples, may reflect variable amounts of exsolved orthopyroxene being separated from clinopyroxene during the cooling process.

As a result of the large range in Ca contents in both X.R.F. and microprobe analyses there is no point in trying to estimate temperatures, either of formation or of final equilibrium.

8. Whole rock geochemistry

Selected whole rock samples, from profiles B and C, have been analysed for a variety of major and trace elements. This data is presented in the tables 8.1 and 8.2. The data for profile C has been included for comparison. These samples were analysed prior to this study.

Figure 8.1 is a diagram showing the approximate stratigraphic positions from where the samples were taken.

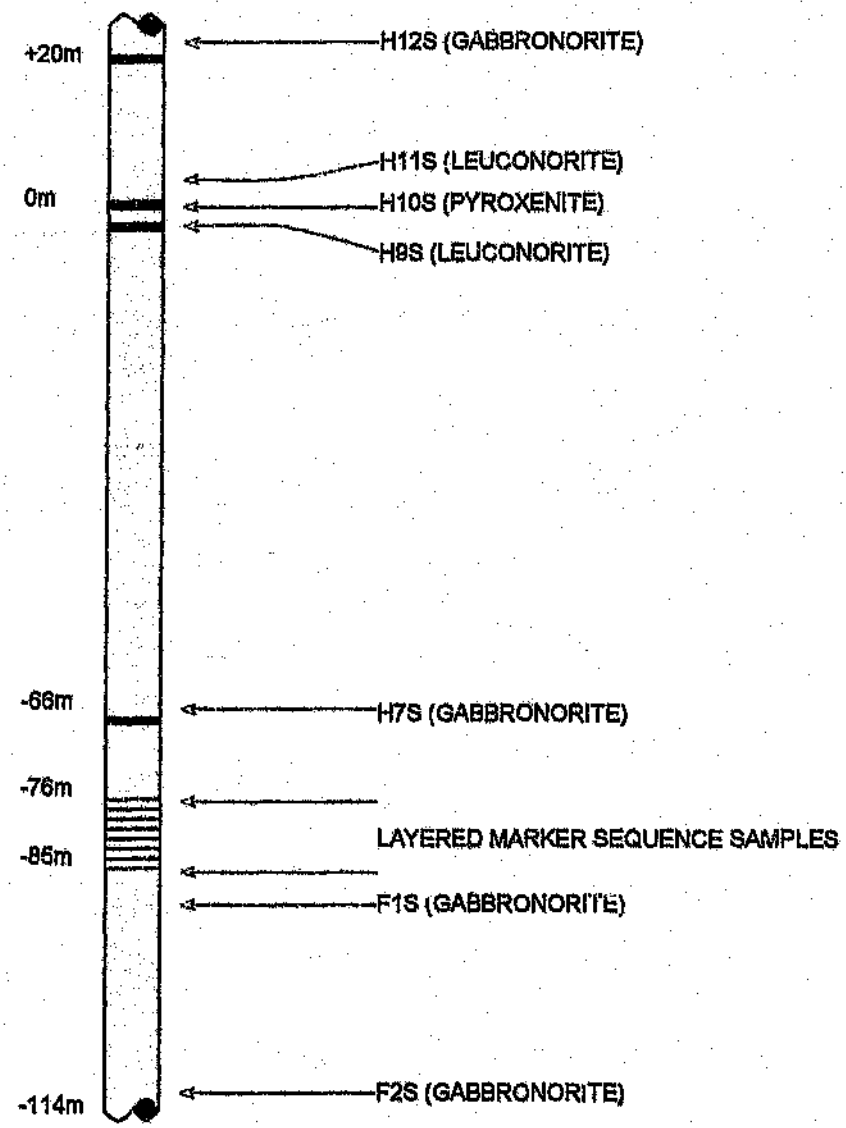


Figure 8.1 Stratigraphic column showing the approximate positions from where the whole rock samples, that have been analysed, were taken.

Table 8.1

Geochemistry of selected whole rock samples from profile B.

Sample	SiO_2	TiO_2	Al_2O_3	Fe_2O_3	MnO	MgO	CaO	Na_2O	K_2O	Total	V	Cr	Co	Ni	Zn	Rb	Sr	Zr	Ba	P
Hangingwall samples																				
H12S	52.00	0.22	14.70	8.63	0.20	11.90	11.80	1.84	0.11	101.21	133	707	50	236	59	12	198	22	66	57
H11S	52.20	0.17	13.10	12.40	0.29	12.60	8.04	1.29	0.15	99.97	143	275	61	168	78	14	253	21	81	133
H10S	52.70	0.21	4.74	18.20	0.41	19.10	5.59	0.67	0.04	100.90	258	448	138	332	122	18	72	23	56	58
H9S	52.70	0.15	16.80	10.60	0.24	9.96	9.21	1.91	0.17	101.48	176	280	79	205	81	15	209	20	87	60
H7S	53.10	0.15	16.50	8.70		8.70	11.20	1.90	0.18	100.60	208	109	49	129	57	13	254	18	88	47
Samples from the Layered Marker Sequence																				
23LS	53.00	0.11	25.70	3.09	0.06	2.40	12.00	3.98	0.38	100.90	69	11	15	29	19	4	397	24	114	122
23MS	51.70	0.22	11.10	11.70	0.24	11.20	12.20	1.53	0.15	99.72	313	32	73	167	66	9	167	22	81	101
19MS	52.50	0.14	20.10	7.26	0.13	6.24	11.20	2.85	0.25	100.65	128	28	34	88	43	3	308	19	88	105
6LS	52.60	0.11	24.30	3.97	0.07	2.95	11.70	3.80	0.33	100.00	73	11	17	39	26	4	382	21	117	129
6MS	52.80	0.20	16.80	8.51	0.17	7.69	12.10	2.26	0.23	100.66	215	20	45	112	51	7	256	23	93	120
5LS	53.40	0.11	23.80	3.92	0.09	3.43	11.80	3.88	0.35	100.90	87	7	20	40	28	4	375	23	114	1[illegible]6
4LS	52.70	0.12	23.20	4.72	0.09	3.86	11.80	3.34	0.33	100.33	102	12	22	50	30	5	361	21	115	159
4MS	52.50	0.20	14.50	9.92	0.19	9.32	12.00	2.20	0.18	100.90	239	31	56	133	53	8	225	22	79	90
3LS	52.90	0.14	22.70	5.08	0.10	4.19	11.80	3.47	0.31	100.83	108	17	24	56	32	4	348	21	106	126
3MS	52.30	0.21	15.50	9.44	0.20	8.78	12.00	2.18	0.21	100.66	231	28	50	128	53	8	237	22	92	114
2LS	52.30	0 14	21.00	5.81	0.11	5.03	12.00	3.14	0.29	99.91	134	18	27	70	36	4	329	23	105	113
Footwall samples																				
F1S	52.60	0.20	16.50	8.30	0.20	8.07	12.20	2.43	0.20	100.56	224	27	46	119	53	15	258	23	98	83
F2S	52.50	0.16	19.10	7.04	0.15	6.24	11.50	2.32	0.25	99.26	173	25	38	85	49	13	307	21	96	89
Calculated analytical errors																				
2σ											30	26	16	12	20	0	18	36	25	39

Table 8.2

Geochemistry of selected whole rock samples from profile C. These samples were analysed prior to this study. P was analysed for in the same run as for samples from profile B.

Sample	SiO_2	TiO_2	Al_2O_3	Fe_2O_3	MnO	MgO	CaO	Na_2O	K_2O	Total	V	Cr	Co	Ni	Zn	Rb	Sr	Zr	P
74L	52.92	0.05	28.26	1.1	0.03	0.38	12.1	3.65	0.52	99.7	[illegible]	1[illegible]	9	6	13	8	462	10	
53M	52.84	0.18	17.4	8.5	0.15	7.37	12.02	2.72	0.25	101.5	190	30	46	106	52	9	278	10	
52M	52.42	0.25	13.41	10.63	0.2	10.08	11.9	1.15	0.14	100.1	235	33	55	143	62	12	216	14	74
52L	52.25	0.09	23.82	4.13	0.07	3.11	11.79	2.37	0.37	98.7	80	15	22	43	27	8	391	10	70
51L	52.48	0.14	21.69	5.68	0.1	4.61	11.54	1.6	0.34	98.6	108	13	28	62	35	9	360	8	73
46M	52.21	0.25	9.86	13.17	0.26	12.21	11.69	0.15	0.1	99.5	288	39	77	194	81	13	158	15	
39M	52.41	0.26	9.81	13.02	0.27	12.6	11.57	0.58	0.1	100.7	285	38	73	195	78	13	157	13	
35M	52.73	0.2	14.39	10.53	0.21	9.44	11.91	1.38	0.17	100.8	228	31	57	141	63	11	229	11	58
34L	54.06	0.07	26.58	2.08	0.03	1.11	11.88	3.02	0.34	99.5	33	13	13	14	16	5	430	9	
31M	52.43	0.22	13.4	11.05	0.22	10.02	11.58	1.23	0.15	100.4	232	23	63	145	67	11	218	12	64
29L	52.81	0.11	24.44	4.2	0.08	2.99	11.82	2.91	0.29	99.9	75	15	21	39	28	6	396	8	
25L	52.72	0.14	22.83	5.22	0.1	3.93	11.95	3.03	0.33	100.4	102	14	26	53	34	8	369	9	
23L	52.99	0.08	28.27	1.16	0.01	0.45	12.2	3.87	0.47	100.1	26	10	9	3	13	7	440	12	89
23M	51.99	0.27	7.99	14.14	0.28	12.56	11.22	0.33	0.08	99.4	316	33	87	209	89	15	128	15	63
22L	52.05	0.1	24.28	3.91	0.08	2.86	11.76	3.28	0.32	99	75	13	22	36	25	6	408	10	
21L	52.25	0.13	21.56	5.57	0.1	4.59	11.93	1.6	0.29	98.1	117	17	30	61	36	8	363	10	
20L	52.27	0.16	19.18	6.99	0.14	6.13	11.71	2.02	0.25	99.1	154	17	37	80	45	8	329	9	
19L	51.89	0.13	21.27	6.07	0.12	4.83	11.51	2.23	0.27	98.5	116	18	27	61	37	8	359	7	
18L	54.28	0.13	21.71	5.14	0.09	4.03	11.44	1.84	0.29	99.2	103	18	24	55	34	6	377	8	66
18M	52.21	0.2	16.53	9.04	0.17	7.92	11.76	1.68	0.21	99.8	210	22	49	115	56	10	265	11	73
16L	52.96	0.12	23.56	4.74	0.1	3.67	11.91	2.7	0.31	100.1	91	14	23	51	31	6	395	8	
16M	52.25	0.22	14.66	10.11	0.22	9.29	12.11	1.89	0.2	100.9	237	23	57	129	57	11	245	11	
15L	52.41	0.14	21.86	5.78	0.11	4.64	11.6	1.93	0.27	99.51	111	15	31	58	37	8	365	8	

8.1 Variation in major element abundances

Major elements vary significantly in their abundances. Element-element plots may be used to show this geochemical variation as they can indicate the effects of differentiation, modal changes and/or the possible influence of a new magma through different trends. MgO is a useful element in such plots as it varies widely in abundance. In addition it is often used as an indicator of differentiation.

If such graphs are plotted two types of patterns emerge. A plot of MnO versus MgO (Fig. 8.2) shows one such trend. In this plot all samples define a good linear trend. The sample that plots off this trend line is that from above the Pyroxenite Marker (the topmost sample stratigraphically). The boxed fields drawn on these plots delineate the range in composition shown by the different mineral phases. These compositions have been determined by the microprobe analysis of samples from profile A and B.

The plots of MgO versus TiO_2 and MgO versus Al_2O_3 (Figures 8.3 and 8.4) show the other type of trend seen in these binary plots. In both plots the samples from the Layered Marker Sequence and those from the hangingwall define two different trends. The sample taken from above the Pyroxenite Marker plots on its own as before.

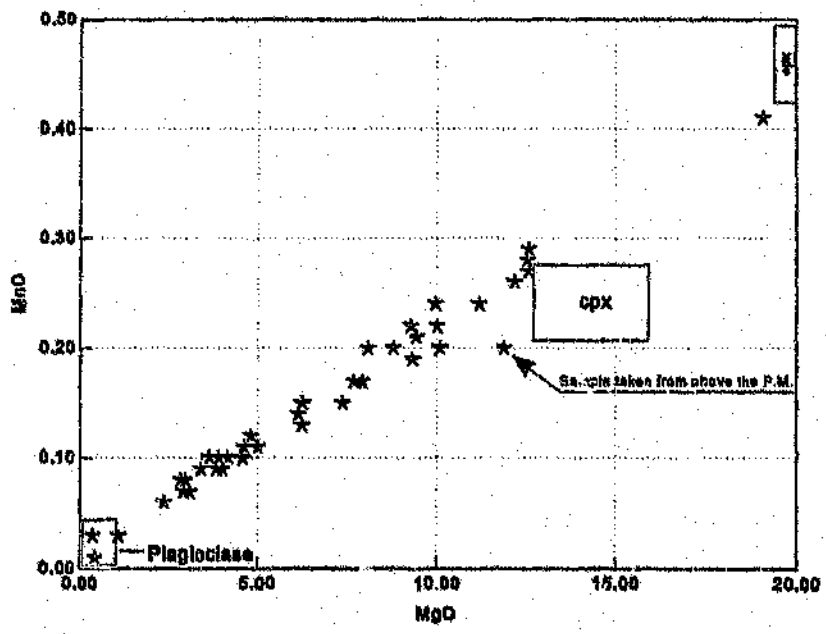


Figure 8.2 Variation of MnO abundance with MgO.

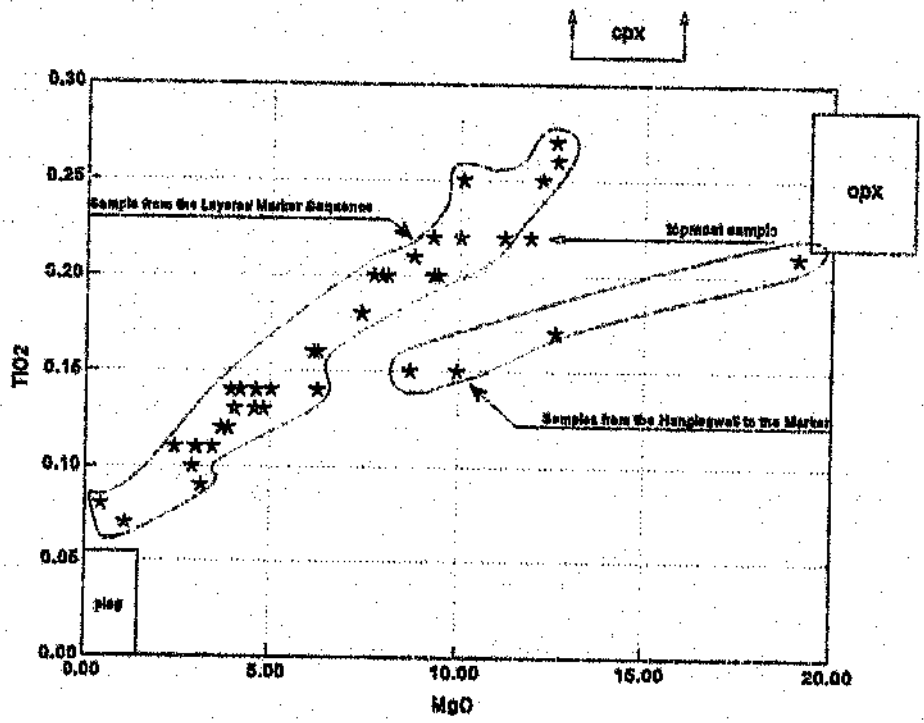


Figure 8.3 Variation of TiO_2 abundance with MgO..

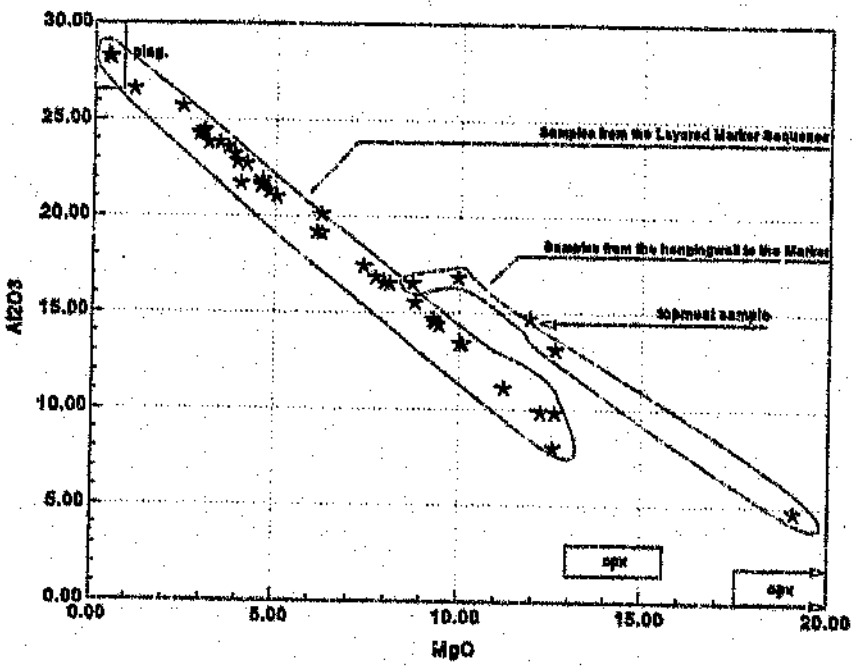


Figure 8.4 Variation of Al_2O_3 abundance with MgO.

What these plots appear to be showing is that the magma producing the leucocratic and melanocratic layers is geochemically very similar. If this were not the case melanocratic and leucocratic samples would plot in significantly different areas of the plot and not on a well defined linear trend. These linear trends can be explained by modal variation of plagioclase relative to the other phases in these samples. The hangingwall samples appear geochemically different and this is most probably due to an enrichment of low-calcium pyroxene in the modal assemblage above the Layered Marker Sequence. The sample from above the Pyroxenite Marker often plots on its own in such plots. This sample is petrographically similar to those below the Marker other than for the appearance of orthopyroxene at the expense of pigeonite.

8.2 Incompatible trace element distribution

The incompatible traces analysed for included Y, Nb, Zr, Rb, Ba and P. Y and Nb occur at levels below detection. The only high field strength element that occurs in reasonable concentrations is Zr. Profile B samples contain around 20ppm Zr. There is no apparent systematic variation in Zr concentration between melanocratic and leucocratic layers. However there appears to be a lateral change in Zr abundance as profile C samples contain only half as much Zr as those from profile B.

P has often been considered as the ideal element for evaluating the role of trapped liquid as it is highly incompatible (Cawthorn and Walsh, 1988).This element appears to be enriched in leucocratic compared to melanocratic layers in profile B (Figure 8.5B) and is only half as abundant in samples from profile C compared to those from profile B. In addition for profile B samples there appears to be a systematic variation in P content with mode (Fig. 8.5A).

Ba is quite incompatible into the whole rock (D_{opx}=0.01, D_{cpx}=0.07 and D_{plag}=0.23 (Henderson, 1986)). This element appears to vary systematically with mode (Fig. 8.6). Note however that the topmost sample analysed, i.e. that from above the pyroxenite marker, again plots on its own.

Rb occurs at very low levels. This element is highly incompatible into both pyroxene phases, but partitions more favourably into plagioclase (D_{plag}<0.5, Henderson 1986). However the variation in abundance of this element is puzzling as samples from the layered marker sequence, at profile B, contain markedly less Rb than the hanging or footwall samples. In addition the Rb concentration is higher in melanocratic compared to leucocratic samples (refer to tables 8.1 and 8.2).

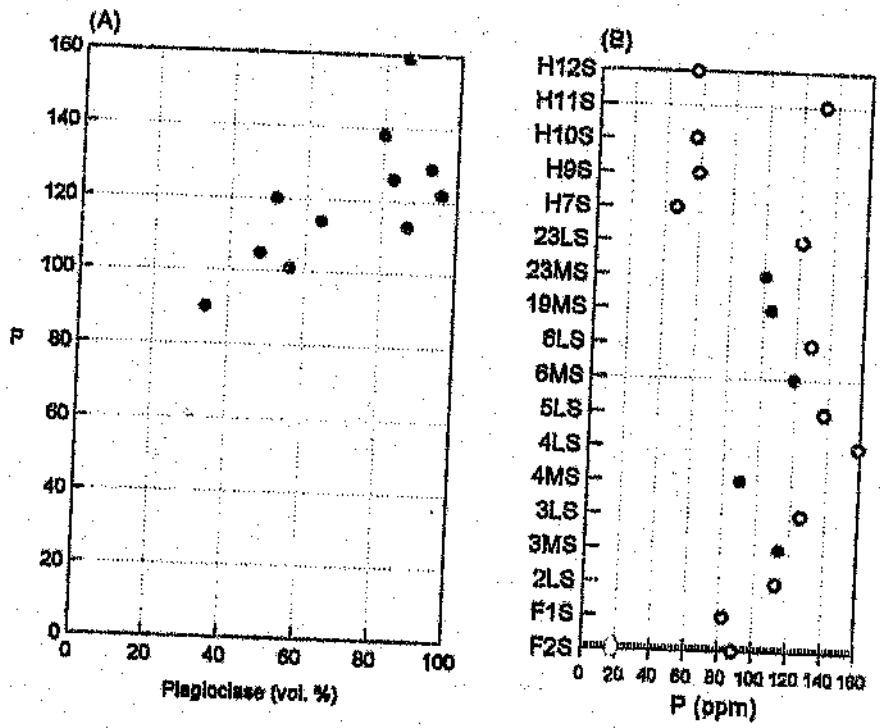


Figure 8.5 (A) Variation in P concentration with changing mode.
(B) Variation in P concentrations between samples from profiles B. Samples are arranged in stratigraphic order but not to scale.

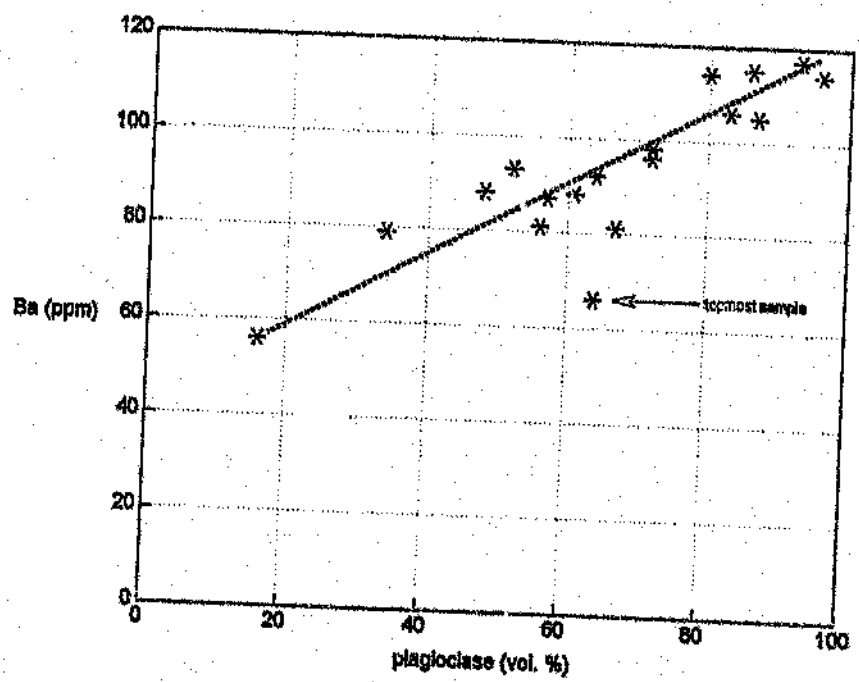


Figure 8.6 variation in Ba concentration with changing mode.

8.3 Variation in compatible trace element abundances

Compatible traces analysed for included Ni, Cr, Co, Sr and V. When Ni, Cr, Co and V are plotted against each other two types of trends emerge. In a plot of Ni versus Co , for example, a good linear trend fitting all the data, excluding the topmost sample, is seen (Fig. 8.7).

A Ni versus Cr plot (Fig 8.8) illustrates the other type of trend that emerges. In this case samples from the layered marker interval plot on a well defined linear trend whilst those from the hangingwall define another. What is important to note however, is the significant enrichment of Cr above the layered marker sequence.

Sr partitions strongly into plagioclase (D_{plag}=1.8). It is almost completely excluded from the pyroxene phases. Therefore the Sr abundance can be related directly to the plagioclase abundance. Similarly Al_2O_3 is almost entirely controlled by the abundance of plagioclase. Therefore when

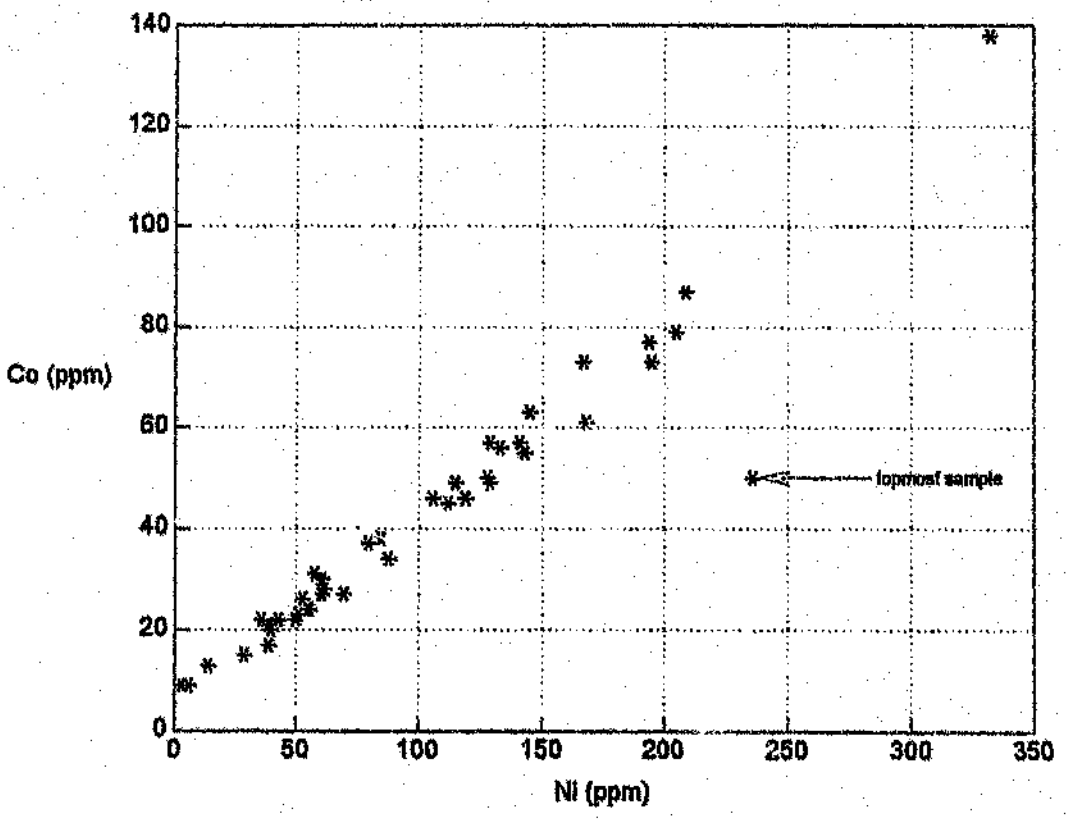


Figure 8.7 Plot of Ni versus Co.

Sr and Al_2O_3 are plotted against each other, a good straight line correlation is evident for samples from the Layered Marker Sequence (Fig. 8.9). This graph shows that there is very little geochemical difference between the magma which produced the melanocratic and leucocratic layers. The significant range in elemental abundances seen in the whole rock samples analysed from the Layered Marker Sequence can therefore be explained by modal changes alone without resorting to other geochemical methods.

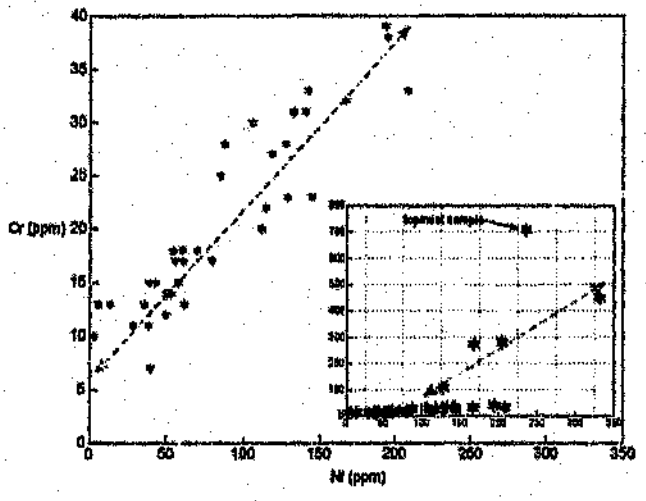


Figure 8.8 Plot of Ni versus Cr. Data points in the main graph are for samples from the layered interval. Additional sample points plotted in the inserted graph reflect the composition of hangingwall samples.

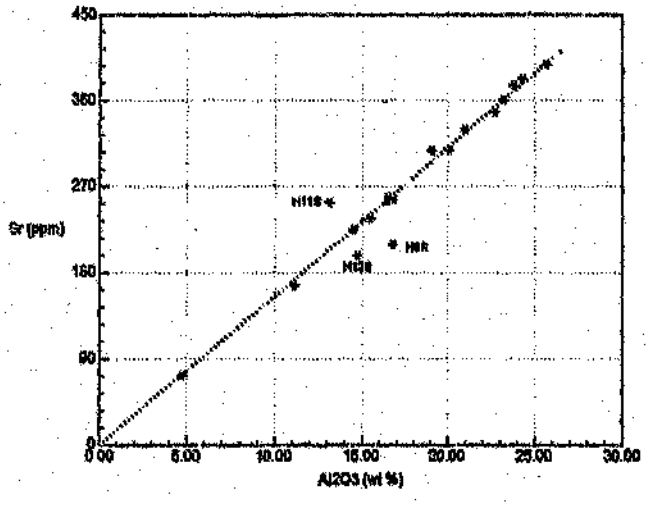


Figure 8.9 Plot of Sr versus Al_2O_3

9. Trace element analysis of mineral separates

9.1 Analysis of mineral separates by Instrumental Neutron Activation Analysis

Selected low-calcium pyroxene, clinopyroxene and plagioclase separates have been analysed by I.N.A.A. The results are presented in Table 9.1. Figures 9.1, 9.2 and 9.3 show the chondrite

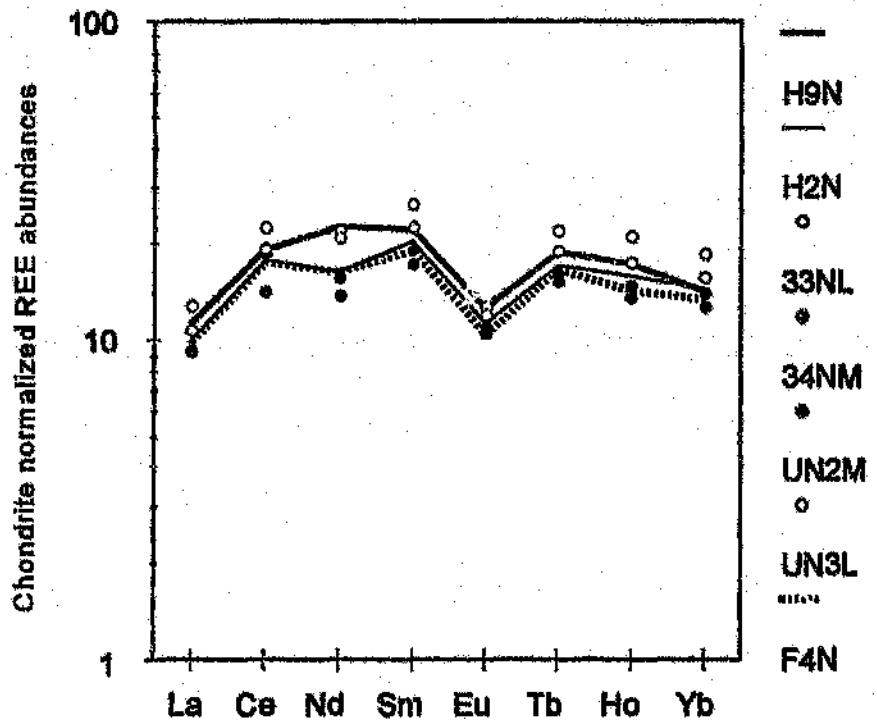


Figure 9.1 Chondrite normalized rare earth element abundances (Evenson, 1978) in clinopyroxene separates from profile A.

normalized REE abundances for each mineral in the samples analysed.

Gd and Lu were also analysed for in these sampler However these two elements are fision products after U and Th. The analytical standards used contain significant quanitities of U and Th. Therefore once the standards are irradiated there are interferences when detecting Lu and Gd. Therefore it was impossible to get a reasonable calibration curve for the determination of these two elements. As a result it was impossible to get realistic values for the abundance of Gd and Lu within these separates. For this reason Gd and Lu abundances have not been included in Table 9.1.

Table 9.1

Concentrations of selected trace elements, as determined by Neutron Activation Analysis, in separates from selected profile A samples.

	La	Ce	Nd	Sm	Eu	Tb	Ho	Yb	Hf	Sc	Ni	Co	Rb	Ba
Clinopyroxene separates														
H8N	2.80	12.24	10.77	3.42	0.73	0.71	0.98	2.34	1.40	87	316	64	1.1	-
H8N (repeat)	2.78	13.44	10.14	3.35	0.73	0.70	0.94	2.49	1.20	-	302	62	1.8	-
H6N	2.48	11.41	7.76	3.15	0.66	0.64	0.90	2.39	1.30	106	231	81	-	-
5LN	3.14	14.37	10.45	4.11	0.74	0.83	1.20	3.08	2.50	121	227	95	1.0	-
5MN	2.27	11.89	7.45	2.95	0.64	0.60	0.84	2.32	1.30	108	216	84	-	-
3MN	2.28	9.09	6.54	2.67	0.61	0.57	0.77	2.11	0.80	95	189	89	-	-
2LN	2.64	12.35	9.92	3.47	0.70	0.71	0.99	2.59	1.90	104	202	79	-	-
F2N	2.45	11.21	7.77	2.94	0.61	0.63	0.81	2.21	1.00	109	225	81	-	-
Orthopyroxene separates														
H8N	0.44			0.14	0.38	0.05	0.09	0.78	0.10	30	494	136	-	-
H8N (repeat)	0.55			0.14	0.41	0.06	0.11	0.76	0.10	30	477	134	-	-
H6N	0.44			0.22	0.25	0.07	0.15	0.84	0.20	37	318	155	-	-
5LN	0.59			0.35	0.26	0.10	0.17	1.08	0.40	36	266	160	2	-
5MN	0.55			0.27	0.27	0.08	0.15	0.87	0.20	37	291	163	-	-
3MN	0.60			0.14	0.24	0.05	0.09	0.86	0.10	35	331	158	-	-
2LN	0.67			0.30	0.25	0.09	0.14	0.90	0.30	35	279	155	-	9
F2N	0.37			0.15	0.26	0.05	0.09	0.76	0.10	36	323	164	-	-
1σ (px separates)	0.1	1.4	1.0	0.1	0.0	0.0	0.0	0.0	0.0	1	10	1	2.4	3.0
Plagioclase separates														
H8N	4.76	7.49	1.39	0.20	0.68	0.03	0.03	0.11	0.10	0.6	6.6	1.4	2.6	126
H8N (repeat)	4.61	7.93	1.33	0.20	0.68	0.03	0.02	0.06	-	0.6	6.5	1.4	2.7	123
H6N	4.02	6.48	1.02	0.16	0.78	0.02	-	0.06	-	0.5	3.2	1.1	3.4	141
5LN	4.21	7.49	1.30	0.20	0.88	0.03	0.04	0.08	-	0.4	3.2	1.0	3.3	141
5MN	3.64	6.34	1.00	0.17	0.79	0.02	-	0.08	-	0.4	3.6	1.3	3.5	134
3MN	3.59	6.10	1.14	0.15	0.81	0.02	0.03	0.00	-	0.4	5.1	1.2	2.2	134
2LN	4.02	6.81	1.20	0.18	0.81	0.03	0.03	0.07	-	0.3	2.6	0.7	3.0	139
F2N	3.80	6.19	0.99	0.15	0.81	0.02	-	0.00	-	0.4	3.5	1.3	2.4	136
1σ (plag. separates)	0.1	3.9	1.0	0.0	0.0	0.0	0.0	0.1	0.1	1	2	1	0.2	7.0

These samples were analysed for Gd and Lu in addition to the elements listed above. However these elements are fision products after U and Th. As the standards used contain significant amounts of U and Th, a reasonable calibration curve, for the calculation of Lu and Gd, could not be generated and therefore the calculated concentrations of these two elements in these samples were unrealistic. For this reason these two elements have been excluded from the data presented.

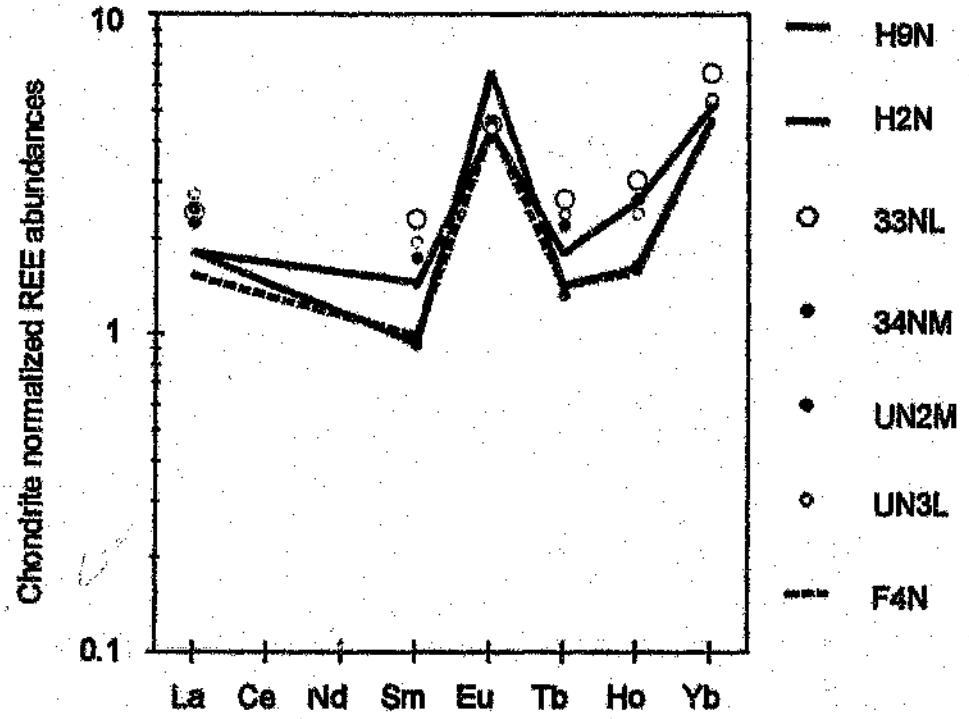


Figure 9.2 Chondrite normalized REE abundances in orthopyroxene separates from selected profile A samples.

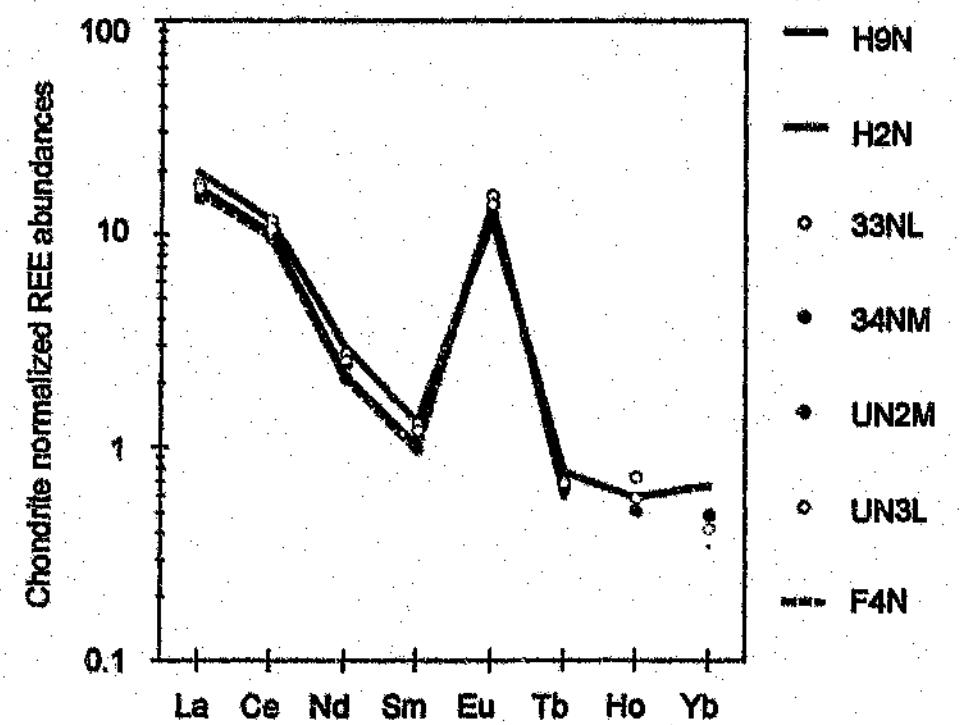


Figure 9.3 Chondrite normalized REE abundances in plagioclase separates from selected profile A samples.

9.1.1 Clinopyroxene

The clinopyroxene hosts most of the REE. This is especially true for the hea ' 'are earths. The chondrite normalized REE pattern for clinopyroxene is essentially flat with a subtle depletion of Eu (Fig. 9.1).

It appears that the separates from the leucocratic samples are enriched in REE compared to those from the melanocratic samples (Figure 9.4). The differences are, in many instances, well in excess of the calculated errors (refer to table 9.1), these errors being based on the accuracy and precision of the calibration standards (method outlined in appendix 4). As a check, on analytical precision, one sample was analysed in duplicate and the results of these analyses suggest that the results are more precise than the calculated errors imply.

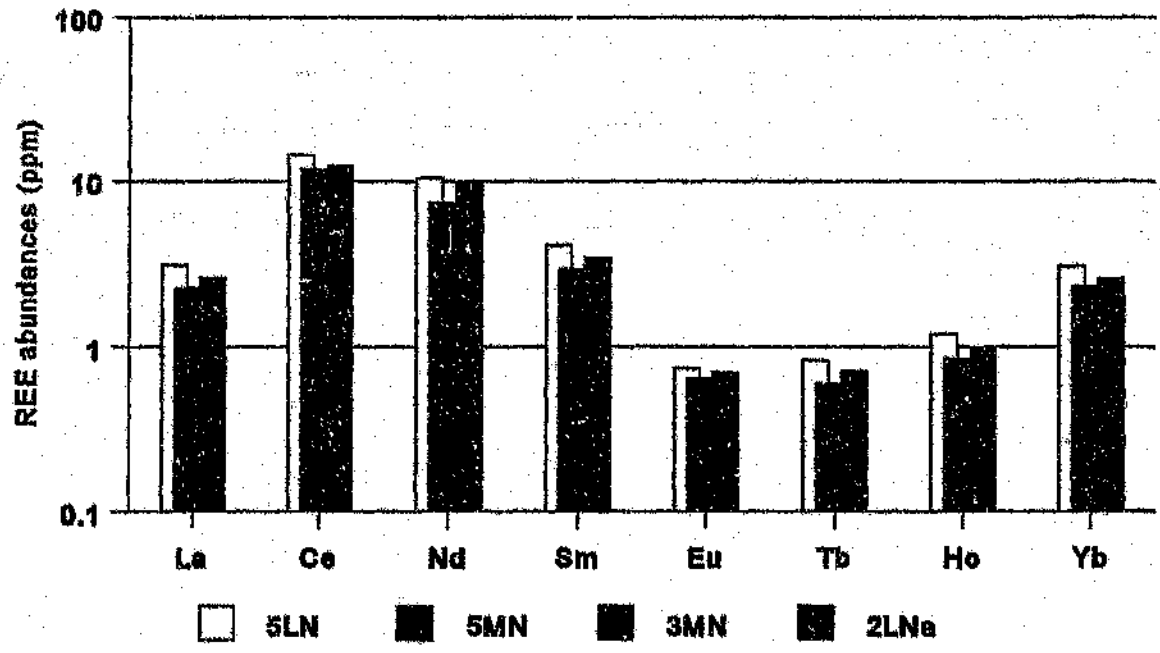


Figure 9.4 Concentration of REE's in clinopyroxene separates from the Layered Marker Sequence.

9.1.2 Low-calcium pyroxene

The low-calcium pyroxene separates contained very low concentrations of REE. Many of these elements were not detected. However again it appears that the separates from the leucocratic samples are enriched in the REE compared to the separates from the melanocratic layers (Fig. 9.5).

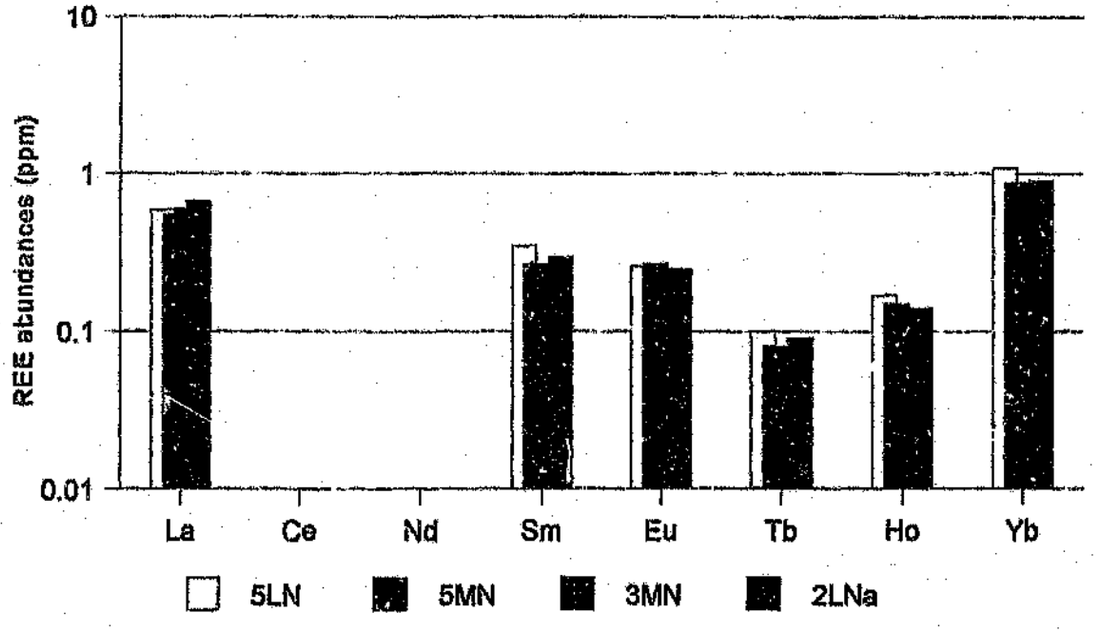


Figure 9.5 Concentration of REE's in low-calcium pyroxene separates analysed from profile A.

9.1.3 Plagioclase separates

The plagioclase separates are enriched in LREE and depleted in the HREE. These separates also show an enrichment in Eu (Fig.9.3). Again the separates, from the leucocratic samples, appear enriched in the REE compared to those separates from the melanocratic layers. This is well

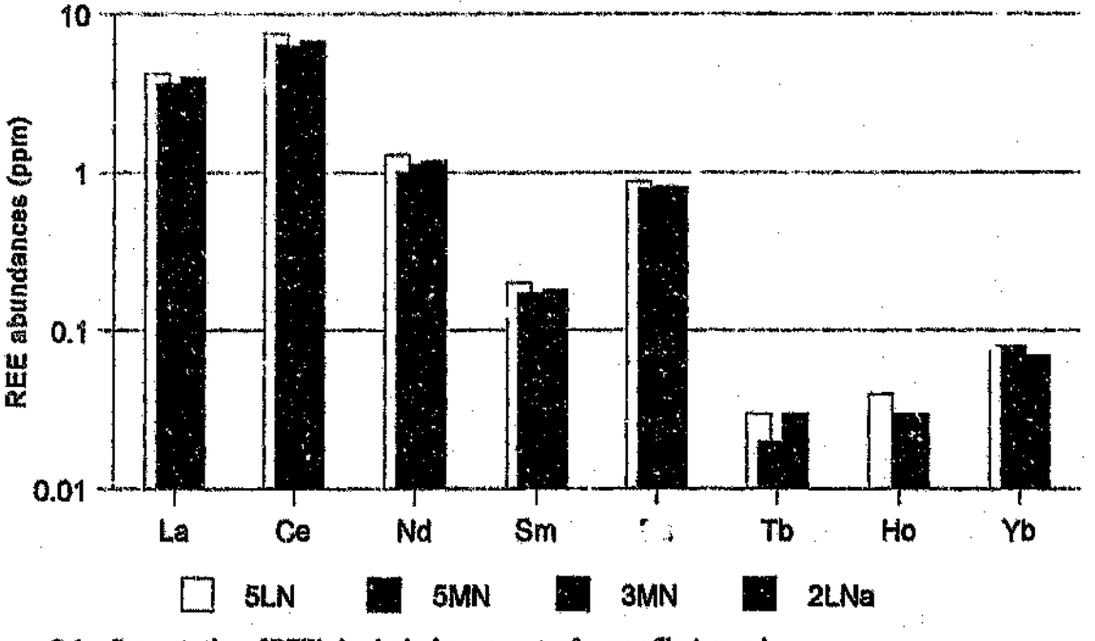


Figure 9.6 Concentration of REE's in plagioclase separates from profile A samples.

demonstrated by the La abundance (Fig. 9.6) The error associated with this element is less than 0.2ppm (the duplicate analyses varied by 0.1ppm) whereas the variation in concentrations between the layer types is around 0.6ppm.

9.2 REE abundances within the whole rock sample

Whole rock samples were not analysed by instrumental neutron activation analysis. Mineral separates were analysed instead as the compositional change within these was considered more important as the whole rock compositions are strongly effected by modal variation and such variations are inherent in these samples.

In order to determine the whole rock REE abundances, the modal proportions have been used to weight the mineral analyses. Accessory phases, especially apatite, are very low in abundances within these samples as evidenced by the whole rock P_2O_5 contents. Table 9.2 lists the REE abundances within the whole rock samples as calculated.

Table 9.2
REE abundances in the whole rock samples as calculated from the individual analyses for the mineral separates.

	La	Ce	Nd	Sm	Eu	Tb	Ho	Yb
H9N	3.12	5.91	2.41	0.68	0.60	0.14	0.20	0.66
H9N	3.07	6.34	2.29	0.67	0.60	0.14	0.19	0.65
H2N	3.15	6.70	2.45	0.86	0.68	0.17	0.23	0.71
34NM	3.30	6.99	2.42	0.83	0.73	0.16	0.24	0.74
34NM	2.31	6.56	2.99	1.17	0.59	0.24	0.34	1.08
UN2M	2.31	5.48	2.72	1.03	0.58	0.22	0.31	0.97
UN3L	3.45	6.94	2.44	0.72	0.73	0.14	0.20	0.57
F4N	2.99	6.48	2.43	0.80	0.68	0.17	0.20	0.62

9.3 Partitioning of selected trace elements between phases

Table 9.3 lists inter-phase partition values for selected trace elements. The La, Ce and Co partition coefficients calculated do not appear to vary significantly and/or systematically between melanocratic and leucocratic samples. This constancy suggests that they are in equilibrium. Ni and Sc partitioning between clinopyroxene and low-calcium pyroxene phases, on the other hand, appear to vary more strongly with the analysed melanocratic samples tending to show a lower value than the analysed contiguous leucocratic samples. This may be explainable as Nielsen (1992) has shown that these elements vary in their partitioning characteristics as a function of calcium content. In this case there is a variable proportion of pigeonite within the low-calcium pyroxene

fraction and this is reflected in the changing calcium content evident in the analyses (Table 7.1a and 7.1b). Therefore even though the partitioning of these elements into the different phases does not appear to be constant, bearing in mind that the number of analyses was very limited, this does not necessarily reflect on the state of equilibrium within the system but may instead relate to the calcium dependence in the partitioning of these elements.

Table 9.3
Ratios of selected trace elements analysed by INAA of separates from profile A.

Sample	Ni_{cpx}:Ni_{opx}	Co_{cpx}:Co_{opx}	Sc_{cpx}:Sc_{opx}	La_{cpx}:La_{plag}	Ce_{cpx}:Ce_{plag}	Ca[1]
HANGINGWALL SAMPLES						
H8N	0.64	0.47	2.90	0.59	1.64	3.1
H6N	0.72	0.52	2.86	0.61	1.76	4.4
SAMPLES FROM THE LAYERED MARKER INTERVAL						
5LN	0.85	0.59	3.36	0.75	1.92	5.7
5MN	0.74	0.52	2.92	0.62	1.88	5.1
3MN	0.57	0.56	2.71	0.64	1.49	3.7
2LNa	0.72	0.51	2.97	0.66	1.81	4.5
FOOTWALL SAMPLES						
F2N	0.70	0.49	3.03	0.64	1.81	3.6

9.4 Rb-Sr isotopes

Recent work on samples from below the Pyroxenite Marker in the Eastern Limb of the complex (Sharpe et al., 1985) indicated initial ^{87}Sr:^{86}Sr ratios varying from 0.7080 to 0.7082. In this study several plagioclase separates have been analysed by isotope dilution and mass spectrometry techniques. Plagioclase separates were used as they contain very low concentrations of Rb and high abundances of Sr. Therefore errors in the analysis of these elements have a small influence on the calculated initial ratio. A few of these separates were analysed for Sr and Rb by X.R.F. and I.N.A.A.. The results are presented in Table 9.4. The initial ratio has been plotted against height within profile A (Fig.9.7).

[1] $\left(\frac{Ca \times 100}{Ca+Mg+Fe}\right)_{cpx}$

The footwall sample exhibits an initial ratio of 0.70812±8. The ratio for rocks from the layered marker varies from 0.7081 to 0.7083. Although this appears to be a significant range, the variation between melanocratic and leucocratic samples is not systematic and in many cases adjacent samples display very similar ratios. In addition, one leucocratic sample was sampled from its top and botto.. contact. There is no significant variation in the initial ratio for these two samples. One layer from locality B was sampled several times along strike. The samples were taken at 6, 16, 22 and 36m from the southern most extent of the outcrop. The variation shown by these samples is small and can be explained by analytical precision.

Above the layered marker interval the ratio is similar (0.70825) but decreases above the Pyroxenite Marker and continues to fall above this layer.

Table 9.4
Rb-Sr isotopic analyses of selected samples from profile A. The error listed is the 95% confidence interval.

Sample	Sr	Rb	R_o	R_i
Hangingwall samples				
H8N	427.9	2.8	0.70766	0.70710±7
H7N	425.0	3.2	0.70865	0.70801±8
H6N	462.0	3.4	0.70888	0.70825±7
samples from the Layered Marker Sequence				
20LN	456.2	3.5	0.70887	0.70821±7
20MN	460.3	2.3	0.70877	0.70833±7
19LN	454.6	5.9	0.70922	0.70811±7
19MN	448.5	2.6	0.70866	0.70815±7
18LaN	454.1	5.0	0.70911	0.70817±7
18LbN	453.2	4.5	0.70899	0.70814±7
18MN	455.1	2.3	0.70861	0.70818±7
5LN	456.9	3.2	0.70880	0.70820±7
5MN	457.0	3.5	0.70889	0.70823±7
3MN	465.0	2.2	0.70860	0.70820±7
2LNb	456.0	3.0	0.70889	0.70832±7
Footwall samples				
F2N	460.0	3.9	0.70883	0.70812±8

Table 9.4
Rb-Sr isotopic analyses of selected samples from profile A. The error listed is the 95% confidence interval.

Samples taken along strike from one layer				
19MS(6m)	457.1	2.6	0.708787	0.70830±7
19MS(16m)	452.3	2.5	0.708744	0.70827±7
19MS(22m)	455.0	2.1	0.708642	0.70825±7
19MS(36m)	458.8	2.2	0.708614	0.70821±7

R_o and R_i are the present day and initial $^{87}Sr/^{86}Sr$ ratio, at 2060 ma, respectively.

9.5 Ba, Sr, Rb and K_2O in plagioclase

A significant amount of work has been done on the plagioclase separates. As a result of this the abundance of certain trace elements within selected plagioclase separates are well constrained. These are presented in table 9.5. The variation of these elements within these samples is graphically illustrated in figure 9.8.

Ba, Rb and K are incompatible into plagioclase with partition coefficients of 0.23, 0.09 and 0.19 respectively (Henderson, 1986). For Ba very few analyses are available. However the variations are small and well within analytical errors. For Rb and K_2O, towards the base of the layered interval, the variation does not appear significantly systematic. However towards the top of the sequence, where the modal contrast between layers is most extreme, the leucocratic samples are invariably significantly enriched in these elements over the contiguous melanocratic sample (Fig. 9.8). For K_2O this variation may reach 0.06 weight %, with an associated error of 0.02 weight % (2σ). Rb shows variations, in abundance, of up to 3.6ppm with an associated error of 0.08 ppm (analyses were by isotope dilution mass spectrometry). These variations are significantly in excess of the associated analytical errors and are therefore considered significant.

Sr is compatible into plagioclase and does not vary significantly between any of the samples below the Pyroxenite Marker. However above this marker the Sr content of plagioclase drops by 20-30ppm.

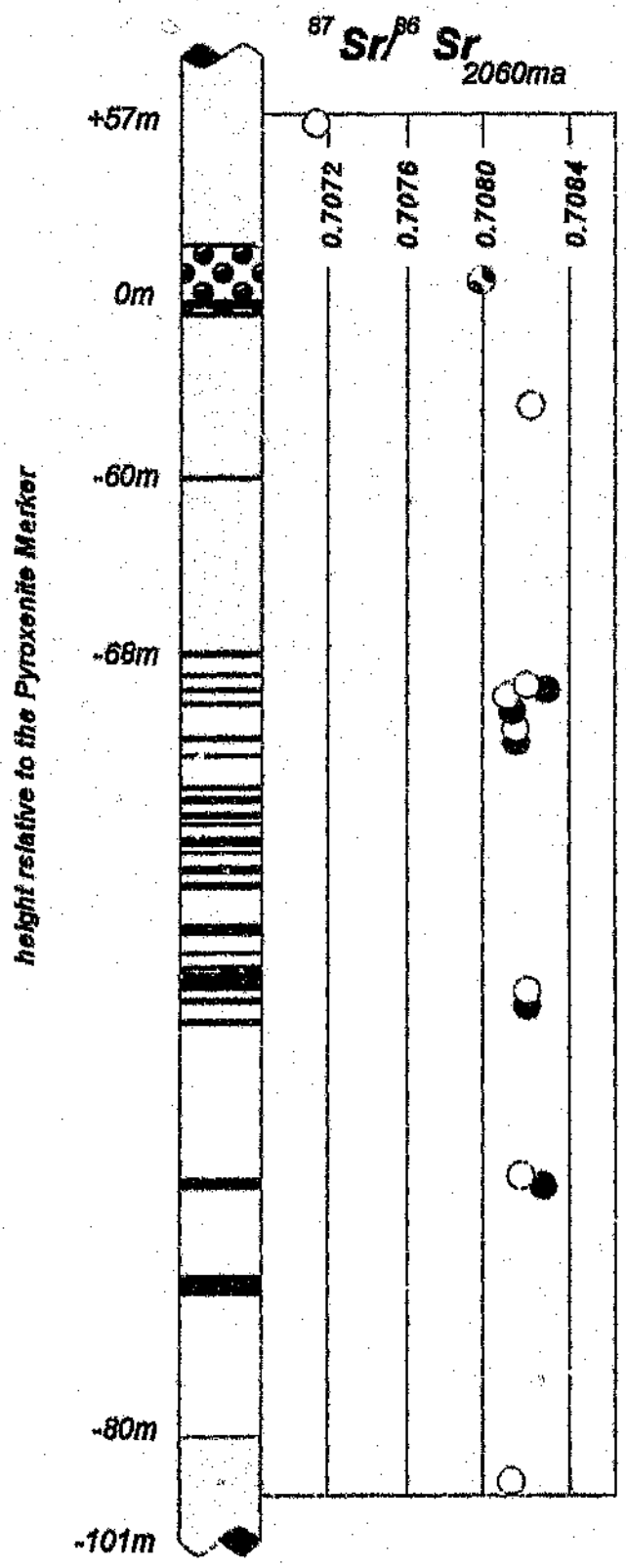


Figure 9.7 Vertical variation in the initial Sr-isotopic ratio. The symbol width reflects the approximate magnitude of analytical precision. Stippled-mafic; open-leucocratic; pale stipple-unlayered.

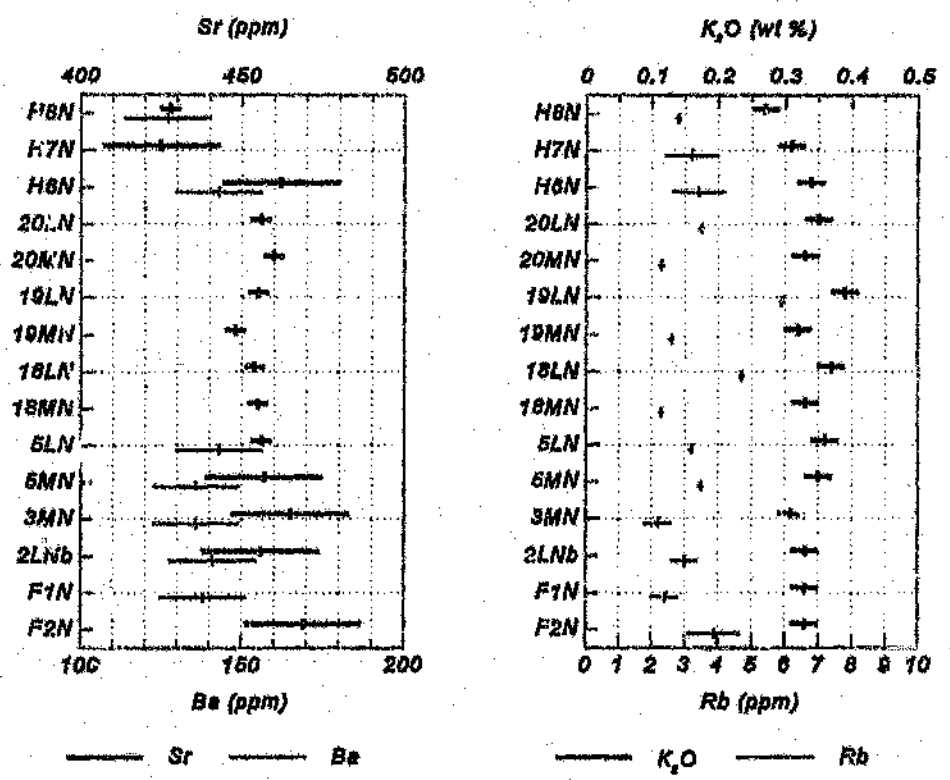


Figure 9.8 Variation in Ba, Rb, Sr and K_2O in selected plagioclase separates from profile A. Samples are in stratigraphic order but not to scale.

Table 9.5

Variation in Ba, Sr, Rb and K_2O in selected plagioclase separates from profile A samples. (Values determined by X.R.F. are in a normal typeface, those determined using I.N.A.A. are in bold and those measured by isotope dilution mass spectrometry are underlined. The errors for each method are listed at the bottom of the table.

sample	Ba	Sr	Rb	K_2O
Hangingwall samples				
H8N	**127**	<u>428</u>	<u>2.8</u>	0.27
H7N		425	3.2	0.31
H6N	**143**	462	3.4	0.34
Samples from the Layered Marker Sequence				
20LN		<u>456</u>	<u>3.5</u>	0.35
20MN		<u>460</u>	<u>2.3</u>	0.33

Table 9.5

Variation in Ba, Sr, Rb and K_2O in selected plagioclase separates from profile A samples. (Values determined by X.R.F. are in a normal typeface, those determined using I.N.A.A. are in bold and those measured by isotope dilution mass spectrometry are underlined. The errors for each method are listed at the bottom of the table.

19LN		<u>455</u>	<u>5.9</u>	0.39
19MN		<u>448</u>	<u>2.6</u>	0.32
18LN		<u>454</u>	<u>4.7</u>	0.37
18MN		<u>455</u>	<u>2.3</u>	0.33
5LN	143	456	<u>3.2</u>	0.36
5MN	136	457	3.5	0.35
3MN	136	465	2.2	0.31
2LNb	141	456	3.0	0.33
Footwall samples				
F1N	138		2.4	0.33
F2N		469	3.9	0.33
Analytical errors				
1σ(X.R.F.)		18	0.8	0.02
2σ(I.N.A.A.)	13.4		0.4	
<u>2σ(I.D.)</u>		<u>3</u>	<u>0.1</u>	

10. Discussion

10.1 Review of salient aspects

10.1.1 Field relations

The Layered Marker Sequence can be followed for at least 80km in the eastern limb of the Bushveld complex. This in itself suggests that the processes producing the layering had a widespread sphere of influence. The sequence is made up of a series of melanocratic and leucocratic layers. The individual layers are normally 10's of centimetres thick whilst the whole package varies from 2 to 20 metres thick. In contrast the layers themselves can only be followed for tens of metres before pinching out (Fig. 2.8). The melanocratic layers pinch out more frequently. The morphology show by the lateral layer terminations (Fig. 2 ould be suggestive of an erosional environment in which melanocratic material was deposited : equivalent of sand bars in a fluvial environment and occasionally eroded where the current activity was focussed. The leucocratic material may then have been deposited, infilling and covering melanocratic bedload.

There is no systematic relationship between melanocratic and leucocratic layer thicknesses. This is consistent with the idea that there was lateral migration of mineral grains. Therefore if the melanocratic and leucocratic layers represent the deposits of two distinctly different flow events then the former may not have flowed consistently as far into the chamber as the latter. The fact that the melanocratic layers comprise less of the package (refer to figures 2.3 to 2.6) towards profiles B and A, when compared to profile C and in particular profile D, may suggest that these localities were closer to the source of the density current.

10.1.2 Petrography

The mineralogy of these rocks is dominated by low-calcium pyroxene, clinopyroxene and plagioclase. The plagioclase is cumulus in all but the most melanocratic samples. The pyroxenes also appear cumulus in all but the anorthositic layers. Magnetite occurs, as an accessory phase, as either euhedral crystals on the boundaries of grains or incl[illegible] with them. There is a wide range of modal abundances, with rocks varying from felspathic pyroxenite to anorthosite. There is also a progressive increase in the modal contrast between adjacent layers towards the top of the Layered Marker Sequence.

The two pyroxene phases occur in approximately the same relative modal proportions.

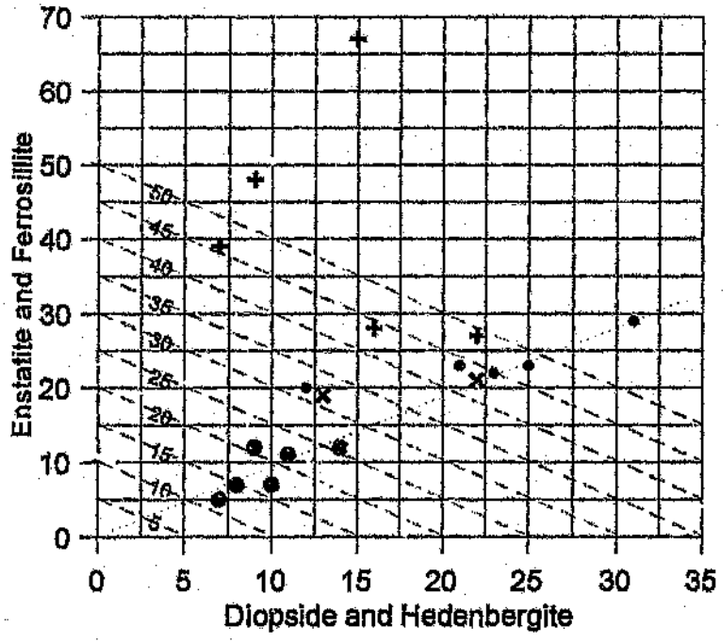


Figure 10.1 Variation in the clinopyroxene and low-calcium pyroxene abundance in selected whole rock samples as measured using a CIPW normalization calculation. The pluses refer to the hangingwall samples, crosses to the footwall samples, large filled circles to leucocratic samples and the smaller filled circles to the melanocratic samples. The weight percent of total pyroxene is shown by the numbered diagonal lines.

Normative proportions based on the geochemical whole-rock analyses provide a reliable check on the modal concentrations of phases within these rocks. Table 10.1 lists the results of a CIPW normalization for whole-rock samples from one profile analysed by XRF. Included in this table are the modal abundances as calculated from point counting measurements. Fig. 10.1 shows the relative abundances of the pyroxene phases as calculated by means of the CIPW norm. The plagioclase varies significantly in its abundance whilst the two pyroxenes, which have similar densities, do not vary much in their relative proportions in the Layered Marker Sequence. This fact would appear to support the idea of a mechanical separation of phases as the difference between these layers, in terms of mode, appears to be primarily in plagioclase abundance, the density of which is significantly less than that of the other phases. However above the Layered Marker there is a very distinct increase in the ratio of low-calcium pyroxene to clinopyroxene. These layers do not appear to be significantly graded. This can be seen in outcrop (plate 2.1) and has been confirmed by specific gravity determinations for numerous samples taken from various positions within individual layers (Table 4.2). This non-graded characteristic is difficult to reconcile with a model involving the mechanical separation of phases since this process normally produces graded layering.

There is a distinct break in the total pyroxene content, between 30 and 40% (Fig. 10.1), which approximates to the expected cotectic proportions of pyroxene to plagioclase. This feature also suggests that mechanical separation of phases has occurred.

Table 10.1
CIPW normalized abundances for selected samples from Profile B. The figures in brackets refer to point counting measurements.

	Sample No.	An+Ab	Di+Hed	En+Fs
Hangingwall samples	H12S	47 (60)	22 (8)	27 (32)
	H11S	40 (64)	9 (7)	48 (29)
	H10S	16 (14)	15 (10)	67 (75)
	H9S	53 (53)	7 (5)	39 (42)
	H7S	52 (57)	16 (23)	28 (20)
Layered Marker Sequence samples	23LS	85 (95)	7 (0)	5 (5)
	23MS	36 (53)	31 (30)	29 (17)
	19MS	65 (44)	12 (34)	20 (23)
	6LS	81 (92)	8 (3)	7 (5)
	6MS	54 (48)	21 (30)	23 (22)
	5LS	79 (77)	10 (14)	7 (9)
	4LS	76 (84)	9 (7)	12 (9)
	4MS	48 (31)	25 (36)	23 (34)
	3LS	75 (81)	11 (9)	11 (11)
	3MS	50 (61)	23 (25)	22 (14)
	2LS	69 (85)	14 (6)	12 (8)
footwall samples	F1S	54 (68)	22 (17)	21 (15)
	F2S	61 (68)	13 (15)	19 (17)

10.1.3 Petrofabrics

These rocks display a planar fabric which can be seen in hand specimen and in outcrop. This fabric is defined by the bedding parallel orientation of tabular plagioclase crystals. It can be seen in thin section (Fig. 5.1A) and has in certain instances been measured. The fabric is occasionally linear (Fig. 5.1B). This would tend to support the idea that a current may have been active. The fact that two orientations of linear fabric appear dominant, i.e. sub-parallel and sub-perpendicular to the dip (Fig. 5.2), suggests that some of the grains were flow orientated whilst others may have been transported as part of a traction load.

Grain size measurements were also undertaken on thin sections cut from the top and bottom contacts of certain layers. Fig. 5.3 diagrammatically illustrates the results of these measurements. It would appear that only towards the top of the sequence does the plagioclase grain size become significantly larger in the leucocratic as opposed to the melanocratic layers. In the melanocratic layers however these plagioclases are mostly interstitial and therefore these grain size

measurements cannot be used for comparison. However the plagioclase grain sizes in the leucocratic layers towards the top of the sequence are significantly larger than those in either the melanocratic or leucocratic layers closer to the base of the sequence.

10.1.4 Mineral chemistry

10.1.4.1 Plagioclase

The vertical variation in plagioclase composition is very small with most of the cores of grains being between An_{61} and An_{62}. Rims to cumulus phases may show reverse zoning. Towards the base of the sequence the plagioclase from the melanocratic layers is slightly enriched in anorthite compared to that from the neighbouring leucocratic layers, direct footwall and hangingwall samples. However, these variations are usually within the range of analytical uncertainty. For profile C however this variation is more pronounced (Fig. 6.4). Towards the top of the sequence, the plagioclase in the melanocratic layers is visibly interstitial and poor in anorthite in comparison to that from the neighbouring leucocratic rock units. This is an effect of the trapped liquid component (Barnes, 1988). The trend shown by the plagioclase towards the base of the sequence may be due to the fact that in the mafic layers the ratio of the mass of reverse zoned rim to cumulus (core) plagioclase will be greater than in the case of the leucocratic layer where there is vastly more cumulus plagioclase present. In this way we may expect the average plagioclase composition, as measured by the XRF analysis of separates, from the mafic layers to be more anorthite rich. There is no apparent change in plagioclase composition between profiles A, B and C.

10.1.4.2 Pyroxene

The pyroxene separates show a far greater range in major-element composition than plagioclase. The pyroxenes from the melanocratic layers are more magnesian than those from the leucocratic layers (Fig. 7.5). Those from the leucocratic layers are more Fe-rich, by 2% mg-number, in comparison to either the melanocratic layers or surrounding rocks. This trend can be ascribed to the trapped liquid shift effect. Pyroxenes from the leucocratic layers show a greater proportion of post-cumulus to cumulus material than in the melanocratic layers. Re-equilibration of Mg and Fe in the pyroxene produces a homogenous grain as seen in the microprobe analyses of these phases. The more melanocratic the layer, the closer the measured composition will be to that of the cumulus mineral. Since there is little cumulus pyroxene in the leucocratic layers, the mg-number of these pyroxenes should be lower than those from contiguous melanocratic layers. This trend can be seen (Fig. 10.2) in that the mg-number declines with decreasing pyroxene

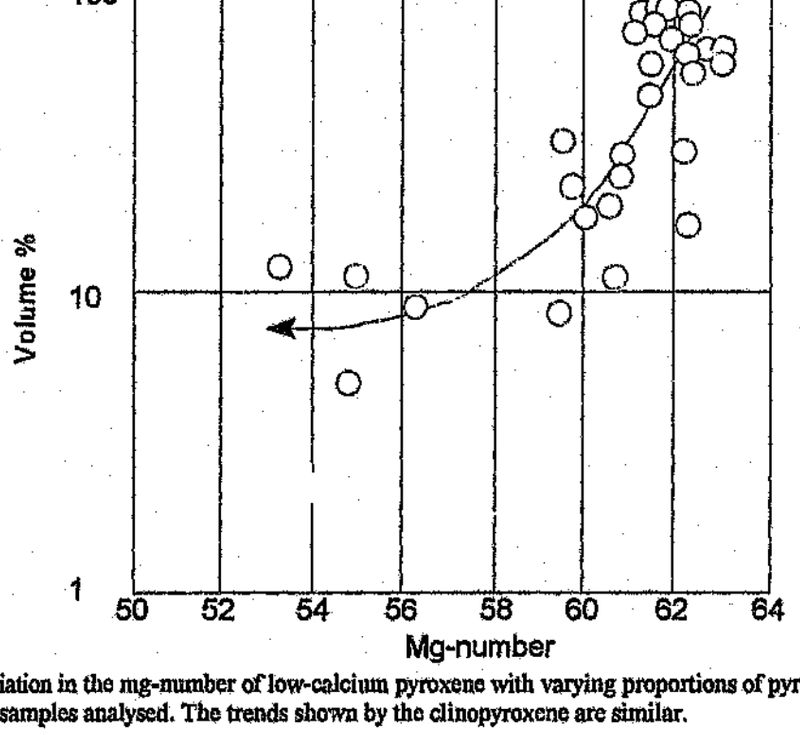


Figure 10.2 Variation in the mg-number of low-calcium pyroxene with varying proportions of pyroxene within the samples analysed. The trends shown by the clinopyroxene are similar.

content of the sample. For low-calcium pyroxene it changes from 63-59 as the modal proportions of pyroxene decrease to around 20%. Below 20% pyroxene content the pyroxenes are chemically distinctly interstitial. The clinopyroxene compositions show similar trends. This suggests that even when the rock contains only 20% pyroxene, the pyroxene is still chemically dominated by the cumulus component. Hence it can be inferred that the differences in present mg-number in the pyroxenes do not represent a primary feature but result from the presence of variable proportions of cumulus and intercumulus material.

10.1.4.3 Trace-element analysis of mineral separates

(a) Analysis by Instrumental Neutron Activation Analysis (INAA)

Individual mineral separates were analysed for a variety of rare earth elements (REE). The separates from the leucocratic samples are enriched in these elements compared to those from the melanocratic samples (Table 9.1) and therefore it might be inferred that the liquid from which the former mineral phases formed must have contained higher REE abundances. However this is an over-simplification and does not take into account the changes in the REE content of different phases due to the crystallization of the interstitial liquid. This principle is illustrated in the following simple example. (The principal investigated, in this section, has been taken from Cawthorn (in press))

Consider a liquid with 1 ppm Yb. Using crystal/liquid partition coefficients of 0.43 and 0.01 for clinopyroxene and plagioclase respectively, the two phases would contain 0.43 and 0.01 ppm Yb. Suppose these two minerals accumulated into two layers, one with 20% plagioclase and 60% clinopyroxene, the other with the proportions of plagioclase and pyroxene reversed and both with 20% trapped liquid. The bulk composition of the crystal mush (C_s) could be calculated using the following equation:

$$C_s=(0.01\times P_p+0.43\times P_c+1\times P_l)\times L \quad \ldots\ldots 1$$

where $P_{p,\ c\ and\ l}$ refer to the proportions of plagioclase, clinopyroxene and trapped liquid. L refers to the elemental concentration in the liquid. The melanocratic assemblage would then contain $(0.01\times0.2+0.43\times0.6+1\times0.2)\times1=0.46$ *ppm Yb* while in contrast the leucocratic assemblage would contain $(0.01\times0.6+0.43\times0.2+1\times0.2)\times1=0.292$ *ppm Yb*. For simplicity it will be assumed that the trapped liquid crystallizes an equal proportion of plagioclase and pyroxene. Therefore the two assemblages will contain 70 and 30% of the two minerals once the trapped liquid has crystallized. The final composition (R) can be written as:

$$R=C_p^*\times P_p+C_c^*\times P_c \quad \ldots\ldots 2$$

where C_p^* and C_c^* are the concentrations of Yb in plagioclase and clinopyroxene within the solid. The relative concentrations of Yb between clinopyroxene and plagioclase is proportional to their partition coefficients, i.e. 0.43/0.01 or 43 and therefore $C_c^*=43\times C_p^*$, which when substituted into equation 2 gives the following expression:

$$R=C_p^*\times P_p+43\times C_p^*\times P_c \quad \ldots\ldots 3$$

For the melanocratic assemblage the composition of the re-equilibrated plagioclase is given by:

$0.46=C_p^*\times0.3+43\times C_p^*\times0.7 \Rightarrow C_p^*=\frac{0.46}{(0.3+43\times0.7)}=0.015$ *ppm*. For the leucocratic assemblage however: $0.292=C_p^*\times0.7+43\times C_p^*\times0.3 \Rightarrow C_p^*=\frac{0.292}{(0.7+43\times0.3)}=0.021$ *ppm*.

It follows therefore that the clinopyroxene in the melanocratic and leucocratic rocks will have 0.65 and 0.90 ppm Yb respectively. This simplified example shows that it is possible for the final plagioclase in the two rocks to contain different proportions of Yb, even though the cumulus compositions and the proportion of trapped liquid were the same. Therefore the observed mineral concentrations may be higher in the leucocratic layers as opposed to the melanocratic layers, but still have formed from the same magma. If the proportion of trapped liquid is allowed to vary, further changes in the concentrations in the minerals can be predicted. It is also important to note that the actual minerals in this example contain in the order of 50% more Yb (0.015 ppm versus

0.01 ppm for plagioclase) than the initial cumulus phases and so there would be an error of 33% encountered if the liquid composition was calculated by dividing the concentration in the mineral by its partition coefficient.

It is now necessary to show quantitatively whether the difference in analysed mineral compositions can be the result of this effect. In this endeavour it is necessary to calculate an appropriate liquid for use in further modelling. In the following calculations it will be assumed that the trapped liquid will crystallize 50% plagioclase and 25% of each of the two pyroxenes. The whole-rock composition can be determined from the mode using the following equation:

$$C_s=(P_c-\frac{T}{4})\times D_c\times C_l+(P_o-\frac{T}{4})\times D_o\times C_l+(P_p-\frac{T}{2})\times D_p\times C_l+T\times C_l \quad \ldots\ldots\ldots\ldots\ldots\ldots 4$$

where $P_{c,\ o\ and\ p}$ refer to the modal proportions of clinopyroxene, low calcium pyroxene and plagioclase measured, $D_{c,\ o\ and\ p}$ are partition coefficients and T is the proportion of trapped liquid. Equation 4 can be rearranged as follows:

$$C_l=\frac{C_s}{(P_c-\frac{T}{4})\times D_c+(P_o-\frac{T}{4})\times D_o+(P_p-\frac{T}{2})\times D_p+T} \quad \ldots\ldots\ldots\ldots\ldots\ldots 5$$

Figure 10.3 shows the chondrite normalized REE compositions of the liquids calculated, using equation 5, to be in equilibrium with each sample. This assumes a constant trapped liquid content of 10%. Note that while many researches have tried to determine partitions for the REE (Frey, 1978, Mc Kay (1986 and 1989), McKay et al. (1986), Johnson (1989), Nielsen et al. (1992) and Hart and Dunn (1993) etc) it is very difficult to get an internally consistent set of values to use in modelling. This is because the coefficients are highly variable depending on a whole range of other variables such as magma composition. Therefore it was decided to use those values presented by Hart and Dunn (1993) and Irving (1978), for clinopyroxene. The coefficients for the low-calcium pyroxene and plagioclase are calculated from the relative abundances of REE between these phases and clinopyroxene. The partition coefficients used in these calculations are listed in table 10.2.

Table 10.2
Crystal/melt partition coefficients for selected REE. Values for clinopyroxene for La, Nd, Sm and Yb have been taken from Hart and Dunn (1993) and those for Ce, Eu, Tb and Ho from Irving (1978)

	La	Ce	Nd	Sm	Eu	Tb	Ho	Yb
Cpx	0.05	0.10	0.19	0.29	0.30	0.35	0.40	0.43
Opx	0.01	0.01	0.02	0.02	0.13	0.04	0.05	0.15
Plag	0.08	0.05	0.02	0.02	0.34	0.01	0.01	0.01

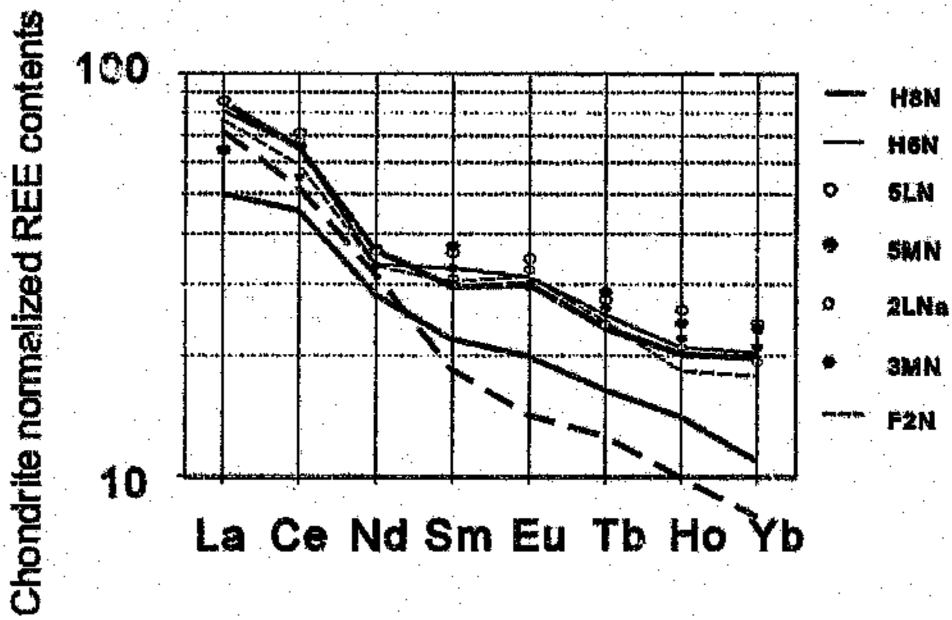


Figure 10.3 Abundance of selected REE in liquids in equilibrium with each sample. In calculating these values 10% trapped liquid has been assumed. The thick solid (green) line represents the top envelope of the compositional range for marginal rocks of the upper critical zone, as determined by Harmer and Sharpe, (1985). The thick dashed (purple) line defines the top envelope of the compositional range for 'B1-type' marginal rocks and sills, including pyroxenites and norites (Harmer and Sharpe, 1985). Note that a greater proportion of trapped liquid would push the calculated curves, for samples from the Layered Marker Sequence, to lower abundances.

It is fair to assume that if one liquid was responsible for all the rock types of the Layered Marker Sequence then this liquid might be similar to that which produced the direct footwall sample. Therefore the liquid calculated to be in equilibrium with this footwall sample (F2N) has been assumed to have been the parent liquid (C_l) in the calculations that follow. The calculated compositions of this liquid is listed in Table 10.3.

Table 10.3
Composition of liquid calculated as having been in equilibrium with the footwall sample (F2N). 10% trapped liquid was assumed.

	La	Ce	Nd	Sm	Eu	Tb	Ho	Yb
Chondrite normalized abundances	76.60	59.27	33.20	30.37	31.41	24.30	18.32	17.82

The composition of the solid rock crystallized from the magma can be expressed as follows:

$$C_s = P_c \times C_c^* + P_o \times C_o^* + P_p \times C_p^* \quad \text{.......} \quad 6$$

$C^*_{c,o,p}$ refer to the composition of clinopyroxene, low-calcium pyroxene and plagioclase in the

solid. Assuming that $C_c^* = C_p^* \times \left(\frac{D_c}{D_p}\right)$ and $C_o^* = C_p^* \times \left(\frac{D_o}{D_p}\right)$, equation 5 and 6 can be combined and solved for the C_p^* (the composition of the plagioclase in the whole-rock sample) giving the following equation:

$$C_p^* = \frac{(P_c - \frac{T}{4}) \times D_c \times C_l + (P_o - \frac{T}{4}) \times D_o \times C_l + (P_p - \frac{T}{2}) \times D_p \times C_l + T \times C_l}{P_c \times \frac{D_c}{D_p} + P_o \times \frac{D_o}{D_o} + P_p} \quad \ldots\ldots\ldots\ldots\ldots\ldots\ldots\ldots\ldots\ldots\ldots\ldots 7$$

Using equation 7 it is possible to calculate what composition of plagioclase, for each sample from the Layered Marker Sequence, would have crystallized assuming a constant parent liquid, equivalent to that calculated to be in equilibrium with the footwall sample, based on the observed mineral proportions. The results of this modelling are presented in Table 10.4 along with the actual values measured by INAA (in the shaded columns). The proportion of trapped liquid used to calculate mineral compositions for each sample is also shown.

Table 10.4

Calculated mineral compositions (in ppm) for each sample assuming that the liquid, which produced each layer, was similar to that which produced the footwall samples. The actual values measured are listed in the shaded columns.

Plagioclase compositions

	La		Ce		Nd		Sm		Eu		Tb		Ho		Yb		T (%)
5LN	4.20	4.21	7.63	7.49	1.26	1.30	0.21	0.20	0.80	0.88	0.03	0.03	0.03	0.04	0.06	0.08	11.5
5MN	3.63	3.64	5.85	5.34	0.73	1.00	0.12	0.17	0.75	0.79	0.02	0.02	0.02	BD	0.04	0.08	7.4
3MN	3.63	3.59	5.85	6.10	0.73	1.14	0.12	0.15	0.75	0.81	0.02	0.02	0.02	0.03	0.04	BD	7.4
2LNa	4.01	4.02	7.35	6.81	1.25	1.20	0.21	0.18	0.80	0.01	0.03	0.03	0.03	0.03	0.06	0.07	11.7
F2N	3.79	3.80	6.64	6.19	0.98	0.99	0.16	0.15	0.78	0.81	0.02	0.02	0.02	[illegible]	0.05	BD	10.0

Low-calcium pyroxene

F2N	0.49	0.37	1.32		0.65		0.19	0.15	0.29	0.26	0.06	0.03	0.09	0.09	0.74	0.75	

Clinopyroxene compositions

F2N	2.41	2.45	9.20	11.21	7.40	7.77	2.90	2.94	0.68	0.61	0.62	0.63	0.75	0.81	2.10	2.21	

BD= below detection

In equation 6 an assumption was made that $C_c^* = C_p^* \times \left(\frac{D_c}{D_p}\right)$ and $C_o^* = C_p^* \times \left(\frac{D_o}{D_p}\right)$. These assumptions are only valid if the minerals are in equilibrium. The composition of the clinopyroxene and low-calcium pyroxenes can be calculated, from the plagioclase composition, by means of these equations. It then follows that if the calculated values agree well with the measured values then these assumptions are valid and the mineral phases within these rocks were in chemical equilibrium when they formed. This has been done and the results for the footwall sample are listed in Table 10.4. There is good agreement for all elements other than Ce and Nd in low-calcium pyroxene. Note that for the low-calcium pyroxene there should have been approximately 1.32 and 0.65 ppm

of Ce and La within this separate, instead of which no peak was registered, for either element, for any of the low-calcium pyroxene separates analysed. This is almost certainly an analytical error.

From Table 10.4 it can be seen that the calculated plagioclase compositions are very similar to those actually determined by the analytical technique. This therefore shows quantitatively that one magma could have been responsible for these samples from the Layered Marker Sequence. It also shows that the differences in the composition of the phases, in the different rock types, has been amplified by differing proportions of trapped liquid with the leucocratic samples containing marginally more trapped liquid than the melanocratic samples.

As the REEs are highly incompatible these calculations are extremely sensitive to the proportion of trapped liquid present in each sample. The fact that the liquid calculated to be in equilibrium with each sample are not the same (Fig. 10.3) is due to the presence of this trapped liquid component, into which the rare earth elements partition strongly. However modal variations have a very much smaller influence on the results as shown in the Table 10.5.

Table 10.5

Variation in the calculated liquid and plagioclase compositions in response to a 10% decrease in plagioclase mode and a 5% increase in the abundance of each pyroxene phases. All values represent averages of calculated values for the Layered Marker Sequence samples. Subscript o refers to the initial condition and subscript m to the modified data. The modes are listed in % plagioclase and the other calculated data in ppm of the listed element.

	La	Ce	Nd	Sm	Eu	Tb	Ho	Yb
average modes for plagioclase in the Layered Marker Sequence samples analysed								
$Mode_o$	53%	53%	53%	53%	53%	53%	53%	53%
$Mode_m$	43%	43%	43%	43%	43%	43%	43%	43%
average liquid compositions calculated to be in equilibrium with the calculated average rock sample								
$Liquid_o$	18.85	42.68	17.25	5.37	1.85	1.01	1.33	3.55
$Liquid_m$	23.19	58.84	26.96	8.29	1.94	1.50	1.92	4.97
change	4.35	16.16	9.72	2.92	0.09	0.49	0.59	1.32
average calculated plagioclase compositions within this average sample								
$Plag_o$	3.87	6.67	0.99	0.16	0.78	0.02	0.02	0.05
$Plag_m$	3.76	6.82	0.95	0.16	0.74	0.02	0.02	0.05
change	0.11	0.21	0.16	0.03	0.04	0.00	0.00	0.01

The plagioclase separates were analysed for Rb, using isotope dilution mass spectrometry. This was done primarily to determine the Sr-isotopic signature of the plagioclase separates from the Layered Marker Sequence. The Rb values are listed in Table 10.6. If a constant proportion of trapped liquid is assumed, with 10ppm Rb in the liquid and partition coefficients into plagioclase, low calcium pyroxene and clinopyroxene, of 0.2, 0.02 and 0.05 respectively, then the calculated plagioclase compositions (using equation 5) are inconsistent with the actual compositions (Table

10.6). In order to match the observed analyses with those calculated, variable trapped liquid contents need to be assumed as shown in Table 10.6. It does however require unrealistic proportions of trapped liquid in a few samples to account for some of the plagioclase compositions. Isotope dilution mass spectrometry does however utilize a very small amount of sample (~50mg) and therefore it is feasible that in certain cases a greater than average proportion of interstitial material might have been analysed. This material would therefore be highly enriched in Rb. The abundances of Rb in plagioclase does however require that the proportion of trapped liquid in the leucocratic layers must have been larger than for the melanocratic layers. It also appears possible that differences in trapped liquid content, between layers types, was increasing towards the top of the sequence in line with varying modal contrasts.

Table 10.6
Calculated Rb abundances in plagioclase (C_p^*) and the whole rock sample (C_s) with differing proportions of trapped liquid (calculated using equation 5) compared to the actual measured abundances.

	Analysed plagioclase compositions	T	C_p^*	C_s	T	C_p^*	C_s
20LN	3.52	10%	2.98	2.68	16%	3.53	3.18
20MN	2.34	10%	4.98	1.47	2%	2.45	0.72
19LN	5.90	10%	2.90	2.90	43%	5.85	5.76
19MN	2.64	10%	4.13	1.71	3%	2.64	1.09
18LN	4.74	10%	2.98	2.68	28%	4.75	4.27
18MN	2.26	10%	3.92	1.80	2%	2.29	1.05
5LN	3.19	10%	3.26	2.28	10%	3.26	2.28
3MN	3.49	10%	3.89	1.85	8%	3.45	1.68
2LNa	3.02	10%	3.05	2.56	10%	3.05	2.56

(b) Sr-isotopes

The Sr-isotopic ratios do not vary significantly until above the Pyroxenite Marker level. At this level the ratio decreases (Fig. 9.8). Numerous determinations for single layers (several samples were taken from various positions both vertically and laterally within a single layer to determine whether there was any heterogeneity in the isotopic signature within a layer) also yielded no significant change. Therefore it appears that the plagioclase, in the samples from the Layered Marker Sequence, came from the same magma.

10.1.5 Whole-rock chemistry as determined by XRF analysis

Selected whole-rock samples from profile B were analysed by XRF for major and trace elements (Table 8.1).

The compatible major and trace elements vary significantly in their abundances. However these variations can be directly related to modal variations (Figures 8.2-8.4 and 8.7-8.9). The insignificant variation in relative modal abundances, of pyroxene phases, between samples, for the Layered Marker Sequence, results in linear trends in compatible element binary plots. Above the Layered Marker Sequence the rocks are richer in low-calcium pyroxene and therefore these samples plot on a separate trend from those from the marker itself.

Several of the compatible trace elements are significantly enriched above the Layered Marker Sequence relative to the footwall. For most of the elements this enrichment is of a magnitude that could have been explained by modal variations alone. However, in the case of Cr, the abundances are markedly enriched above the Layered Marker Sequence and this cannot be explained in the same way. However above the Pyroxene Marker a new more primitive magma was crystallizing. It is plausible that the new magma was intruded and plumed to the top of the chamber whilst the Layered Marker Sequence was being crystallized. In this case it is also plausible that, that magma may have started crystallizing whilst the hangingwall sequence to the Layered Marker Sequence was being formed. Therefore it is possible that the pyroxenes crystallizing from the new more mafic liquid may have settled through the interface between the two magmas, prior to their mixing. This may explain the elevated levels of many of the compatibles, especially Cr. It may also explain the apparent reversal in pyroxene major element composition towards the Pyroxenite Marker (Fig. 7.4).

Ni and Co have been analysed in mineral separates and therefore the partition coefficients for these elements into the different phases can be calculated (Table 10.7). These two elements vary linearly, with respect to the modes, in the whole-rock samples. It is possible to calculate whether a single liquid could have produced these layers, using the Ni and Co abundances in the whole-rock samples, in a similar way as in the case of the REE. However in this instance, since these elements are highly compatible into two of the three cumulus phases, the trapped liquid effect is likely to be far less. The liquid that produced the direct footwall sample may have been similar to that which produced the Layered Marker Sequence rocks. The composition of this liquid can be calculated using equation 5. Assuming that this liquid was responsible for all the rock types from the Layered Marker Sequence the composition of the solid rock forming from the accumulation of crystal phases crystallization out of this magma can be calculated using equation 4. The results of this modelling exercise are presented in Table 10.7. From this table it can be seen that the liquid

which produced the direct footwall sample could also have produced the melanocratic and leucocratic rock types of the Layered Marker Sequence.

Table 10.7

Calculated Ni and Co abundances in the solid rock ,(using equation 4) assuming the composition of the liquid is as calculated for sample F2S (using equation 5), compared to the actual measured concentrations. The partition coefficients listed have been calculated from those presented by Frey (1981) for cpx as the abundances of these two elements within certain mineral separates is known.

	Ni	Co	Cs (Ni)	Cs (Co)
23LS	29	15	27	10
23MS	167	73	167	64
19MS	88	34	91	35
6LS	39	17	38	15
6MS	112	45	122	47
5LS	40	20	43	17
4LS	50	22	57	22
4MS	133	56	131	51
3LS	56	24	58	23
3MS	128	50	123	48
2LS	70	27	71	27
F2S	119	46	119	46
	Ni partition coefficient		Co partition coefficient	
cpx	4.00		1.20	
opx	5.83		2.31	
plag.	0.07		0.02	

Cl (Ni)=59 and Cl(Co)=23ppm as calculated from F2S.

Incompatible elements are potentially more informative as their abundances are significantly less dependent on the modal variations. Incompatible trace elements analysed include Y, Nb, Zr, Rb, P and Ba. Y and Nb occur at levels below detection for the method employed. Zr occurs at around 20 ppm for rocks from profile B and 10 ppm for rocks from profile C. There is no apparent systematic variation in Zr between analysed melanocratic and leucocratic samples throughout either sequence. Rb, P and Ba do however show variations. The Rb in the melanocratic layers (refer Table 8.1 and 8.2) is higher than in the leucocratic layers. Given a uniform trapped liquid content, the reverse would be expected as plagioclase makes a significant contribution to total Rb in the whole-rock. The whole-rock thus requires that a greater proportion of trapped liquid be present in the melanocratic compared to the leucocratic layers. This is the converse of that inferred from the plagioclase compositional data (Table 10.6). In addition the fact that Ba, P and K_2O concentrations in the whole-rock samples (Table 8.1)show the converse trends would tend to support the idea that the Rb analyses in the whole-rock samples are in error.

Both Ba and P are incompatible into the whole rock (Ba, for example, whilst being more compatible into plagioclase, has a partition coefficient D_{plag}^{Ba} for basaltic/andesitic rocks ranging from 0.05-0.59 (Henderson, 1986)). P is enriched in the leucocratic layers (Fig. 8.5B). However the uncertainty associated with its analysis as a trace are quite large and this may explain the significant scatter in a plot of P versus mode (Fig. 8.5A). Interestingly enough the P, as with Zr, is only half as abundant for samples from profile C compared to those from profile B (Tables 8.1 and 8.2). This observation could suggest that the layers at profile C contained less trapped liquid that those at profile B. This may have resulted from more trapped liquid being expelled from the layers at profile C due to more efficient compaction as the proportion of melanocratic to leucocratic material at C is larger. Ba shows a very good linear variation with mode (Fig. 8.6), the slope of which might be more than can be explained by modal variation alone and could point to more trapped liquid in the leucocratic layers in a similar way as P appears to do. The good correlation show when Ba and P abundances are plotted against each other (Fig. 10.4) is further proof of this. More trapped liquid in the leucocratic layers could be the result of the deposition by way of two different flow types. The melanocratic layers may represent a well packed 'sediment', a deposited bedload, whilst the leucocratic layers may represent one that was initially a suspended load and was effectively dumped. The second type would invariably contain more interstitial space and therefore greater concentration of trapped liquid.

These results summarized thus far appear to be the most significant findings of this study. How they relate to models that have been suggested in the literature will be discussed below.

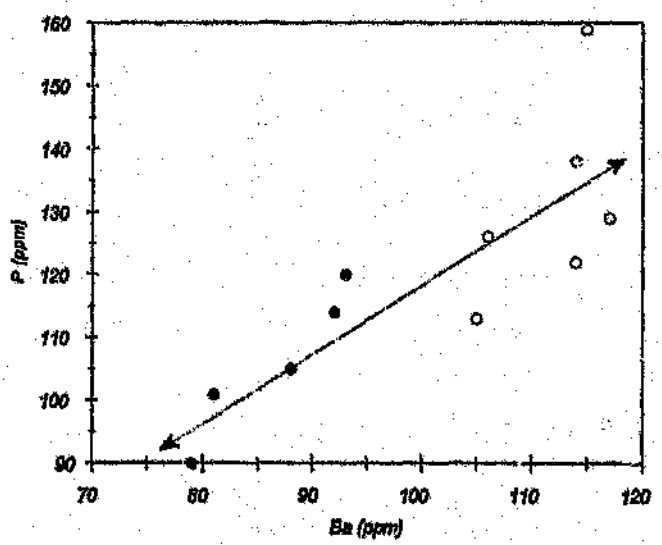


Figure 10.4 Ba versus P diagram for selected samples from profile B. The empty symbols refer to the leucocratic and the filled symbols to the melanocratic samples.

10.2 Models to explain the layering

Many layered intrusions display rhythmic/modal layering. This has intrigued many researchers. The mechanisms invoked by these different studies are relatively few. These include:

Mechanical separation of the phases

Different minerals have different specific gravities and this in conjunction with current activity may result in the differential rates of settling for the different minerals and therefore lead to modal layering.

In situ crystallization

It has been pointed out (McBirney and Noyes, 1979 & 1985) that due to viscosity and Newtonian strength of magmas, especially more differentiated ones, mineral grains may not be able to sink very efficiently. Therefore crystals may be forced to grow in situ and in so doing geochemical gradients might form in the magma, forcing the preferential growth of a single phase and thereby producing modal layering.

Rhythmic nucleation

Periodically supercooling of the liquid, below its liquidus, would produce rapid nucleation of whichever mineral was stable at that temperature (Maaloë, 1978). This could drive the liquid to oversaturation of another phase, and to induce oscillatory crystallization.

Change in pressure

As with temperature changes, pressure changes can influence the assemblage crystallizing (Cameron, 1980). Any variation in pressure would influence the relative stability of the minerals. These pressure changes can force the liquid off the cotectic and into the phase volume of one of the cumulus phases.

Magma mixing

It is a well known fact that when two magmas, of different compositions, mix, the new magma will occupy a new position in the phase diagram. Therefore the most likely result of magma mixing is the production of monominerallic layers.

Pattern formation

This process is driven by the surface area of grains. In essence all crystals that have formed

are in dynamic equilibrium with the magma. In this way material is continually dissolving from their crystal faces and reprecipitating. In addition a smaller crystal exposes a relatively larger surface area than does a larger grain. The smaller grain will have a higher surface energy and the difference will tend to allow the larger grain to grow at the expense of the smaller grains (Boudreau, 1987). Therefore there will be the diffusion of chemical components away from the unfavoured grains and towards the favoured grains. In addition it is suggested (Boudreau, 1987) that the surface energy between like minerals is lower than at contacts between different phases. This will result in the destruction of certain unfavourable grain contacts in favour of a more stable assemblage. Pattern formation is driven by a textural pattern that has developed within the developing crystal pile. This process might then develop this pattern and with the mass transfer of material produce modal layering.

The plausibility of these ideas as a means of producing the layering will be discussed below.

10.2.1 Pattern formation

This process will tend to allow the earlier formed crystals to grow preferentially compared to grains forming within the liquid subsequently, due to the relative differences in grain size and therefore in surface energies. This process was however proposed for inch-scale layering as these thermodynamic effects are only likely to occur over limited distances within the liquid. Pattern formation is therefore considered unlikely to work for layering that is considerably thicker. In the layered sequence under discussion the melanocratic layers vary from 1 to 56 cm and leucocratic layers from 0.5 to 116 cm in thickness. Layers also tend to vary in thickness laterally (Fig. 2.8) and occasionally split. However, some layers pinch out without splitting. Therefore, the length scales seen in this occurrence of modal layering do not appear to easily support this method of layering. As a post-cumulus process of sharpening the layer definition, this method may have considerably more merit (Boudreau, 1987).

In addition, if this method were to have played a key role in the formation of these layers, then we might expect a distinctly bimodal variation in grain size between layers, with the dominant phase having the larger grain size. Pyroxene grains were not studied, in this regard, as they often form oikiocrysts and the original grain boundaries are difficult to discriminate. Towards the base of the sequence plagioclase grains from the leucocratic and melanocratic layers vary very little in

average size (Table 5.1). Towards the top of the marker however differences in grain size are greater with the leucocratic layers containing some very large and melanocratic layers some very small grains. However the plagioclase in the melanocratic layers is distinctly interstitial and probably represents a significant proportion of trapped liquid crystallization. Therefore their grain sizes are not strictly comparable to those in the leucocratic layers. Therefore based on the grain size variations between layers from the bottom of the sequence, it appears as though the grain size is not varying markedly and systematically between layers. However there does appear to be an increase in grain size, of the cumulus plagioclase crystals, towards the top of the sequence.

On geochemical grounds the method of pattern formation has little merit since if the pyroxenes were forming by means of mass transfer of material we might expect them to have similar compositions throughout. As the melanocratic layers contain pyroxenes which are more magnesian than in the leucocratic layers (Fig. 7.5), there was obviously little chemical interaction between these layers, during the post-cumulus stage.

10.2.2 Chemical effects of a magma injection

It has been suggested from various studies of the complex that a new magma was introduced into the chamber at the level of the pyroxenite marker (von Gruenewaldt, 1973; Hamilton, 1977; Sharpe, 1985 and Cawthorn et al., 1991). As this marker occurs only ~60 m above the Layered Marker Sequence and in the light of the suggestion that mixing started below the Pyroxenite Marker within the western limb (Cawthorn et al., 1991), it would be tempting to try and link the layering to this new injection.

Compatible trace elements vary with modal abundances within each layer, but they do not define two different trends, for the different layer types. Geochemical modelling of both REE and selected compatible trace elements suggests that one magma was responsible for all the rock types present in the sequence. Plagioclase compositions are for the most part invariant and only show a significant change when the modal contrast between layers is at their most extreme. This trend shows that the compositional variance has been influenced strongly by the trapped liquid shift effect (Barnes, 1988). The pyroxene compositional variation is systematic and more well defined than that for plagioclase. However it too can be explained by the trapped liquid shift effect. Therefore by inference it appears that the cumulus mineral compositions, between layer types, may have been very similar. This is not conducive to any idea of another magma producing the layering event. The lack of significant systematic variation in the Sr-isotopic ratios between layer types points to one magma producing at least all the plagioclase in the different layers in

the ratio above the lowermost pyroxenite of the Pyroxenite Marker is in accordance with other studies and suggests that the new magma had no effect until some distance above the Layered Marker Sequence.

10.2.3 Change in a physical parameter

If the magma that intruded above the Pyroxenite Marker did so before or during the time the Layered Marker Sequence was forming, but plumed upwards to form a layer well above the floor without significantly mixing with the residual magma, then it is feasible that no immediate chemical influence need to have been recorded in the cumulates. However this process would mean that pressure was changing as batches of new magma were being pumped into the chamber. Such pressure changes could manifest themselves in two ways in the accumulating minerals. An increase in pressure would move the composition of the plagioclase-pyroxene cotectic towards higher plagioclase content, thus increasing the modal proportion of plagioclase crystallizing (Osborn, 1978). However, the range of plagioclase:pyroxene ratios observed is far too great to be the result of cotectic crystallization over any plausible range in crustal pressure. Secondly, any change in pressure would shift the cotectic, causing the liquid at the cotectic under the original pressure conditions, to find itself in the stability field of a single mineral (Cameron, 1980). Thus, the most likely effect of a pressure change would be to produce a monominerallic rock before reaching the cotectic under the new pressure conditions. As monominerallic rock types are not well represented in this marker sequence, such a model is not considered applicable. The occurrence of thick pyroxenites in the hangingwall to the marker could (Figures 2.3 and 2.4) however be the result of such pressure variations.

10.2.4 Rhythmic nucleation

The model of rhythmic nucleation is an appealing one and has been appealed to by numerous workers to explain modal layering (Komor and Elthon, 1990; Hort et al., 1993 and Maaloe, 1978). However there are several points from the present study that are difficult to reconcile with such a model. The most convincing of these is the grain size data. The grain size systematics conclusively show that an oscillatory mechanism by undercooling is unlikely to have resulted in the layering seen. With rhythmic nucleation the dominant mineral in each layer should have a smaller relative grain size (Brandeis et al., 1984) due to rapid nucleation of that phase. In addition theoretical modelling of thermal oscillation, which is the driving force of this process, as a method of explaining layering, has shown that this process can at best explain layering on the inch scale (Jaupart and Brandeis, 1986). Rapid growth, related to undercooling, ought to produce vertical

and not bedding-parallel alignment of plagioclase. This is clearly not seen (Fig. 5.1).

10.2.5 In situ crystallization

Campbell et al. (1978) showed convincingly that plagioclase is very unlikely to be denser than the liquid at any stage and would therefore not settle, unless it formed aggregates with other grains. McBirney and Noyes (1979 & 1985) used viscosity and Newtonian strength criteria to rule out settling as a significant method of layer formation. There have been studies of crystal settling in natural magmatic systems. Helz et al. (1989), studying the processes within a lava lake, could not demonstratibly show any accumulation of olivine by settling within the lake. Gibb and Henderson (1992), studying several sills, showed conclusively that in many of these sills settling did not take place. Therefore if the minerals cannot not settle then they must have grown in situ. Crystallization will occur primarily at the floor of the chamber due to the effects of pressure on the liquidus temperature. These authors suggested that layering may be the result of diffusion of components in the boundary layer. In this way magma may eventually become undersaturated with respect to a particular mineral at a certain height within the boundary layer and this would in turn inhibit its growth there.

The most convincing argument against this method in the formation of this layering is the planar and linear fabrics seen in these rocks. This suggests that a current may have been involved, which would have destroyed any diffusion gradient that might otherwise have developed. In addition with high to moderate degrees of undercooling a chemical gradient is likely to produce comb layering (Lofgren and Donaldson, 1975) with the cumulus minerals orientated at a high angle to the plane of layering. This is not seen for the cumulates under discussion.

10.2.6 The mechanical separation of minerals into different layers

Many igneous intrusions display pseudo-sedimentary structures, on the basis of which many researchers have tried to apply ideas of gravitational sorting and current activity to cumulate formation. Wager and Deer (1939) suggested that gravitational sorting may have been responsible for the layering seen in the Skaergaard intrusion. Conrad and Naslund (1989), studying layering of a similar type to that under discussion here, concurred with this idea. Their layered units were however internally graded unlike those being studied here.

A fundamental assumption that has to be made when applying such a model is that all the cumulus phases should be able to settle in the magma. In light of the viscosity of the magma some researchers believe that settling is unlikely to occur (McBirney and Noyes, 1985). In addition work

by Campbell et al. (1978) suggests that for the Skaergaard intrusion the plagioclase was never denser than the magma. Using experiments conducted in centrifuge furnaces Campbell et al. (1978) reported that plagioclase does not sink in basaltic magmas. However, this was for single crystals of plagioclase. Plagioclase does not nucleate readily and will tend to nucleate by heterogeneous nucleation. In other words the plagioclase crystals will tend to cluster. In Campbell et al.'s experiments whenever this happened, these clusters tended to sink. Therefore, particle size is important in the settling history. If individual grains are settling, however, then the layers will be grain-size graded.

10.2.5.1 Current activity

The rocks of the Layered Marker sequence all appear to show a planar and occasionally linear fabric. This might indicate the importance of a current. Two types of current are discussed in the literature, these being convection and density flows. Convection is driven by temperature differences that affect the density of a package of magma and force it to circulate. Density currents result in the movement of magma due to negative buoyancy produced by a greater load of crystals.

The presence of pseudo-sedimentary structures, such as crossbeds, in the Skaergaard intrusion, prompted researchers tc postulate that convection may have had a significant role to play in the deposition of the cumulates. Convection should occur in magma chambers due to significantly large Rayleigh numbers even in very slowly cooled magmas (Martin and Nokes, 1987). Experiments conducted by Martin et al. (1988) showed that settling can occur even in turbulently convecting magmas. However, the residence time for plagioclase in such magmas may be much larger than for pyroxenes. In all of their experiments the 'crystals' were denser than the liquid. One interesting aspect of this study is the realization that the presence of significant concentrations of particles within the magma will tend to dampen the turbulence of the convective system. Similar ideas have been expounded by Koyaguchi et al. (1990). Sparks et al. (1993) suggested a model whereby in very dilute suspensions, convection will produce a homogenous distribution of crystals. This is provided the convective velocity is in excess of the settling velocity. However with time a critical concentration will be reached at which stage the convection ceases and discrete settling events will occur. Different minerals/sizes will have different settling velocities and therefore it is feasible that complex changes in sedimentation rate and consequently in relative proportions of minerals can occur.

Some researchers do not support the idea that convection is an important process in a magma, especially in the middle of the chamber and long after the initial magma injection. Brandeis and

Marsh (1989) suggested the idea of a convective liquidus. This term describes a point at which convection ceases in a similar way to how the liquidus signifies a point at which the magma starts to crystallize. Therefore when the magma is intruded it has an amount of superheat inherent to it. As a result the liquid convects violently. However once the superheat has dissipated the convection stops and subsequent cooling is by convection alone. This point is defined by the convective liquidus and was established by experiments using paraffins heated from below. It is the considered opinion of these authors that the convective liquidus is close to the true liquidus in basaltic magmas. This idea of inefficient convection in a magma for most of their cooling histories was echoed by Marsh (1988, 1989a and 1989b).

However if a magma chamber is wider than it is deep, the most significant heat loss will be via the roof. This will produce a negative buoyancy of the boundary layer at the roof (Martin et al., 1987). It is an established fact that even temperature differences of only several degrees or crystal contents of a few percent can lead to substantial instability of the boundary layer (Sharpe et al., 1990). The result of such instability may produce density flows that may either plume down into the chamber from the roof (Jaupart and Brandeis, 1986) or flow down the sides of the chamber (Irvine, 1980). Such a layer might then be internally turbulent.

In light of the data presented it would appear that the following model, employing the physical separation of phases, might best explain the present occurrence of modal layering.

10.3 A depositional model for the formation of the marker

Convection and current activity in a magma is probably very sluggish (Marsh, 1988). Close to the boundary of the chamber heat losses are invariably faster than the magma can supply by conduction alone and current activity may well occur. However, the coolest parts of the boundary layer are kept immobile (Marsh, 1988). Within this boundary layer on the roof or sidewalls the magma was crystallizing plagioclase and two pyroxene phases in cotectic proportions. The boundary layer, being cooler and loaded with crystals, was denser than that further into the chamber and occasionally became unstable. It may then have periodically detached itself from the edges or roof of the chamber and flowed as a density current (Irvine, 1980). Initial turbulence, especially in the head of the current, would have kept the pyroxene buoyant. Flow of the magma would have lowerad its viscous yield strength making it more likely that the crystals could settle. The denser phases would have been deposited as a bedload in many elongate bars. Only material exceeding a bulk density could settle. This would have included a certain amount of trapped plagioclase. The flow became progressively unsteady as it decelerated due to the limited supply

of denser material (Leeder, 1982). The suspended material became concentrated towards the base of the flow. Hindered settling, buoyant lift provided by interstitial liquid, dispersive pressure (Lowe, 1982) and the yield strength of the magma (McBirney et al., 1979) supported the grains within the developing traction carpet. Eventually these forces could no longer support the growing weight of crystals and the suspended material was effectively dumped as a layer. The shearing contact between the bedload and the suspended load would subsequently have occurred at a higher level. Current activity could feasibly have eroded the melanocratic layers in areas (McBirney, 1979).

10.3.1 Observations which support such a model

The extensive development of the Layered Marker Sequence within the eastern limb of the complex requires a model that would have had a wide influence. If the magma could have become detached from the wall or roof of the intrusion due to its density and form a density current that rushed into the chamber laden with crystals, then this process is likely to have occurred right around the chamber walls It is likely that such a current would have deposited material evenly over the floor. The lateral discontinuity of the layers, both along strike (Fig. 2.8) and down dip (Fig. 2.10) may suggest the development of such elongate bars of denser material. Material deposition is likely to have occasionally been interrupted by scouring where the flow was more focussed. The occurrence of the en echelon terminations of successive melanocratic layers may point to this fact.

The sharply-defined layer boundaries are inconsistent with the normal depositional models but can best be explained by the model proposed here. The sharp layer contacts were the result of a physical boundary along which shearing occurred with the melanocratic material as a bedload and the leucocratic material suspended in the magma and flowing overhead. When the forces suspending the crystals within the traction carpet could no longer support the growing weight of crystals overhead, the shearing contact at the base of the carpet would effectively have jumped up to a new position and the leucocratic material beneath would have been dumped into place. No other model discussed previ y can be switched off as efficiently so as not to produce a graded contact.

The fact that the pyroxene phases occur in similar relative proportions in each layer, whilst the plagioclase, the lighter phase, varies significantly in its relative abundance, is also supportive of the proposed physical separation of phases. The fabrics in individual samples support the idea that a current was active. The increase in modal contrast towards the top of the sequence can be

ascribed to the effective increase in vigour of the system.

Compositions of the primary plagioclase and pyroxene phases are the same in all the layers. The fact that the leucocratic layers have been shown geochemically, to have more trapped liquid within them is also highly consistent with the model suggested as it is expected that the leucocratic layers should contain more interstitial space, as this sediment was dumped rapidly, unlike that in the melanocratic layers. Compatible trace elements vary significantly within the whole rock but these variations can be ascribed to modal variation. This is consistent with the idea that a chemical gradient had not developed due to the current activity. REE distribution within mineral separates appear to be reconciliable with the crystallization of all these layered rocks out of a similar magma. The Sr-isotopic systematics also appear to support one magma.

10.4 Conclusions

A wide variety of different types of data, pertaining to the interlayered sequence of melagabbronorite and leucogabbronorite that occurs tens of metres below the Pyroxenite Marker in the eastern limb of the complex, has been presented. These data have been tested against several processes that have been invoked by numerous researchers to explain modal layering in a variety of different layered complexes. It appears that the Layered Marker Sequence under discussion cannot adequately be explained by using models such as the in situ crystallization of phases, rhythmic nucleation employing oscillatory crystallization following undercooling, chemical perturbations resulting from the injection of a new magma, a change in pressure, or the mass transfer of material due to differences in grain surface energies.

The magma at the time of the layering formed precipitated two pyroxene phases and plagioclase. This crystallization took place primarily in a thin boundary layer, close to the edges of the intrusion. Periodically, as it was cooler and contained a greater load of crystals than the magma further into the chamber, this layer became detached from the roof and/or wall of the intrusion and flowed into the chamber as a density flow. The flowing of this magma would have lowered its viscous yield strength. The crystals were initially suspended in the magma due to its turbulence and the concentration of crystals was low. With time the pyroxenes were able to settle. However, physical trapping of plagioclase with more abundant pyroxene occurred. Only a specific density of material was capable of settling at any particular point. These melanocratic layers, were deposited in many elongate bars. Periodically these cumulates were eroded by scour channels. With time the flow became less steady. The plagioclase and some suspended pyroxene started to settle closer to the base of the flow, in this way the concentration of crystals in the flow directly

overlying the melanocratic bedload became higher. This would have dampened the turbulence of the system, thus further weakening one of the supportive mechanisms. With continual slowing down of the current, due to a limited supply of material from the source, the forces suspending the crystals (dispersive pressure, magma yield strength and upwelling magma) were no longer able to support the growing weight of crystals overhead and the shear contact between the melanocratic bedload and the suspended flow jumped up to a higher position. In this way the leucocratic layer was dumped into position below it.

This model appears to account for most of the data presented in this study and as a result is believed to have resulted in the formation of the Layered Melagabbronorite/Leucogabbronorite Marker sequence of the Main Zone, in the eastern compartment of the Bushveld Complex.

References

Abbey, S., (1978). U.S.G.S. II Revisited. Geostandards Newsletter, Vol. 2, No. 2, 141-146.

...ins, F.B., (1976). Pyroxenes of the Bushveld Intrusion, South Africa. J. Petrol., 10, 222-249.

Barnes, S.J., (1988). The effect of trapped liquid on cumulus mineral compositions in layered intrusions. Contrib. Mineral. Petrol., 93, 524-531.

Boudreau, A.E., (1987). Pattern formation during crystallization and the formation of fine-scale layering. In: Origins of igneous layering. Parsons, I. (Ed.), Reidel Dordrecht, Boston, 453-471.

Brandeis, G., Jaupart, C. and Allegre, C.J., (1984). Nucleation and crystal growth and the thermal regime of cooling magmas. J. Geophys. Res., 89, 10'61-101[illegible].

Brandeis, G. And Marsh, B.D., (1989). The convective liquidus in a solidifying magma chamber: a fluid dynamic investigation. Nature, 339, 613-61[illegible]

Brown, P.E., Chambers, A.D. and Beck[illegible] ...rge soft-sediment fold in the Lilloise Intrusion, East Greenland. In: Origins of ig[illegible] ...s, I. (Ed.), Reidel Dordrecht, Boston, 125-141.

Button, A., (1976). Stratigraphy and relations ... ...the Eastern Transvaal. Trans. Geol. Soc. S. Afr., 79, 3-12.

Cameron, E.N., (1980). Evolution of the Lower Critical Zone, central sector, Eastern Bushveld Complex, and its chromite deposits. Econ. Geol., 75, 845-971.

Campbell, I.H., Roeder, P.L. and Dixon, J.M., (1978). Plagioclase buoyancy in basaltic liquids as determined by a centrifuge furnace. Contrib. Mineral. Petrol., 67, 367-377.

Cawthorn, R.G. and Walsh, K.L., (1988). The use of phosphorous contents in yielding estimates of the proportion of trapped liquid in cumulates of the Upper Zone of the Bushveld Complex. Mineral. Mag., 52, 81-89.

Cawthorn, R.G., Meyer, P.S. and Kruger, F.J., (1991). Major addition of magma at the Pyroxenite Marker in the Western Bushveld Complex, South Africa. J. Petrol., 32, 739-763.

Cawthorn, R.G., (in press). Incompatible element abundances in minerals in layered intrusions- the effect of re-equilibration with trapped liquid.

Conrad, M.E. and Naslund, H.R., (1989). Modally-graded rhythmic layering in the Skaergaard Intrusion. J. Petrol., 30, 251- 269.

Eales, H.V., De Klerk, W.J., Butcher, A.R. and Kruger, F.J., (1990). The cyclic unit beneath the UG1 chromite (UG1Fw unit) at RPM Union Section Platinum Mine- Rosetta Stone of the Bushveld Upper Critical Zone. Mineral. Mag., 54, 23-43.

Flanagan, F.J., (1973). 1972 values for international geochemical reference samples. Geochim. Cosmochim. Acta, 37, 1189-1200.

Frey, F.A., Green, D.H. and Roy, S.D., (1978). Integrated models of basalt petrogenesis: a study of quartz tholeiites to olivine melilites fro south eastern Australia utilizing geochemical and experimental petrological data. J. Petrol., 19, 463-513.

Gibb, F.G.F. and Henderson, C.M.B., (1992). Convection and crystal settling in sills. Contrib. Mineral. Petrol., 109, 538-545.

Hamilton, J.O., (1977). Sr-isotopic and trace element studies of the Great Dyke and Bushveld Mafic Phase and their relation to early proterozoic magma genesis in Southern Africa. J. Petrol., 18, 24-52.

Harmer, R.E. and Sharpe, M.R., (1985). Field relations and Strontium Isotope Systematics of the Marginal Rocks of the Eastern Bushveld Complex. Econ. Geol., 80, 813-837.

Harney, D.M.W., Merkle, R.K.W. and von Gruenewladt, G., (1990). Plagioclase composition in the Upper Zone, Eastern Bushveld Complex- Support for magma mixing at the Main Magnetite Layer. Institute for Geological Research on the Bushveld Complex, 87, 19pp.

Hart, S.R. and Dunn, T., (1993). Experimental cpx/melt partitioning of 24 trace elements. Contrib. Mineral. Petrol., 113, 1-8.

Helz, R.T., Kirschenbaum, H. And Marinenko, J.W., (1989). Diapiric transfer of melt in Kilauea Iki lava lake, Hawaii. A quick, efficient process of igneous differ ion. Geol. Soc. Amer. Bull., 101, 578-594.

Henderson, P.H., (1986). Inorganic Geochemistry. Pergamon Press, Oxford- New York- Toronto- Sydney- Frankfurt, 353pp

Hort, M., Marsh, B.D. and Spohn, T., (1993). Igneous layering through oscillatory nucleation and crystal settling in well-mixed magmas. Contrib. Mineral. Petrol., 114, 425-440.

Irvine, T.N., (1980). Magmatic density currents and cumulus processes. Amer. J. Sci., 280A, 1-58.

Irving, A.J., (1978). A review of experimental studies of crystal/liquid trace element partitioning. Geochim. Cosmochim. Acta, 42, 743-770.

Jaupart, C. and Brandeis, G., (1986). On the interaction between convection and crystallization in cooling magma chambers. In: Loper, D.E. (Ed.), Workshop on the structure and dynamics of partially solidified systems. Prog. And abst., Tallahasse, Fl: Geophysical Fluid Dynamic Institute, Florida State University, 26.

Johnson, K.T.M., (1989). Partitioning of REE, Ti, Zr, Hf and Nb between clinopyroxene and basaltic liquid: an ion microprobe study, EOS Trans. Am. Geophys. Union, 70, 1388.

Klein, C., Cornelius, S. And Hurlburt, JR., (1985). Manual of mineralogy. John Wiley and Sons, USA, 596pp

Klemm, D.D., Ketterer, S., Reichhardt, F., Steindl, J. And Weber Diefenbach, K., (1985). Implications of vertical and lateral compositional variations across the Pyroxenite Marker and its associated rocks in the Upper part of the Main Zone in the Eastern Bushveld Complex. Econ. Geol., 85, 877-883.

Komor, S.C. and Elthon, D., (1990). Formation of Anorthosite-Gabbro Rhythmic Phase Layering: An example at North Arm Mountain, Bay of Islands Ophiolite. J. Petrol., 31, 1-50.

Koyaguchi, T., Hallworth, M.A., Huppert, H.E. and Sparks, S.J., (1990). Sedimentation of particles from a convecting fluid. Nature, 343, 447-450.

Leeder, M.R., (1982). Sedimentology: Process and Product. Fletcher and Son, Norwich, 344pp.

Lofgren, G.E. and Donaldson, C.H., (1975). Curved branching crystals and differentiation in comb layered rocks. Contrib. Mineral. Petrol., 49, 309-319.

Lowe, D.R., (1982). Sediment gravity flows: II depositional models with special reference to the deposits of high density turbidity currents. J. Sed. Petrol., 52, 279-297.

Maaloë, S., (1978). The origin of rhythmic layering. Mineral. Mag. 42, 337-345.

Marais, L.C., (1977). An investigation of the Pyroxenite Marker and the associated rocks in the Main Zone of the Eastern Bushveld Complex. Msc Thesis (unpubl.), University of Pretoria, 87pp.

Marsh, B.D., (1988). Crystal capture, sorting, and retention in convecting magma. Geol. Soc. Amer. Bull., 100, 1720-1737.

Marsh, B.D., (1989a). Magma chambers. Ann. Rev. Earth. Planet. Sci., 17, 439-474.

Marsh, B.D., (1989b). On convective style and vigour in sheet-like magma chambers. J. Petrol., 30, 479-530.

Martin, D., Griffiths, R.W. and Campbell, I.H., (1987). Compositional and thermal convection in magma chambers. Contrib. Mineral. Petrol., 96, 465-475.

Martin, D. And Nokes, R., (1988). Crystal settling in a vigorously convecting magma chamber. Nature, 332, 534-536.

Mathison, C.I. and Booth, R.A., (1990). Macrorythmically layered gabbronorite in the Windimurra Gabbroid Complex, Western Australia, Lithos, 24, 171-180.

McBirney, A.R. and Noyes, R.M., (1979). Crystallization and layering of the Skaergaard Intrusion. J. Petrol. 20, 487-554.

McBirney, A.R., (1985). Further considerations of double-diffusive stratification and layering in the Skaergaard Intrusion. J. Petrol., 26, 993-1001.

McKay, G.A., (1986). Crystal/liquid partitioning of REE in basaltic systems: extreme fractionation of REE in olivine. Geochim. Cosmochim. Acta 50, 69-79.

Mckay, G.A., Wagstaff, J. And Yang, S-R, (1986). Clinopyroxene REE distribution coefficients for Shergottites: the REE content of the shergotty melt. Geochim. Cosmochim. Acta 50, 927-937.

McKay, G.A, (1989). Partitioning of rare earth elements between major silicate minerals and basaltic melts. In: Lipin, B.R. and McKay, G.A. (Eds.) Geochemistry and mineralogy of rare earth elements (Reviews in Mineralogy 21). Mineral Soc. Am., Washington, D.C., 45-78.

Mitchell, A.A., (1985). The petrology, mineralogy and geochemistry of the Main Zone of the Bushveld Complex at Rustenburg Platinum Mines, Union Section. Phd thesis, Rhodes University, Grahamstown.

Molyneux, T.G., (1974). A geochemical investigation of the Bushveld Complex in Sekhukhuneland and part of the Steelpoort Valley. Trans. Geol. Soc. S. Afr., 77, 329-338.

Nielsen, R.L., Gallahan, W.E. and Newberger, F., (1992). Experimentally determined mineral-melt partition coefficients for Sc, Y and REE for olivine, orthopyroxene, pigeonite, magnetite and ilmenite. Contrib. Mineral. Petrol. 110, 488-499.

Osborn, E.F., (1978). Changes in phase relations in response to change in pressure from 1 to 10 kbar for the system Mg_2SiO_4-iron oxide-$CaAl_2Si_2O_8$-SiO_2; Carnegie Inst. Washington Year Book 77, 784-790.

Parsons, I. (Ed.) (1987). Origins of igneous layering. Reidel Dordrecht, Boston, 666 p.

Pillay, P., (1990). A geochemical analysis of the Little Dwars River layered locality- Eastern Bushveld Igneous Complex. Bsc (Honours) Thesis (unpubl.), University of the Witwatersrand, 86pp.

Potts, P.J., Thorpe, O.W., Isaacs, M.C. and Wright, D.W., (1985). High-precision instrumental neutron-activation analysis of geological samples employing simultaneous counting with both planar and coaxial detectors. Chem. Geol., 48, 145-155.

South African Committee on Stratigraphy (SACS), (1980). (Compiler, L.E. Kent). Geol. Surv. S. Afr., Handbk. 8, 690pp.

Sharpe, M.R. and Snyman, J.A., (1980). A model for the emplacement of the Eastern Compartment of the Bushveld Complex. Tectonophysics, 65, 58-110.

Sharpe, M.R., (1981). The chronology of magma influxes to the Eastern Compartment of the Bushveld Complex as exemplified by its marginal groups. J. Geol. Soc. London, 138, 307-326.

Sharpe, M.R., (1985). Strontium isotope evidence for preserved density stratification in the Main Zone if the Bushveld Complex, South Africa. Nature, 316, 119-126.

Skoog, D. A., West, D.M. and Holler, F.J., (1988). Fundamentals of analytical chemistry. Saunders College Publishing, USA, 894pp.

Sparks, R.S.J. and Huppert, H.E., (1984). Density changes during the fractional crystallization of basaltic magmas: Fluid dynamical implications. Contrib. Mineral. Petrol., 85, 300-309.

Sparks, R.S.J. (1990). Crystal capture, sorting, and retention in convecting magma: Discussion and reply. Geol. Soc. Amer. Bull, 102, 847-850.

Sparks, R.S., Huppert, H.E., Koyaguchi, T. and Hallworth, M.A., (1993). Origin of modal and rhythmic igneous layering by sedimentation in a convecting magma chamber. Nature, 361, 246-249.

Wager, L.R. and Deer, W.A., (1939). Geological investigation in East Greenland: part III. The petrology of the Skaergaard Intrusion, Kargerdlugssuaq, East Greenland. Meddelelser om, Gonland, 105, 4, 343pp.

Walraven, F., Armstong, R.A. and Kruger, F.J., (1990). A chronostratigraphic framework for the north-central Kaapvaal craton, the Bushveld Complex and Vredefort structure. Tectonophysics, 171, 23-48.

Watkins, P.J. and Nolan, J., (1992). Determination of rare-earth elements, yttrium, scandium and hafnium using cation-exchange separation and inductively coupled plasma-atomic emission spectrometry. Chem. Geol., 95, 131-139.

Willemse, J., (1969). The geology of the Bushveld Igneous Complex, the largest repository of magmatic ore deposits in the world. Econ. Geol. Monog., 4, 187-208.

Wilson, J.R., Menuge, J.F., Pedersen, S. and Engell-Sørensen, O. (1987). In: Origins of igneous layering. Parsons I. (Ed.), Reidel Dordrecht, Boston, 145-184.

von Gruenewaldt, G., (1970). On the phase change orthopyroxene-pigeonite and the resulting textures in the Main and Upper Zones of the Bushveld Complex in the Eastern Transvaal. Trans. Geol. Soc. S. Afr., Spec. Publ. 1, 67-73.

von Gruenewaldt, G., (1971). A petrographic and mineralogical investigation of the rocks of the Bushveld Igneous Complex in the Tauteshoogte-Roossenekal area of the Eastern Transvaal. Dsc Thesis (unpubl.), University of Pretoria, 228p.

von Gruenewaldt, G., (1973). The main and Upper Zone of the Bushveld Complex. Trans. Geol. Soc. S. Afr., 71, 1324-1336.

von Gruenewaldt, G. and Weber-Diefenbach, K., (1977).Coexisting Ca-poor pyroxenes in the Main Zone of the Bushveld Complex. Contrib. Mineral. Petrol., 65, 11-18.

List of Appendices

Appendix 1 ..... XRF calibration standards

Appendix 2 ..... Rb calibration for isotope work

Appendix 3 ..... Modal data (volume %)

Appendix 4 ..... Error analysis

Appendix 5 ..... Derivation of plagioclase calibration curves

Appendix 6 ..... REE, Ni, Co and Sc analysis in mineral separates

Appendix 1 - XRF calibration standards

Major elements (wt %)

Fe_2O_3					
Standard	Std. Conc.	Cal. Conc.	Abs. Error	Rel. Error (%)	Corr. C.P.S.
NIM-G(A)	2.041	1.985	0.056	2.731	1204.4
NIM-N(A)	8.900	8.962	-0.062	-0.657	5081.7
NIM-P(A)	12.711	12.590	0.121	0.951	7098.0
NIM-D(A)	16.834	16.914	-0.080	-0.477	9501.2
NIM-S(A)	1.406	1.393	0.013	0.953	875.0
AN-G(A)	3.382	3.316	0.066	1.955	1943.9
AC-E(A)	2.545	2.806	-0.261	-10.258	1660.6
MA-N(A)	0.480	0.488	-0.008	-1.653	372.3
AGV-1(A)	6.884	6.846	0.038	0.547	3905.9
NIM-G/N(A)	5.488	5.463	0.025	0.452	3137.2
NIM-G(B)	2.036	1.975	0.061	3.009	1198.6
NIM-N(B)	8.916	8.986	-0.070	-0.786	5095.1
NIM-P(B)	12.729	12.667	0.062	0.491	7140.5
NIM-D(B)	16.834	16.922	-0.088	-0.524	9505.5
NIM-S(B)	1.406	1.413	-0.007	-0.522	886.6
AN-G(B)	3.379	3.348	0.031	0.919	1961.7
AC-E(B)	2.545	2.513	0.032	1.255	1497.7
MA-N(B)	0.479	0.437	0.042	8.687	344.2
AGV-1(B)	6.894	6.978	-0.084	-1.224	3979.3
NIM-G/N(B)	5.458	5.476	-0.018	-0.338	3144.6
NIM-G(C)	2.041	1.966	0.075	3.673	1193.7
NIM-N(C)	8.913	8.952	-0.039	-0.439	5076.2
NIM-P(C)	12.702	12.532	0.170	1.339	7065.7
NIM-D(C)	16.858	16.817	0.041	0.245	9446.9
NIM-S(C)	1.406	1.436	-0.030	-2.146	899.2
AN-G(C)	3.382	3.398	-0.016	-0.474	1989.3
AC-E(C)	2.543	2.541	0.002	0.072	1513.3
MA-N(C)	0.479	0.473	0.006	1.217	364.1
AGV-1(C)	6.892	6.904	-0.012	-0.172	3937.9
NIM-G/N(C)	5.498	5.563	-0.065	-1.177	3192.6
AV.ABS.ERROR IS		0.056	AV.REL ERROR IS		1.65
CALIBRATION SLOPE		0.1799E-02	BLANK CONCENTRATION		-0.182

Appendix 1 - XRF calibration standards

MnO					
Standard	Std. Conc.	Cal. Conc.	Abs. Error	Rel. Error (%)	Corr. C.P.S.
NIM-G(A)	0.021	0.015	0.006	29.712	44.0
NIM-N(A)	0.180	0.180	0.000	-0.025	67.8
NIM-P(A)	0.219	0.218	0.001	0.287	73.3
NIM-D(A)	0.218	0.216	0.002	0.849	72.9
NIM-S(A)	0.010	0.015	-0.005	-31.979	44.1
AN-G(A)	0.040	0.038	0.002	5.013	47.4
AC-E(A)	0.060	0.060	0.000	0.237	50.5
MA-N(A)	0.041	0.045	-0.004	-10.685	48.4
AGV-1(A)	0.092	0.103	-0.011	-12.300	56.7
NIM-G/N(A)	0.100	0.106	-0.006	-5.942	57.1
NIM-G(B)	0.021	0.019	0.002	7.903	44.7
NIM-N(B)	0.180	0.191	-0.011	-5.922	69.3
NIM-P(B)	0.219	0.224	-0.005	-2.312	74.1
NIM-D(B)	0.218	0.218	0.000	0.125	73.2
NIM-S(B)	0.010	0.009	0.001	12.905	43.2
AN-G(B)	0.040	0.050	-0.010	-24.158	49.0
AC-E(B)	0.060	0.059	0.001	1.685	50.4
MA-N(B)	0.041	0.038	0.003	7.214	47.4
AGV-1(B)	0.092	0.091	0.001	1.164	55.0
NIM-G/N(B)	0.100	0.095	0.005	5.140	55.5
NIM-G(C)	0.021	0.011	0.010	46.100	43.5
NIM-N(C)	0.180	0.177	0.003	1.803	67.7
NIM-P(C)	0.219	0.215	0.004	1.882	72.8
NIM-D(C)	0.219	0.207	0.012	5.545	71.6
NIM-S(C)	0.010	0.009	0.001	12.892	43.2
AN-G(C)	0.040	0.048	-0.008	-19.575	48.8
AC-E(C)	0.060	0.058	0.002	3.023	50.3
MA-N(C)	0.041	0.041	0.000	-0.122	47.8
AGV-1(C)	0.092	0.094	-0.002	-2.510	55.5
NIM-G/N(C)	0.100	0.094	0.006	6.078	55.4
AV.ABS.ERROR IS		0.004	AV.REL ERROR IS		9.50
CALIBRATION SLOPE		0.6970E-02	BLANK CONCENTRATION		-0.292

Appendix 1 - XRF calibration standards

TiO_2					
Standard	Std. Conc.	Cal. Conc.	Abs. Error	Rel. Error (%)	Corr. C.P.S.
NIM-G(A)	0.091	0.087	0.004	3.944	324.4
NIM-N(A)	0.200	0.182	0.018	9.155	410.2
NIM-P(A)	0.199	0.186	0.013	6.526	414.2
NIM-D(A)	0.020	0.021	-0.001	-3.167	263.6
NIM-S(A)	0.044	0.034	0.010	22.580	275.8
AN-G(A)	0.221	0.229	-0.008	-3.620	453.3
AC-E(A)	0.111	0.106	0.005	4.765	341.0
MA-N(A)	0.010	0.023	-0.013	-134.316	266.1
AGV-1(A)	1.069	1.071	-0.002	-0.211	1220.1
NIM-G/N(A)	0.150	0.147	0.003	1.837	378.9
NIM-G(B)	0.091	0.102	-0.011	-11.588	337.3
NIM-N(B)	0.200	0.197	0.003	1.258	424.6
NIM-P(B)	0.200	0.188	0.012	5.787	416.4
NIM-D(B)	0.020	0.027	-0.007	-35.407	269.5
NIM-S(B)	0.044	0.048	-0.004	-8.314	288.2
AN-G(B)	0.221	0.230	-0.009	-4.059	454.2
AC-E(B)	0.111	0.107	0.004	3.228	342.6
MA-N(B)	0.010	0.022	-0.012	-119.922	264.8
AGV-1(B)	1.071	1.079	-0.008	-0.728	1227.0
NIM-G/N(B)	0.150	0.148	0.002	1.514	379.3
NIM-G(C)	0.091	0.091	0.000	-0.040	327.7
NIM-N(C)	0.200	0.200	0.000	-0.100	427.1
NIM-P(C)	0.199	0.197	0.002	1.158	423.9
NIM-D(C)	0.020	0.029	-0.009	-42.831	270.8
NIM-S(C)	0.044	0.045	-0.001	-1.439	285.4
AN-G(C)	0.221	0.214	0.007	3.281	439.4
AC-E(C)	0.111	0.103	0.008	7.023	338.8
MA-N(C)	0.010	0.022	-0.012	-115.455	264.4
AGV-1(C)	1.070	1.067	0.003	0.304	1216.0
NIM-G/N(C)	0.150	0.148	0.002	1.273	379.6
AV.ABS.ERROR IS		0.006	AV.REL.ERROR IS		18.45
CALIBRATION SLOPE		0.1098E-02	BLANK CONCENTRATION		-0.269

Appendix 1 - XRF calibration standards

CaO					
Standard	Std. Conc.	Cal. Conc.	Abs. Error	Rel. Error (%)	Corr. C.P.S.
NIM-G(A)	0.788	0.812	-0.024	-3.012	603.1
NIM-N(A)	11.488	11.645	-0.157	-1.363	8556.5
NIM-P(A)	2.650	2.664	-0.014	-0.530	1963.1
NIM-D(A)	0.278	0.304	-0.026	-9.264	230.2
NIM-S(A)	0.683	0.718	-0.035	-5.120	534.3
AN-G(A)	16.003	16.200	-0.197	-1.234	11901.4
AC-E(A)	0.342	0.397	-0.055	-16.224	299.0
MA-N(A)	0.602	0.644	-0.042	-7.025	480.2
AGV-1(A)	5.031	4.954	0.077	1.533	3644.2
NIM-G/N(A)	6.170	6.080	0.090	1.455	4471.2
NIM-G(B)	0.786	0.796	-0.010	-1.332	591.9
NIM-N(B)	11.508	11.416	0.092	0.796	8389.0
NIM-P(B)	2.653	2.597	0.056	2.099	1914.1
NIM-D(B)	0.278	0.302	-0.024	-8.793	229.2
NIM-S(B)	0.683	0.721	-0.038	-5.505	536.2
AN-G(B)	15.992	16.077	-0.085	-0.529	11810.4
AC-E(B)	0.342	0.392	-0.050	-14.676	295.1
MA-N(B)	0.602	0.640	-0.038	-6.383	477.3
AGV-1(B)	5.038	4.927	0.11	2.213	3624.1
NIM-G/N(B)	6.130	5.997	0.133	2.171	4410.0
NIM-G(C)	0.780	0.797	-0.009	-1.127	592.2
NIM-N(C)	11.504	11.399	0.105	0.911	8376.4
NIM-P(C)	2.648	2.586	0.062	2.352	1905.5
NIM-D(C)	0.278	0.308	-0.030	-10.871	233.4
NIM-S(C)	0.683	0.715	-0.032	-4.691	532.1
AN-G(C)	16.003	15.927	0.076	0.474	11700.7
AC-E(C)	0.342	0.371	-0.029	-8.559	279.7
MA-N(C)	0.601	0.629	-0.028	-4.695	469.1
AGV-1(C)	5.036	4.945	0.091	1.798	3638.0
NIM-G/N(C)	6.180	6.148	0.032	0.518	4520.9
AV.ABS.ERROR IS		0.062	AV.REL.ERROR IS		4.24
CALIBRATION SLOPE		0.1362E-02	BLANK CONCENTRATION		-0.010

Appendix 1 - XRF calibration standards

K_2O					
Standard	Std. Conc.	Cal. Conc.	Abs. Error	Rel. Error (%)	Corr. C.P.S.
NIM-G(A)	5.043	5.043	0.000	-0.009	2692.5
NIM-N(A)	0.250	0.219	0.031	12.291	161.7
NIM-P(A)	0.090	0.074	0.016	17.455	85.6
NIM-D(A)	0.010	0.004	0.006	62.211	48.6
NIM-S(A)	15.411	15.579	-0.168	-1.089	829.3
AN-G(A)	0.131	0.135	-0.004	-3.177	117.6
AC-E(A)	4.516	4.557	-0.041	-0.919	2437.5
MA-N(A)	3.245	3.241	0.004	0.121	1746.9
AGV-1(A)	2.964	2.981	-0.017	-0.566	1610.4
NIM-G/N(A)	2.619	2.658	-0.039	-1.475	1440.9
NIM-G(B)	5.030	5.093	-0.063	-1.257	2718.6
NIM-N(B)	0.250	0.237	0.013	5.021	171.2
NIM-P(B)	0.090	0.087	0.003	3.464	92.2
NIM-D(B)	0.010	-0.004	0.014	138.853	44.6
NIM-S(B)	15.416	15.364	0.052	0.340	8106.3
AN-G(B)	0.131	0.130	0.001	0.998	114.7
AC-E(B)	4.516	4.527	-0.011	-0.236	2421.3
MA-N(B)	3.244	3.286	-0.042	-1.299	1770.6
AGV-1(B)	2.968	2.948	0.020	0.684	1593.0
NIM-G/N(B)	2.639	2.624	0.015	0.566	1423.2
NIM-G(C)	5.043	5.040	0.003	0.053	2690.8
NIM-N(C)	0.250	0.229	0.021	8.202	167.1
NIM-P(C)	0.090	0.079	0.011	12.732	87.9
NIM-D(C)	0.010	-0.004	0.014	140.696	44.5
NIM-S(C)	15.411	15.250	0.161	1.045	8046.7
AN-G(C)	0.131	0.131	0.000	-0.201	115.5
AC-E(C)	4.513	4.481	0.032	0.709	2397.4
MA-N(C)	3.239	3.232	0.007	0.211	1742.3
AGV-1(C)	2.967	2.968	-0.001	-0.049	1603.9
NIM-G/N(C)	2.619	2.655	-0.036	-1.394	1439.7
AV.ABS.ERROR IS		0.028	AV.REL.ERROR IS		13.91
CALIBRATION SLOPE		0.1906E-02	BLANK CONCENTRATION		-0.089

Appendix 1 - XRF calibration standards

P_2O_5					
Standard	Std. Conc.	Cal. Conc.	Abs. Error	Rel. Error (%)	Corr. C.P.S.
NIM-G(A)	0.010	0.001	0.009	94.197	154.7
NIM-N(A)	0.030	0.015	0.015	50.871	160.0
NIM-P(A)	0.020	0.018	0.002	7.956	161.4
NIM-D(A)	0.010	0.017	-0.007	-66.379	160.7
NIM-S(A)	0.120	0.116	0.004	3.120	198.5
AN-G(A)	0.010	0.004	0.006	63.123	155.8
AC-E(A)	0.010	0.024	-0.014	-140.086	163.5
MA-N(A)	1.418	1.397	0.021	1.496	683.6
AGV-1(A)	0.499	0.511	-0.012	-2.428	348.1
NIM-G/N(A)	0.020	0.022	-0.002	-8.471	162.7
NIM-G(B)	0.010	0.003	0.007	72.297	155.5
NIM-N(B)	0.030	0.036	-0.006	-18.851	168.0
NIM-P(B)	0.020	0.030	-0.010	-49.784	165.8
NIM-D(B)	0.010	0.012	-0.002	-22.811	159.3
NIM-S(B)	0.121	0.101	0.020	16.192	152.9
AN-G(B)	0.010	0.017	-0.007	-74.957	161.1
AC-E(B)	0.010	0.024	-0.014	-144.402	163.7
MA-N(B)	1.418	1.435	-0.017	-1.208	698.1
AGV-1(B)	0.500	0.488	0.012	2.321	339.5
NIM-G/N(B)	0.020	0.013	0.007	35.563	159.3
NIM-G(C)	0.010	0.012	-0.002	-17.974	158.9
NIM-N(C)	0.030	0.017	0.013	43.457	160.9
NIM-P(C)	0.020	0.042	-0.022	-108.705	170.3
NIM-D(C)	0.010	0.011	-0.001	-5 043	158.4
NIM-S(C)	0.120	0.106	0.014	11 907	194.5
AN-G(C)	0.010	0.19	-0.009	-93.501	161.8
AC-E(C)	0.010	0.004	0.006	55.940	156.1
MA-N(C)	1.416	1.412	0.004	0.272	689.4
AGV-1(C)	0.500	0.523	-0.023	-4.586	352.5
NIM-G/N(C)	0.020	0.012	0.008	39.060	159.1
AV.ABS.ERROR IS		0.010	AV.REL.ERROR IS		41.90
CALIBRATION SLOPE		0.2640E-02	BLANK CONCENTRATION		-0.408

Appendix 1 - XRF calibration standards

SiO_2					
Standard	Std. Conc.	Cal. Conc.	Abs. Error	Rel. Error (%)	Corr. C.P.S.
NIM-G(A)	76.501	76.317	0.184	0.240	7417.9
NIM-N(A)	52.583	52.901	-0.318	-0.605	5201.7
NIM-P(A)	50.903	51.049	-0.146	-0.286	5026.4
NIM-D(A)	38.670	38.476	0.194	0.501	3836.4
NIM-S(A)	63.881	63.445	0.436	0.683	6199.6
AN-G(A)	46.601	46.636	-0.035	-0.075	4608.7
AC-E(A)	70.761	71.158	-0.397	-0.561	6929.7
MA-N(A)	67.958	68.501	-0.643	-0.798	6678.1
AGV-1(A)	59.871	60.552	-0.681	-1.137	5925.8
NIM-G/N(A)	64.350	64.728	-0.378	-0.587	6321.0
NIM-G(B)	76.310	75.464	0.846	1.108	7337.2
NIM-N(B)	52.677	52.532	0.145	0.274	5166.8
NIM-P(B)	50.975	50.675	0.300	0.588	4991.0
NIM-D(B)	38.670	38.288	0.382	0.989	3818.5
NIM-S(B)	63.904	63.252	0.652	1.020	6181.4
AN-G(B)	46.567	46.877	-0.310	-0.666	4631.5
AC-E(B)	70.761	70.911	-0.150	-0.212	6906.2
MA-N(B)	67.934	68.291	-0.357	-0.525	6658.2
AGV-1(B)	59.956	60.412	-0.456	-0.761	5912.6
NIM-G/N(B)	64.450	64.282	0.168	0.261	6278.8
NIM-G(C)	76.501	75.991	0.510	0.666	7387.1
NIM-N(C)	52.659	52.373	0.286	0.543	5151.7
NIM-P(C)	50.866	50.844	0.022	0.044	5006.9
NIM-D(C)	38.725	38.547	0.178	0.459	3843.1
NIM-S(C)	63.881	63.801	0.080	0.126	6233.3
AN-G(C)	46.601	46.846	-0.245	-0.525	4628.5
AC-E(C)	70.711	71.003	-0.292	-0.413	6915.0
MA-N(C)	67.837	67.498	0.339	0.500	6583.2
AGV-1(C)	59.935	60.122	-0.187	-0.312	5885.1
NIM-G/N(C)	64.330	64.560	-0.230	-0.358	6305.2
AV.ABS.ERROR IS		0.315	AV.REL ERROR IS		0.53
CALIBRATION SLOPE		0.1057E-01	BLANK CONCENTRATION		-2.038

Appendix 1 - XRF calibration standards

Al_2O_3					
Standard	Std. Conc.	Cal. Conc.	Abs. Error	Rel. Error (%)	Corr. C.P.S.
NIM-G(A)	12.208	11.950	0.258	2.116	4198.8
NIM-N(A)	16.482	16.886	-0.404	-2.449	5595.4
NIM-P(A)	4.164	4.192	-0.028	-0.662	2003.8
NIM-D(A)	0.298	0.471	-0.173	-58.148	951.2
NIM-S(A)	17.408	17.321	0.087	0.497	5718.7
AN-G(A)	29.994	30.253	-0.259	-0.865	9377.6
AC-E(A)	14.786	14.901	-0.115	-0.779	5033.9
MA-N(A)	17.979	18.098	-0.119	-0.665	5938.6
AGV-1(A)	17.455	17.319	0.136	0.777	5718.1
NIM-G/N(A)	14.347	14.361	-0.014	-0.097	4881.1
NIM-G(B)	12.177	11.912	0.265	2.175	4188.2
NIM-N(B)	16.512	16.696	-0.184	-1.111	5541.6
NIM-P(B)	4.170	4.292	-0.122	-2.918	2032.1
NIM-D(B)	0.298	0.423	-0.125	-42.099	937.6
NIM-S(B)	17.415	16.953	0.462	2.650	5614.6
AN-G(B)	29.972	30.153	-0.181	-0.604	9349.2
AC-E(B)	14.786	14.843	-0.057	-0.388	5017.6
MA-N(B)	17.973	18.208	-0.235	-1.305	5969.4
AGV-1(B)	17.480	17.291	0.189	1.083	5710.0
NIM-G/N(B)	14.327	14.043	0.284	1.983	4791.1
NIM-G(C)	12.208	11.932	0.276	2.258	4193.9
NIM-N(C)	16.506	16.606	-0.100	-0.604	5516.2
NIM-P(C)	4.161	4.191	-0.030	-0.724	2003.6
NIM-D(C)	0.298	0.419	-0.121	-40.629	936.4
NIM-S(C)	17.408	17.168	0.240	1.381	5675.2
AN-G(C)	29.994	29.906	0.088	0.292	9279.5
AC-E(C)	14.775	14.702	0.073	0.493	4977.6
MA-N(C)	17.947	18.012	-0.065	-0.362	5914.1
AGV-1(C)	17.474	17.389	0.085	0.485	5737.9
NIM-G/N(C)	14.347	14.456	-0.109	-0.759	4907.9
AV.ABS.ERROR IS		0.163	AV.REL ERROR IS		5.71
CALIBRATION SLOPE		0.3534E-02	BLANK CONCENTRATION		-2.890

Appendix 1 - XRF calibration standards

MgO					
Standard	Std. Conc.	Cal. Conc.	Abs. Error	Rel. Error (%)	Corr. C.P.S.
NIM-G(A)	0.061	0.013	0.046	78.492	524.6
NIM-N(A)	7.492	7.545	-0.053	-0.711	1722.3
NIM-P(A)	25.232	25.359	-0.127	-0.502	4554.9
NIM-D(A)	43.186	43.539	-0.353	-0.819	7445.8
NIM-S(A)	0.462	0.506	-0.044	-9.599	603.0
AN-G(A)	1.812	1.871	-0.059	-3.259	820.0
AC-E(A)	0.030	0.040	-0.010	-31.734	528.8
MA-N(A)	0.041	0.066	-0.025	-60.678	533.0
AGV-1(A)	1.558	1.596	-0.038	-2.452	776.3
NIM-G/N(A)	3.802	3.759	0.043	1.143	1120.2
NIM-G(B)	0.060	-0.005	0.065	107.704	521.8
NIM-N(B)	7.505	7.497	0.008	0.110	1714.6
NIM-P(B)	25.268	24.988	0.280	1.107	4496.0
NIM-D(B)	43.186	43.139	0.047	0.110	7382.1
NIM-S(B)	0.462	0.431	0.031	6.748	591.0
AN-G(B)	1.810	1.890	-0.080	-4.406	823.0
AC-E(B)	0.030	0.050	-0.020	-66.664	530.5
MA-N(B)	0.041	0.057	-0.016	-39.504	531.6
AGV-1(B)	1.560	1.708	-0.148	-9.476	794.1
NIM-G/N(B)	3.772	3.695	0.077	2.047	1110.0
NIM-G(C)	0.061	0.013	0.048	78.744	524.6
NIM-N(C)	7.503	7.435	0.068	0.912	1704.7
NIM-P(C)	25.214	25.008	0.206	0.819	4499.0
NIM-D(C)	43.247	43.144	0.103	0.238	7383.0
NIM-S(C)	0.462	0.522	-0.060	-13.085	605.6
AN-G(C)	1.812	1.904	-0.092	-5.074	825.3
AC-E(C)	0.030	0.011	0.019	61.872	524.3
MA-N(C)	0.041	-0.020	0.061	149.000	519.3
AGV-1(C)	1.560	1.606	-0.046	-2.924	777.8
NIM-G/N(C)	3.802	3.736	0.066	1.738	1116.6
AV.ABS.ERROR IS		0.078	AV.REL ERROR IS		24.72
CALIBRATION SLOPE		0.6289E-02	BLANK CONCENTRATION		-3.286

Appendix 1 - XRF calibration standards

Na_2O					
Standard	Std. Conc.	Cal. Conc.	Abs. Error	Rel. Error (%)	Corr. C.P.S.
NIM-G(A)	3.396	3.287	0.109	3.207	485.8
NIM-N(A)	2.457	2.429	0.028	1.153	446.8
NIM-P(A)	0.369	0.519	-0.150	-40.540	360.0
NIM-D(A)	0.040	0.176	-0.136	-340.366	344.5
NIM-S(A)	0.432	0.453	-0.021	-4.775	357.0
AN-G(A)	1.641	1.713	-0.072	-4.373	414.3
AC-E(A)	6.578	6.706	-0.128	-1.940	641.0
MA-N(A)	5.959	6.140	-0.181	-3.037	615.3
AGV-1(A)	4.338	4.243	0.095	2.179	529.2
NIM-G/N(A)	2.920	2.758	0.162	5.557	461.7
NIM-G(B)	3.387	3.219	0.168	4.956	482.7
NIM-N(B)	2.462	2.497	-0.035	-1.415	449.9
NIM-P(B)	0.369	0.432	-0.063	-17.033	356.1
NIM-D(B)	0.040	0.150	-0.110	-274.102	343.3
NIM-S(B)	0.432	0.419	0.013	3.121	355.5
AN-G(B)	1.639	1.597	0.042	2.561	409.0
AC-E(B)	6.578	6.599	-0.021	-0.315	636.2
MA-N(B)	5.957	6.146	-0.189	-3.180	615.6
AGV-1(B)	4.345	4.234	0.111	2.544	528.8
NIM-G/N(B)	2.920	2.769	0.151	5.170	462.2
NIM-G(C)	3.396	3.230	0.166	4.882	483.2
NIM-N(C)	2.461	2.503	-0.042	-1.688	450.1
NIM-P(C)	0.368	0.478	-0.110	-30.000	358.2
NIM-D(C)	0.040	0.156	-0.116	-291.075	343.6
NIM-S(C)	0.432	0.377	0.055	12.703	353.6
AN-G(C)	1.641	1.546	0.095	5.805	406.7
AC-E(C)	6.574	6.611	-0.037	-0.569	636.8
MA-N(C)	5.948	6.017	-0.069	-1.166	609.8
AGV-1(C)	4.343	4.192	0.151	3.477	526.9
NIM-G/N(C)	2.920	2.788	0.132	4.520	463.1
AV.ABS.ERROR IS		0.099	AV.REL.ERROR IS		35.91
CALIBRATION SLOPE		0.2202E-01	BLANK CONCENTRATION		-7.408

Appendix 1 - XRF calibration standards

Trace elements (ppm)

V			Cr		
Standard	Std. Conc.	Cal. Conc.	Standard	Std. Conc.	Cal. Conc.
AGV-1	125	119	AGV-1	10	20
GA	38	46	GA	12	15
GH	5	12	GH	6	4
G-2	36	43	G-2	8	2
GSP-1	55	57	NIM-G	12	4
PCC-1	29	36	NIM-S	12	17
NIM-L	81	77	NIM-N	30	42
NIM-P	230	228	BR	380	363
NIM-N	220	202	SY-1	56	40
NIM-D	40	49	GR	110	94
BR	235	232	BHVO-1	300	287
SY-1	69	84	SGR-1	33	36
GR	65	66	SCO-1	71	77
BHVO-1	320	295	QLO-1	4	1
SGR-1	125	115	RGM-1	4	7
SCO-1	135	139	SDC-1	66	68
QLO-1	61	55	DR-N	42	33
RGM-1	14	20	GS-N	55	55
SDC-1	105	102	MICA-MG	100	104
DR-N	220	218	MICA-FE	90	83
GS-N	65	68	UB-N	290	304
MICA-MG	90	83	DT-N	240	275
MICA-FE	135	132			
UB-N	75	67			
BX-N	310	366			
DT-N	150	143			

Appendix 1 - XRF calibration standards

Co			Ni		
Standard	Std. Conc.	Cal. Conc.	Standard	Std. Conc.	Cal. Conc.
Al_2O_3	0	3	Al_2O_3	0	1
SiO_2	0	5	SiO_2	0	0
AGV-1	16	15	AGV-1	15	20
GA	5	6	GA	7	11
G-2	5	6	G-2	4	6
GSP-1	8	8	GSP-1	9	11
PCC-1	110	99	NIM-G	8	8
NIM-G	4	4	NIM-S	7	7
NIM-S	3	5	NIM-P	560	556
NIM-P	110	100	NIM-N	120	104
NIM-N	58	46	NIM-D	2000	2002
NIM-S	210	225	SY-1	43	56
SY-1	19	16	GR	55	48
GR	10	12	BHVO-1	120	114
BHVO-1	45	37	SCO-1	30	26
SCO-1	11	13	SIM-1	3	7
SDC-1	17	18	SDC-1	36	33
DR-N	35	35	DR-N	16	17
MICA-MG	20	28	MICA-MG	110	119
MICA-FE	20	26	BX-N	200	198

Appendix 1 - XRF calibration standards

Zn			Rb		
Standard	Std. Conc.	Cal. Conc.	Standard	Std. Conc.	Cal. Conc.
Al_2O_3	0	1	SiO_2	0	-6
SiO_2	0	7	Fe+2O%	0	6
AGV-1	86	81	AGV-1	57	67
GA	80	86	GA	175	173
G-2	84	81	GH	390	386
GSP-1	105	97	G-2	170	161
PCC-1	41	42	GSP-1	250	259
NIM-G	50	45	NIM-G	320	324
NIM-S	10	9	NIM-P	5	7
NIM-P	100	107	NIM-N	6	8
NIM-N	68	59	GR	175	182
NIM-D	90	90	BHVO-1	10	19
SY-1	219	239	SGR-1	81	69
GR	60	78	SCO-1	115	108
BHVO-1	105	102	QLO-1	74	70
SCO-1	105	95	SIM-1	120	115
SIM-1	240	226	SDC-1	120	125
SDC-1	105	93	DR-N	73	76
MICA-MG	290	294	GS-N	185	187

Appendix 1 - XRF calibration standards

Sr			Zr		
Standard	Std. Conc.	Cal. Conc.	Standard	Std. Conc.	Cal. Conc.
SiO_2	0	0	SiO_2	0	10
Fe+2O%	0	15	Fe+2O%	0	11
Fe_2O_3	0	-7	Fe_2O_3	0	13
AGV-1	660	641	AGV-1	230	232
GH	10	8	GH	150	148
GSP-1	240	235	G-2	300	273
NIM-G	10	8	GSP-1	500	496
NIM-S	62	61	NIM-G	300	251
NIM-P	32	34	NIM-S	33	29
NIM-N	260	265	NIM-P	30	21
GR	550	570	NIM-N	23	22
MAG-1	140	124	BR	250	276
SCO-1	170	174	GR	180	183
SIM-1	700	705	BHVO-1	180	177
RGM-1	100	98	SGR-1	55	53
SDC-1	180	183	QLO-1	175	193
DR-N	400	399	RGM-1	200	206
GS-N	570	568	SDC-1	300	285
MICA-MG	27	22	DR-N	125	129
FK-N	35	36	MICA-FE	800	822
BX-N	110	113	BX-N	520	522
DT-N	27	31			

Appendix 1 - XRF calibration standards

Ba			P		
Standard	Std. Conc.	Cal. Conc.	Standard	Std. Conc.	Cal. Conc.
AGV-1	1200	1234	GH	44	48
GA	840	314	FK-N	87	73
NIM-S	120	109	DT-N	393	377
NIM-P	46	42	GA	524	524
NIM-N	100	99	G2	567	635
SY-1	282	307	NIM-S	575	528
BHVO-1	135	152	SY-1	960	988
SCO-1	590	544	DR-N	1091	1061
SIM-1	560	561	NIM-J	50	55
RGM-1	800	807			
DR-N	385	396			

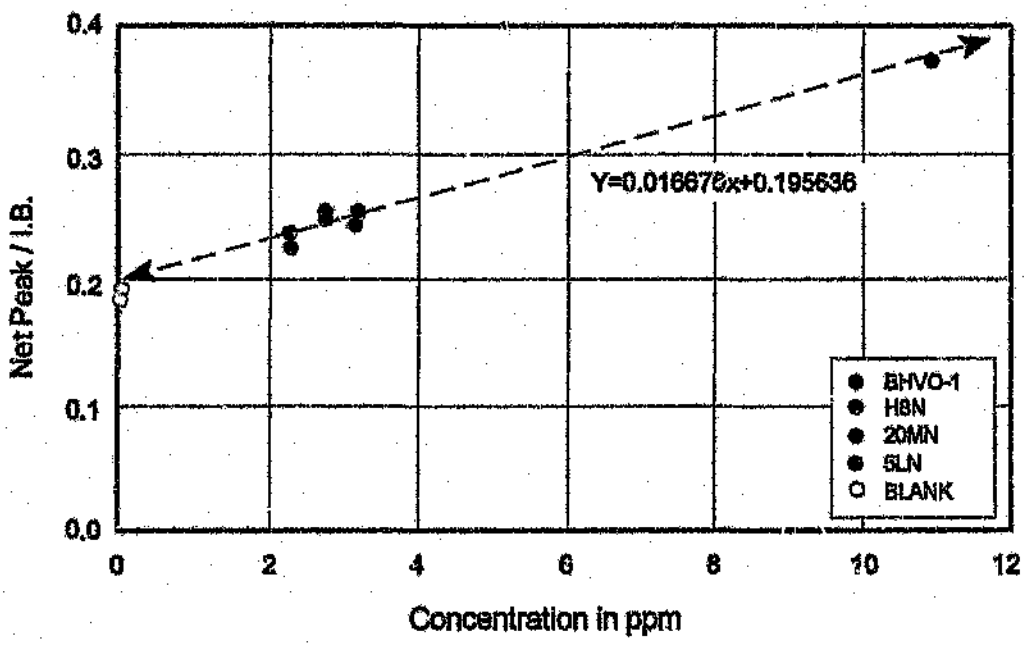


Figure A2 Calibration curve for the analysis of Rb by XRF techniques. Net peak= gross peak - background intensity (I.B.). Samples 20MN, H8N and 5LN were analysed for Rb by isotope dilution mass spectrometry and were used as standards to try an attain reasonable numbers for samples analysed with <10ppm of Rb. The blank sample was precipitated silica.

For Sr-isotopic work on plagioclase separates the accuracy of the Rb analyses are of paramount importance as the errors for the ratios calculated are strongly effected by any error in Rb. Sr by comparison, is far more abundant in these samples and as a result any small error in its analysis has a much smaller influence on the isotopic ratios calculated.

Due to the expense of the isotope dilution method for determining elemental concentrations in samples, a concerted effort was made to analyse Rb and Sr using XRF. For analysis of Sr by XRF an error of 16ppm has been calculated. This possible error in the analysis is large and therefore it was decided to use isotope dilution methods for the analysis of Sr within the plagioclase separates.

In the case of Rb it was important to create a calibration for the detection of this element at <10ppm levels and to determine realistic errors for the results calculated using this calibration. For this reason three of the plagioclase separates were analysed by isotope dilution mass spectrometry. These separates were then analysed by X.R.F., in duplicate, along with a blank (precipitated silica) and the analytical standard BHVO-1. From this exercise a calibration curve was determined (refer to Fig. A2). The calculated concentrations for these standards is listed in Table A2, along with the recommended concentrations.

Appendix 2 - Rb calibration for isotope work

With the duplicate analyses it is possible to calculated a pooled sample standard deviation (S_{pooled}), as described in appendix 4. For these samples S_{pooled}=0.4ppm. The pooled standard deviation may be assumed to be approximately equal to the population standard deviation (σ). Therefore the uncertainty (precision) associated with the analysis of Rb by XRF, using this calibration, is approximately equal to 0.8ppm (2σ). For the purpose of calculating the Sr-isotopic ratios this error (imprecision) is extreme and therefore every plagioclase separate, analysed for Rb and Sr isotopes, has had Rb analysed for by isotope dilution methods as that method is more accurate and precise.

Table A2
Calculated concentration of Rb within standards, as determined by XRF analysis, compared to the ID concentrations.

Sample	Calculated concentrations (ppm)	Concentration by ID (ppm)
Blank (precipitated silica)	-0.6	0.0
20MN (plagioclase separate)	2.5	2.3
20MN (plagioclase separate)	1.7	2.3
H8N (plagioclase separate)	3.3	2.8
H8N (plagioclase separate)	3.5	2.8
5LN (plagioclase separate)	3.0	3.2
5LN (plagioclase separate)	3.5	3.2
BHVO-1 (basalt)	10.8	11

Appendix 3 - Modal data (volume %)

Profile A samples	Plag	Cpx	Opx	Pigeonite	other*
H8N	59.9	14.2	25.9	0.00	0.0
H7N	62.8	7.10	23.5	6.30	0.3
H6N	67.6	16.5	12.8	1.80	0.3
H4N	65.6	14.5	1.40	18.5	0.0
H3N	13.2	27.8	11.5	46.8	0.6
H2N	66.2	12.2	0.30	21.3	0.0
H1N	81.7	3.30	2.00	13.1	0.0
22MN	16.0	14.0	28.4	41.4	0.2
21LN	95.3	1.90	1.30	1.50	0.0
20LN	88.8	10.0	0.30	0.60	0.3
20MN	16.9	47.1	1.50	34.0	0.5
19LN	97.9	1.60	0.00	0.00	0.5
19MN	39.5	8.00	3.80	47.5	1.2
18LN	90.8	1.60	0.60	7.00	0.0
18MN	45.3	3.70	2.20	47.0	1.8
11MN	25.0	42.2	10.2	22.0	0.6
10LN	83.0	7.90	0.40	8.80	-0.1
10MN	28.4	41.9	9.60	19.9	0.2
9LN	97.4	1.90	0.00	0.00	0.7
9MN	42.4	32.5	2.90	22.3	0.0
8LN	78.1	13.1	2.00	6.60	0.2
8MN	72.7	20.7	1.30	5.30	0.0
7LN	91.6	6.10	1.60	0.20	0.5
6MN	30.7	41.5	5.10	22.6	0.1
5LN	69.5	19.5	1.90	14.8	0.3
4LN	81.0	9.50	1.00	8.30	0.2
4MN	23.1	42.1	3.00	31.6	0.2
3LN	88.9	5.80	1.10	3.60	0.6
3MN	42.6	32.6	11.4	12.8	0.6
2LNb	84.0	8.80	0.30	6.80	0.1
2LNa	76.7	13.6	2.20	7.30	0.2
2MN	48.2	30.8	6.60	14.0	0.4
F1N	46.7	30.5	1.40	21.4	0.0
F2N	67.7	20.7	3.90	7.70	0.0

*Other minerals include opaque oxides (dominantly), biotite and amphibole

Appendix 3 - Modal data (volume %)

Profile B samples	Plag	Cpx	Opx	Pigeonite	other*
H12S	64.2	7.30	21.9	6.50	0.1
H11S	67.2	6.80	18.3	7.40	0.3
H10S	16.3	10.3	41.6	30.5	1.3
H9S	56.8	4.80	29.2	9.10	0.1
H8S	59.8	18.9	2.90	18.5	0.0
H7S	61.4	21.0	1.60	16.0	0.0
H6S	5.80	52.0	28.7	12.3	1.2
H5S	75.3	8.70	0.30	15.7	0.0
H1S	84.8	8.20	1.50	5.20	0.3
25LS	87.9	10.3	0.40	1.40	0.0
23LS	95.9	0.00	1.70	2.10	0.3
23MS	56.4	27.8	0.20	15.4	0.2
19LS	94.3	0.70	0.70	4.10	0.2
19bMS	47.6	31.8	2.30	18.4	0.0
18LS	98.6	1.00	0.00	0.00	0.4
6LS	93.2	2.40	0.60	3.80	0.0
6MS	51.8	28.0	2.40	17.6	0.2
5LS	79.6	12.6	0.60	7.00	0.2
5MS	72.0	16.5	2.30	8.90	0.3
4LS	85.7	6.60	0.40	7.30	0.0
4MS	34.1	34.4	5.80	25.5	0.2
3LS	83.1	7.90	1.20	7.90	0.0
3MS	64.4	23.2	5.60	6.90	0.0
2LS	87.1	5.70	0.70	6.40	0.1
1LS	81.8	9.40	0.80	8.00	0.0
F1S	71.5	15.3	1.00	12.2	0.0
F2S	71.1	13.7	1.70	13.3	0.2

*Other minerals include opaque oxides (dominantly), biotite and amphibole

The modal data for profile C has been taken from Pillay (1990).

Appendix 4 - Error analysis

For plagioclase separates duplicate analysis has allowed for the precise constraining of analytical precision attained. For every pair of analyses the following is calculated: $A_i=\sum (x_i-\bar{x})^2$ where A_i is the squared deviation from the mean for the ith set of replicate analyses. Then by pooling the squared standard deviations from the mean, for all the replicates, it is possible to get a reasonably good idea of the standard deviation for the population as a whole. This is done using the following equation: $s_{pooled}=\frac{\sqrt{(\sum A_i)}}{N-n}$ where N equals the number of analyses and n equals the number of replicates considered.

For the pyroxene, whole rock, and REE analyses few duplicates were run. Therefore a realistic analytical error based on the precision and accuracy of the standards used in the calibration has been calculated. The following equations describe the method with which these errors have been calculated. The method has been taken from Skoog et al. (1988). X= concentration of the element within the standard; y= (c)orrected (c)ounts (p)er (s)econd (ccps) for the standards; N=number of standards run; M=number of duplicate analyses undertaken (if the sample was analysed only once then M=1); y_c= the average ccps for the data set employed. A number of convenient quantities can be calculated from the calibration curve:

$$S_{xx}=\sum (x_i-\bar{x})^2=\sum x_i^2-\frac{(\sum x_i)}{N}$$

$$S_{yy}=\sum (y_i-\bar{y})^2=\sum y_i^2-\frac{(\sum y_i)}{N}$$

$$S_{xy}=\sum (x_i-\bar{x})(y_i-\bar{y})=\sum x_i y_i-\frac{\sum x_i \sum y_i}{N}$$

Using these variables and the following equation we can calculate the standard deviation about the regression line (S_r):

$$S_r=\sqrt{\frac{S_{yy}-b^2S_{xx}}{N-2}} \quad \text{where} \quad b=\frac{S_{xy}}{S_{xx}}$$

It is then possible to determine the standard deviation of a result obtained from the calibration curve using the following expression (note y_c refers to the counts for the sample and y to those related to the standards):

$$S_c=\frac{S_r}{b}\sqrt{\frac{1}{M}+\frac{1}{N}+\frac{(\bar{y}_c-\bar{y})^2}{b^2S_{xx}}}$$

These two approaches allow for the calculation of realistic errors for the analyses and both approaches have been used throughout this study. The first approach (employing the pooled standard deviations) gives a measure of precision whereas the second method is a measure of both precision and accuracy.

Appendix 5 - Derivation of plagioclase calibration curves

The plagioclase series of minerals ranges from pure anorthite $CaAl_2Si_2O_8$ (An_{100}) to pure albite $NaAlSi_3O_8$. The following table lists the modelled elemental abundances of CaO and Na_2O within plagioclase containing differing proportions of Anorthite. This table is presented to show that the concentrations of these oxides within the plagioclase, and for that matter SiO_2 and Al_2O_3, do not vary linearly with respect to mode.

Anorthite content (y_i)	CaO (x_i)	Na_2O (x_i)
100	20.16	0.00
90	18.25	1.12
80	16.31	2.25
70	14.36	3.40
60	12.38	4.56
50	10.38	5.73
0	0.00	11.82

Using the least squared approximation method it is possible to derive formulae that describe the variation in concentration of these oxides. As the data used in this modelling has been derived mathematically and is theoretically exact (internally consistent) it is reasonable to require that these functions fit the data as well as is possible.

Using the following formulae:

$$a_0\sum_{i=1}^{m}x_i^0+a_1\sum_{i=1}^{m}x_i^1 \quad +\ldots\ldots\ldots\ldots+a_n\sum_{i=1}^{m}x_i^n=\sum_{i=1}^{m}y_ix_i^0$$

$$a_0\sum_{i=1}^{m}x_i^1+a_1\sum_{i=1}^{m}x_i^2 \quad +\ldots\ldots\ldots\ldots+a_n\sum_{i=1}^{m}x_i^{n+1}=\sum_{i=1}^{m}y_ix_i^1$$

$$\updownarrow$$

$$a_0\sum_{i=1}^{m}x_i^n+a_1\sum_{i=1}^{m}x_i^{(n+1)}+\ldots\ldots\ldots\ldots+a_n\sum_{i=1}^{m}x_i^{2n}=\sum_{i=1}^{m}y_ix_i^n$$

where x_i=*CaO* or Na_2O abundanceand y_i= *Anorthite content* (*An*%). For i=1000 the following polynomials have been calculated:

$$f(Na_2O)=-0.00025x^3+0.04644x^2-8.97827x+100.0017$$

$$f(CaO)=+0.00005x^3+0.01315x^2+4.67699x+0.00002$$

Appendix 5 - Derivation of plagioclase calibration curves

$$f(Al_2O_3) = +0.000069x^3 + 0.014168x^2 + 4.849145x - 100.130052$$
$$f(SiO_2) = -0.000021x^3 + 0.012569x^2 - 5.121516x + 299.461252$$

When these formulae are used to calculate the anorthite content from theoretical oxide abundances the comparison with the theoretical anorthite content is good (Table 6.6). Therefore these formulae appear to describe the variation in the major oxide abundance, within plagioclase, with changing anorthite content.

Appendix 6 - REE, Ni, Co and Sc analysis in mineral separates

For the analysis of the mineral separates by Instrumental Neutron Activation Analysis (INAA), plagioclase and pyroxene separates were analysed separately due to their significantly different chemistries. Therefore two different sets of calibration samples were made up and as a result two separate sets of calibrations curves have been calculated.

Table A6.1a and b list the calibration data for selected REE and other traces as analysed for in pyroxene separates. Note that the standard concentrations have been taken from Abbey (1978), Flanagan (1973) and Potts et al. (1985). These tables are followed by graphically illustrations of each calibration curve. Most of the calibration curves have high correlation coefficients (R^2>0.99). However calibration curves for Gd and Lu were difficult to attain as these elements are fission products after Th and U. As Th and U occur in significant quantity in certain of the standards it is difficult to get a reasonable calibration curve for these elements. Table A6.2 lists the REE analyses (raw counts) for the pyroxene separates and the calculated REE abundances (in ppm) within these samples. Table A6.3 (a and b) list the calibration data for selected REE and other traces as analysed for in the plagioclase separates. This table is followed by graphical illustrations of each of these calibrations. Table A6.4 lists the REE analyses for the plagioclase separates (raw counts) and the calculated REE abundances within these samples. Table A6.5 lists the Ni, Sc and Co analyses (raw counts) for orthopyroxene, clinopyroxene and plagioclase separates and the calculated abundances of these three elements in each sample analysed. Figure A6.1 shows the average chondrite normalized REE abundances in the orthopyroxene, clinopyroxene and plagioclase separates analysed.

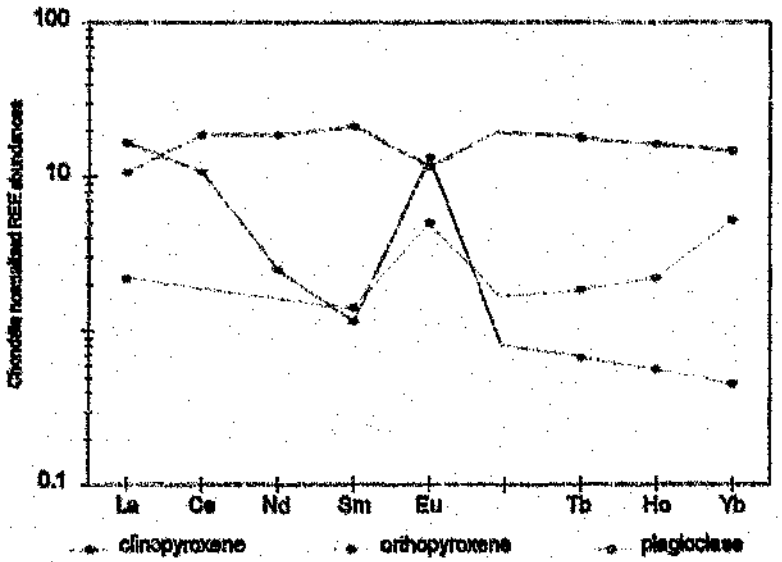


Figure A6.1 Average chondrite normalized REE abundances in plagioclase, clinopyroxene and orthopyroxene separates analysed by INAA.

Appendix 6 - REE, Ni, Co and Sc analysis in mineral separates

Table A6.1a

Calibration data for the analysis of REE in the pyroxene separates. Standards in bold have been excluded from the calculation of a calibration curve.

	La	Ce	Nd	Sm	Eu	Gd	Tb	Ho	Yb
W-1	1132000	*84550*	68350	41660000	41420	115000	145200	*2626000*	*94920*
BHVO-1	1568000	141900	126900	73440000	81170	62240	217700	3048000	90730
G-2	8718000	572500	305600	86410000	49040	2195000	106300	1242000	29890
DTS-1				858400	*16850*	7300	5659		
PCC-1		*89630*		956500	*17810*	11590			
AGV-1		245300	*173900*	71160000	60210	82850	150100	2091000	74180
standard concentrations									
W-1	10	23	12.8	3.6	1.1	4	0.65	0.69	2.3
BHVO-1	15.6	39.6	24	6.1	2	6	1	1.06	2.13
G-2	82	160	58	7.54	1.27	4.13	0.5	0.4	0.77
DTS-1	0.032	0.083	0.033	0.0061	**0.001**	0	0.001	0.003	0.014
PCC-1	0.04	17	1	0.01	**0.002**	-	-	-	-
AGV-1	36	68.3	31.7	5.9	1.7	5.5	0.7	0.71	1.71
calibration curve y=mx+c									
constant	0.09	-0.2	-0.2	-0.07	0.18	-0.26	-0.01	-0.05	0
R^2	0.9996	1	1	0.9984	0.9544	1	0.9985	1	0.9942
slope	9.4×10^{-6}	2.8×10^{-4}	1.9×10^{-4}	8.59×10^{-5}	2.31×10^{-5}	3.71×10^{-5}	4.74×10^{-6}	3.65×10^{-7}	2.35×10^{-5}

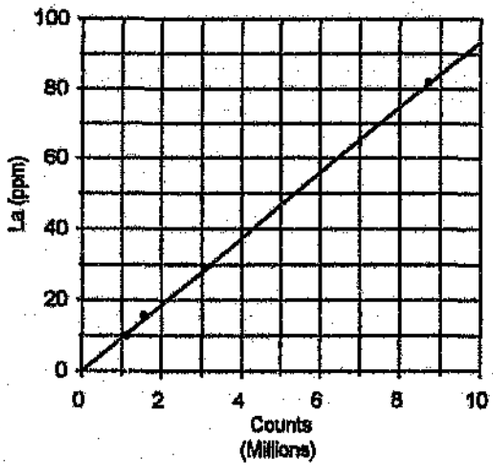
(The calibration for Lu was found to be poor and the calculated values, based on this calibration, varied considerably therefore it was decided to leave Lu out of the data set as unreliable. This element is a fission product after U and Th, as is Gd, and these standards all contain some of these elements and this is probably the reason why the calibration is so poor)

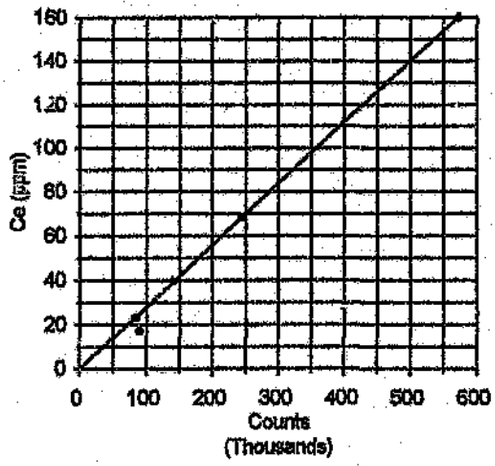
Table A6.1b

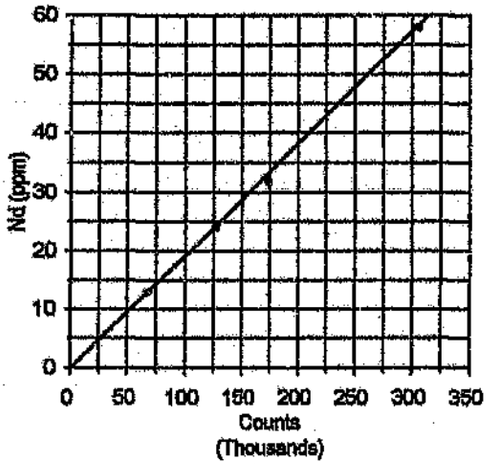
Calibration data for the analysis of Ni, Sc and Co in the pyroxene separates. Standards in bold have been excluded from the calculation of a calibration curve.

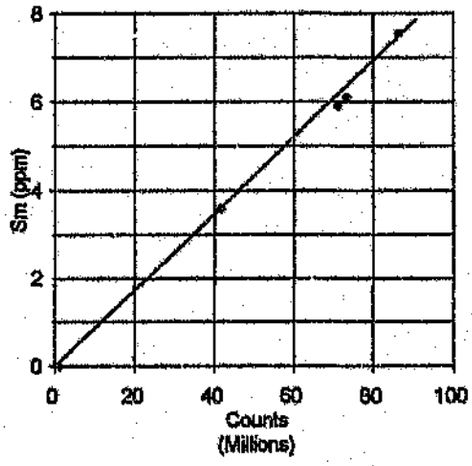
	Ni	Sc	Co
W-1	207000	2544000	423900
BHVO-1	312300	2501000	412600
G-2	11010	301700	40780
DTS-1	5912000	216900	1218000
PCC-1	6185000	529700	1047000
AGV-1	44280	942200	139800
standard concentrations			
W-1	*76*	35	47
BHVO-1	120	33.3	45
G-2	3.5	3.8	4.4
DTS-1	2269	3	133
PCC-1	*2400*	7.4	114
AGV-1	15	12.3	14.1
calibration curve y=mx+c			
constant	0.00	0.11	0.27
R^2	0.9995	0.9991	1.0000
slope	3.84×10^{-4}	1.36×10^{-5}	1.09×10^{-4}

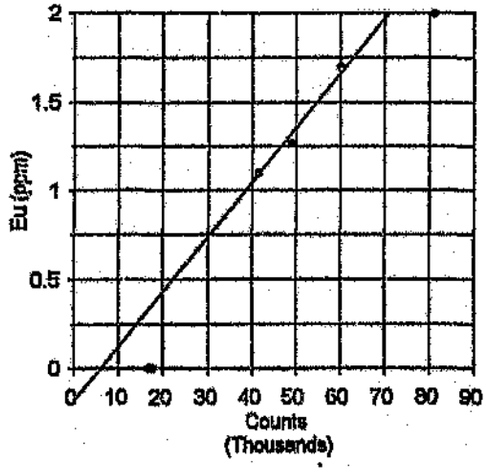
(These calibration curves are graphically illustrated on the following two pages)

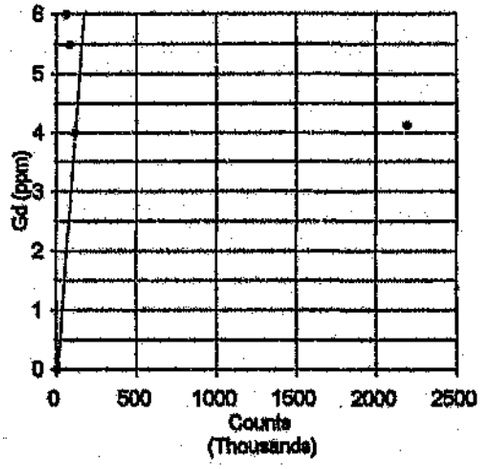

La (ppm)
Counts
(Millions)

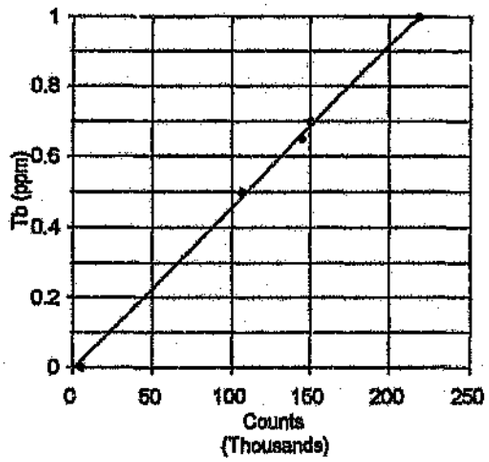

Ce (ppm)
Counts
(Thousands)

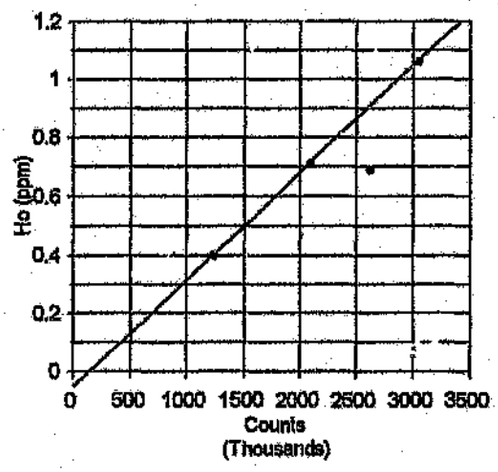

Nd (ppm)
Counts
(Thousands)

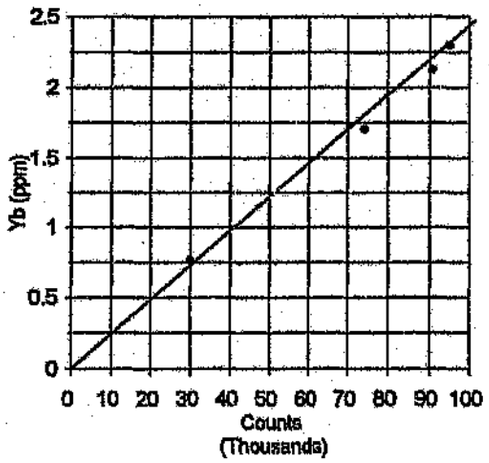

Sm (ppm)
Counts
(Millions)

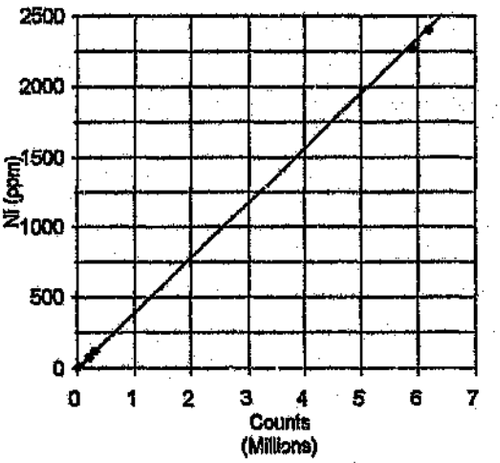

Eu (ppm)
Counts
(Thousands)

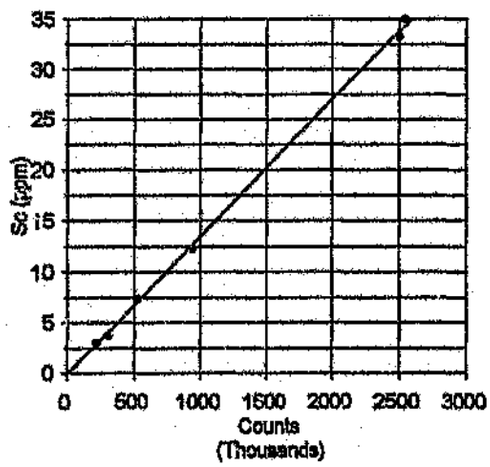

Gd (ppm)
Counts
(Thousands)

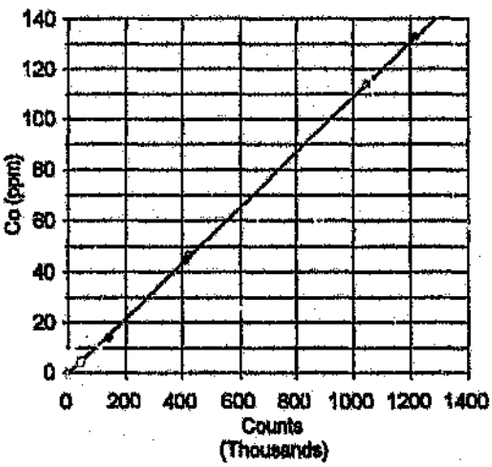

Tb (ppm)
0
0.2
0.4
0.6
0.8
1
0
50
100
150
200
250
Counts
(Thousands)


Ho (ppm)
0
0.2
0.4
0.6
0.8
1
1.2
0
500
1000
1500
2000
2500
3000
3500
Counts
(Thousands)


Yb (ppm)
0
0.5
1
1.5
2
2.5
0
10
20
30
40
50
60
70
80
90
100
Counts
(Thousands)


Ni (ppm)
0
500
1000
1500
2000
2500
0
1
2
3
4
5
6
7
Counts
(Millions)


Sc (ppm)
0
5
10
15
20
25
30
35
0
500
1000
1500
2000
2500
3000
Counts
(Thousands)


Co (ppm)
0
20
40
60
80
100
120
140
0
200
400
600
800
1000
1200
1400
Counts
(Thousands)

Appendix 6 - REE, Ni, Co and Sc analysis in mineral separates

Table A6.2
Calculated REE abundances within pyroxene separates analysed by INAA

Peak data from INAA of pyroxenes

	La	Ce	Nd	Sm	Eu	Tb	Ho	Yb
H8NC	288200	44440	57580	40630000	24090	152700	2836900	99950
H8NC	286700	48740	54290	39770000	23790	150000	2711000	106000
H6NC	253000	41490	41770	37490000	20780	138500	2611000	102100
5LNC	324800	52080	55880	48720000	24340	177200	3421000	131300
5NMC	231800	43220	40170	35140000	20050	130500	2443000	98780
3MNC	233000	33180	35350	31860000	18840	123500	2257000	89790
2LNaC	271700	44850	53120	41270000	22510	153400	2860000	110500
F2NC	251000	40790	41850	35020000	18570	135100	2376000	94370
H8NO	37650			2449000	8935	14210	397500	33100
H8NO	48930			2469000	10010	14810	450700	32300
H6NO	37670			3350000	3245	17220	551200	35880
5LNO	53560			4922000	3655	24040	619000	46130
5MNO	48970			3917000	3794	20430	559700	37230
3MNO	54960			2463000	2628	13480	402800	36800
2LNaO	62250			4291000	3310	21880	520900	38310
F2NO	30180			2558000	3352	14150	390900	32350

Calculated REE abundances in separates

H8NC	2.80	12.24	10.77	3.42	0.73	0.71	0.98	2.34
H8NC	2.78	13.44	10.14	3.35	0.73	0.70	0.94	2.49
H6NC	2.48	11.41	7.76	3.15	0.66	0.64	0.90	2.39
5LNC	3.14	14.37	10.45	4.11	0.74	0.83	1.20	3.08
5LNO	2.27	11.89	7.45	2.95	0.64	0.60	0.84	2.32
3MNC	2.28	9.09	6.54	2.67	0.61	0.57	0.77	2.11
2LNaC	2.64	12.35	9.92	3.47	0.70	0.71	0.99	2.59
F2NC	2.45	11.21	7.77	2.94	0.61	0.63	0.81	2.21
H8NO	0.44			0.14	0.38	0.05	0.09	0.78
H8NO	0.55			0.14	0.41	0.06	0.11	0.76
H6NO	0.44			0.22	0.25	0.07	0.15	0.84
5LNC	0.59			0.35	0.26	0.10	0.17	1.08
5MNO	0.55			0.27	0.27	0.08	0.15	0.87
3MNO	0.60			0.14	0.24	0.05	0.09	0.86
2LNaO	0.67			0.30	0.25	0.09	0.14	0.90
F2NO	0.37			0.15	0.26	0.05	0.09	0.76

chondrite normalized REE abundances

	La	Ce	Nd	Sm	Eu	Tb	Ho	Yb
H8NC	11.43	19.18	22.73	22.21	12.67	18.94	17.33	14.20
H8NC	11.37	21.07	21.41	21.73	12.55	18.60	16.52	15.06
H6NC	10.15	17.89	16.38	20.46	11.35	17.15	15.88	14.51
5LNC	12.84	22.53	22.05	26.72	12.77	22.04	21.10	18.65
5LNO	9.26	18.65	15.73	19.15	11.06	16.13	14.79	14.03
3MNO	9.31	14.24	13.79	17.32	10.58	15.25	13.60	12.76
2LNaC	10.80	19.36	20.94	22.56	12.04	19.03	17.48	15.70
F2NC	10.00	17.58	16.41	19.08	10.47	16.72	14.36	13.41
H8NO	1.80			0.92	6.63	1.42	1.61	4.70
H8NO	2.23			0.93	7.06	1.49	1.95	4.59
H6NO	1.80			1.42	4.37	1.80	2.60	5.09
5LNO	2.41			2.30	4.53	2.66	3.04	6.
5MNO	2.24			1.74	4.58	2.21	2.66	5.
3MNO	2.47			0.93	4.12	1.33	1.64	5.
2LNaO	2.75			1.95	4.39	2.39	2.41	5.44
F2NO	1.51			0.98	4.41	1.41	1.57	4.60

Chondrite normalization factors — Evensen et al. (1978)

	0.2446	0.6379	0.4738	0.154	0.05802	0.03745	0.0567	0.1651

Appendix 6 - REE, Ni, Co and Sc analy... in mineral separates

Table A6.3a

Calibration data for the analysis of REE in the plagioclase separates. Standards in bold have been excluded from the calculation of a calibration curve.

	La	Ce	Nd	Sm	Eu	Gd	Tb	Ho	Yb
W-1	840900	152300	140400	49286000	15740	994200	371000	3140000	309800
BHVO-1	1192000	226300	262500	87980000	31300	14560[illegible]	544200	3376000	135200
G-2	4685000	724400	338100	72820000	14220	3961000	193400	1104000	34710
DTS-1		-	-	1055000	-	-	799	103800	-
PCC-1		-	-	1745000	-	14690	12340	-	134100
AGV-1	2812000	426200	269900	81070000	21950	666100	364300	2453000	121500
standard concentrations									
W-1	10	23	12.8	3.6	1.1	4	0.65	0.69	2.3
BHVO-1	15.6	39	24	6.1	2	6	1	1.15	2.13
G-2	82	160	58	7.54	1.27	4.13	0.5	0.33	0.77
DTS-1	0.032	0.083	0.035	0.0061	0.001	0	0.007	0.003	0.014
PCC-1	0.04	17	1	0.01	0.002	-	-	-	-
AGV-1	35	68.3	31.7	5.9	1.57	5.5	0.7	0.71	1.9
calibration curve y=mx+c									
constant	0.07	-0.12	-0.08	-0.06	0.25	0.00	-0.0004	0	-0.1398
R^2	0.9978	0.9917	1	0.9983	0.9801	1	0.9963	0.9958	1
slope	1.25×10^{-5}	1.61×10^{-4}	9.17×10^{-5}	7.02×10^{-6}	5.69×10^{-5}	4.02×10^{-6}	1.84×10^{-6}	3.26×10^{-7}	1.68×10^{-5}

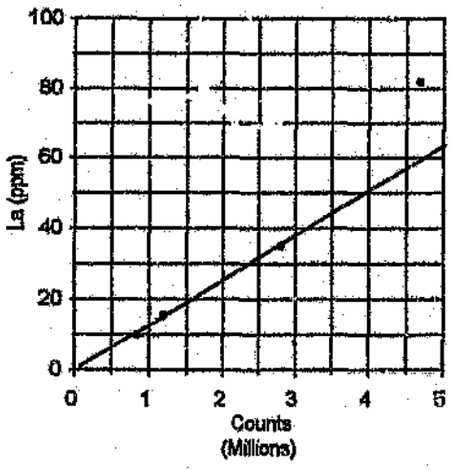
(The calibration for Lu was found to be poor and the calculated values, based on this calibration, varied considerably therefore it was decided to leave Lu out of the data set as unreliable. This element is a fusion product after U and Th, as is Gd, and these standards all contain some of these elements and this is probably the reason why the calibration is so poor)

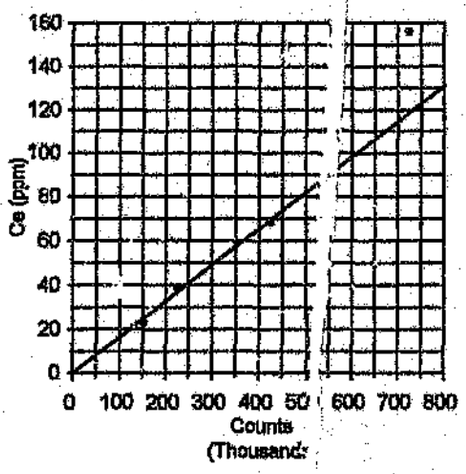
Table 6.3b

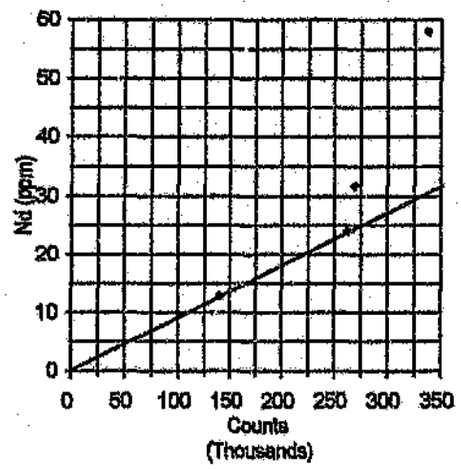
Calibration data for the analysis of Ni, Sc and Co in the plagioclase separates. Standards in bold have been excluded from the calculation of a calibration curve.

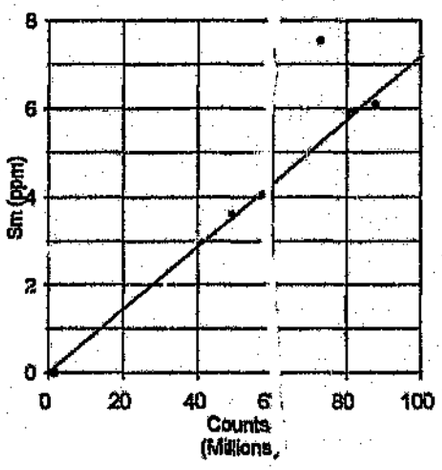
	Ni	Sc	Co
W-1	481500	6403000	1054000
BHVO-1	742200	6308000	1045000
G-2	19170	532700	77850
DTS-1	12750000	553400	3092000
PCC-1	19680000	2041000	3897000
AGV-1	97850	2247000	335800
standard concentrations			
W-1	***76***	35	47
BHVO-1	120	33.3	45
G-2	3.5	3.8	4.4
DTS-1	2269	3	133
PCC-1	***2400***	7.4	114
AGV-1	15	12.3	14.1
calibration curve y=mx+c			
constant	0.00	0.12	0.00
R^2	0.9999	0.9990	0.9996
slope	1.62×10^{-4}	5.36×10^{-6}	4.32×10^{-5}

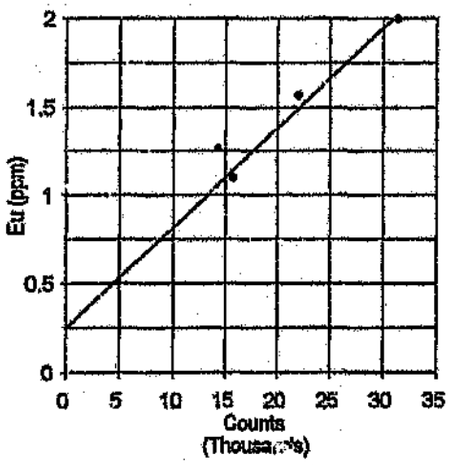
(These calibration curves are graphically illustrated on the following two pages)

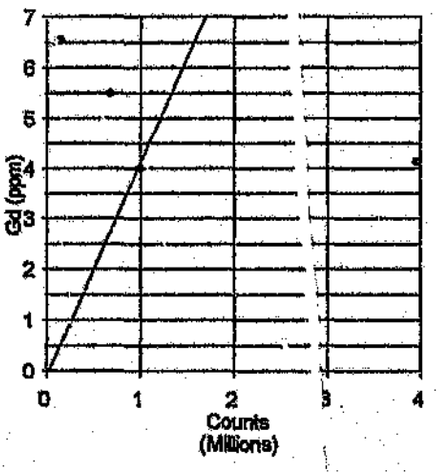

La (ppm)
Counts
(Millions)

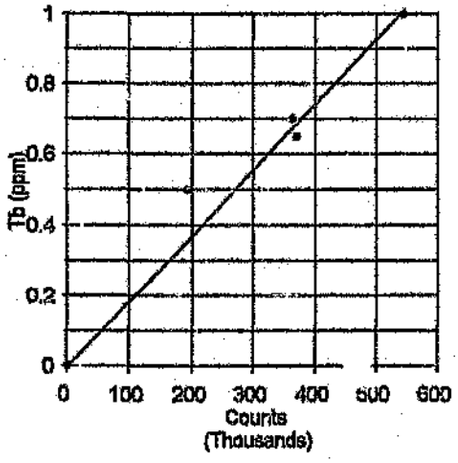

Ce (ppm)
Counts
(Thousands)

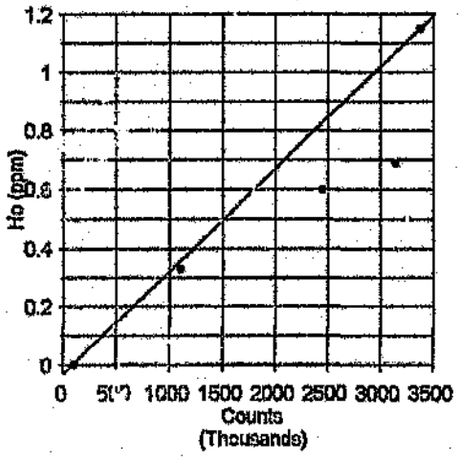

Nd (ppm)
Counts
(Thousands)

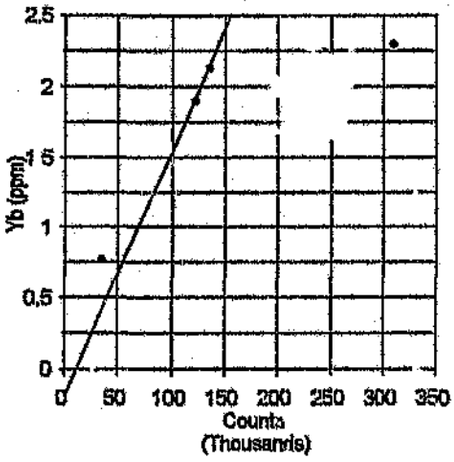

Sm (ppm)
Counts
(Millions)

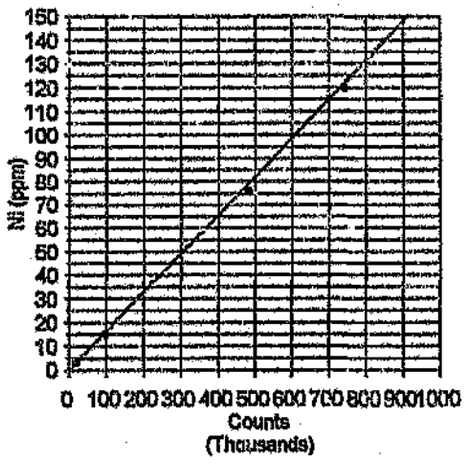

Eu (ppm)
Counts
(Thousands)

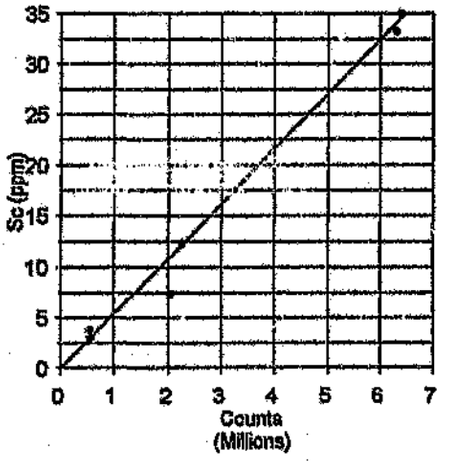

Gd (ppm)
Counts
(Millions)

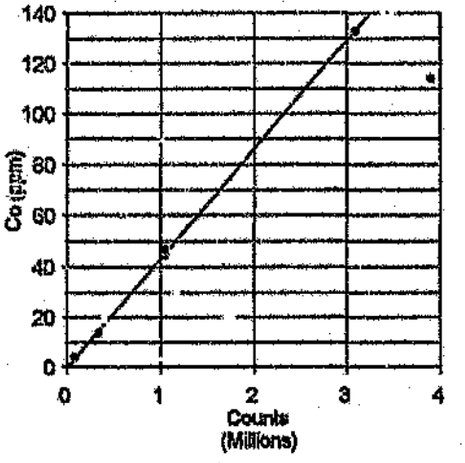

Tb (ppm)
0
0.2
0.4
0.6
0.8
1
0 100 200 300 400 500 600
Counts
(Thousands)


Ho (ppm)
0
0.2
0.4
0.6
0.8
1
1.2
0 500 1000 1500 2000 2500 3000 3500
Counts
(Thousands)


Yb (ppm)
0
0.5
1
1.5
2
2.5
0 50 100 150 200 250 300 350
Counts
(Thousands)


Ni (ppm)
0
10
20
30
40
50
60
70
80
90
100
110
120
130
140
150
0 100 200 300 400 500 600 700 800 900 1000
Counts
(Thousands)


Sc (ppm)
0
5
10
15
20
25
30
35
0 1 2 3 4 5 6 7
Counts
(Millions)


Co (ppm)
0
20
40
60
80
100
120
140
0 1 2 3 4
Counts
(Millions)

Appendix 6 - REE, Ni, Co and Sc analysis in mineral separates

Table A6.4
Calculated REE abundances in plagioclase separates analysed by INAA

Peak data from INAA of plagioclase

	La	Ce	Nd	Sm	Eu	Tb	Ho	Yb
H8NPL	376400	45639	16020	3687000	7527	15910	98340	6513
H8NPL	363900	48395	15390	3618000	7531	14950	71960	3490
H6NPL	316600	39407	12010	3068000	9410	12800		3393
5LNPL	332400	45639	15050	3620000	11160	14480	123200	4724
5MNPL	286200	38509	11710	3208000	9456	13630		4822
3MNPL	282500	37071	13280	2973000	9847	13150	85880	
2LNaPL	316900	41445	13960	3419000	9834	14150	97720	4147
F2NPL	299200	37610	11610	2953000	9860	12230		

Calculated REE abundances in separates

H8NPL	4.76	7.49	1.39	0.20	0.68	0.03	0.03	0.11
H8NPL	4.61	7.93	1.33	0.20	0.68	0.03	0.02	0.06
H6NPL	4.02	6.48	1.02	0.16	0.78	0.02		0.06
5LNPL	4.21	7.49	1.30	0.20	0.88	0.03	0.04	0.08
5MNPL	3.64	6.34	1.00	0.17	0.79	0.02		0.08
3MNPL	3.59	6.10	1.14	0.15	0.81	0.02	0.03	0.00
2LNaPL	4.02	6.81	1.20	0.18	0.81	0.03	0.03	0.07
F2NPL	3.80	6.19	0.99	0.15	0.81	0.02		0.00

chondrite normalized REE abundances

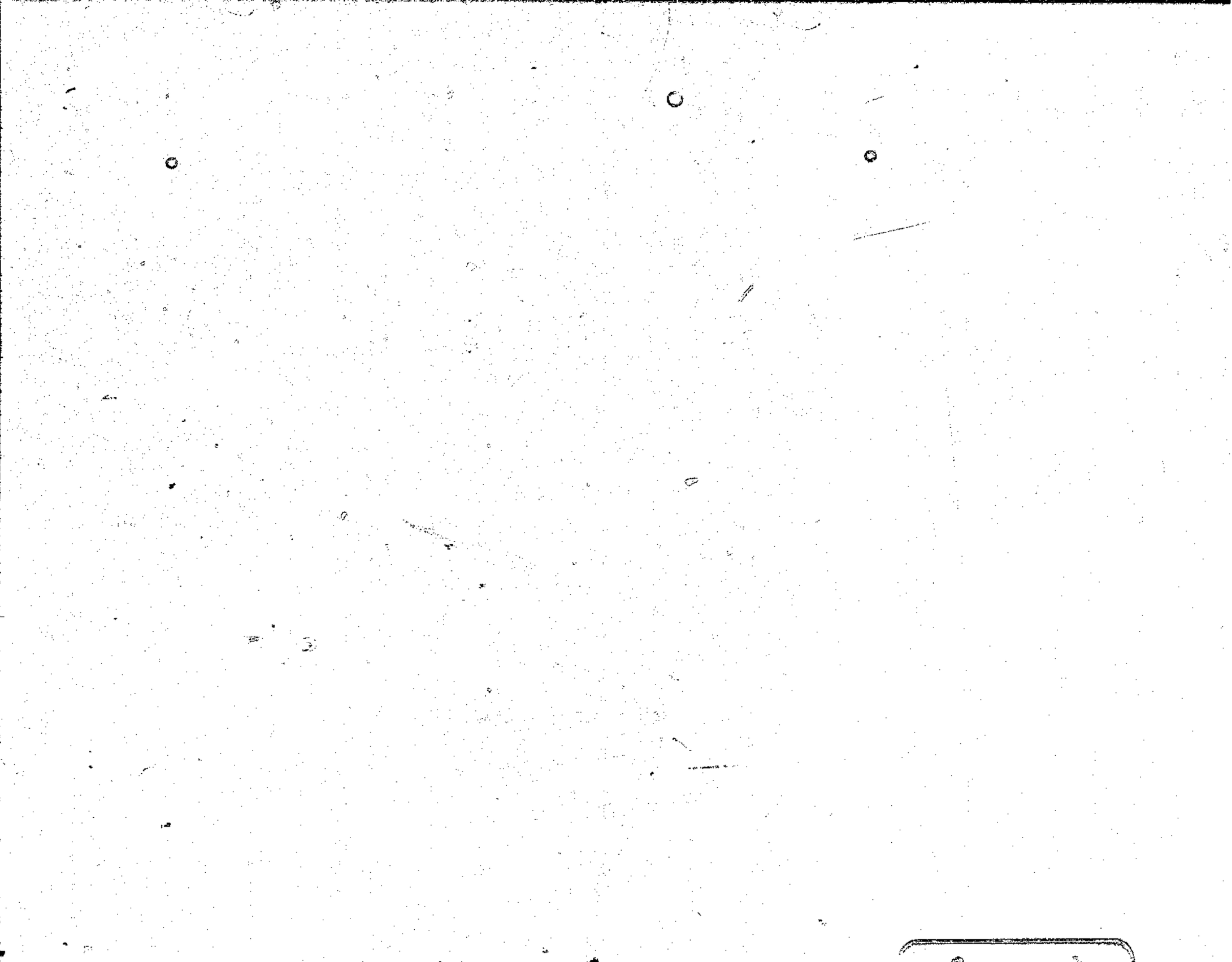
	La	Ce	Nd	Sm	Eu	Tb	Ho	Yb
H8NPL	19.47	11.74	2.94	1.32	11.66	0.77	0.58	0.66
H8NPL	18.83	12.44	2.81	1.29	11.66	0.72	0.43	0.35
H6NPL	16.42	10.16	2.16	1.03	13.51	0.62		0.35
5LNPL	17.23	11.74	2.75	1.29	15.22	0.70	0.73	0.48
5MNPL	14.88	9.93	2.10	1.09	13.55	0.66		0.49
3MNPL	14.69	9.57	2.41	0.98	13.94	0.63	0.51	
2LNaPL	16.44	10.68	2.54	1.19	13.92	0.68	0.58	0.42
F2NPL	15.54	9.71	2.08	0.97	13.95	0.59		

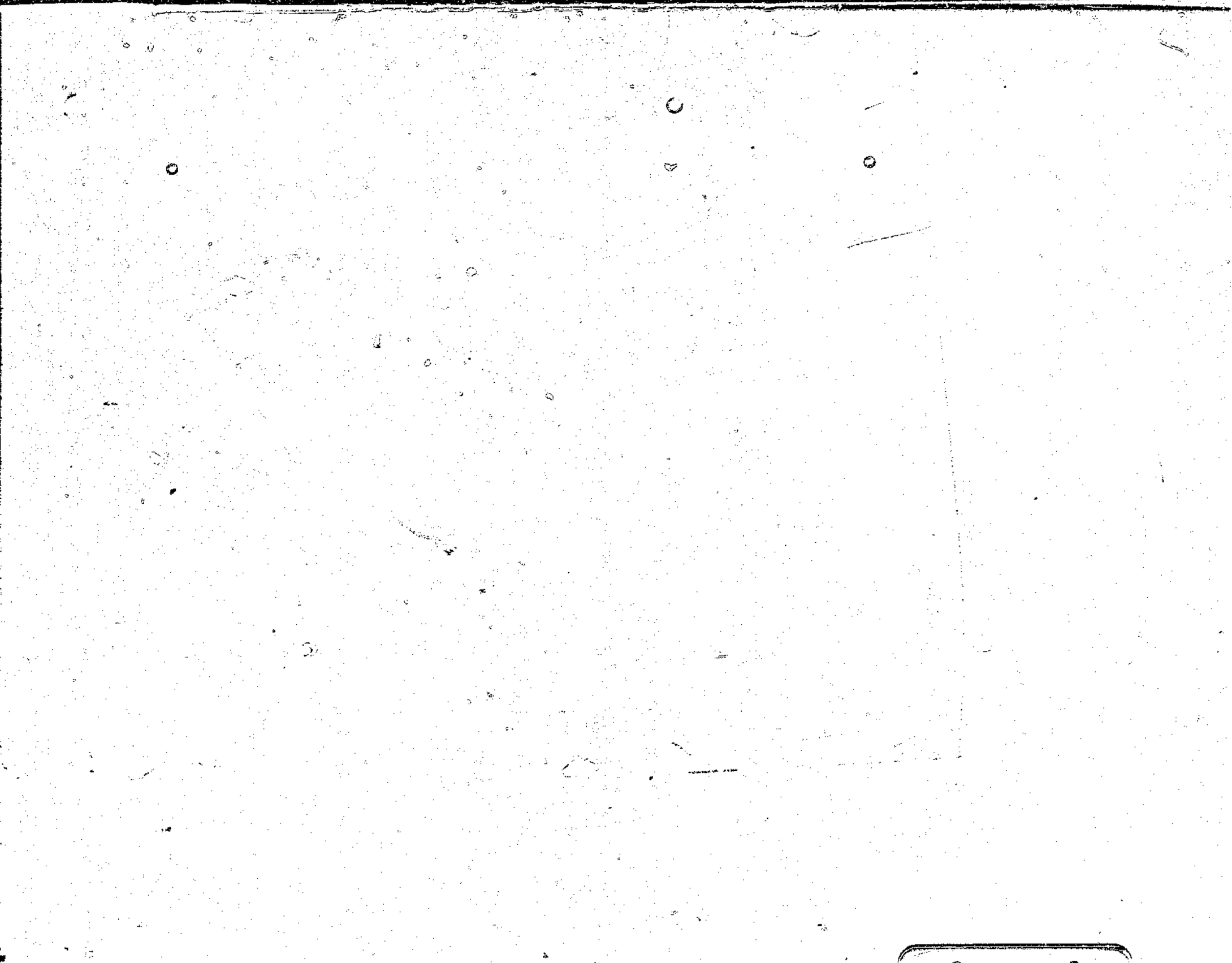
Chondrite normalization factors							Evensen et al. (1978)	
2.45	0.2446	0.6379	0.4738	0.154	0.05802	0.03745	0.0567	0.1651

Appendix 6 - REE, Ni, Co and Sc analysis in mineral separates

Table A6.5
Calculation of Ni. Sc and Co abundances in mineral separates analysed by INAA

Counts for clinopyroxene separates				Abundances within clinopyroxene (ppm)			
	Ni	Sc	Co		Ni	Sc	Co
H8N	824300	6433000	585900	H8N	316	87	64
H8N	786600	25770	571600	H8N	302		62
H6N	601100	7790000	744100	H6N	231	106	81
5LN	590900	8899000	869100	5LN	227	121	95
5MN	563300	7986000	772700	5MN	216	108	84
3MN	492900	7041000	820000	3MN	189	95	89
2LNa	527200	7707000	722100	2LNa	202	104	79
F2N	585200	8044000	745700	F2N	225	109	81
Counts for low-calcium pyroxene separates				Abundances within low-calcium pyroxene (ppm)			
H8N	1288000	2207000	1246000	H8N	494	30	136
H8N	1244000	2202000	1231000	H8N	477	30	134
H6N	828100	2719000	1419000	H6N	318	37	155
5LN	693300	2692000	1467000	5LN	266	36	160
5MN	759000	2753000	1496000	5MN	291	37	163
3MN	863500	2601000	1450000	3MN	331	35	158
2LNa	726100	2611000	1417000	2LNa	279	35	155
F2N	841300	2629000	1500000	F2N	323	36	164
Counts for plagioclase separates				Abundances within plagioclase (ppm)			
H8N	40580	95240	31410	H8N	6.6	0.6	1.4
H8N	40080	93200	33150	H8N	6.5	0.6	1.4
H6N	19840	65290	26500	H6N	3.2	0.5	1.1
5LN	19600	47410	23680	5LN	3.2	0.4	1.0
5MN	22300	51510	30550	5MN	3.6	0.4	1.3
3MN	31580	52460	28180	3MN	5.1	0.4	1.2
2LNa	15910	41280	15440	2LNa	2.6	0.3	0.7
F2N	20210	57960	29370	F2N	3.3	0.4	1.3





Author: Quadling Kevin Edward.

Name of thesis: The layered marker sequence, main zone. Eastern Bushveld Complex • a model for modal layering.

PUBLISHER:

University of the Witwatersrand, Johannesburg
©2015

LEGALNOTICES:

Copyright Notice: All materials on the University of the Witwatersrand, Johannesburg Library website are protected by South African copyright law and may not be distributed, transmitted, displayed or otherwise published in any format, without the prior written permission of the copyright owner.

Disclaimer and Terms of Use: Provided that you maintain all copyright and other notices contained therein, you may download material (one machine readable copy and one print copy per page)for your personal and/or educational non-commercial use only.

The University of the Witwatersrand, Johannesburg, is not responsible for any errors or omissions and excludes any and all liability for any errors in or omissions from the information on the Library website.